

# **Shear Performance of Heavily Reinforced High-Strength Concrete Coupling Beams**

by

Andrew Walter Fisher

A thesis submitted in conformity with the requirements  
for the degree of Master of Applied Science

Graduate Department of Civil Engineering  
University of Toronto

© Copyright by Andrew Walter Fisher 2016

# Shear Performance of Heavily Reinforced High-Strength Concrete Coupling Beams

Andrew Walter Fisher

Master of Applied Science

Graduate Department of Civil Engineering  
University of Toronto

2016

## Abstract

High-strength, heavily reinforced concrete coupling beams that have compact designs are critical to the building economics of high-rise structures. There is concern with these heavily reinforced designs that the phenomenon of concrete side cover spalling may occur as the coupling beams approach failure, causing an unintended loss of strength and stiffness. To investigate these consequences, four full-scale coupling beams with varying concrete strengths, reinforcement ratios, and side cover thicknesses were tested. It was observed that the concrete side cover spalled for all four specimens. In situations where the beam design capacity is close to the upper limits of shear capacity, a significant reduction in strength could occur as the concrete crushes before the stirrups yield. While the CSA Code had an average test-to-prediction ratio of 1.05 for the specimen peak load, the limits imposed by the ACI Code under predicted the peak load with test-to-prediction ratios as high as 1.45.

## Acknowledgments

I am very grateful to my supervisors, Professor Michael P. Collins and Professor Evan C. Bentz, for their guidance, education, and encouragement throughout the duration of this project. Their knowledge of reinforced concrete structures is remarkable, and I am glad to have had the privilege of furthering the research in this field.

I would like to thank the University of Toronto Director of Technical Services: Renzo Basset, for helping manage the laboratory requirements of this project. I would also like to thank laboratory technicians Giovanni Buzzeo, Bryant Cook, Michel Fiss, John MacDonald, Alan McClenaghan, and Xiaoming Sun for their assistance during the construction, instrumentation, and testing phases; their practical advice was critical to the success of this project.

To my research group, I thank you for your assistance in the lab, encouragement in the office, and friendship during my time in Toronto. I'd like to thank Paolo Calvi, Giorgio Proestos, Paola Miglietta, Phil Quach, and David Ruggiero for their early morning help on casting days. I also want to thank Edvard Bruun, Giorgio Proestos, Phil Quach, and Allan Quan for their complete assistance during my time with an injured ankle. The laboratory tests would have had to be put on hold without their two weeks of dedicated support. I want to specifically thank Giorgio Proestos for being a mentor and good friend. His willingness to teach the fine art of the lab helped turn what at the start seemed a daunting task to the reality presented in this thesis.

To my good friend Rami Mansour, I am glad to have shared the graduate school experience with you. To my parents, your endless encouragement and support has always been valued. Lastly, I would like to thank my partner, Jesse McGinnis, for his unconditional support over these last two and a half years.

# Table of Contents

<b>Acknowledgments .....</b>	<b>iii</b>
<b>Table of Contents .....</b>	<b>iv</b>
<b>List of Tables .....</b>	<b>viii</b>
<b>List of Figures.....</b>	<b>ix</b>
<b>Chapter 1 : Introduction and Research Justification .....</b>	<b>1</b>
1.1 Coupling Beam Design Code Limitations .....	3
1.2 Coupling Beam Concrete Side Cover Spalling.....	4
1.3 Objective of Research.....	7
<b>Chapter 2 : Analysis and Design Methods.....</b>	<b>8</b>
2.1 The CSA A23.3-14 Code.....	8
2.1.1 <i>The Modified Compression Field Theory</i> .....	8
2.1.2 <i>The CSA General Method</i> .....	10
2.2 The ACI 318-14 Code.....	11
<b>Chapter 3 : Experimental Design and Construction .....</b>	<b>13</b>
3.1 Test Assembly Design .....	13
3.2 Specimen Design and Geometry.....	15
3.3 Shear Wall Design and Geometry .....	17
3.3.1 <i>Cantilever Beam Design</i> .....	18
3.3.2 <i>Post-Tensioning Design</i> .....	19
3.3.3 <i>Lifting Insert Design</i> .....	19
3.4 Material Properties.....	20
3.4.1 <i>Steel Reinforcing Bars</i> .....	20
3.4.2 <i>Concrete</i> .....	21
3.5 Construction of Test Assembly.....	27
3.5.1 <i>Formwork</i> .....	27

3.5.2	<i>Reinforcing Cages</i> .....	28
3.5.3	<i>Accessory Placement</i> .....	31
3.5.4	<i>Concrete Casting and Finishing</i> .....	32
<b>Chapter 4 : Testing of Specimens</b>	.....	<b>36</b>
4.1	Experimental Setup.....	36
4.1.1	<i>Lateral Bracing</i> .....	38
4.1.2	<i>Boundary Conditions</i> .....	39
4.1.3	<i>Self-Weight Jacks</i> .....	40
4.2	Test Assembly Setup .....	43
4.2.1	<i>LVDTs and Linear Pots</i> .....	47
4.2.2	<i>LED Targets and Metris K610 Camera System</i> .....	50
4.2.3	<i>Reinforcement Strain Gauges</i> .....	52
4.3	Testing of Specimens.....	53
4.3.1	<i>Test Preparations</i> .....	53
4.3.2	<i>Loading Protocol</i> .....	56
4.3.3	<i>Test Overview</i> .....	57
4.3.4	<i>Test Observations for Specimen CBF1</i> .....	60
4.3.5	<i>Test Observations for Specimen CBF2</i> .....	65
4.3.6	<i>Test Observations for Specimen CBF3</i> .....	69
4.3.7	<i>Test Observations for Specimen CBF4</i> .....	73
<b>Chapter 5 : Discussion of Experimental Results</b>	.....	<b>78</b>
5.1	Sectional Strains .....	79
5.1.1	<i>LVDT Shear Strains</i> .....	79
5.1.2	<i>LVDT z-Direction Strains</i> .....	81
5.2	Local Reinforcement Strains .....	83
5.2.1	<i>Transverse Reinforcement Strains</i> .....	84

<i>5.2.2 Longitudinal Reinforcement Strains .....</i>	<i>85</i>
5.3 Element Strains .....	88
<i>5.3.1 LED Shear Strains .....</i>	<i>93</i>
<i>5.3.2 LED x-Direction and z-Direction Strains .....</i>	<i>94</i>
<i>5.3.3 LED Principal Compressive Strains.....</i>	<i>94</i>
5.4 Shear on the Crack.....	95
5.5 Out-of-Plane Expansion.....	99
<i>5.5.1 Out-of-Plane Linear Pot Displacements.....</i>	<i>99</i>
<i>5.5.2 Out-of-Plane Reinforcement Strains.....</i>	<i>101</i>
<i>5.5.3 Out-of-Plane LED Displacements .....</i>	<i>103</i>
<i>5.5.4 Influence of Concrete Side Cover Thickness.....</i>	<i>105</i>
<i>5.5.5 Influence of Concrete Strength .....</i>	<i>106</i>
<i>5.5.6 Influence of Transverse Reinforcement Ratios .....</i>	<i>107</i>
<b>Chapter 6 : Comparison of Observed Response to MCFT and Code Predictions .....</b>	<b>109</b>
6.1 MCFT Predictions using Program Membrane.....	109
6.2 MCFT Predictions using Program Response.....	112
6.3 Code Predictions for the Strength of Coupling Beams .....	115
6.4 Influence of Cover Spalling on Predicated Shear Strength .....	116
<b>Chapter 7 : Conclusions and Recommendations .....</b>	<b>118</b>
<b>References .....</b>	<b>120</b>
<b>Appendix A : Digital Drawings for Experimental Program .....</b>	<b>124</b>
<b>Appendix B : Design Calculations for Test Assembly .....</b>	<b>149</b>
<b>Appendix C : Material Test Data .....</b>	<b>155</b>
C.1 Steel Coupon Test Data .....	155
C.2 Concrete Cylinder Test Data.....	160
<b>Appendix D : Photographs of Specimens.....</b>	<b>165</b>

D.1 Photographs of Specimen CBF1 .....	165
D.2 Photographs of Specimen CBF2.....	172
D.3 Photographs of Specimen CBF3 .....	183
D.4 Photographs of Specimen CBF4.....	193
<b>Appendix E : Strain Gauge Data .....</b>	<b>201</b>
<b>Appendix F : LED Element Data .....</b>	<b>205</b>
F.1 LED Element Data for Specimen CBF1 .....	205
F.2 LED Element Data for Specimen CBF2.....	216
F.3 LED Element Data for Specimen CBF3 .....	224
F.4 LED Element Data for Specimen CBF4.....	235
<b>Appendix G : Mander Model for Confined Concrete .....</b>	<b>245</b>

## List of Tables

<b>Table 3-1: Summary of Coupling Beam Specimen Properties .....</b>	<b>17</b>
<b>Table 3-2: Reinforcing Cage Assembly for Coupling Beam Specimens .....</b>	<b>29</b>
<b>Table 3-3: Reinforcing Cage Assembly for Shear Wall Components .....</b>	<b>30</b>
<b>Table 4-1: Testing Schedule for CBF1-4.....</b>	<b>57</b>
<b>Table 4-2: Machine Load, P, at Load Stages, Peak Load, and End of Post-Peak [kN].....</b>	<b>58</b>
<b>Table 5-1: Summary of Experimental Observations .....</b>	<b>78</b>
<b>Table 5-2: Tangential Displacement due to Pure Shear at Peak Load .....</b>	<b>80</b>
<b>Table 5-3: LVDT and LED Average Shear Strain Comparison for CBF1 to CBF4 .....</b>	<b>93</b>
<b>Table 5-4: Shear Capacity at the Crack for CBF1 to CBF4 .....</b>	<b>99</b>
<b>Table 5-5: Summary of Out-of-Plane Mid-Height Expansion for CBF1 to CBF4 .....</b>	<b>101</b>
<b>Table 6-1: Code Predictions for Strengths of Coupling Beams .....</b>	<b>115</b>

## List of Figures

<b>Figure 1-1: Reinforced Concrete Coupled Shear Wall System for the Burj Khalifa .....</b>	<b>2</b>
<b>Figure 1-2: Loading of Coupled Shear Wall System .....</b>	<b>2</b>
<b>Figure 1-3: Shear Strength as a Function of the Normalized Shear Reinforcement Ratio....</b>	<b>4</b>
<b>Figure 1-4: Side Cover Spalling Due to Torsion .....</b>	<b>5</b>
<b>Figure 1-5: Side Cover Spalling Due to Shear.....</b>	<b>5</b>
<b>Figure 1-6: Observed and Predicted Results for SA Test Series .....</b>	<b>6</b>
<b>Figure 2-1: Equations of the Modified Compression Field Theory (MCFT) .....</b>	<b>9</b>
<b>Figure 3-1: Sadler Test Rig .....</b>	<b>13</b>
<b>Figure 3-2: Conceptual Design of Test Assembly .....</b>	<b>14</b>
<b>Figure 3-3: Interchangeable Test Setup by Montgomery .....</b>	<b>15</b>
<b>Figure 3-4: Test Assembly Reinforcement Design .....</b>	<b>18</b>
<b>Figure 3-5: M24 (1") Type EC-2FW Insert.....</b>	<b>20</b>
<b>Figure 3-6: Coupon Test Data for Reinforcing Bars .....</b>	<b>21</b>
<b>Figure 3-7: Moist Curing of Concrete.....</b>	<b>22</b>
<b>Figure 3-8: Cast 1 Concrete Slump Test Before and After Superplasticizer .....</b>	<b>22</b>
<b>Figure 3-9: Cast 2 Concrete Slump Test.....</b>	<b>23</b>
<b>Figure 3-10: Cast 3 Concrete Slump Flow Test Before and After Superplasticizer .....</b>	<b>24</b>
<b>Figure 3-11: Cast 4 Concrete Slump Flow Test Before and After Mixing .....</b>	<b>24</b>
<b>Figure 3-12: Concrete Cylinder Strength Gain.....</b>	<b>25</b>
<b>Figure 3-13: Cast 3 Stress-Strain Curves for Test-Day Concrete Cylinders.....</b>	<b>26</b>

<b>Figure 3-14: Cast 4 Stress-Strain Curves for Test-Day Concrete Cylinders.....</b>	<b>26</b>
<b>Figure 3-15: Formwork for Shear Wall Components (left) and Specimens (right).....</b>	<b>28</b>
<b>Figure 3-16: Reinforcing Cage Assembly for Coupling Beam Specimens.....</b>	<b>29</b>
<b>Figure 3-17: Reinforcing Cage Assembly for Shear Wall Components .....</b>	<b>30</b>
<b>Figure 3-18: Post-Tensioning Duct Placement for Coupling Beam Specimens .....</b>	<b>31</b>
<b>Figure 3-19: Post-Tensioning Duct Placement for Shear Wall Components .....</b>	<b>31</b>
<b>Figure 3-20: Lifting Insert Placement for Coupling Beam Specimens .....</b>	<b>32</b>
<b>Figure 3-21: Lifting Insert Placement for Shear Wall Components .....</b>	<b>32</b>
<b>Figure 3-22: Cast 1 and Cast 2 Concrete Bucket and Vibrator Usage .....</b>	<b>33</b>
<b>Figure 3-23: Highlights from Cast 1 and Cast 2 .....</b>	<b>33</b>
<b>Figure 3-24: Cast 4 Formwork Failure .....</b>	<b>34</b>
<b>Figure 3-25: Highlights from Cast 3 and Cast 4 .....</b>	<b>34</b>
<b>Figure 3-26: Grouting of Coupling Beam End Sections.....</b>	<b>35</b>
<b>Figure 4-1: Meccano Frame Test Setup.....</b>	<b>37</b>
<b>Figure 4-2: Spreader Beam Assembly with Brackets .....</b>	<b>38</b>
<b>Figure 4-3: Lateral Bracing for Test Setup .....</b>	<b>39</b>
<b>Figure 4-4: Pin Support Reaction with and without Bearing Plate .....</b>	<b>40</b>
<b>Figure 4-5: Influence Self-Weight on Coupling Beam Loading .....</b>	<b>41</b>
<b>Figure 4-6: Placement of Self-Weight Hydraulic Jacks .....</b>	<b>42</b>
<b>Figure 4-7: West and East Self-Weight Hydraulic Jack Assemblies.....</b>	<b>42</b>

<b>Figure 4-8: Installation of West Cantilever and East Rectangular Components .....</b>	<b>43</b>
<b>Figure 4-9: Installation of Coupling Beam Specimen CBF1.....</b>	<b>44</b>
<b>Figure 4-10: Installation of West Rectangular Shear Wall Component.....</b>	<b>45</b>
<b>Figure 4-11: Installation of East Cantilever Shear Wall Component .....</b>	<b>46</b>
<b>Figure 4-12: Post-Tensioning of Test Assembly Components .....</b>	<b>47</b>
<b>Figure 4-13: Installed Coupling Beam LVDTs and Linear Pots .....</b>	<b>48</b>
<b>Figure 4-14: Tangential Displacement Setup .....</b>	<b>49</b>
<b>Figure 4-15: LVDTs and Linear Pot Instrumentation of Coupling Beam .....</b>	<b>50</b>
<b>Figure 4-16: Metris K610 LED Target Layout and Labelling Scheme .....</b>	<b>51</b>
<b>Figure 4-17: Metris K610 Camera System Field of View.....</b>	<b>52</b>
<b>Figure 4-18: Strain Gauge Layouts for CBF1 to CBF4.....</b>	<b>52</b>
<b>Figure 4-19: West-East Alignment of Test Assembly .....</b>	<b>54</b>
<b>Figure 4-20: Real-time Visualization of Data Channels for Test of CBF2 .....</b>	<b>55</b>
<b>Figure 4-21: Experimental Test Setup .....</b>	<b>56</b>
<b>Figure 4-22: Machine Load Variation due to Self-Weight Jack Friction.....</b>	<b>58</b>
<b>Figure 4-23: Shear Force vs. Tangential Displacement for CBF1 to CBF4 .....</b>	<b>59</b>
<b>Figure 4-24: Shear Force vs. Tangential Displacement for CBF1 (repeat of Fig. 4-23).....</b>	<b>60</b>
<b>Figure 4-25: Photograph of CBF1 at Load Stage 1.....</b>	<b>61</b>
<b>Figure 4-26: Photograph of CBF1 at Load Stage 3.....</b>	<b>61</b>
<b>Figure 4-27: Crack Propagation in East Shear Wall End Block for CBF1.....</b>	<b>63</b>

<b>Figure 4-28: Photograph of CBF1 at Load Stage 6.....</b>	<b>63</b>
<b>Figure 4-29: Flexural Crack Offset Observed from Bottom Surface of CBF1 .....</b>	<b>63</b>
<b>Figure 4-30: Photograph of CBF1 at Peak Load .....</b>	<b>64</b>
<b>Figure 4-31: Photograph of CBF1 at end of Post-Peak .....</b>	<b>64</b>
<b>Figure 4-32: Loose Concrete Cover Removed for CBF1 .....</b>	<b>65</b>
<b>Figure 4-33: Shear Force vs. Tangential Displacement for CBF2 (repeat of Fig. 4-23).....</b>	<b>65</b>
<b>Figure 4-34: Photograph of CBF2 at Load Stage 1.....</b>	<b>66</b>
<b>Figure 4-35: Photograph of CBF2 at Load Stage 3.....</b>	<b>66</b>
<b>Figure 4-36: Photograph of CBF2 at Load Stage 6.....</b>	<b>67</b>
<b>Figure 4-37: Crack Propagation in East Shear Wall End Block for CBF2.....</b>	<b>68</b>
<b>Figure 4-38: Photograph of CBF2 at Load Stage 7.....</b>	<b>68</b>
<b>Figure 4-39: Photograph of CBF2 at Peak Load .....</b>	<b>68</b>
<b>Figure 4-40: Photograph of CBF2 at end of Post-Peak .....</b>	<b>69</b>
<b>Figure 4-41: Loose Concrete Cover Removed for CBF2 .....</b>	<b>69</b>
<b>Figure 4-42: Shear Force vs. Tangential Displacement for CBF3 (repeat of Fig. 4-23).....</b>	<b>70</b>
<b>Figure 4-43: Photograph of CBF3 at Load Stage 1.....</b>	<b>70</b>
<b>Figure 4-44: Photograph of CBF3 at Load Stage 3.....</b>	<b>71</b>
<b>Figure 4-45: Crack Propagation in East Shear Wall End Block for CBF3.....</b>	<b>71</b>
<b>Figure 4-46: Photograph of CBF3 at Load Stage 6.....</b>	<b>72</b>
<b>Figure 4-47: Photograph of CBF3 at Peak Load .....</b>	<b>72</b>

<b>Figure 4-48: Photograph of CBF3 at end of Post-Peak .....</b>	<b>73</b>
<b>Figure 4-49: Loose Concrete Cover Removed for CBF3 .....</b>	<b>73</b>
<b>Figure 4-50: Shear Force vs. Tangential Displacement for CBF4 (repeat of Fig. 4-23).....</b>	<b>74</b>
<b>Figure 4-51: Photograph of Shear Cracks on North Face of CBF4 at Load Stage 2 .....</b>	<b>74</b>
<b>Figure 4-52: Photograph of South Face of CBF4 at Load Stage 2 .....</b>	<b>75</b>
<b>Figure 4-53: Photograph of CBF4 at Load Stage 3.....</b>	<b>75</b>
<b>Figure 4-54: Crack Propagation in East Shear Wall End Block for CBF4.....</b>	<b>76</b>
<b>Figure 4-55: Photograph of CBF4 at Load Stage 6.....</b>	<b>76</b>
<b>Figure 4-56: Photograph of CBF4 at Peak Load .....</b>	<b>76</b>
<b>Figure 4-57: Photograph of CBF4 at end of Post-Peak .....</b>	<b>77</b>
<b>Figure 4-58: Loose Concrete Cover Removed for CBF4 .....</b>	<b>77</b>
<b>Figure 5-1: Sectional Shear Stress vs. Shear Strain for CBF1 to CBF4 .....</b>	<b>79</b>
<b>Figure 5-2: Evaluation of Elastic Stiffness for CBF1.....</b>	<b>81</b>
<b>Figure 5-3: Sectional Shear Stress vs. z-Direction Strain for CBF1 to CBF4 .....</b>	<b>82</b>
<b>Figure 5-4: Zoomed in Stirrup Yield Points on Stress-Strain Plots for CBF1 to CBF4.....</b>	<b>83</b>
<b>Figure 5-5: Local Transverse Reinforcement Strains for CBF1 to CBF4 .....</b>	<b>84</b>
<b>Figure 5-6: Local Longitudinal Reinforcement Strains for CBF1 to CBF4 .....</b>	<b>86</b>
<b>Figure 5-7: LED Element Labelling Scheme.....</b>	<b>88</b>
<b>Figure 5-8: LED Elements at Peak Load for CBF1 .....</b>	<b>89</b>
<b>Figure 5-9: LED Elements at Peak Load for CBF2.....</b>	<b>90</b>

<b>Figure 5-10: LED Elements at Peak Load for CBF3.....</b>	<b>91</b>
<b>Figure 5-11: LED Elements at Peak Load for CBF4.....</b>	<b>92</b>
<b>Figure 5-12: Crack Widths for CBF1 to CBF4 .....</b>	<b>95</b>
<b>Figure 5-13: Widths and Angles of Largest Cracks at Final Load Stage for CBF1&amp;2.....</b>	<b>96</b>
<b>Figure 5-14: Widths and Angles of Largest Cracks at Final Load Stage for CBF3&amp;4.....</b>	<b>96</b>
<b>Figure 5-15: Crack Widths and Angles at Final Stage for CBF1 and CBF2 .....</b>	<b>97</b>
<b>Figure 5-16: Crack Widths and Angles at Final Stage for CBF3 and CBF4 .....</b>	<b>98</b>
<b>Figure 5-17: Sectional Shear Stress vs. Shear Strain for CBF1 to CBF4 .....</b>	<b>100</b>
<b>Figure 5-18: Out-of-Plane Reinforcement Strains for CBF1 and CBF2 .....</b>	<b>101</b>
<b>Figure 5-19: Longitudinal Cracking along Length of CBF2 .....</b>	<b>102</b>
<b>Figure 5-20: Visualization of LED Element Out-of-Plane Strains for CBF1 .....</b>	<b>103</b>
<b>Figure 5-21: Visualization of LED Element Out-of-Plane Strains for CBF2 .....</b>	<b>103</b>
<b>Figure 5-22: Visualization of LED Element Out-of-Plane Strains for CBF3.....</b>	<b>104</b>
<b>Figure 5-23: Visualization of LED Element Out-of-Plane Strains for CBF4.....</b>	<b>104</b>
<b>Figure 5-24: Shear Force vs. Tangential Displacement for CBF1 and CBF2 .....</b>	<b>105</b>
<b>Figure 5-25: Shear Force vs. Tangential Displacement for CBF2 and CBF3 .....</b>	<b>106</b>
<b>Figure 5-26: Shear Force vs. Tangential Displacement for CBF3 and CBF4 .....</b>	<b>107</b>
<b>Figure 6-1: Stress-Strain Curve for Confined Concrete of Rectangular Members.....</b>	<b>109</b>
<b>Figure 6-2: MCFT Predictions for Midspan Elements of CBF1 to CBF4.....</b>	<b>110</b>
<b>Figure 6-3:Shear Key Developed along Failure Crack of CBF4 .....</b>	<b>112</b>

**Figure 6-4: Stress-Strain of Confined Concrete using Popovics-Mander Model..... 112**

**Figure 6-5: Crack Patterns in Shear Wall End Blocks (repeat of figures)..... 113**

**Figure 6-6: Shear Force vs. Tangential Displacement Predictions for CBF1 to CBF4..... 114**

**Figure 6-7: Influence of Side Cover Spalling on the Code Predicted Shear Strength..... 117**

# Chapter 1: Introduction and Research Justification

As Canada's urbanization trends remain strong, the need for high-density development in urban centres has continued to rise. Toronto, Vancouver, and Montreal all show high-rise development remaining steady due to increased economic growth in 2015, with trends showing it continuing into 2016 [1]. Toronto alone had 56 buildings over 100 meters tall being constructed or completed in 2015 [2]. This trend is not exclusive to Canada, with 988 buildings over 150 meters tall being constructed or completed worldwide in 2015, with 12% of those buildings being over 300 meters tall [2].

As engineers design buildings to be taller and more slender to meet the demand for high-density development, the more sensitive they become to lateral dynamic loading typically caused by the wind. As these loads exceed certain levels, accelerations of the building can become perceivable to the occupants causing mild to extreme discomfort. The design of the lateral load resisting system of a building is typically governed at the Service Limit State (SLS) by these accelerations.

One of the most common lateral load resisting systems for high-rise buildings are reinforced concrete coupled shear wall systems. Figure 1-1a shows a photo of the Burj Khalifa in Dubai, currently the tallest structure in the world [2], and its coupled shear wall system in Figure 1-1b. These systems consist of large concrete walls that rise the full height of the building. In order to accommodate floorplan designs, these walls typically require openings for doorways, hallway corridors, or windows at regular intervals over the full building height. The walls are connected by coupling beams located above each of these openings. Figure 1-1c [3] shows a sample floorplan of the Burj Khalifa, which highlights some locations of the shear walls and coupling beams.

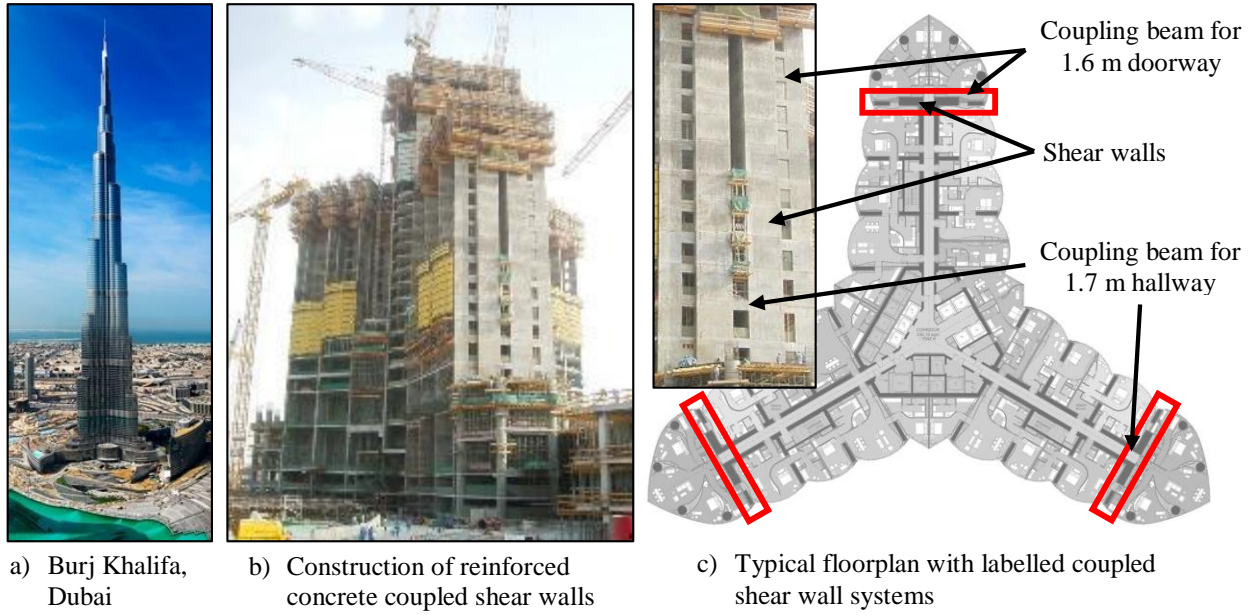


*Figure 1-1: Reinforced Concrete Coupled Shear Wall System for the Burj Khalifa*

As the name implies, coupling beams couple the set of shear walls together, allowing them to act as one unit under lateral loading and thereby significantly improving the stiffness of the building. Under lateral wind or earthquake loads, these coupling beams experience significant shear forces and shear deformations shown in Figure 1-2b. The forces generated in a coupling beam under lateral loading are summarized in Figure 1-2c as shear force and bending moment diagrams.

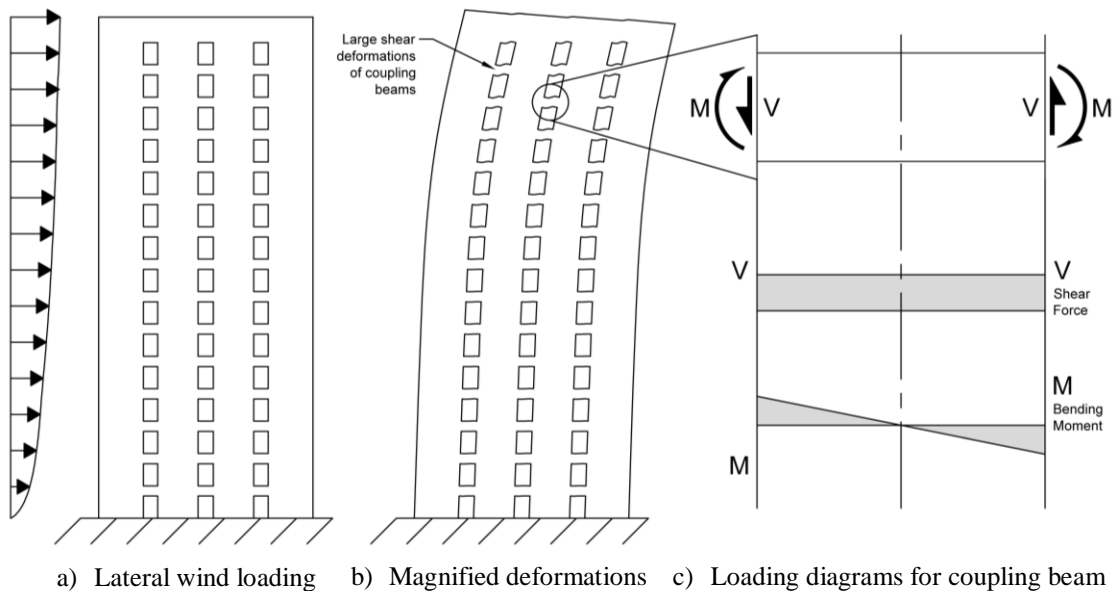


*Figure 1-2: Loading of Coupled Shear Wall System*

In many high-rise reinforced concrete structures, the coupling beam depth is what dictates the floor-to-floor storey height. With many cities having restrictions on building height due to permitting requirements, engineers design coupling beams to be as shallow as possible in order to maximize the number of storeys and improve the economy of the building. As a result, coupling beams are often designed using high-strength concrete with large longitudinal and shear reinforcement ratios in order to resist the large shear forces in a compact design. The overall size is often governed by the code specified upper limits on shear capacity.

## 1.1 Coupling Beam Design Code Limitations

The American Concrete Institute (ACI) 318-14 Code [4] and the Canadian Standards Association (CSA) A23.3-14 Code [5] are the two primary design standards for reinforced concrete structures in North America. Each of these standards have specified limits on the maximum shear capacity of a reinforced concrete beam in order to prevent an over-reinforced shear failure. This undesirable sudden failure mode is characterized by diagonal crushing of the concrete prior to yielding of the shear reinforcement. In 1962, the ACI-ASCE Committee 326 on “Shear and Diagonal Tension” [6] recommended that the failure shear stress of a reinforced concrete beam not exceed an empirically derived value of  $0.83\sqrt{f'_c}$  MPa. This limit is the sum of a conservative concrete contribution of  $0.17\sqrt{f'_c}$  MPa and a maximum shear reinforcement contribution of  $0.66\sqrt{f'_c}$  MPa. These design limits were implemented in 1963 ACI 318 Code [7] and are still present today. The CSA code uses entirely different shear design procedures which are based on the Modified Compression Field Theory (MCFT) [8]. These design procedures limit the failure shear stress to  $0.25f'_c$  MPa, which is based on the crushing capacity of cracked concrete in diagonal compression [9].

An experimental study by Lee and Hwang [10] demonstrated the ACI Code shear capacity limits were far too conservative for high-strength concrete beams with large amounts of shear reinforcement. The experimental results shown in Figure 1-3 [10] which show each code limit as vertical lines, clearly demonstrates that heavily reinforced high-strength concrete beams can achieve strengths well above, and in some cases double the ACI Code limit.

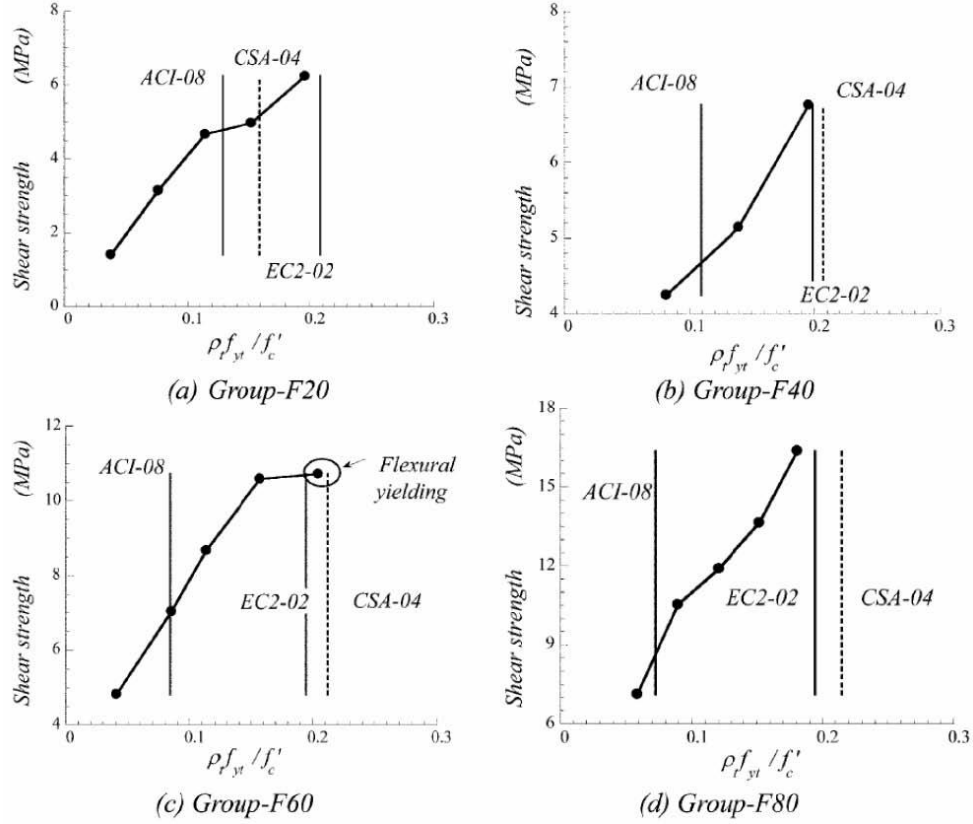


Figure 1-3: Shear Strength as a Function of the Normalized Shear Reinforcement Ratio

a)  $f'_c = 27 \text{ MPa}$  b)  $f'_c = 37 \text{ MPa}$  c)  $f'_c = 63 \text{ MPa}$  d)  $f'_c = 85 \text{ MPa}$

The ACI Code upper limit on shear capacity significantly hinders the design and optimization of reinforced concrete coupling beams. In some cases, coupling beams could be over-designed by a factor of two. Revisiting the validity of this limit could significantly reduce the size and amount of reinforcement needed in coupling beams, which would improve both the building economics and reduce the complexities involved in coupling beam construction.

## 1.2 Coupling Beam Concrete Side Cover Spalling

There is concern that shear-critical heavily reinforced concrete beams, such as coupling beams, could experience concrete side cover spalling as it approaches failure. Due to the design requirements that the longitudinal reinforcement of coupling beams be anchored inside the layers of shear wall reinforcement, coupling beams tend to have significant side cover thicknesses. With a loss of this side cover, the effective width of the coupling beam can significantly reduce and potentially cause premature failure.

Side cover spalling due to both torsion and shear is caused by the change in direction of the diagonal compression stresses as they approach the corner of the member. The principal compression stress trajectory in the concrete side cover curves in towards the corner longitudinal bar, resulting in principal tensile stresses that are perpendicular to the transverse reinforcement. At higher shear stresses, there can be enough perpendicular tension in the concrete side cover to cause it to split away from the transverse reinforcement down to its centerline. Figure 1-4 [11] and Figure 1-5, modified from [11], show the compression stress trajectories for torsion and shear, and the resulting side cover spalling phenomenon.

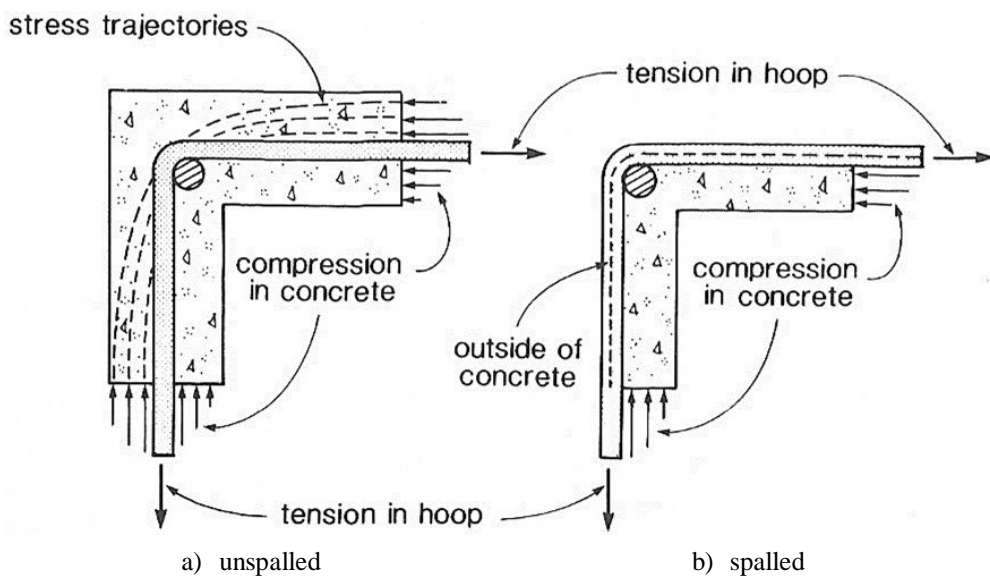


*Figure 1-4: Side Cover Spalling Due to Torsion*

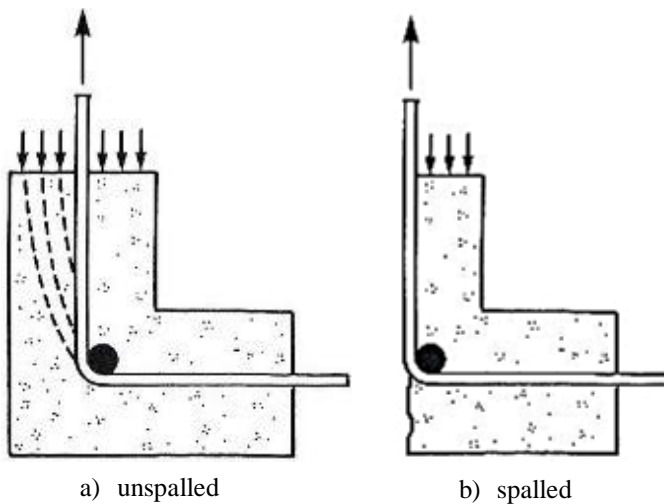


*Figure 1-5: Side Cover Spalling Due to Shear*

Tests performed by Arbesman at the University of Toronto for development of the Compression Field Theory (CFT) [12] investigated this phenomenon. Specimens SA3 and SA4 were identical in design except SA3 had zero concrete side cover, while SA4 had 40 mm. Both beams had a large amount of shear reinforcement with  $\rho_v f_y / f'_c$  equaling 0.116. The full geometric properties of the specimens are presented in Figure 1-6 [13] along with the observed and predicted failure shears.

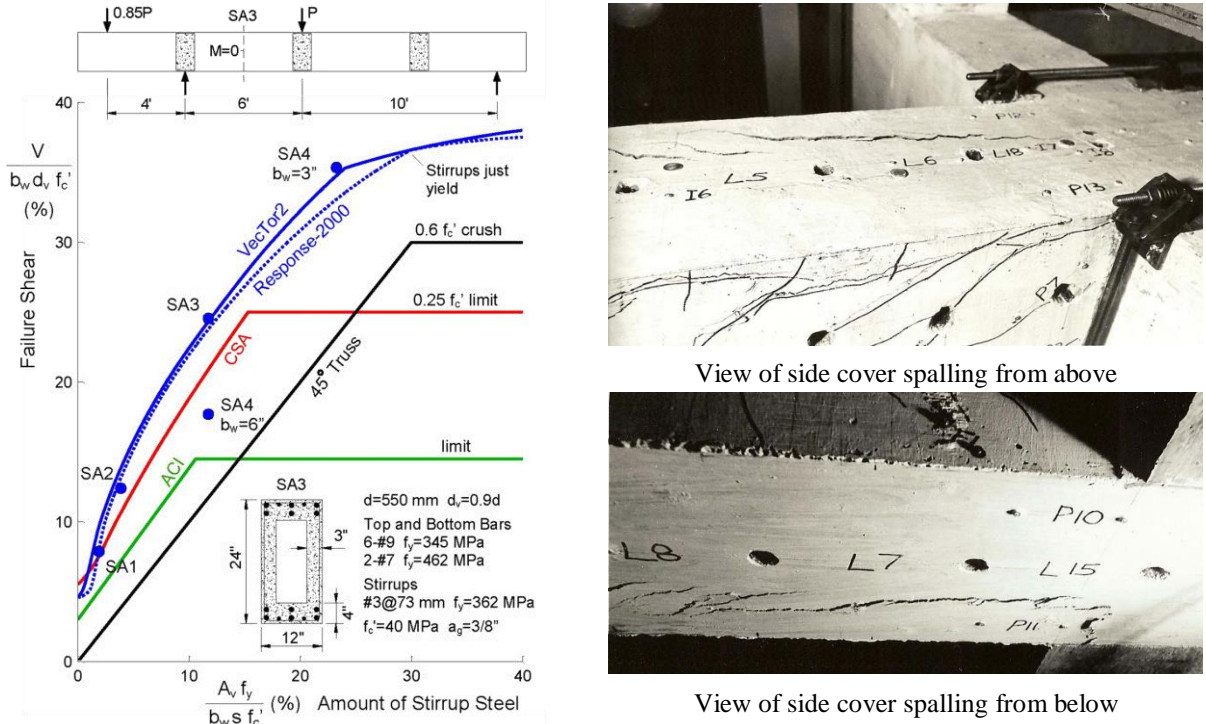


Figure 1-6: Observed and Predicted Results for SA Test Series

During testing of SA4, it was observed that the concrete side cover spalled as the stirrups began to yield, reducing the effective width of the beam from 152 mm (6") to 76 mm (3"). This resulted in a capacity that was 73% that of SA3. If the width of the beam is assumed to remain at 152 mm (6"), the observed failure is substantially below the predicted values (labelled SA4,  $b_w=6"$  in Figure 1-6). However, if the width is assumed to be the spalled width of 76 mm (3"), the experimental value is accurately predicted (labelled SA4,  $b_w=3"$  in Figure 1-6).

In order to account for this side cover loss in the design standards, Clause 11.2.10.5 was recently added to the CSA A23.3-14 Code [4]. The clause states:

*“The minimum area of shear reinforcement specified by Equation (11-1) is calculated using the unspalled web width. When the area of shear reinforcement exceeds eleven times this calculated minimum amount, spalling of the concrete side cover shall be accounted for in determining  $b_w$ ; otherwise spalling may be neglected. If spalling is to be accounted for, the concrete side cover down to the centreline of the outermost reinforcement shall be assumed to have spalled off unless the ends of the compression diagonals are restrained against spalling.”*

Equation (11-1), the minimum shear reinforcement, is defined as  $A_v \geq 0.06\sqrt{f'_c}b_w s/f_y \text{ mm}^2$ . Rearranging this equation, dividing by  $d$ , and multiplying by the specified eleven results in  $v \geq 0.66\sqrt{f'_c} \text{ MPa}$ . This value is identical to the limit imposed on the shear contribution of the transverse reinforcement in the ACI Code. This implies that concrete side cover spalling does not need to be accounted for in the ACI Code since there is no beam that can be designed with enough shear reinforcement to have spalling significantly impact the shear capacity.

Although the SA test series showed that concrete side cover spalling can occur in beams with high shear reinforcement levels, the specimens had unique box beam geometry not typical to industry. To create a more robust experimental database on this issue, full scale coupling beams need to be tested in order to accurately demonstrate that the side cover spalling phenomenon can occur with typical industry designs.

### 1.3 Objective of Research

The experimental program conducted for this thesis is designed to show that concrete side cover spalling can occur for a typical coupling beam design. Four coupling beam specimens with varying concrete strengths, reinforcement ratios, and side cover thicknesses will be tested to failure in order to demonstrate how side cover spalling influences the overall shear capacity. The failure shear will be compared to that predicted by the CSA and ACI Codes in order to demonstrate the inadequacy of the ACI Code shear capacity limits. Results of this research will also improve understanding of the conditions in which spalling of the concrete side cover will be critical.

# Chapter 2: Analysis and Design Methods

The CSA and ACI design codes provide guidance on the use of sectional and strut-and-tie models for the shear design of reinforced concrete members. Sectional models are based on the assumption that plane sections remain plane, and are largely independent of how the forces are introduced to the member [14]. Strut-and-tie models however, are primarily used for disturbed regions where there is a complex flow of internal stresses and the principles of sectional design do not apply. Strut-and-tie models are typically used for the design of deep beams where the shear span to depth ( $a/d$ ) ratio is less than 2.0. Since the coupling beams designed for this experimental program have  $a/d$  ratios greater than 2.0, this chapter will focus on the development of the sectional shear models used in the CSA and ACI codes.

## 2.1 The CSA A23.3-14 Code

The sectional shear model used in the CSA design code is based on the Modified Compression Field Theory (MCFT). This theory was developed at the University of Toronto as a rational method for designing and analyzing complex reinforced and prestressed concrete structures subjected to shear.

### 2.1.1 The Modified Compression Field Theory

In 1974, Mitchell and Collins [15], based on research at the University of Toronto, proposed a rational method for predicting the response of reinforced concrete members in pure torsion. Using concepts from the truss analogy proposed by Ritter (1899) [16] and Mörsch (1902) [17] in combination with the principles of the tension field theory developed by Wagner (1929) [18] for aluminum aircraft structures, the diagonal compressional field theory was developed. In 1978, this method for solving the response of members in pure torsion was applied to members in pure shear in the form of the Compression Field Theory (CFT) [12]. This model is able to predict the full load-deformation response of reinforced concrete members subjected to shear using equilibrium, compatibility, and stress-strain relationships. Since the CFT ignores the average concrete tensile stresses between cracks, it is unable to model members that contain no transverse reinforcement.

Additional research performed by Collins and Vecchio [19] in 1982, and further developed into a classic ACI paper in 1986 [8], enabled the CFT to be extended to account for the tensile stresses that on average exist in cracked reinforced concrete. This research resulted in the development of the Modified Compression Field Theory (MCFT) which is able to predict the response of reinforced concrete members with and without transverse reinforcement [20]. The 15 equations used in the MCFT are presented in Figure 2-1.

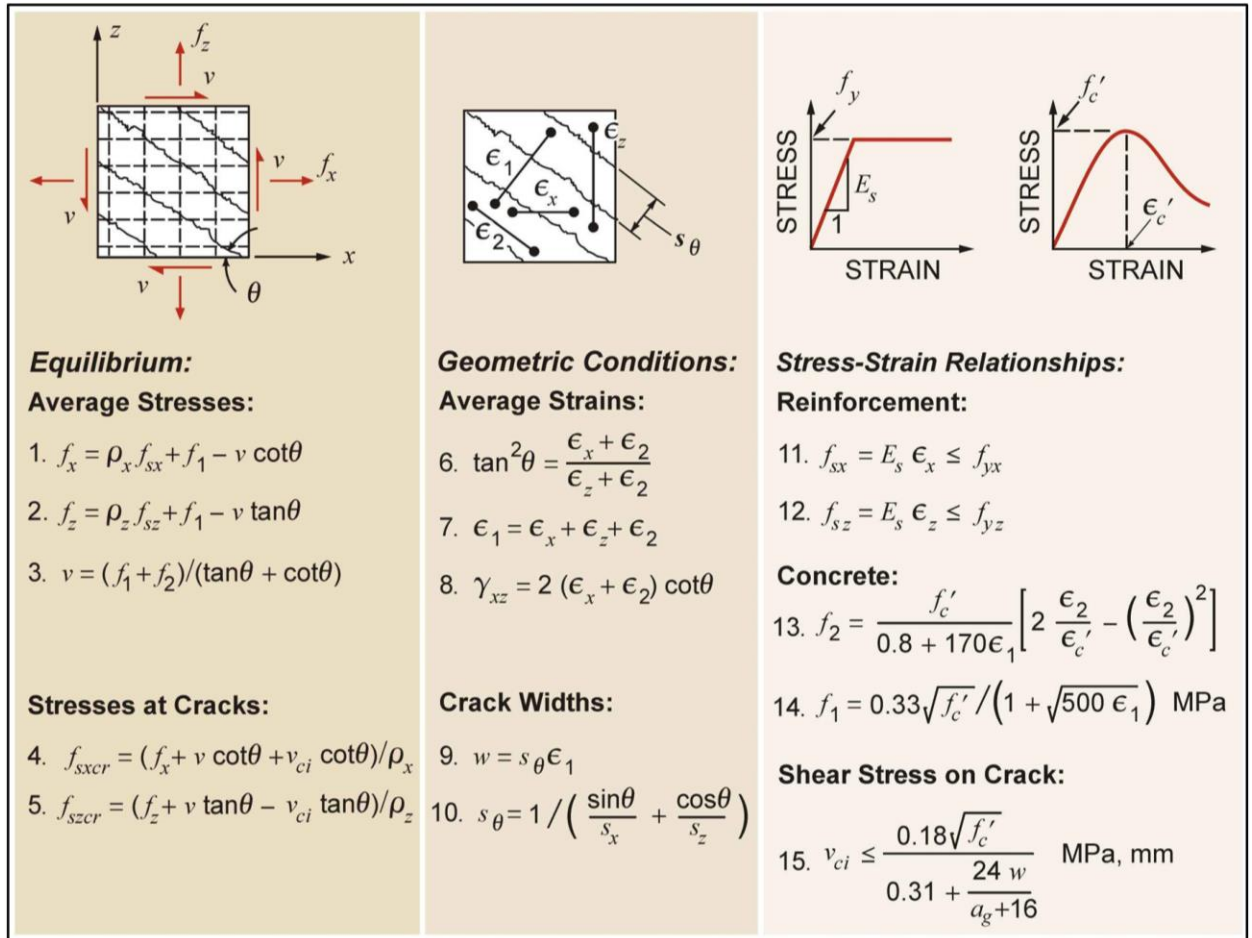


Figure 2-1: Equations of the Modified Compression Field Theory (MCFT)

Compression softening, tension stiffening, and shear stress on a crack are of particular importance to the MCFT (equations 13, 14 and 15 in Figure 2-1). Diagonally cracked concrete in the web of a member experiences significant tensile strains not captured in a standard concrete cylinder test. Investigations by Vecchio and Collins [19] showed that the concrete compressive strength is not only a function of the principal compressive strain,  $\epsilon_2$ , but also the principal

tensile strain,  $\varepsilon_1$ . As this tensile strain increases, there is a reduction in concrete strength known as compression softening.

Once the concrete has cracked, on average, the concrete is still able to carry tensile stresses. This is due to the phenomenon of tension stiffening, where the concrete tensile stress are zero at a crack and increase to a maximum between the cracks. These tensile stresses allow for the MCFT to predict the capacity of members without transverse reinforcement [8].

The average stresses and strains do not capture the local variations at crack locations. At the crack, in addition to a loss of concrete tensile capacity, there is an increase in tensile stresses in the reinforcement. The ability for a member to carry shear across the crack is based on the concrete strength, crack width, and maximum aggregate size, also known as aggregate interlock. If the crack widths become large enough, the shear capacity of a member can be governed by the ability for shear to be carried across a crack.

### 2.1.2 The CSA General Method

The sectional shear model used in the CSA design code implements a more simplified version of the MCFT called the General Method. The shear strength is derived from the MCFT and is comprised of an aggregate interlock component,  $V_c$ , and a steel component based on the amount of transverse reinforcement that crosses a diagonal crack,  $V_s$  [9]. The shear strength formula is summarized in Equation 2-1 in SI units.

$$V_r = V_c + V_s \leq 0.25 f'_c b_w d_v$$

$$\frac{V_c}{b_w d_v} = \lambda \cdot \frac{0.4 \sqrt{f'_c}}{(1+1500\varepsilon_x)} \cdot \frac{1300}{(1000+s_{ze})} \quad (2-1)$$

$$\frac{V_s}{b_w d_v} = \rho_v f_y \cot(29^\circ + 7000\varepsilon_x)$$

The shear capacity is limited to  $0.25 f'_c b_w d_v$ , which is based on the crushing capacity of diagonally cracked concrete. The shear area of the member is computed using the effective web width,  $b_w$ , and the flexural lever arm,  $d_v$ , where  $d_v$  is calculated as the larger of  $0.9d$  or  $0.72h$ .

The formula for  $V_c$  is a product of three distinct terms. The first term  $\lambda$ , is a factor that accounts for low-density concrete. The second term is a simplification of equation 15 from Figure 2-1, where the effective crack spacing is set to 300 mm and the diagonal crack width is modelled as a linear relationship with the longitudinal strain,  $\varepsilon_x$ , shown in Equation 2-2.

$$w = 0.2 + 1000\varepsilon_x \quad (2-2)$$

The longitudinal strain,  $\varepsilon_x$ , is taken as the strain at mid-depth of the member and is derived from compatibility and the applied loading of the member, shown in Equation 2-3.

$$\varepsilon_x = \frac{M_f/d_v + V_f - V_p + 0.5N_f - A_p f_{po}}{2(A_s E_s + A_p E_p)} \quad (2-3)$$

This formula makes the assumption that at mid-depth,  $0.5 \cot \theta$  is equal to approximately 1.0, therefore eliminating the need for iteration when solving for  $\varepsilon_x$  [9]. The final condition for the second term is that the concrete strength  $\sqrt{f'_c}$  is not to be taken larger than 8 MPa. This is to account for the reduced crack capacity in high strength concrete caused by smoother cracks that form through the aggregate.

The third term in the formula for  $V_c$  is a size effect term that accounts for member depth and aggregate size. The effective crack spacing,  $s_{ze}$ , is calculated using Equation 2-4.

$$s_{ze} = \frac{35s_z}{(15+a_g)} \geq 0.85s_z \quad (2-4)$$

For members with stirrups, the term  $s_z$  is taken as 300 mm, and for members without stirrups, the term is taken as the depth  $d_v$ .

The term  $V_s$  is calculated using a variable-angle truss model where the angle of principal compression,  $\theta$ , is defined as  $29^\circ + 7000\varepsilon_x$ . This linear relationship fits within the bounds of possible angles governed by the maximum shear stress of  $0.25f'_c$  [9].

## 2.2 The ACI 318-14 Code

Unlike the CSA code which is based on the MCFT, the ACI sectional shear model is an empirical extension of the 45-degree truss model originally proposed by Mörsch in 1902 [14], [17]. The shear strength formula is comprised of a concrete contribution,  $V_c$ , equal to the shear

that causes diagonal cracking, and a steel component,  $V_s$ , calculated using the 45-degree truss equations. The simplified shear strength formula is summarized in Equation 2-5 in SI units.

$$V_n = V_c + V_s \leq 0.83\sqrt{f'_c}b_w d$$

$$V_c = 0.17\lambda\sqrt{f'_c}b_w d \quad (2-5)$$

$$V_s = \frac{A_v f_y d}{s} \leq 0.66\sqrt{f'_c}b_w d$$

The shear capacity is limited to a maximum of  $0.83\sqrt{f'_c}b_w d$ . The shear area of the member is computed using the effective web width,  $b_w$ , and effective depth  $d$ . This differs from the CSA code which recommends the use of the approximate flexural lever arm  $d_v$  for calculating the shear area.

The concrete contribution,  $V_c$ , is a simplified formula used for non-prestressed members derived from empirical test data. The concrete strength  $\sqrt{f'_c}$  is not to be taken larger than 8.3 MPa to account for the reduced crack capacity of high strength concrete.

The steel contribution,  $V_s$ , is limited to  $0.66\sqrt{f'_c}b_w d$  which is intended to prevent an over-reinforced failure by diagonal crushing of the concrete. Since this limit is a function of  $\sqrt{f'_c}$  rather than  $f'_c$  like the CSA code, members that utilize high strength concrete do not receive a proportional increase in this limit. As a result, the limit is often described as “penalizing” the use of high-strength concrete.

# Chapter 3: Experimental Design and Construction

Four full scale coupling beam specimens were tested under simulated building loading in the University of Toronto Mark Higgins Structures Laboratory. The coupling beam specimens were constructed with varying concrete side cover thicknesses, concrete strengths, and amounts of shear reinforcement. To test the specimens under appropriate loading, a new test assembly was developed. This section will elaborate on the design and construction of the specimens and test assembly. Properties of the materials used in the construction will also be presented. A full set of design drawings for the coupling beam specimens and test assembly components are given in Appendix A.

## 3.1 Test Assembly Design

In order to properly test a coupling beam, it is important to allow full rotation of its ends in order to prevent any undesired restraint which could artificially strengthen the member. The original experimental design planned to use the test rig developed by Sadler [21]. This rig transfers an applied load, having a line of action through the specimen centreline, into end blocks cast monolithically with the specimen. Unfortunately, this setup has a design capacity of only 890 kN which did not permit the loading to failure of the fully sized heavily reinforced coupling beam designs needed to demonstrate the concrete side cover spalling phenomenon. The Sadler test rig is shown in Figure 3-1 [21].

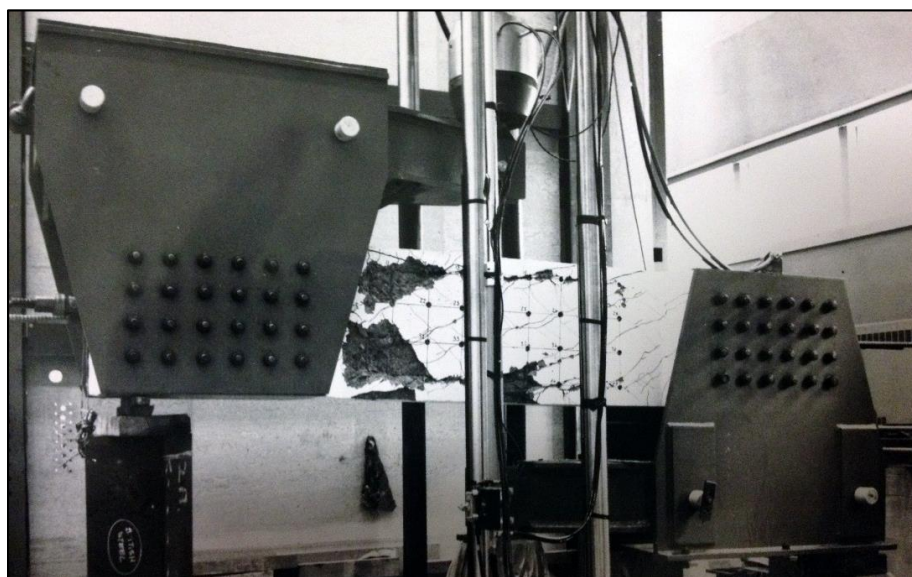
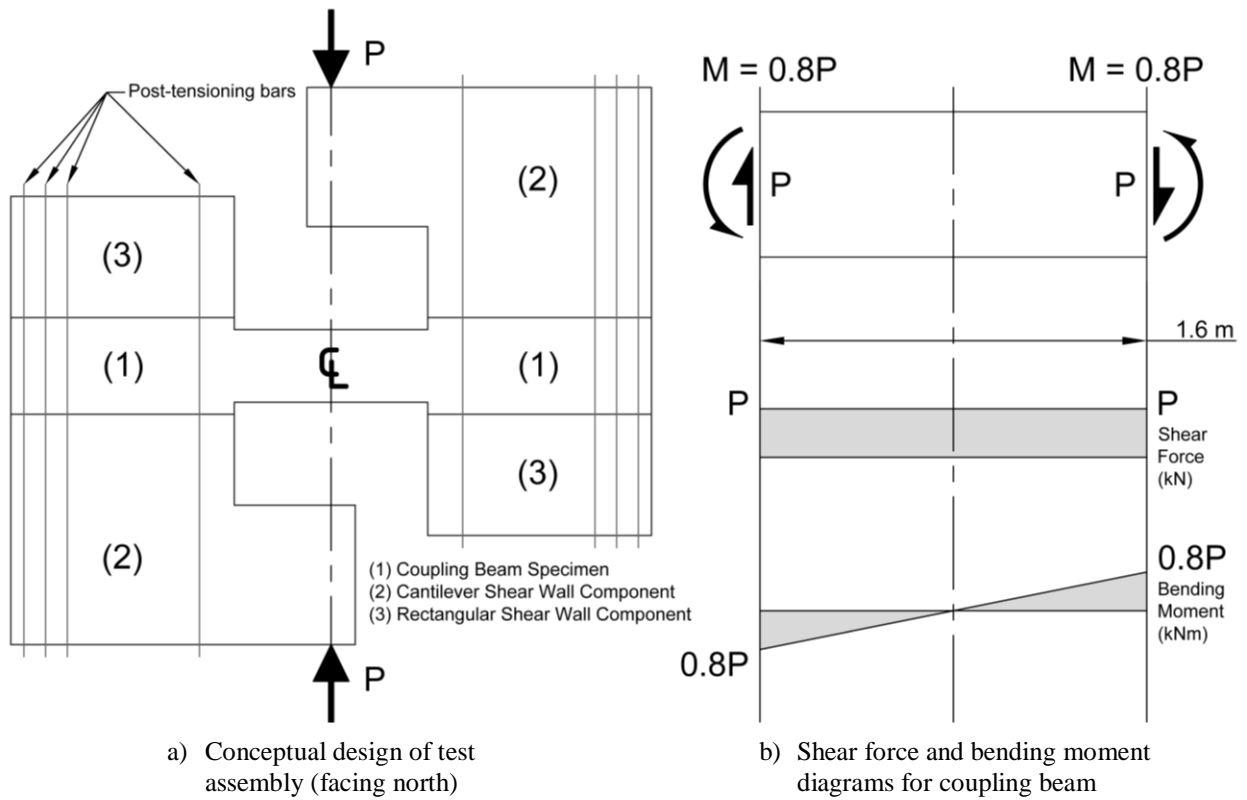


Figure 3-1: Sadler Test Rig

Instead of modifying the Sadler test rig to increase its design capacity, it was decided that an entirely new test assembly be designed and constructed. The new test assembly was composed of a full scale 1.6 m long coupling beam with representative shear walls. The shear walls were included in the design to better represent the boundary conditions of the coupling beam and to observe the interaction between the wall and coupling beam at failure. The test assembly was designed to simulate the double curvature of a coupling beam by applying a point load with a line-of-action through the coupling beam centreline, similar to the Sadler test rig, as illustrated in Figure 3-2a. Cantilever beams constructed monolithically with the shear walls transfer the point load into the coupling beam, resulting in the shear force and bending moment diagrams illustrated in Figure 3-2b.



*Figure 3-2: Conceptual Design of Test Assembly*

In order to minimize materials while still being able to test multiple specimens, the test assembly was further divided into five components. Inspiration for this test assembly originated from the test setup used by Montgomery [22] shown in Figure 3-3 [22].



*Figure 3-3: Interchangeable Test Setup by Montgomery*

The coupling beam was constructed monolithically with shear wall end blocks to ensure proper development of the longitudinal steel. The coupling beam with shear wall end blocks, labelled (1) in Figure 3-2a, is considered the coupling beam specimen and is what is interchangeable for each test. The two cantilever and two rectangular shear wall components, labelled (2) and (3) in Figure 3-2a, are identical in design due to the symmetry of the applied load. These components are reused for each test. High-strength post-tensioning bars that run through cast-in steel ducts are used to post-tension the test assembly components together.

### 3.2 Specimen Design and Geometry

The experimental program consists of four coupling beam specimens named CBF1, CBF2, CBF3 and CBF4. The test specimens are composed of a 1600 mm long x 600 mm deep coupling beam constructed monolithically with 1850 x 800 x 400 mm shear wall end blocks. The thickness of the shear walls and the length and depth of the coupling beams were chosen based on sizes used in two high-rise reinforced concrete structures. This was done to ensure the designs were typical of industry practice. As shown in Table 3-1, all specimens were designed with twelve 30M longitudinal bars near the top and bottom faces of the cross-section. The bars had a tested yield strength of 563 MPa and gave the coupling beam sections a predicted flexural capacity that was

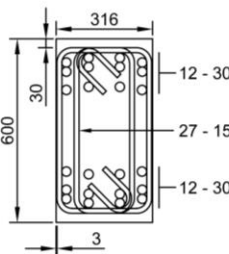
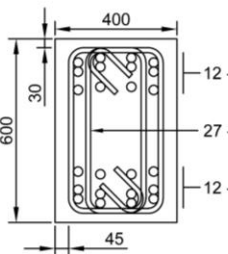
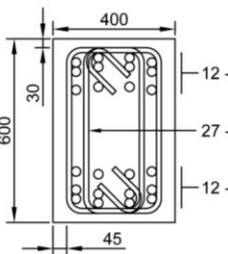
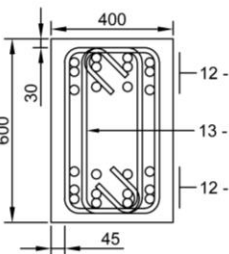
1.3 times higher than the highest predicted shear capacity, thus ensuring that all four specimens would fail in shear. The longitudinal bars continue into the full length of the shear wall end blocks in order to allow for proper bar development. The transverse reinforcement, shown in Table 3-1, was designed using 15M stirrups with a tested yield strength of 422 MPa. Each stirrup wraps around three of the four rows of longitudinal bars so that the stirrups could be offset along the length of the beam. This was done to prevent closely spaced stirrups from influencing the side cover spalling phenomena. The specimens were cast in pairs using high-strength self-consolidating concrete with a specified maximum aggregate size of 14 mm. CBF1 and CBF2 were cast on April 13, 2015 reaching a test-day concrete strength of 80.3 MPa. CBF3 and CBF4 were cast on June 17, 2015 reaching a test-day concrete strength of 66.5 MPa.

The primary variables altered between the specimens was the concrete side cover thickness, concrete strength, and percentage of shear reinforcement. CBF1 had a concrete side cover of 3 mm while CBF2 had a concrete side cover of 45 mm; all other variables between these two specimens were identical. CBF1 creates a baseline which CBF2 can be compared to, making it easier to detect when the concrete side cover starts to spall and how it influences the coupling beam behavior. It is predicted that if the concrete side cover spalls, CBF2 will behave similarly to CBF1.

CBF2 had a concrete strength of 80.3 MPa while CBF3 had a concrete strength of 66.5 MPa; all other variables between these two specimens were identical. The original intention for these specimens was to have concrete strengths close to 60 MPa and 40 MPa. CBF2 was to have a predicted capacity just below the  $0.25f'_c$  CSA Code shear capacity limit while CBF3 would be over. However, due to the variable nature of concrete mix design, the test day strengths far exceeded the original specifications, resulting in all specimens being below the  $0.25f'_c$  limit.

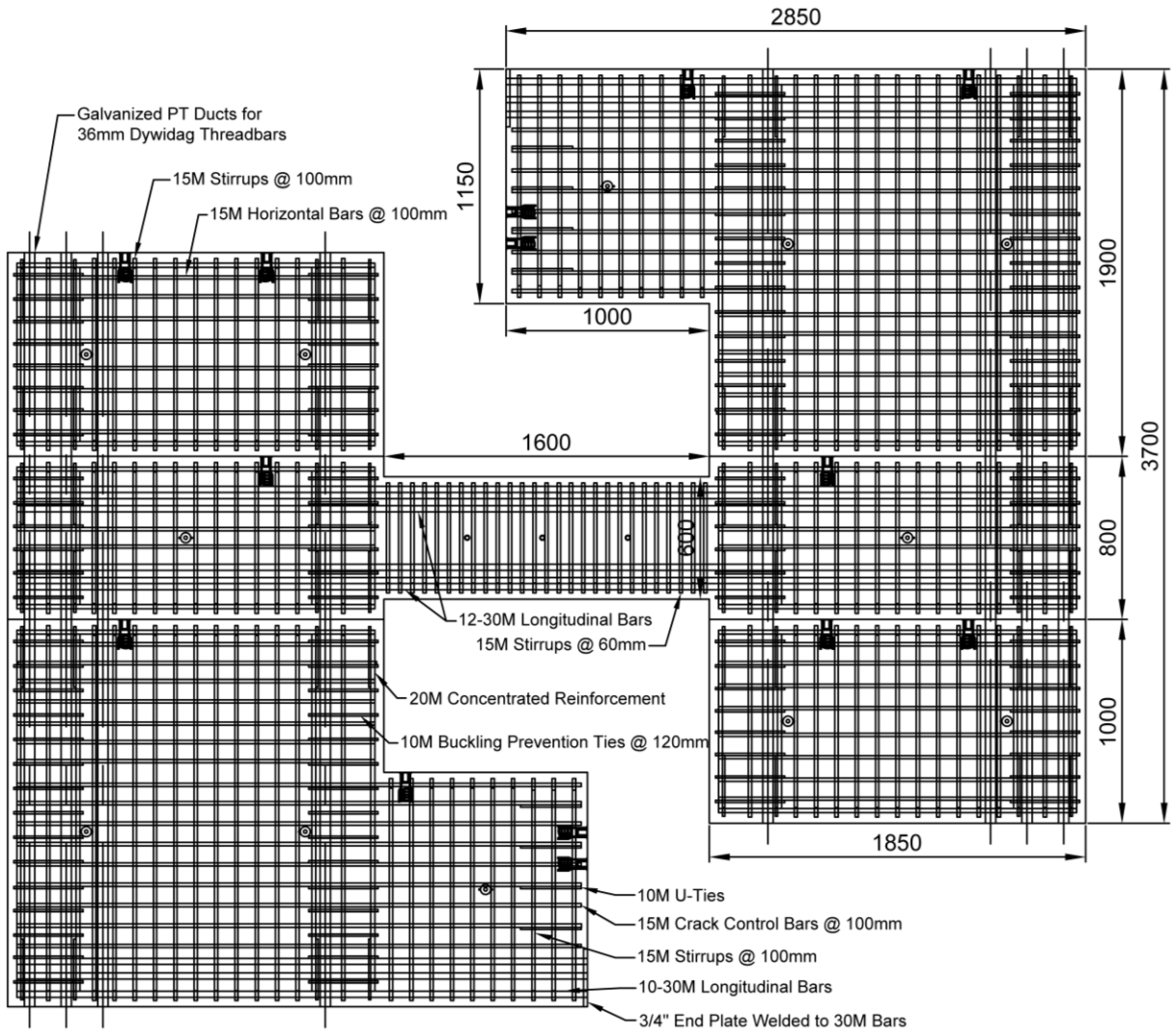
CBF3 had a shear reinforcement ratio of 1.67% while CBF4 had a shear reinforcement ratio of 0.83%; all other variables between these two specimens were identical. The amount of shear reinforcement in CBF3 greatly exceeded the eleven times minimum specified in CSA Clause 11.2.10.5, while CBF4 was below this minimum. This suggests that the side cover would spall for CBF3 but not for CBF4. The full set of properties for each coupling beam specimen are outlined in Table 3-1.

Table 3-1: Summary of Coupling Beam Specimen Properties

Geometry:	$L = 1600 \text{ mm}$	$h = 600 \text{ mm}$	$d = 488 \text{ mm}$	$d_v = 439 \text{ mm}$
x-Steel:	$A_{s,top} = 8400 \text{ mm}^2$	$A_{s,bot} = 8400 \text{ mm}^2$	$f_y = 563 \text{ MPa}$	
z-Steel:	$A_v = 400 \text{ mm}^2$	$f_{yz} = 422 \text{ MPa}$		
				
<b>CBF1</b>	$f_c' = 80.3 \text{ MPa}$ $b_w = 316 \text{ mm}$ $s = 60 \text{ mm}$ $\rho_z = A_v / b_w s = 2.11\%$ $\rho_z f_{yz} = 8.9 \text{ MPa}$ $A_{v,min} = 0.06 \sqrt{f_c' b_w s} / f_{yz} = 24 \text{ mm}^2$ $A_v / A_{v,min} = 18$	$f_c' = 80.3 \text{ MPa}$ $b_w = 400 \text{ mm}$ $s = 60 \text{ mm}$ $\rho_z = 1.67\%$ $\rho_z f_{yz} = 7.0 \text{ MPa}$ $A_{v,min} = 31 \text{ mm}^2$ $A_v / A_{v,min} = 14$	$f_c' = 66.5 \text{ MPa}$ $b_w = 400 \text{ mm}$ $s = 60 \text{ mm}$ $\rho_z = 1.67\%$ $\rho_z f_{yz} = 7.0 \text{ MPa}$ $A_{v,min} = 28 \text{ mm}^2$ $A_v / A_{v,min} = 15$	$f_c' = 66.5 \text{ MPa}$ $b_w = 400 \text{ mm}$ $s = 120 \text{ mm}$ $\rho_z = 0.83\%$ $\rho_z f_{yz} = 3.5 \text{ MPa}$ $A_{v,min} = 56 \text{ mm}^2$ $A_v / A_{v,min} = 8$

### 3.3 Shear Wall Design and Geometry

The shear walls are comprised of three sections: an 800 mm tall end block constructed monolithically with the coupling beam, a 1900 mm tall cantilever component, and a 1000 mm tall rectangular component. When assembled, the shear walls were 1850 mm long, 3700 mm tall, and 400 mm thick as shown in Figure 3-4. The shear walls were designed with 15M distributed wall reinforcement with a tested yield strength of 422 MPa and spaced at 100 mm in both directions. The vertical reinforcement was designed using stirrups rather than straight bars to ensure proper anchorage at the interfaces between the wall components. The shear walls are also designed with 20M concentrated reinforcement and 10M buckling prevention ties spaced at 120 mm as prescribed in CSA A23.3-04 Chapter 21: Special Provisions for Seismic Design [23]. The yield strengths of the bars were 436 MPa and 464 MPa respectively. The wall components were cast in pairs using high-strength concrete with a specified maximum aggregate size of 14 mm. The first pair of wall components were cast on December 4, 2014 reaching a test-day concrete strength of 87.7 MPa. The second pair of wall components were cast on January 9, 2015 reaching a test-day concrete strength of 83.8 MPa.



*Figure 3-4: Test Assembly Reinforcement Design*

In addition to the CSA Chapter 21 Special Provisions for Seismic Design, the shear walls were designed using the CSA A23.3-04 Chapter 11.4: Strut and Tie Model [23]. Since the wall components were to be reusable, they were designed with a capacity of 1.5 times the flexural capacity of the strongest coupling beam. The strongest specimen, CBF2, had a flexural failure load of 2556 kN, resulting in a design capacity of 3834 kN for the shear wall test assembly. A full set of calculations for the shear wall components are presented in Appendix B.

### 3.3.1 Cantilever Beam Design

The cantilever beam constructed monolithically with shear wall was 1000 mm long, 1150 mm deep, and 400 mm thick. The beam was designed with ten 30M longitudinal bars with a tested

yield strength of 563 MPa. The longitudinal bars continued into the full length of the shear wall in order to allow for proper bar development. In order to ensure proper anchorage at the face of the cantilever, a 400 x 285 x 19 mm thick plate was welded to the ends of the longitudinal bars. The transverse reinforcement was designed using 15M stirrups with a tested yield strength of 422 MPa and spaced at 100 mm. The 15M horizontal shear wall reinforcement spaced at 100 mm was continued into the cantilever in order to provide crack control reinforcement. 10M U-ties with a yield strength of 464 MPa were spaced 200 mm down the face of the cantilever to prevent out-of-plane splitting.

### 3.3.2 Post-Tensioning Design

Eight 36 mm (1-3/8") G150 THREADBARS supplied by DYWIDAG-Systems International (DSI) were used to post-tension the wall components together. The bars were 4.6 m long and had an ultimate strength of 1126 MPa: a number provided by DSI. In order to accommodate the post-tensioning bars, 50 mm O.D. galvanized steel ducts were cast into the shear wall components, running the entire height of each component.

Using the strut and tie design for the test assembly, it was determined that three post-tensioning bars were needed on the tension face of the wall to resist the overturning moment caused by the applied load. In order to balance the post-tensioning compressive force by the three bars, a single bar was added to the compression face of the wall in order to create a uniform stress over the wall length. The single bar was tensioned to 790 MPa. This value is 0.7 times the ultimate strength, and is the specified post-tensioning limit. This bar governed the amount of post-tensioning stress that could be applied to the shear wall components. The three bars in the tension face were each tensioned to one third, 265 MPa, of the stress used in the single bar. The post-tensioning resulted in a 2 MPa uniform stress over the length of the shear wall prior to loading.

### 3.3.3 Lifting Insert Design

In order to easily assemble the shear wall components, lifting inserts were placed in locations such that the laboratory crane would lift at the centre-of-mass. M24 (1") Type EC-2FW structural connection inserts, sourced from a Toronto supplier and shown in Figure 3-5, were chosen due to their compact size and ability to be cast flush with the surface of the concrete. The

inserts had a working load of 27 kN (3 tons) in both tension and shear. Two inserts were needed for the rectangular shear wall components; four inserts were needed for the cantilever shear wall components and the coupling beam specimens.



*Figure 3-5: M24 (1") Type EC-2FW Insert*

In addition to the M24 inserts, M16 (5/8") Type LF-W structural connection inserts were installed in the side surfaces of the coupling beam specimens and shear wall components. The purpose of these inserts was to act as connection points for anything that was needed during the testing process; whether it be ropes to help guide the components into place or cables from the instrumentation.

## 3.4 Material Properties

### 3.4.1 Steel Reinforcing Bars

The reinforcement used for this project was sourced from a supplier in Ontario. The 10M, 15M and 20M bars were ordered as Grade 400W; the 30M bars were order as Grade 500W. The 30M bars were sourced to have the highest strength available in order to increase the flexural capacity of the coupling beams while minimizing the number of bars. The bars were delivered in 6.0 m long bundles and were cut and bent into the desired shape in the University of Toronto Structures Laboratory. Three coupon tests were performed for each bar size. The coupon samples were taken from three different bar lengths to ensure a representative sample of test data. Figure 3-6

shows a representative coupon test for each bar type. The table in Figure 3-6 highlights the average properties for the three coupon tests including the stress,  $f_y$ , at which yielding occurred, the strain,  $\varepsilon_{sh}$ , at which strain hardening commenced, the maximum stress,  $f_u$ , which the coupon reached and associated strain,  $\varepsilon_u$ . The full set of coupon test data is available in Appendix C.1.

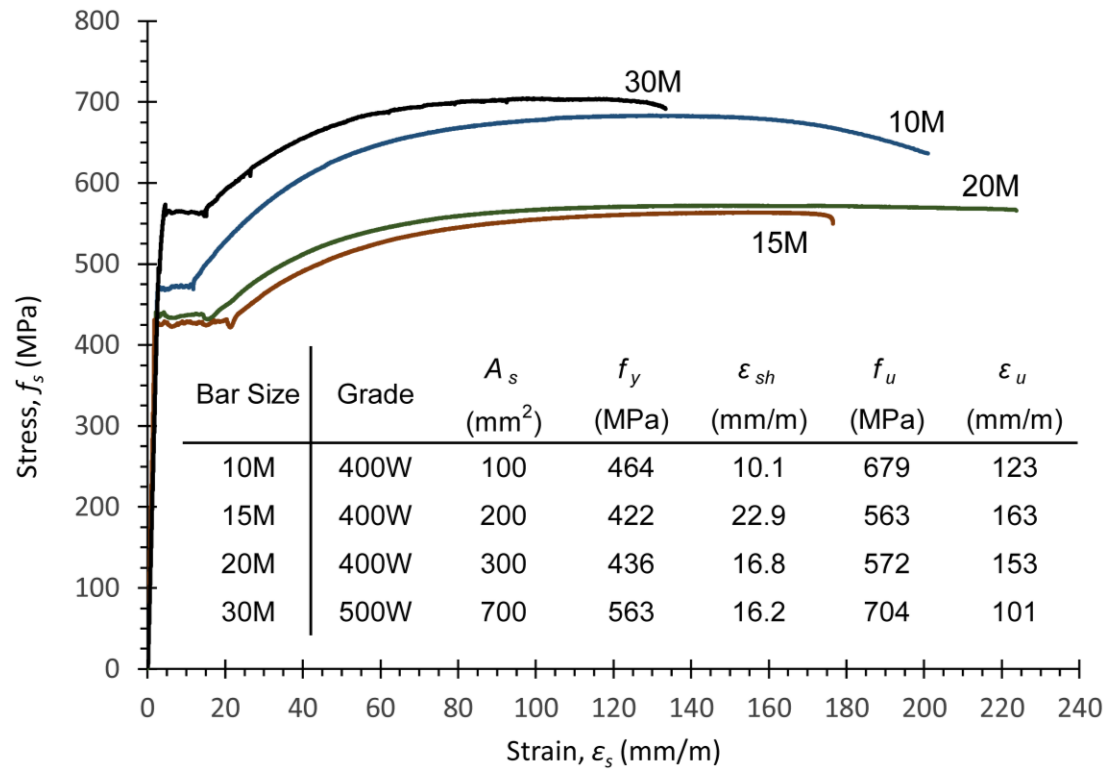


Figure 3-6: Coupon Test Data for Reinforcing Bars

### 3.4.2 Concrete

There were four concrete casts completed in order to construct the shear wall components and coupling beam specimens. All concrete was sourced from the same Toronto ready-mix supplier. The shear wall components were cast using high-strength concrete while the coupling beam specimens used high-strength self-consolidating concrete. Self-consolidating concrete was chosen for the specimens due to significant reinforcement congestion in the coupling beam. All casts used a specified maximum aggregate size of 14 mm to ensure proper consolidation around the congested reinforcement. Standard 6-inch diameter concrete cylinders were cast with each concrete pour and tested over the 28-day curing period. Cylinders were also saved and tested on the day of the coupling beam tests. All concrete was moist cured 5-7 days using wet fabric tarps and vapor barrier, shown in Figure 3-7, to achieve adequate strength gain.



*Figure 3-7: Moist Curing of Concrete*

Cast 1 occurred on December 4, 2014 for the first pair of shear wall components. Three cubic meters of concrete with a slump of 100 mm and a specified 28-day strength of 70 MPa was ordered. A standardized slump test prior to pouring resulted in a slump of 65 mm which was deemed too low. Superplasticizer was added to the concrete mix, resulting in a slump of 105 mm as shown in Figure 3-8. The specified 28-day strength was achieved in the first 9 days of curing, having an average 9-day cylinder strength of 72.3 MPa. The 33-day cylinder tests achieved an average strength of 85.4 MPa. Due to the limited number of cylinders cast, only a single cylinder was tested at 264 days, achieving a test-day strength of 87.7 MPa.



*Figure 3-8: Cast 1 Concrete Slump Test Before and After Superplasticizer*

Cast 2 occurred on January 9, 2015 for the second set of shear wall components. An identical concrete mix to Cast 1 was ordered. A standardized slump test prior to pouring resulted in a slump of 125 mm as shown in Figure 3-9. The specified 28-day strength was achieved in the first 14 days of curing, having an average 14-day cylinder strength of 78.6 MPa. The 26-day cylinder tests achieved an average strength of 82.3 MPa. Due to the limited number of cylinders cast, only a single cylinder was tested at 228 days, achieving a test-day strength of 83.8 MPa.



*Figure 3-9: Cast 2 Concrete Slump Test*

Cast 3 occurred on April 13, 2015 for specimens CBF1 and CBF2. Four cubic meters of concrete with a specified 28-day strength of 50 MPa was ordered. A standardized slump flow test prior to pouring resulted in a spread of 450 mm which was deemed too low. Superplasticizer was added to the concrete mix, resulting in a spread of 550 mm as shown in Figure 3-10. The specified 28-day strength was achieved in the first 7 days of curing, having an average 7-day cylinder strength of 61.0 MPa. The 28-day cylinder tests achieved an average strength of 75.7 MPa. Cylinder tests at 134 days achieved an average test-day strength of 80.3 MPa.



*Figure 3-10: Cast 3 Concrete Slump Flow Test Before and After Superplasticizer*

Cast 4 occurred on June 17, 2015 for specimens CBF3 and CBF4. Four cubic meters of concrete with a specified 28-day strength of 30 MPa was ordered. A standardized slump flow test prior to pouring resulted in an average spread of 690 mm. The concrete showed significant bleed water at the edges of the spread as well as some aggregate segregation. At the advice of the concrete truck driver, the concrete was re-mixed to eliminate any separation due to the truck travel time. The new concrete spread averaged 700 mm and showed less bleed water and aggregate segregation, shown in Figure 3-11. The specified 28-day strength was achieved in the first 5 days of curing, having an average 5-day cylinder strength of 43.5 MPa. The 28-day cylinder tests achieved an average strength of 60.4 MPa. Cylinder tests at 106 days achieved an average test-day strength of 66.5 MPa.



*Figure 3-11: Cast 4 Concrete Slump Flow Test Before and After Mixing*

A summary of the average concrete cylinder strength gains for each of the casts are shown in Figure 3-12. It is important to point out how quickly the concrete gained its specified 28-day strength. All four casts achieved this strength in less than 14 days, with the quickest being under 5 days. Of other significance is how quickly the strength gain tapered off after 28 days for the high-strength concrete in Cast 1 and 2. This can pose problems to engineers who rely on the later-in-life strength gain to overcome the strength loss due to long term loading [14]. While of concern, this will not be elaborated on for this thesis.

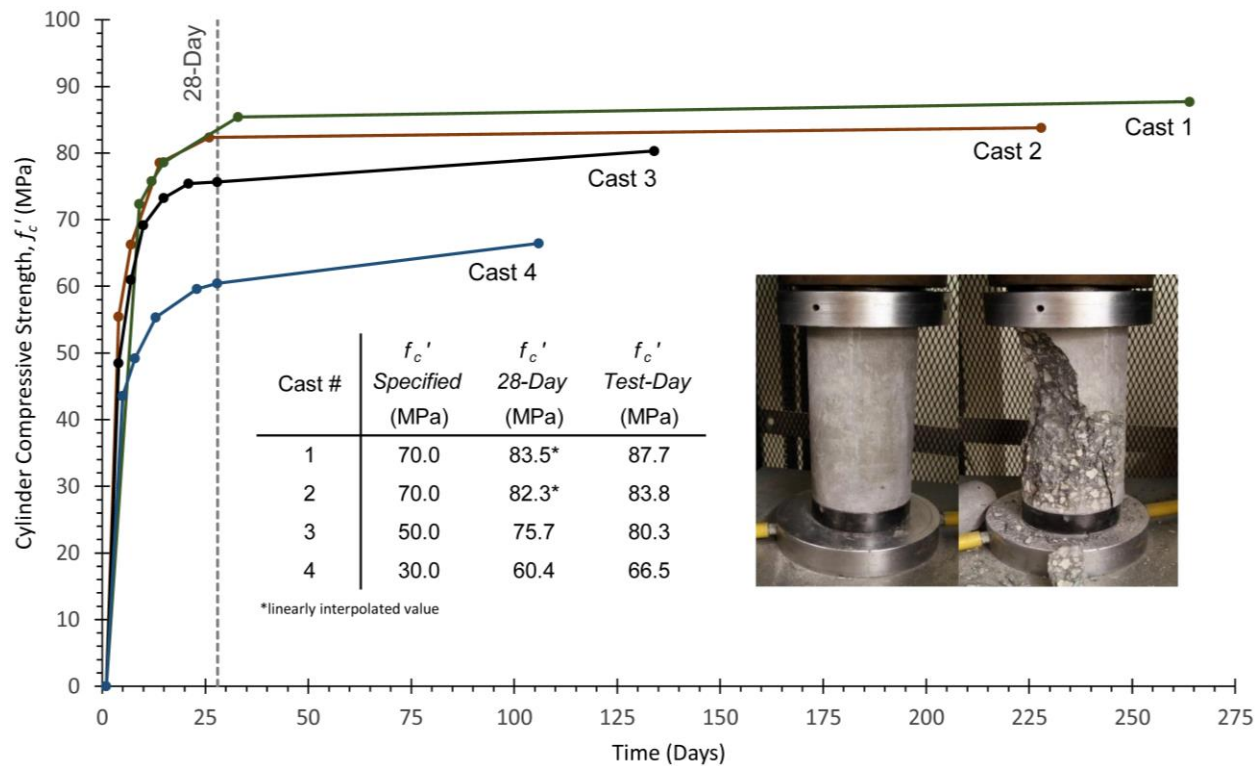


Figure 3-12: Concrete Cylinder Strength Gain

In addition to the concrete strength, the stress-strain curves were measured for the 28-day and test-day cylinder tests. The measured stress-strain curves for the test-day cylinders of Cast 3 corresponding with CBF1 and CBF2, and Cast 4, corresponding with CBF3 and CBF4 are presented in Figure 3-13 and Figure 3-14 respectively.

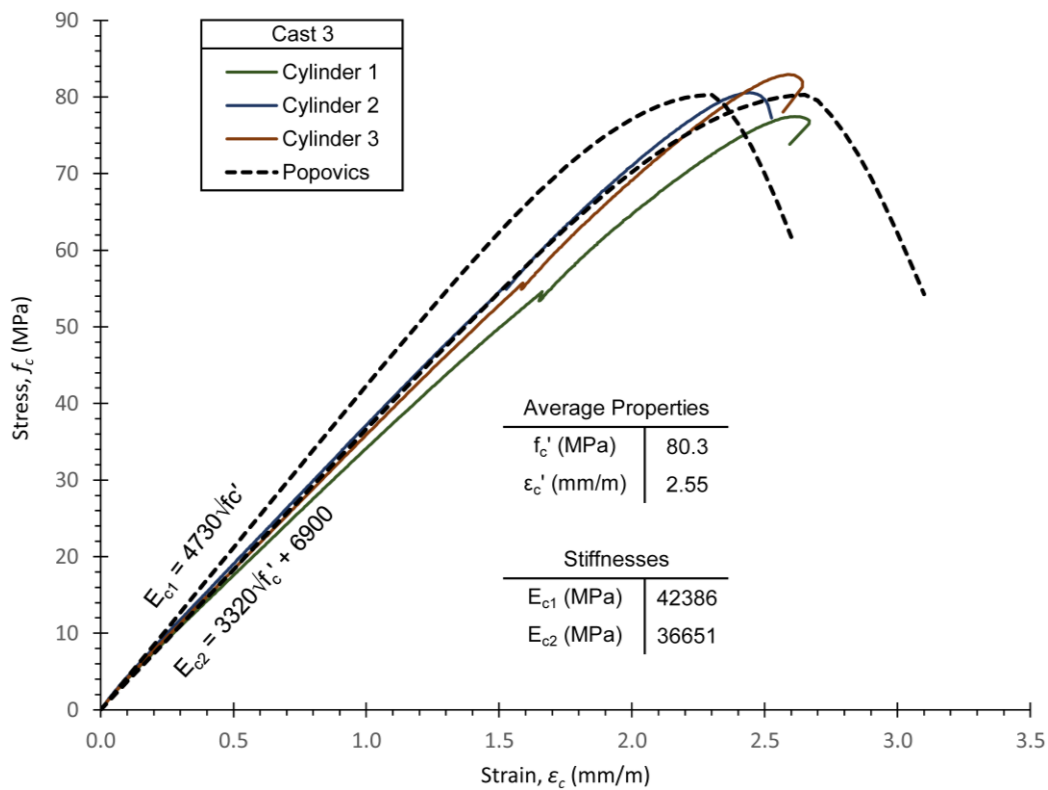


Figure 3-13: Cast 3 Stress-Strain Curves for Test-Day Concrete Cylinders

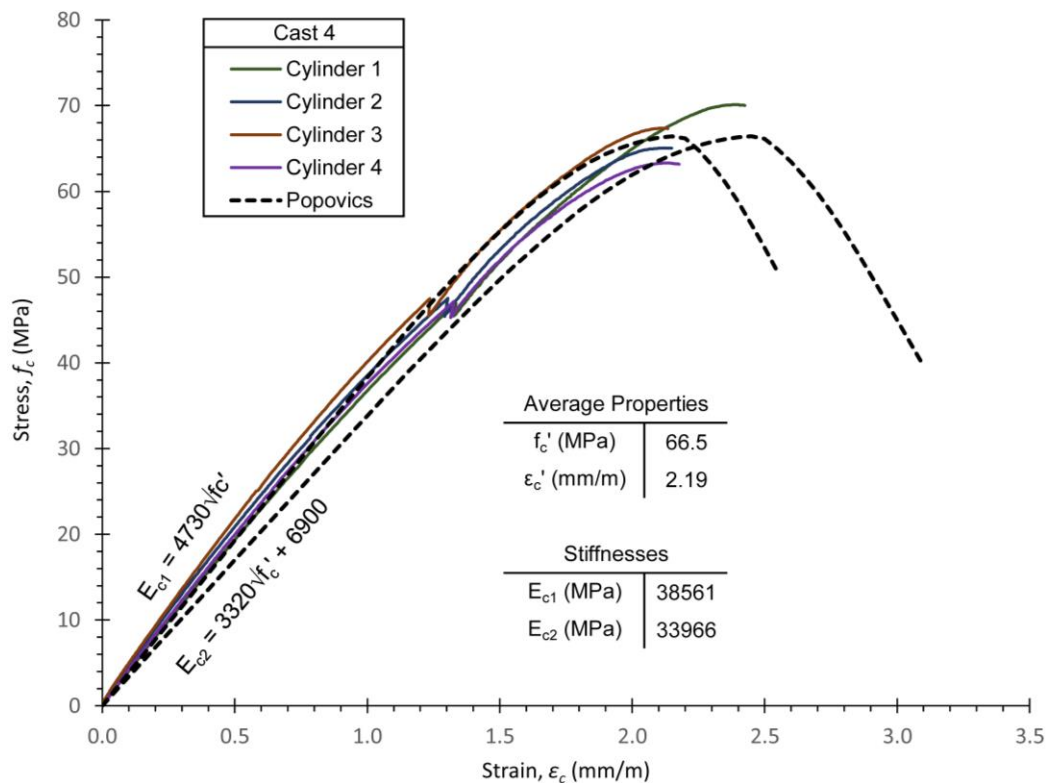


Figure 3-14: Cast 4 Stress-Strain Curves for Test-Day Concrete Cylinders

The concrete stiffness,  $E_c$ , was estimated using the Pauw [24] relationship for normal-weight concrete shown in Equation 3-1, and the modified Carrasquillo, Nilson, and Slate [25] relationship for high strength normal-weight concrete shown in Equation 3-2.

$$E_{c1} = 4730\sqrt{f'_c} \text{ MPa} \quad (3-1)$$

$$E_{c2} = 3320\sqrt{f'_c} + 6900 \text{ MPa} \quad (3-2)$$

Both stiffness calculations are used with a generalization of the Popovics [26] equations developed by Thorenfeldt, Thomaszewicz, and Jensen [27], and later calibrated by Collins and Porasz [28], shown in Equation 3-3.

$$\begin{aligned} \frac{f_c}{f'_c} &= \frac{n(e_{cf}/e'_c)}{n-1+(e_{cf}/e'_c)^{nk}} \\ e'_c &= \frac{f'_c}{E_c} \frac{n}{n-1} \\ n &= 0.8 + \frac{f'_c}{17} \text{ MPa} \quad k = 0.67 + \frac{f'_c}{62} \text{ MPa} \end{aligned} \quad (3-3)$$

These relationships are plotted with the stress-strain curves in Figure 3-13 and Figure 3-14. The concrete stiffness for Cast 3 is best represented by Equation 3-2, having a calculated stiffness of 36651 MPa. The concrete stiffness for Cast 4 is best represented by Equation 3-1, having a calculated stiffness of 38561 MPa. A full set of stress-strain and strength data for all casts are available in Appendix C.2.

## 3.5 Construction of Test Assembly

### 3.5.1 Formwork

All formwork was constructed using lumber sourced from a Toronto supplier. The formwork was designed assuming it would be reused multiple times, and therefore all surfaces in contact with concrete were made from formply plywood. All gaps between formply surfaces were sealed with waterproof caulking. Prior to the final placement of the reinforcing cages, the formply surfaces were coated in oil to make it easier to debond the formwork from the hardened concrete.

The formwork for the coupling beam specimens, shown on the right in Figure 3-15, was designed so that specimens could be cast vertically, and two at a time. The decision to cast

vertically ensured an even distribution of aggregate and cement paste over the width of the beam. Casting two specimens at a time allowed CBF1 and CBF2; and CBF3 and CBF4, to be cast using the same batch of concrete. The formwork for CBF1 required additional layers of formply along the edges of the coupling beam in order to reduce the thickness of the concrete side cover from the standard 45 mm to the design specification of 3 mm. The formwork for the shear wall components, shown on the left in Figure 3-15, were designed so that the components could be cast on their sides. This decision was made to reduce the complexity and structural requirements of the formwork design. A full set of formwork design drawings are available in Appendix A.



*Figure 3-15: Formwork for Shear Wall Components (left) and Specimens (right)*

### 3.5.2 Reinforcing Cages

The reinforcing cages for the test assembly were constructed in the University of Toronto Structures Laboratory. The reinforcing bars were cut to length and bent using an electric bending machine. Prior to assembly, reinforcing bars were outfitted with strain gauges in order to measure the local reinforcement strains during testing. This is further elaborated in section 4.2.3. The bars were tied together manually using rebar ties and assembled in the pre-built formwork to ensure proper cover tolerances were maintained. The assembly of the reinforcing cages for the four coupling beam specimens and four shear wall components are outlined in Table 3-2 and Table 3-3 respectively. Prior to the final placement of the cages into the oiled formwork, plastic risers were attached to the bottom layers of reinforcing bars to ensure the appropriate amount of side cover was provided between the cage and the formwork.

*Table 3-2: Reinforcing Cage Assembly for Coupling Beam Specimens*

Process	Description
1) Assembly of End Block Cages	The end block cages for the coupling beam specimens were constructed following the processes outlined in Table 3-3
2) Placement of First End Cage and Bottom Longitudinal Bars	One end block cage was setup standing vertically, and the bottom layer of longitudinal 30M bars tied into place; plywood templates and spacers ensured the bars had proper alignment (Figure 3-16a)
3) Placement of Stirrups	15M stirrups were threaded onto the bottom longitudinal reinforcement; a template of the longitudinal bars was used prior to placement to ensure the stirrups would fit properly over the longitudinal bars (Figure 3-16b)
4) Placement Second End Cage	The second end block cage was pushed onto the bottom longitudinal reinforcement and tied into place
5) Placement of Top Longitudinal Bars	The top layer of 30M bars were threaded through the end block cages and stirrups, and tied into place (Figure 3-16c)
6) Spacing of Stirrups and Final Assembly	The stirrups were spaced accordingly and tied into place creating the final reinforcing cage (Figure 3-16d)

Three PVC ducts with an outer diameter of 25 mm were cast through the coupling beam width for instrumentation purposes. These ducts were tied to the stirrup legs at mid-height, shown in Figure 3-16e, during cage assembly.

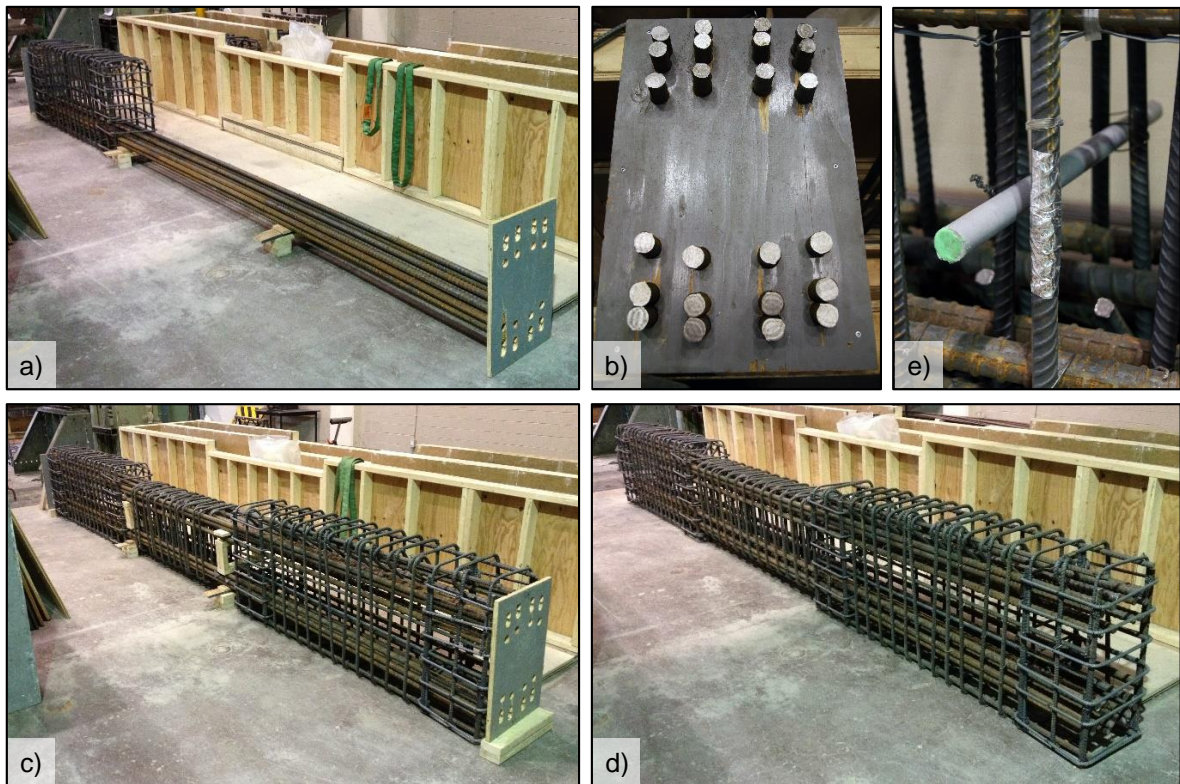


*Figure 3-16: Reinforcing Cage Assembly for Coupling Beam Specimens*

*Table 3-3: Reinforcing Cage Assembly for Shear Wall Components*

Process	Description
1) Assembly of Concentrated Reinforcement	10M buckling prevention ties, spaced at 120 mm, were tied to four 20M reinforcing bars, creating the concentrated reinforcement ‘columns’ of the shear wall
2) Placement of Vertical Stirrups	15M vertical stirrups were placed side by side next to the concentrated reinforcement columns (Figure 3-17a)
3) Placement of Horizontal Reinforcement	15M horizontal reinforcing bars, spaced at 100 mm, were threaded through the concentrated reinforcement columns and vertical stirrups
4) Placement of Cantilever Reinforcement*	30M bars were threaded through the concentrated reinforcement columns and vertical stirrups (Figure 3-17b); a plywood template was utilized to ensure proper spacing of 30M bars (Figure 3-17c)
5) Assembly of Wall Reinforcement	The vertical stirrups were spread out in 100 mm intervals and tied to the horizontal bars creating the cage superstructure (Figure 3-17d-e)
6) Placement of U-Ties*	U-Ties, spaced at 200 mm, were tied to the horizontal bars at the end face of the cantilever
7) Welding of End Plate*	A 19 mm thick plate was welded to the ends of the 30M longitudinal bars at the cantilever face (Figure 3-17f)

\*Assembly process for cantilever shear wall components only

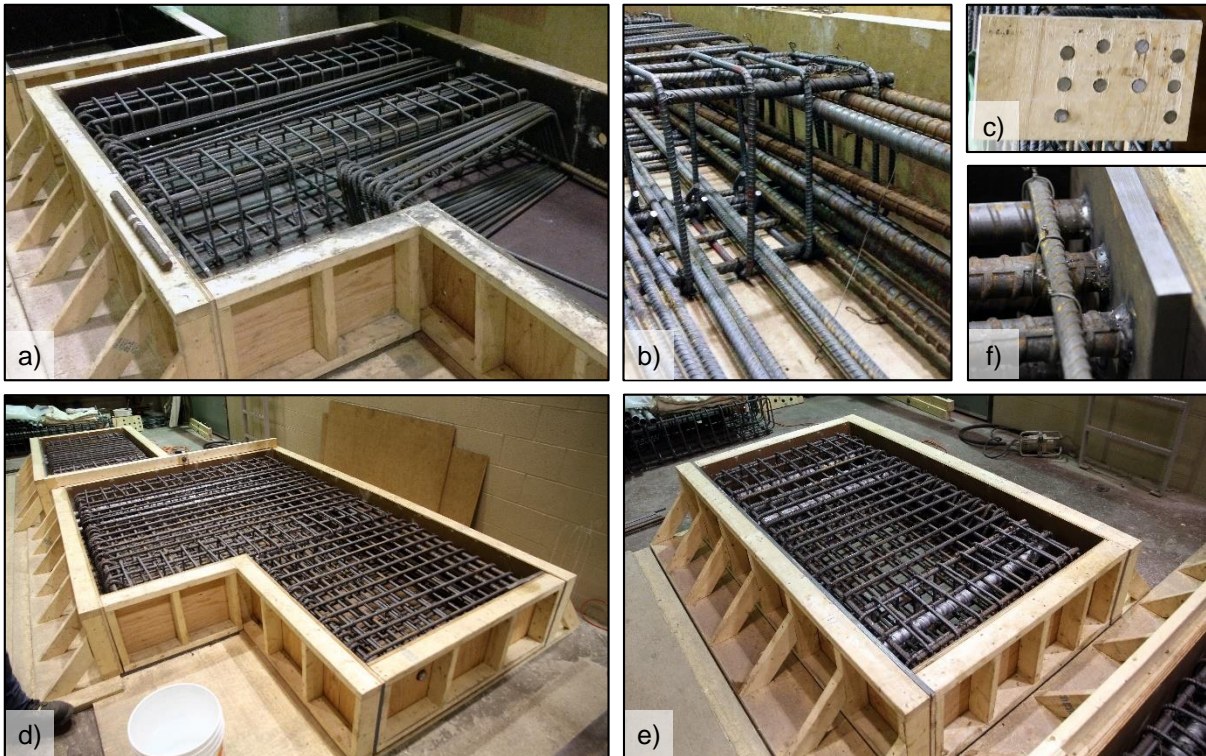


*Figure 3-17: Reinforcing Cage Assembly for Shear Wall Components*

### 3.5.3 Accessory Placement

To ensure the post-tensioning ducts were properly aligned, plywood guides shown in Figure 3-18, were added to the top of the coupling beam formwork. For the shear wall components, holes were drilled directly into the sides of the formwork with waterproof caulking used to seal any gaps between the formwork and duct, as shown in Figure 3-19.



*Figure 3-18: Post-Tensioning Duct Placement for Coupling Beam Specimens*



*Figure 3-19: Post-Tensioning Duct Placement for Shear Wall Components*

Lifting inserts for the coupling beam specimens were placed using a plywood assembly shown in Figure 3-20. This allowed the inserts to be cast flush with the surface of the concrete. For the shear wall components, the lifting inserts were attached directly to the sides of the formwork using predrilled holes and bolts, shown in Figure 3-21.



*Figure 3-20: Lifting Insert Placement for Coupling Beam Specimens*

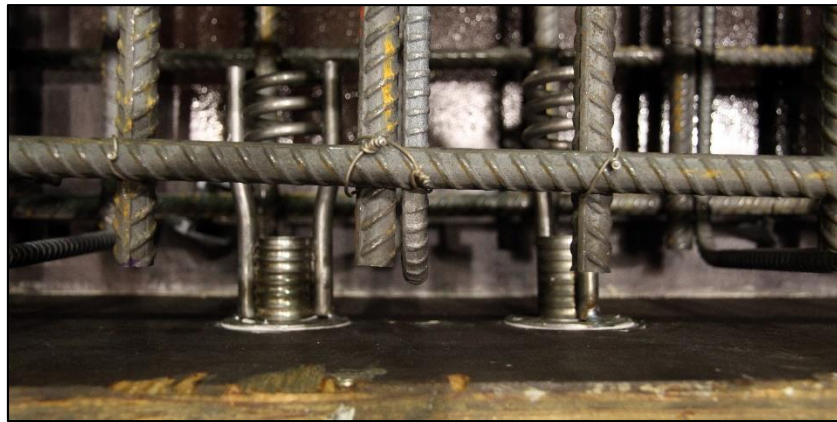


*Figure 3-21: Lifting Insert Placement for Shear Wall Components*

### 3.5.4 Concrete Casting and Finishing

Concrete casting took place in the University of Toronto Structures Laboratory. The laboratory crane and concrete bucket were used to transfer the concrete from the ready-mix truck to the formwork as shown in Figure 3-22. Two electric vibrators were used for cast 1 and 2 to consolidate the high-strength concrete of the shear wall components. The concrete for cast 1 started stiffening up near the end of the pour, resulting in less vibrating of the concrete than planned. Cast 2 ran short of concrete at the end of the pour, however the shortage was mitigated by reducing the number of concrete cylinders cast. The full process for cast 1 and 2 of the shear wall components is highlighted in Figure 3-23.



*Figure 3-22: Cast 1 and Cast 2 Concrete Bucket and Vibrator Usage*



*Figure 3-23: Highlights from Cast 1 and Cast 2*

Since self-consolidating concrete was used for cast 3 and 4, vibrators were not needed. Once the formwork was filled up to the coupling beam surface, a sheet of formply was screwed on top to keep the concrete from overflowing when filling the remainder of the shear wall end blocks. Near the end of cast 4, one end of the formwork broke open, but the incident was quickly mitigated with the use of clamps. Only a small gap in the formwork remained, shown in Figure 3-24. This gap only affected the width of the east shear wall end block which was deemed not to be critical to the tests. The full casting process for the cast 3 and 4 are highlighted in Figure 3-25.



Figure 3-24: Cast 4 Formwork Failure

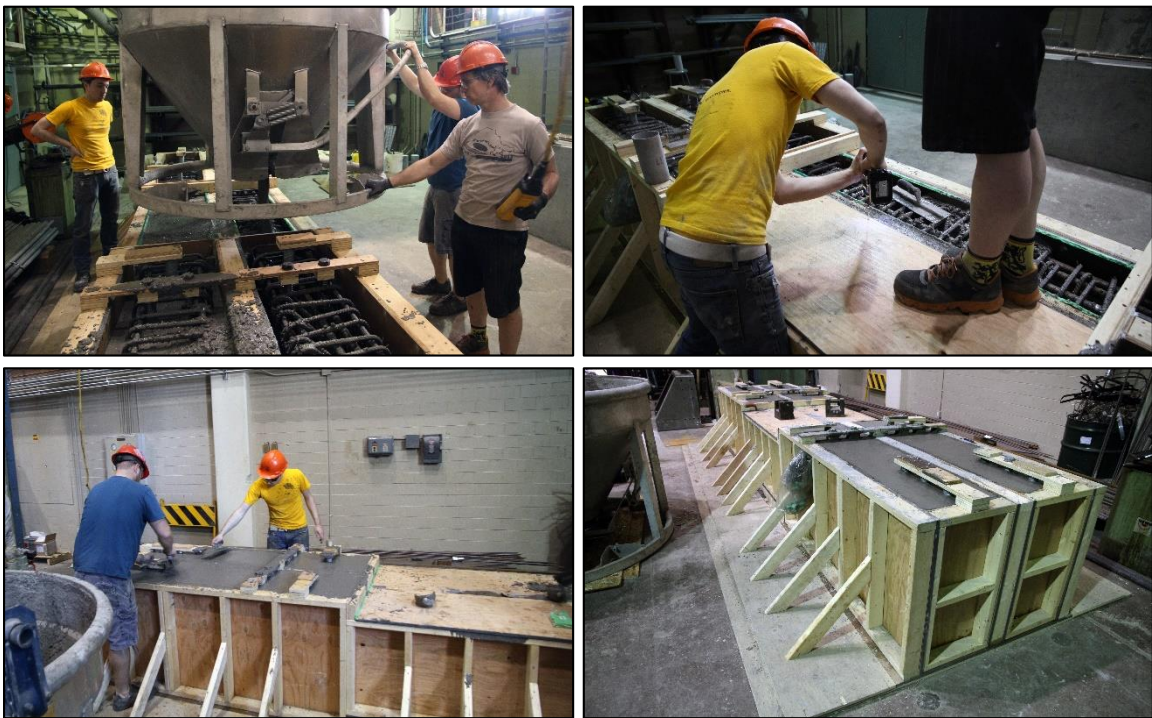


Figure 3-25: Highlights from Cast 3 and Cast 4

After casting, the concrete was moist cured for 5-7 days, followed by formwork removal. The post-tensioning duct extensions were cut off flush with the concrete surface. A coat of watered down white latex paint, having a 50/50 paint-to-water ratio, was applied to all of the concrete surfaces in order to make cracks more visible during testing. Due to difficulties with surface troweling around the ducts and inserts, the top surfaces of the coupling beam end blocks were significantly uneven. A level surface was required to ensure the assembled shear wall components remained on the same vertical plane. The solution was to use the high strength grout compound SikaQuick-1000 to level out the surfaces. Figure 3-26 shows a grouted surface with corresponding formwork.



*Figure 3-26: Grouting of Coupling Beam End Sections*

# Chapter 4: Testing of Specimens

The experimental program consisted of testing four coupling beam specimens to failure. A Meccano frame test setup was used to stabilize the coupling beam test assembly during loading. Important measurements obtained during testing were the average beam strains, the tangential deviation between the coupling beam ends, out-of-plane expansion of the coupling beam, and the rotation of the test assembly. Instrumentation including linearly varying differential transformers (LVDTs), infra-red light emitting diodes (LED) targets, and strain gauges were used to obtain the experimental data. The following sections further elaborate on the test setup, data acquisition methods, and summary of qualitative observations during testing.

## 4.1 Experimental Setup

There were many factors which determined the type of experimental setup needed to test the coupling beams. With the test assembly weighing 18.5 tonnes and having an assembled height of 4.6 m, it was not possible to pre-assemble the components then roll them into place. With these two limitations in mind, a Meccano frame setup installed on the laboratory strong floor was determined to be ideal for the experimental program. A full set of drawings of the experimental setup is available in Appendix A.

The Meccano frame experimental setup consisted of four columns with a spreader beam assembly. The Meccano test frame is shown in Figure 4-1. The spreader beam assembly consisted of four connector beams and the main spreader beam. The columns were bolted directly into the strong floor using two bolts per column, each post-tensioned with a force of approximately 1000 kN. The location of the columns was chosen such that there was a full side view of the coupling beam during testing. The Meccano frame components were connected using A325 1-inch bolts having a tensile capacity of 251 kN and a shear capacity of 141 kN. Each pair of columns were joined by two connector beams in the north-south direction. The beams each used eight bolts to connect to the columns, giving the column-beam connections a total capacity of 4512 kN. The main spreader beam was bolted to the top flanges of the connector beams using four bolts per flange, resulting in a total beam-flange connection capacity of 4016 kN. These connections provided a 1.5 factor of safety of above the highest predicted flexural failure load of 2665 kN for CBF2.

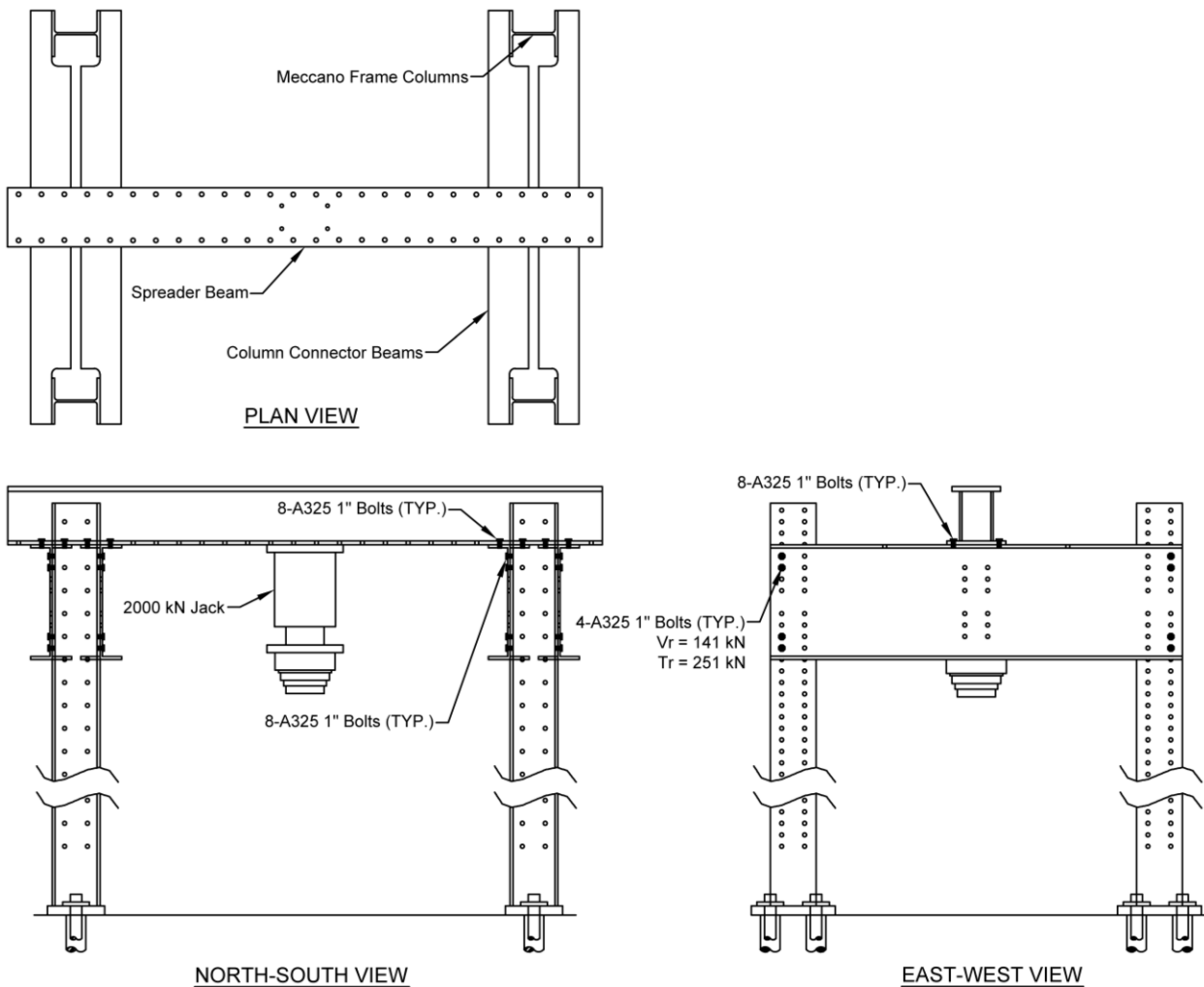


*Figure 4-1: Meccano Frame Test Setup*

A displacement-controlled hydraulic loading jack was attached to the bottom flange of the spreader beam. The hydraulic jack had a working load capacity of 2000 kN, and an ultimate load capacity of 4500 kN. The primary laboratory pumps were able to supply high-flow oil to a maximum jack load of 2000 kN. It was decided that with the coupling beam capacities close to 2000 kN, and with the potential for them to go higher, the main pumps would not be used for the test. Instead, a secondary pump was used with the ability to pump the oil to a jack load of 2500 kN. This secondary pump was portable and used its own supply of oil, meaning other experiments using the primary pumps would not affect the testing schedule.

With the hydraulic jack bolted directly to the Meccano spreader beam assembly, it was possible to lift the entire assembly off of the columns to allow for unhindered passage of the crane and test assembly components. The total weight of this setup was approximately four tonnes, making

it possible to lift the spreader beam assembly with the crane. For safety precautions and ease of assembly, brackets were installed onto the Meccano columns, shown in Figure 4-2, which would allow the crane to set the spreader beam assembly in place prior to being bolted to the columns.

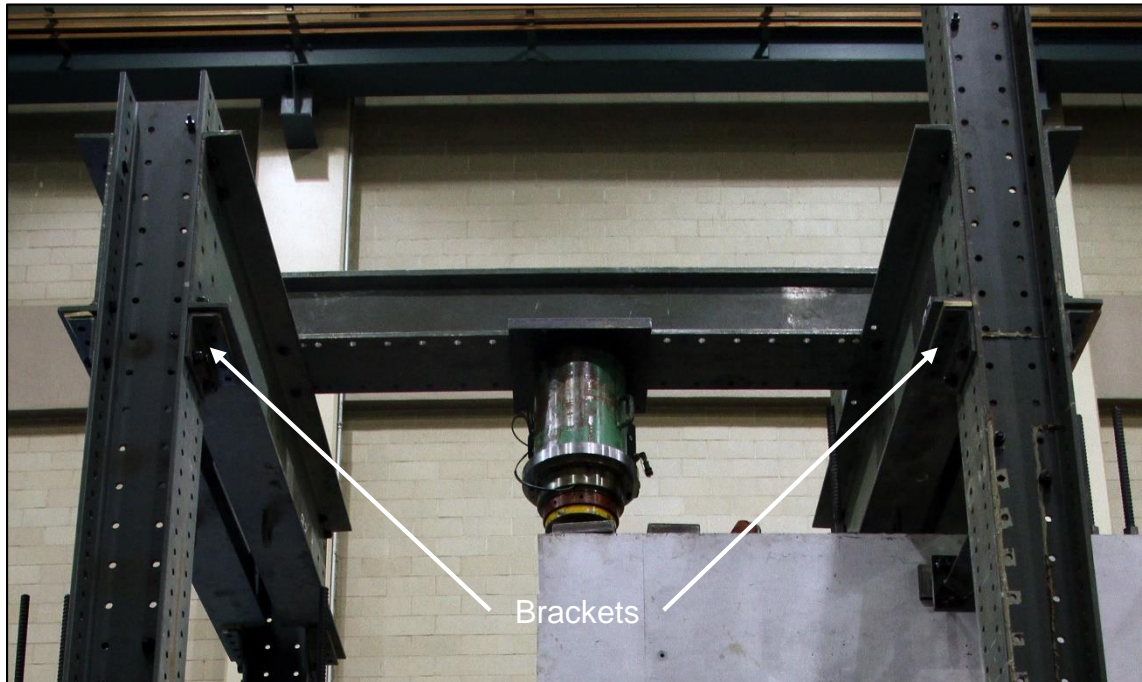


*Figure 4-2: Spreader Beam Assembly with Brackets*

#### 4.1.1 Lateral Bracing

Due to the height of the test assembly and the unknown behavior at the failure load, lateral bracing was added to the test setup. These lateral braces were made from HSS steel sections and bolted directly to the Meccano frame columns. Two braces were used per column to provide stability near the top and bottom of the concrete test assembly. The braces used high strength bolts at their ends in order to adjust the length of the brace. Rubber bearing pads with an aluminum surface were used as the interface between the bolt heads and concrete surface of the test assembly. The pad surface was thought to be smooth enough to slide with the test assembly during loading. Figure 4-3 shows an example of one lateral brace.



*Figure 4-3: Lateral Bracing for Test Setup*

#### 4.1.2 Boundary Conditions

The experimental setup required a single support on the strong floor which had the same line of action as the loading jack. The loading jack had a spherical loading plate built into it, meaning it was able to act as a pin during loading. A pin support was also used for the floor reaction. By having pin connections for the boundary conditions, the test assembly would be free to rotate as the coupling beam deformed, but would be prevented from moving horizontally due to friction. Prior to the test, the pin support was locked in a fixed position to prevent any unwanted rotation during placement of the components. These locks were removed once testing began. In order to ensure an adequate distribution of load over the concrete surfaces, 400 x 250 x 50 mm bearing plates were used for both the support reaction and loading jack.

Two load cells were installed under the pin support in order to have a secondary measure of the applied load. The two load cells were aligned over the width of the test assembly. If the test assembly wasn't aligned in the north-south direction, the load cells would be able to detect this by registering unequal loads. Figure 4-4 shows the support reaction and load cells with and without the bearing plate attached.

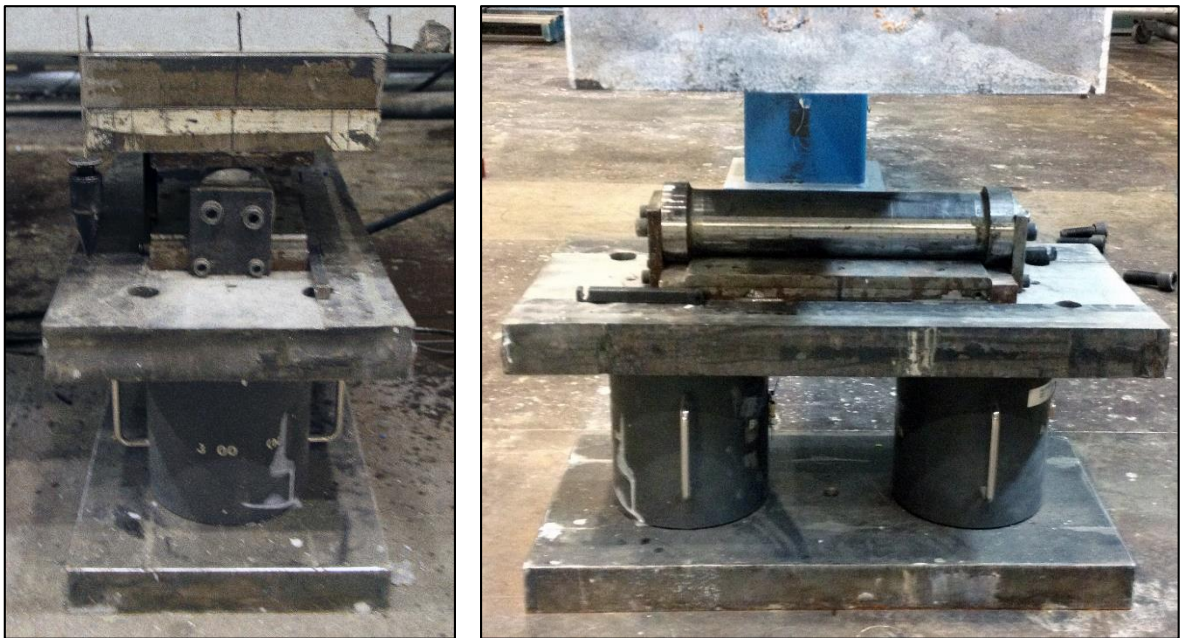


*Figure 4-4: Pin Support Reaction with and without Bearing Plate*

#### 4.1.3 Self-Weight Jacks

The full test assembly weighs in at 18.5 tonnes (181.5 kN), half of which acts 1.45 m to either side of the coupling beam centreline. This self-weight can have a major impact on the shear force and bending moment diagrams. If ignored, the self-weight would cause the shear in the coupling beam to increase and would shift the location of zero moment to the east as shown in Figure 4-5a. This phenomenon was also observed during tests performed using the Sadler setup by Kim [29]. Kim's solution involved installing self-weight jacks under each side of the test rig in order to 'float' the self-weight. This method was deemed the appropriate solution and was adapted for this experimental program. The resulting shear force and bending moment diagrams with the self-weight jacks are shown in Figure 4-5b.

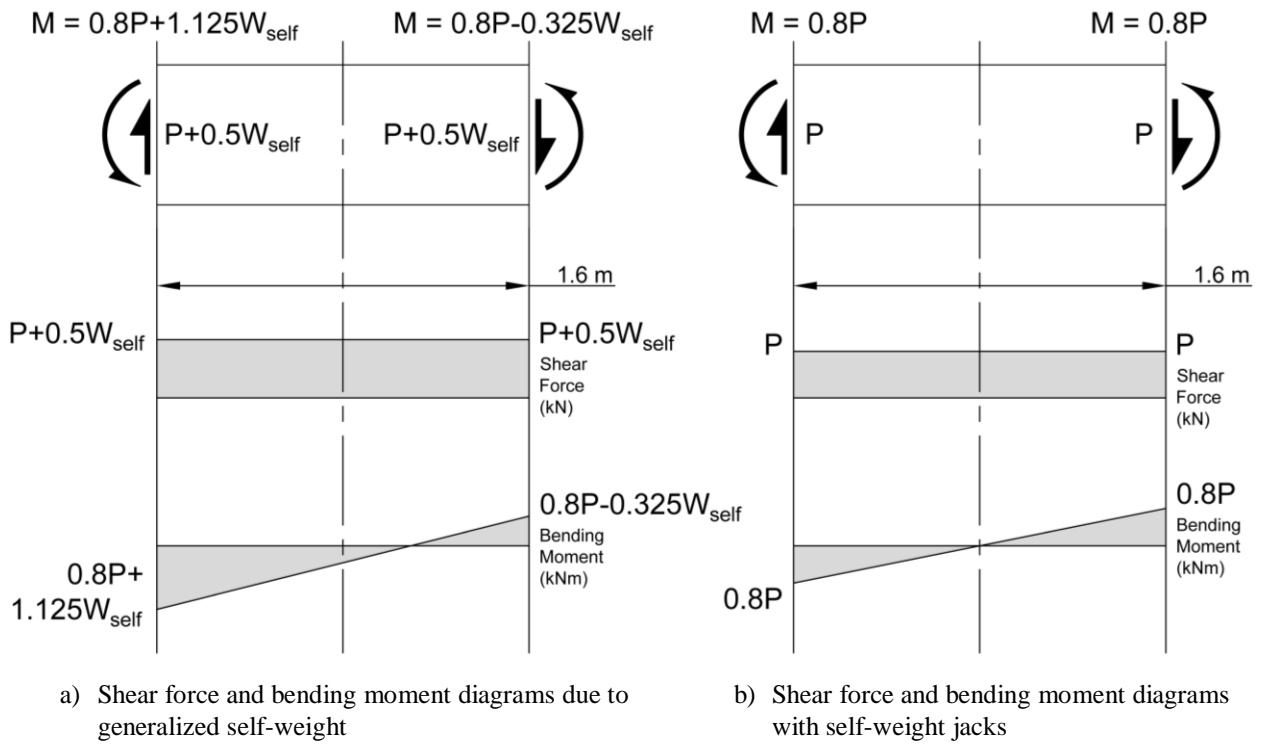


*Figure 4-5: Influence Self-Weight on Coupling Beam Loading*

Two ENERPAC RC-506 45.4 tonne (50 ton) hydraulic jacks with a 159 mm (6.25") stroke were used to ‘float’ the self-weight of the test assembly. The jacks were placed under the centre-of-mass for each half of the test assembly resulting in a line of action 1446 mm either side of the coupling beam centreline. Each jack supported approximately 90 kN during the test. In order to provide proper contact with the concrete surfaces, 300 x 180 x 52 mm bearing plates with a 6 mm (1/4") inset for the jack head were used. An additional 25 mm thick rubber pad was placed between the loading plate and the concrete surfaces to allow for any small rotations of the shear walls to occur. The placement of the self-weight jacks is shown in Figure 4-6 while Figure 4-7 shows photos of the fully assembled self-weight jack setup. The central pin support governed the height at which the test assembly was elevated off of the strong floor. Due to the stroke limitations of the self-weight jacks, the east jack was raised up by 52 mm with the use of a steel plate, and the west jack was raised up by 938 mm with the use of a concrete pedestal and combination of steel plates.

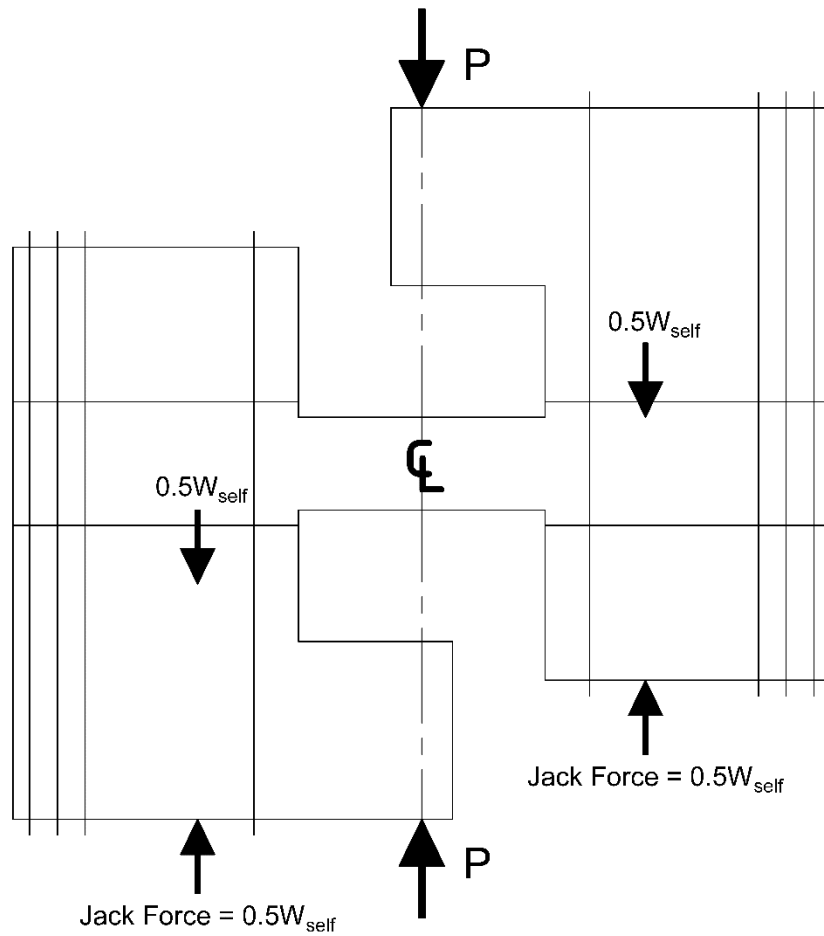


*Figure 4-6: Placement of Self-Weight Hydraulic Jacks*



*Figure 4-7: West and East Self-Weight Hydraulic Jack Assemblies*

The self-weight jacks were operated with a load maintainer that was hooked up to the same pump that fed oil to the loading jack. The load maintainer ensured each self-weight jack held the 90 kN while still being able to move with the displacements of the test assembly. The self-weight jacks were able to accommodate approximately 100 mm of jack travel downward and approximately 50 mm of jack travel upward in order to lift and align the specimen off of the supports.

## 4.2 Test Assembly Setup

Temporary supports were used to elevate the test assembly while it was being installed. The self-weight jacks were initially considered for this purpose, however the small loading plates and potential to move due to a loss in oil pressure raised concerns about stability of the system. The temporary supports were constructed using large rectangular HSS pedestals and spacers. A single pedestal together with the pin-support were used to support the west side of the test assembly. Two temporary supports for the east side of the test assembly were each constructed out of two pedestals and eight spacers. The west cantilever shear wall component was lifted by crane and placed on its supports, followed by the east rectangular shear wall component. Figure 4-8 shows both components in place on their temporary supports.

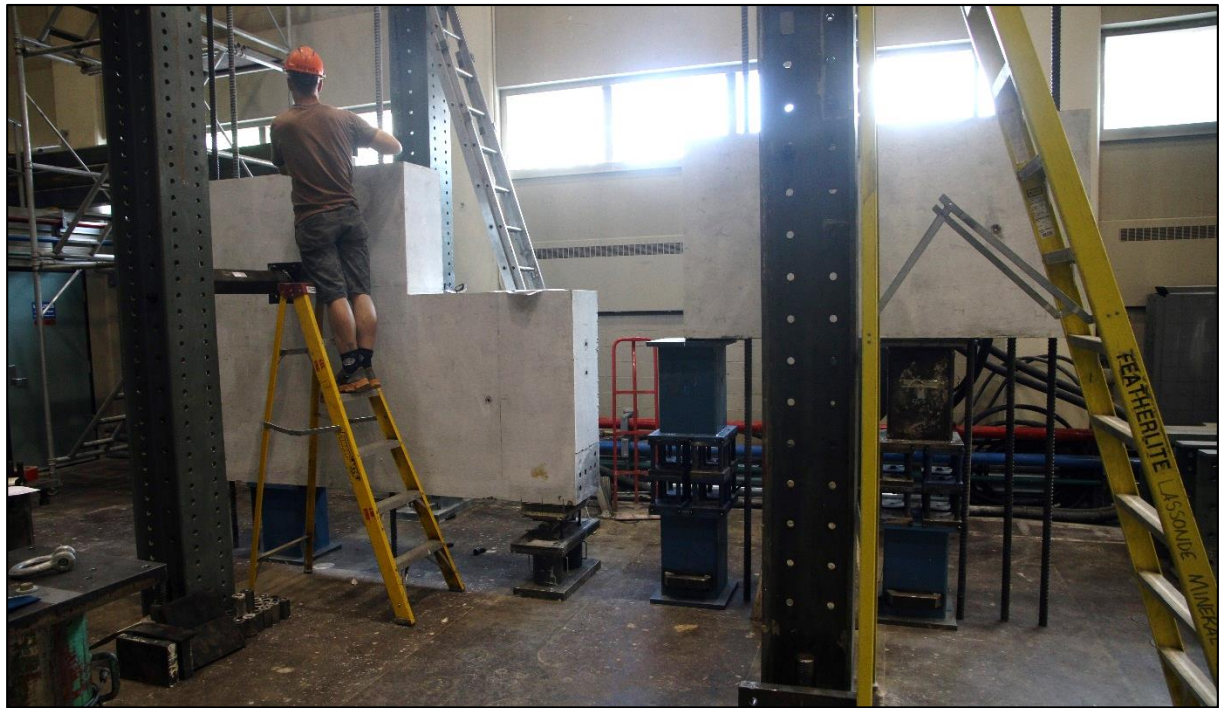


*Figure 4-8: Installation of West Cantilever and East Rectangular Components*

The post-tensioning bars were inserted into the ducts of the first components, and the remaining components were carefully threaded overtop. The ends of the bars were left to rest on the strong floor until all of the components were in place. Figure 4-9 shows the installation of the coupling beam specimen, followed by the west rectangular shear wall component in Figure 4-10, and the east cantilever shear wall component in Figure 4-11.

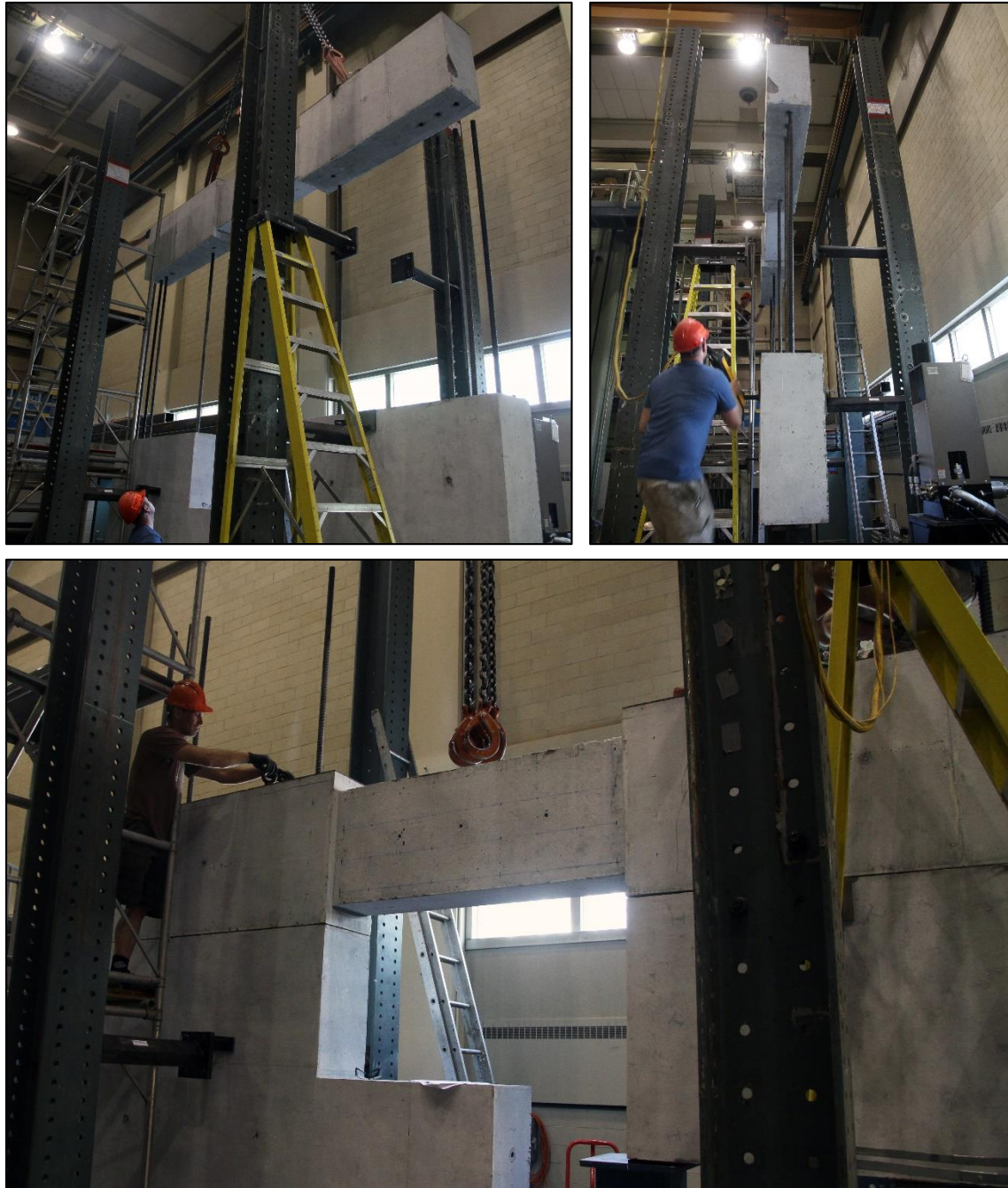


*Figure 4-9: Installation of Coupling Beam Specimen CBF1*



*Figure 4-10: Installation of West Rectangular Shear Wall Component*

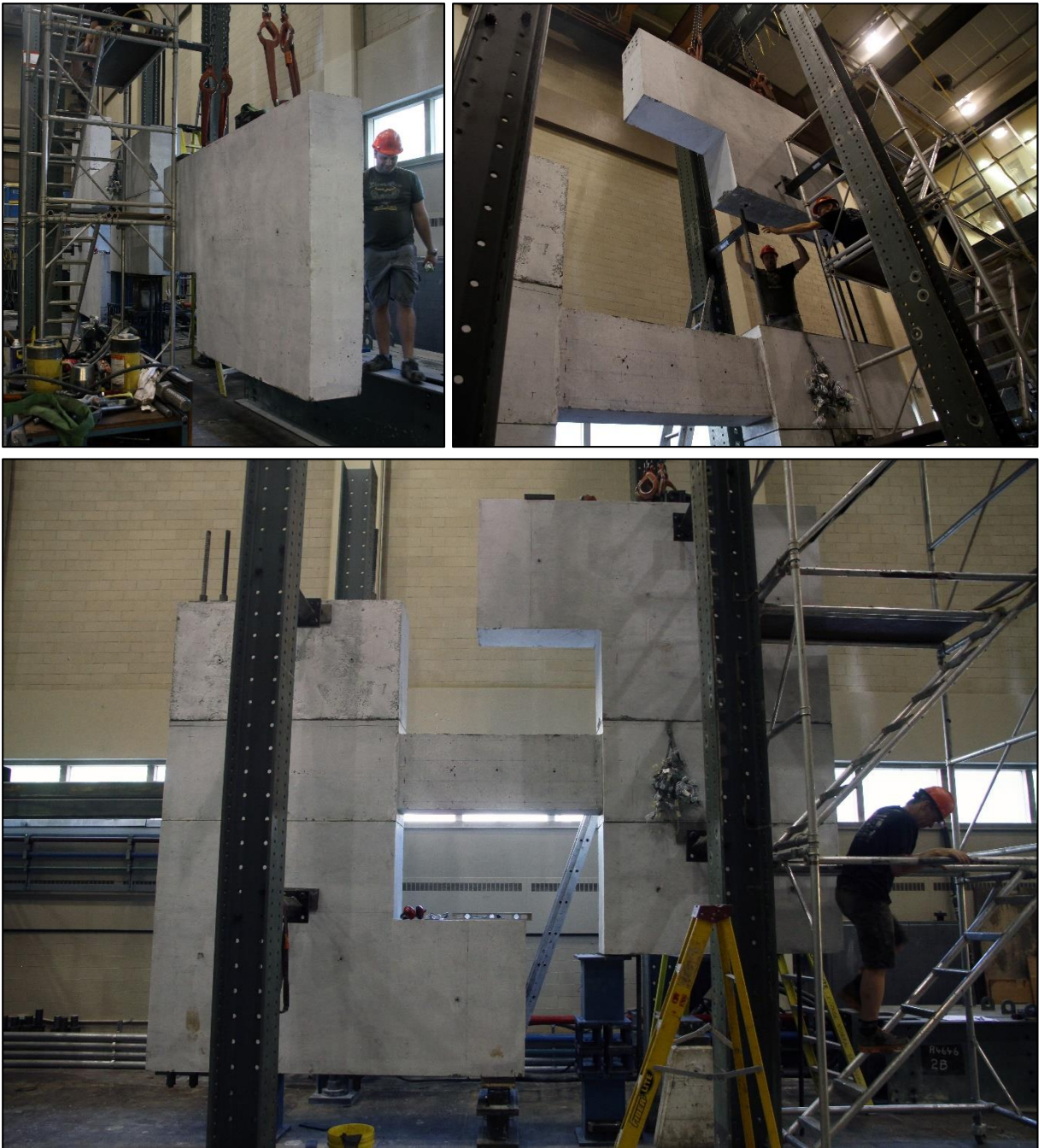


*Figure 4-11: Installation of East Cantilever Shear Wall Component*

The post-tensioning process was performed on top of the test assembly. Each bar was lifted off of the strong floor until approximately 250 mm was protruding from the bottom face. Anchor plates and hex nuts were threaded on top and bottom. The three post-tensioning bars on the tension face were each post-tensioned using a 54.4 tonne (60 ton) jack to a force of 247 kN. The single post-tensioning bar on the compression face was post-tensioned using a 90.7 tonne (100

ton) jack to a force of 740 kN. Figure 4-12 shows the anchor plates and hex nuts located at the bottom west of the test assembly prior to lifting the three post-tensioning bars, as well as after one bar had been post-tensioned.

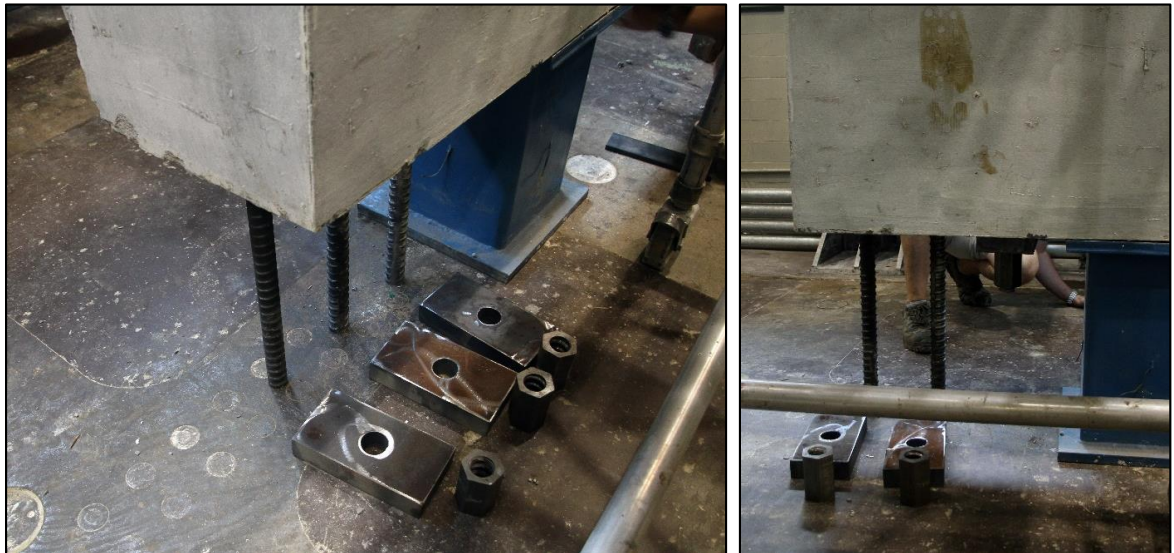


*Figure 4-12: Post-Tensioning of Test Assembly Components*

With the components post-tensioned together, the test assembly acted as a single unit. It was observed at this time that despite grouting the surfaces of the shear wall end blocks, there were still gaps at the component interfaces. These gaps were approximately 1 mm wide and were caused by an uneven surface due to construction inaccuracies with the formwork. These gaps occurred in middle of the shear walls. Near the ends of the walls, where the post-tensioning was applied, the surface was in direct contact. It was decided that these gaps would not significantly impact the test and were left as they were.

#### 4.2.1 LVDTs and Linear Pots

All of the linearly varying differential transformers (LVDTs) and linear potentiometers (pots) were installed on the north face of the test assembly in order to have an unobstructed view of the coupling beam on the south face. All of the holes for the instrumentation mounting brackets were pre-drilled into the concrete prior to stacking the test assembly components. The lengths of the LVDTs were measured between the centrelines of the LVDT mounting brackets. All of the instrumentation was hooked up to a central computer data acquisition system set at a sampling frequency of 10 Hz.

Nine LVDTs were installed on the north face of the coupling beam in order to measure the average beam strains. See Figure 4-13. The LVDTs were grouped in sets of three, with one set being installed at mid-span and the other two located a distance  $d_v$  (439 mm) away from the face of each shear wall. In each group, one LVDT was installed vertically to measure the average z-direction strain,  $\varepsilon_z$ . The other two were installed at 45 and 135 degree angles in order to measure the average shear strain,  $\gamma_{xy}$ .

In order to measure the occurrence of concrete side cover spalling, four LDVTs and three linear pots were used to measure out-of-plane expansion of the coupling beam. The four LVDTs were installed on the top and bottom of the coupling beam, 300 mm away from the face of each shear wall. The two on the bottom face are visible in Figure 4-13. These LVDTs measured the expansion at the coupling beam corners. The three linear pots were mounted on custom brackets in order to measure the mid-height expansion at mid-span and at  $d_v$  (439 mm) away from the shear wall faces. See Figure 4-13. Using the cast-in PVC ducts which ran the full width of the beam, wooden dowels were placed in the ducts and hot-glued to the south face of the beam. The dowels were attached to the linear pots on the north face. It is important to note that the linear pots measured the full expansion of the coupling beam whereas the LVDTs only measured the expansion on the north face. The installed LVDTs and linear pots are shown in Figure 4-13.

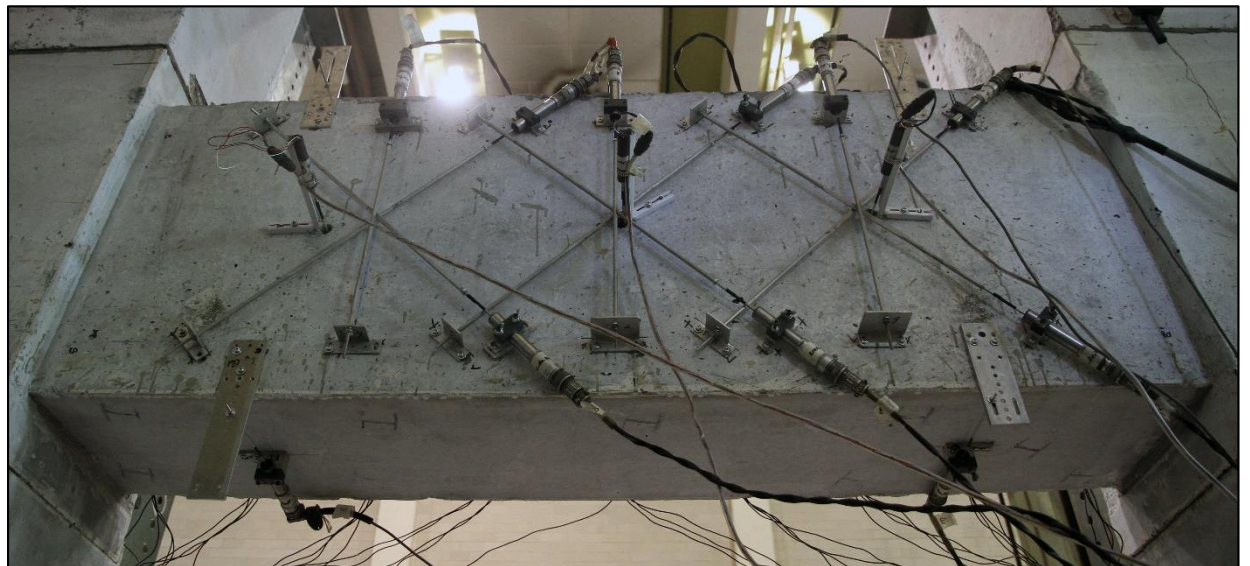


*Figure 4-13: Installed Coupling Beam LVDTs and Linear Pots*

The tangential displacement of the coupling beam was the most important measurement recorded during the tests. This measurement was obtained by affixing a long aluminum rod to the east shear wall, and recording the vertical displacement of the rod with an LVDT mounted on the west shear wall. An additional brace was attached to the rod and east shear wall in order to stiffen the setup. During the first load stage of the first test, it was observed that the stiffness of the aluminum rod on its own was similar to the stiffness of the LVDT spring and so the diagonal brace, shown in Figure 4-14, was added for the remainder of the first test and the three tests following.



*Figure 4-14: Tangential Displacement Setup*

In addition to the coupling beam instrumentation, LVDTs were used to measure the movement of the shear walls. Two LVDTs were placed under the east and west shear walls in order to measure vertical displacement and rotation. LVDTs were mounted over the tension side of the east and west shear wall interfaces in order to measure any expansion due to elongation of the pot-tensioning bars. Figure 4-15 shows the full LVDT and linear pot instrumentation layout, viewed from the north side.

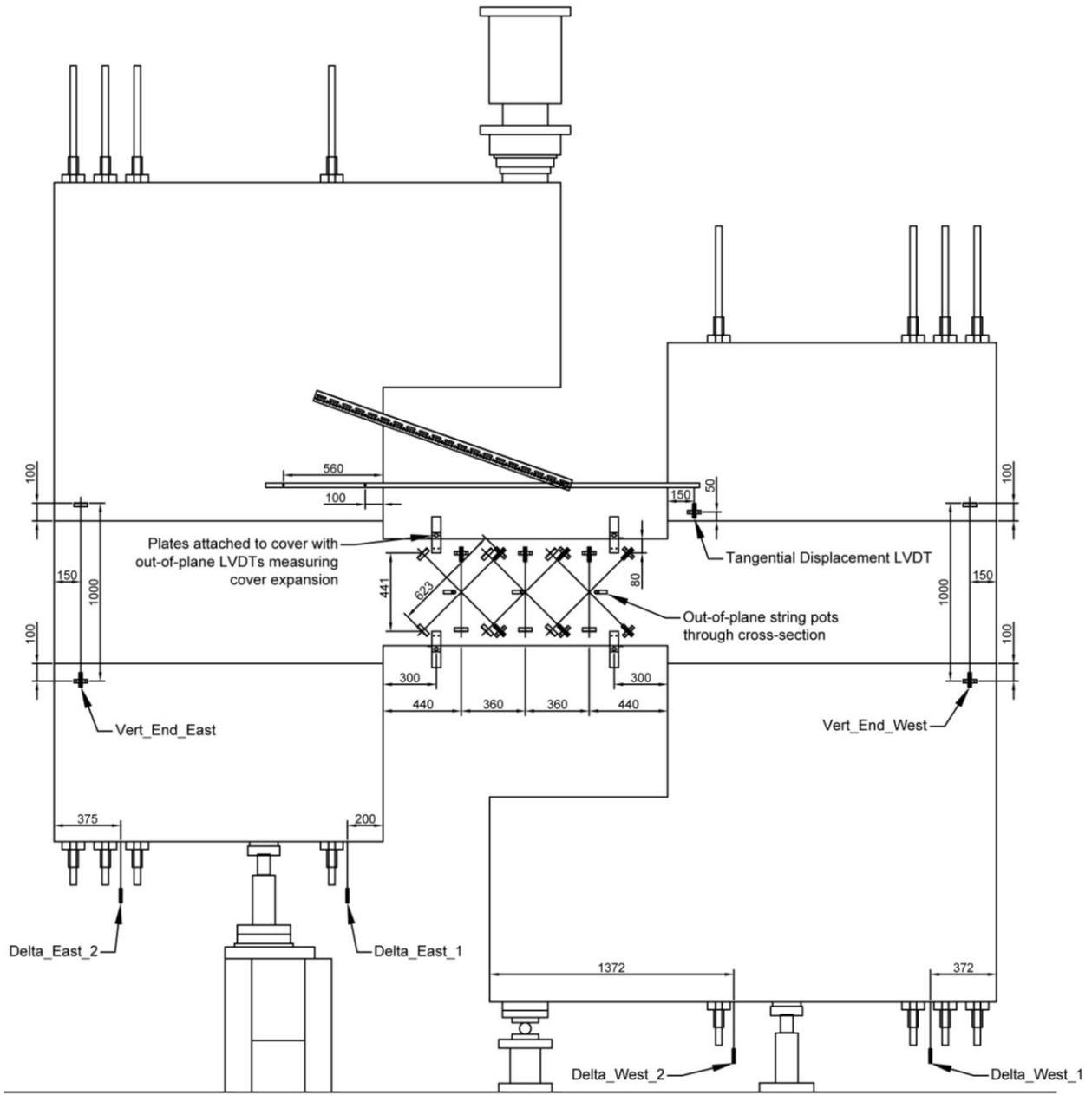
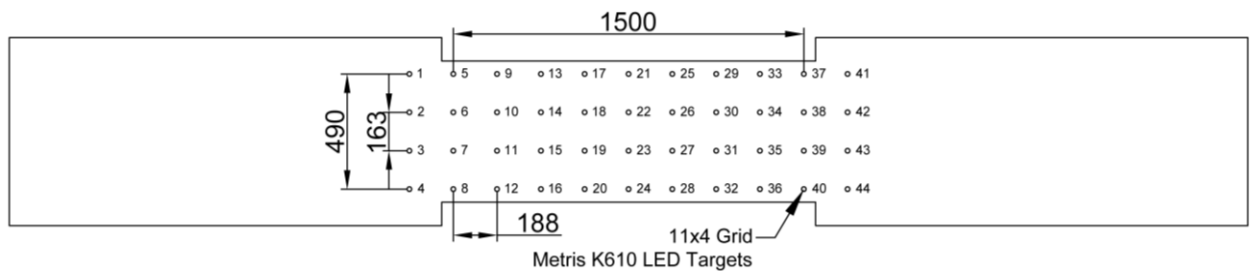


Figure 4-15: LVDTs and Linear Pot Instrumentation of Coupling Beam

#### 4.2.2 LED Targets and Metris K610 Camera System

A more detailed data collection of element strains was performed using LED targets. These targets were installed in a 4x11 grid on the south face of the coupling beam. One column of LEDs was installed on each of the shear walls in order to provide a stable reference frame for future LED calculations. The installed LED targets and associated labelling scheme each are shown in Figure 4-16.



*Figure 4-16: Metris K610 LED Target Layout and Labelling Scheme*

The three-dimensional position of these LED targets were continuously measured using the Metris K610 camera system at a sampling frequency of 10 Hz. The field of view of the camera system was of importance for this test due to the elevation of the coupling beam. For optimal data acquisition, the camera was placed 4.32 m south of the test assembly, as illustrated in Figure 4-17.

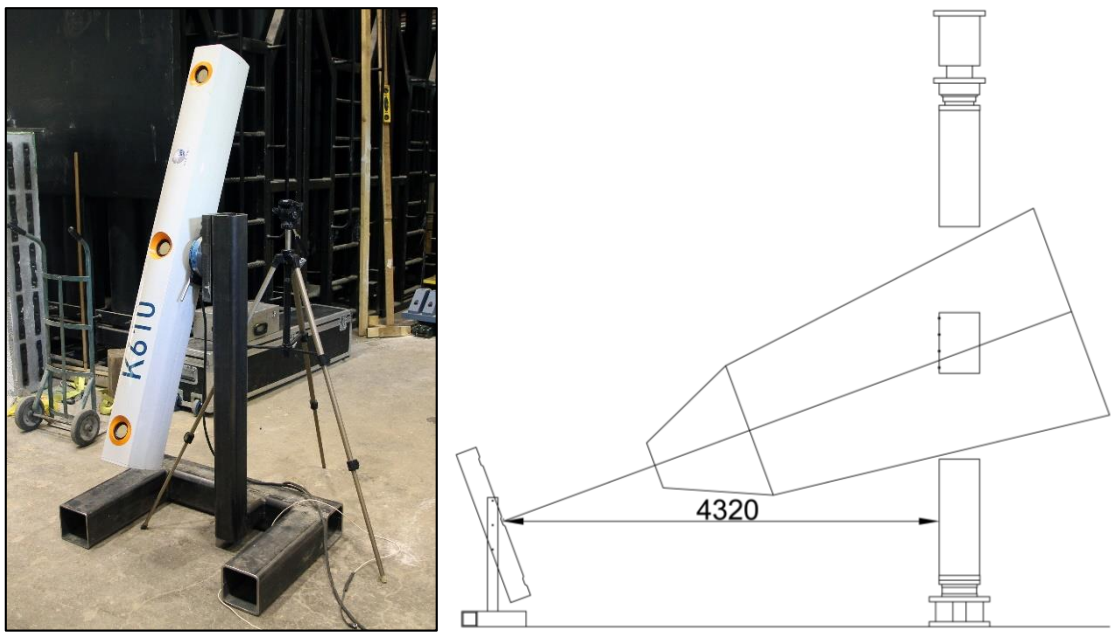


Figure 4-17: Metris K610 Camera System Field of View

#### 4.2.3 Reinforcement Strain Gauges

Local reinforcement strains were measured using strain gauges which were attached directly to the reinforcing bars during the cage assembly process. The typical strain gauge layouts for CBF1 to CBF4 are presented in Figure 4-18.

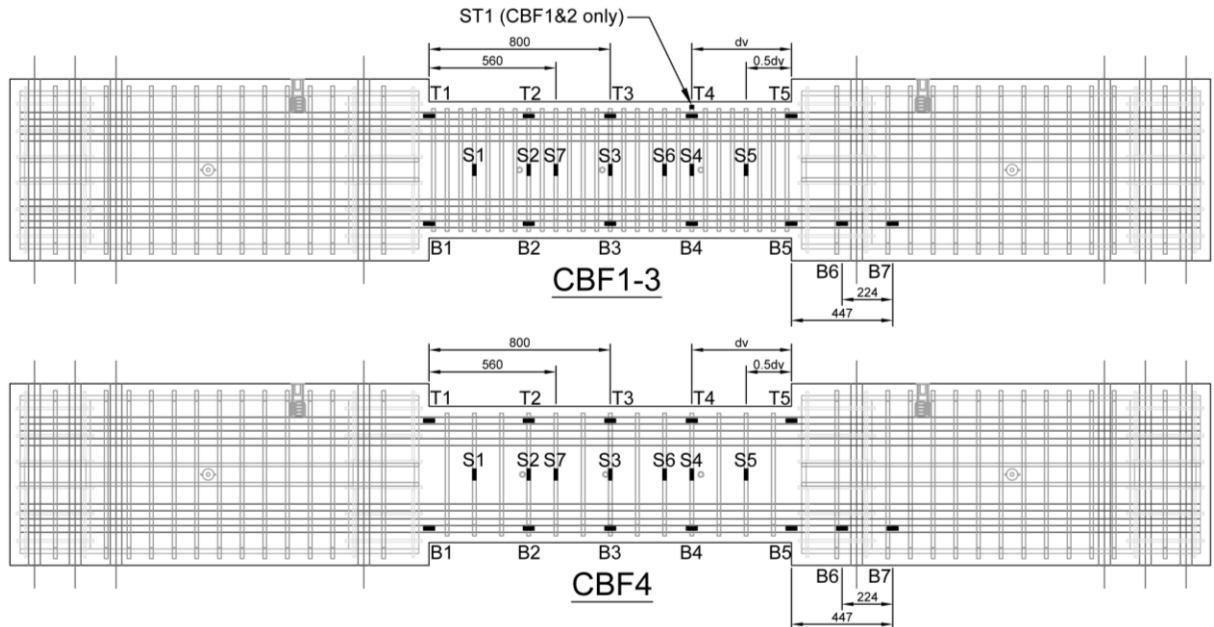


Figure 4-18: Strain Gauge Layouts for CBF1 to CBF4

Five strain gauges were installed on the top and bottom layers of longitudinal reinforcement, labelled T1-T5 and B1-B5 respectively. Two additional strain gauges were installed on the longitudinal bars in the shear wall a distance  $0.5d_v$  and  $d_v$  away from the shear wall interface, labelled B6 and B7. These were used to directly measure the yield penetration of the longitudinal bars. An additional strain gauge, labelled B5-X, was installed as a precautionary measure due to initial placement issues with the B5 strain gauges. Seven strain gauges were installed mid-depth on the stirrups, labelled S1-S7. These strain gauges alternated on the north and south facing legs of the stirrups to detect any torsion that may have occurred during the test. A single strain gauge, labelled ST1, was installed on the top of a stirrup for CBF1 and CBF2 in order to measure any out-of-plane strains in the stirrups. The strain gauges were hooked up to the same central computer data acquisition as the LVDTs and linear pots with a sampling frequency of 10 Hz.

## 4.3 Testing of Specimens

### 4.3.1 Test Preparations

The test assembly alignment was refined immediately before testing. To aid with this endeavor, a plumb bob was attached to the edge of the load bearing plate and hung just below the support bearing plate. The plumb bob was first aligned in the north-south direction. The lateral bracing was used to tilt the test assembly until the plumb bob measured the same distance away from concrete surfaces along its height. This was accomplished by adjusting the bolts at the ends of the lateral braces to tilt the assembly in the desired direction. The plumb bob was then aligned in the west-east direction. This was accomplished using the self-weight jacks to lift the test assembly off of its temporary supports, then raise and lower each jack until the plumb bob aligned with the edge of the bottom loading plate, shown in Figure 4-19.

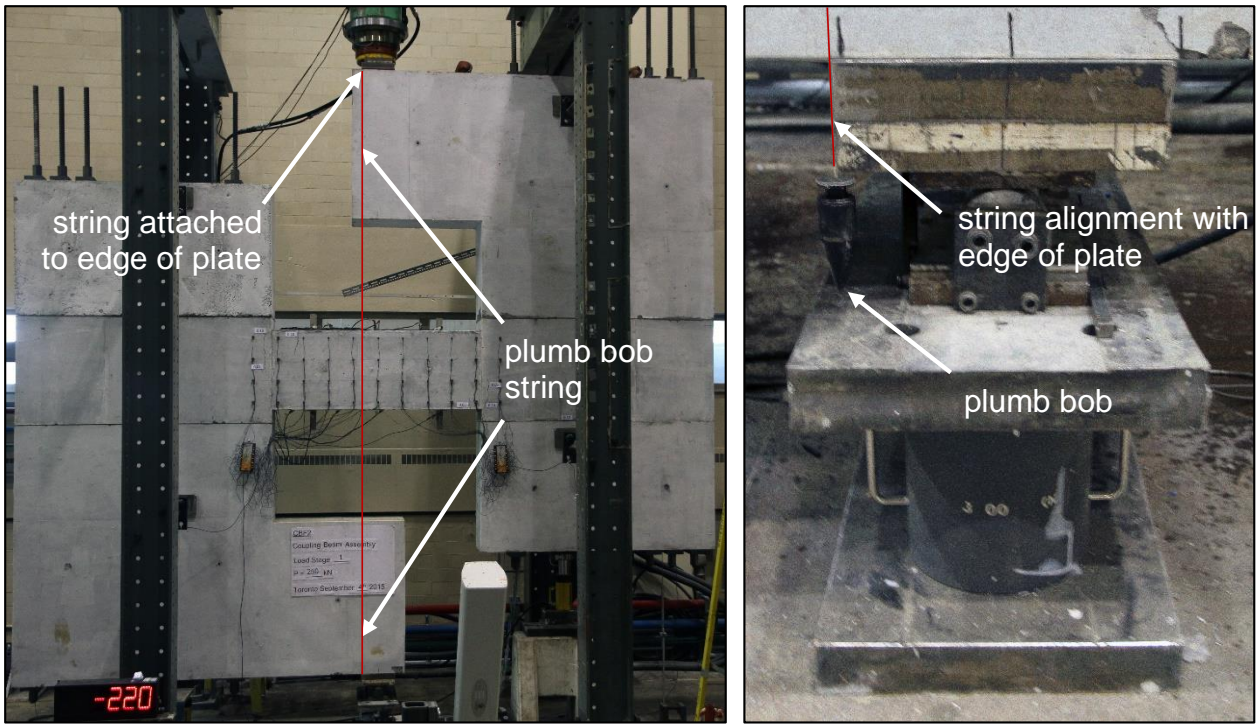


*Figure 4-19: West-East Alignment of Test Assembly*

Once aligned, the two hydraulic lines for the self-weight jacks were paired together so that any change in oil pressure would change both jacks by the same proportional increment. The load cells underneath the pin support were zeroed while the test assembly was lifted off of it. With the self-weight jacks paired, they were slowly lowered until the load cells registered a sum of 0.5 kN, at which point the load maintainer for the self-weight jacks was locked. This ensured the jacks were holding only the self-weight of the test assembly, and any additional load would be applied to the coupling beam. With the test assembly in place, the loading jack was lowered until it registered 1 kN. This readout was double-checked against the sum of the load cells under the pin support.

The bolts on the lateral braces were backed-off to prevent large frictional forces between the braces and the test assembly. Enough pressure was maintained to hold the pads in place while still allowing them to move with the test assembly. The pin-support was also unlocked to allow for rotation of the test assembly. Wood blocks were placed underneath the ends of the test assembly in order to provide support in the event that the pump lost its pressure, causing the

loading jack and/or self-weight jacks to retract. These wood blocks were adjusted throughout the test to ensure there was enough of a gap to allow displacement of the test assembly.

The Metris K610 camera system was initiated and all LED targets checked to ensure they were visible to the camera. All of the instrumentation was zeroed except the load cells. In order to be able to view real time data during the test, various channels were displayed using the data acquisition computer system, shown in Figure 4-20. Readouts of particular importance were the load versus tangential displacement plot and the shear-strain versus time plot. Both of these were used to detect significant events such as the occurrence and spreading of cracking, yielding of steel, and maximum load resisted by the specimens.

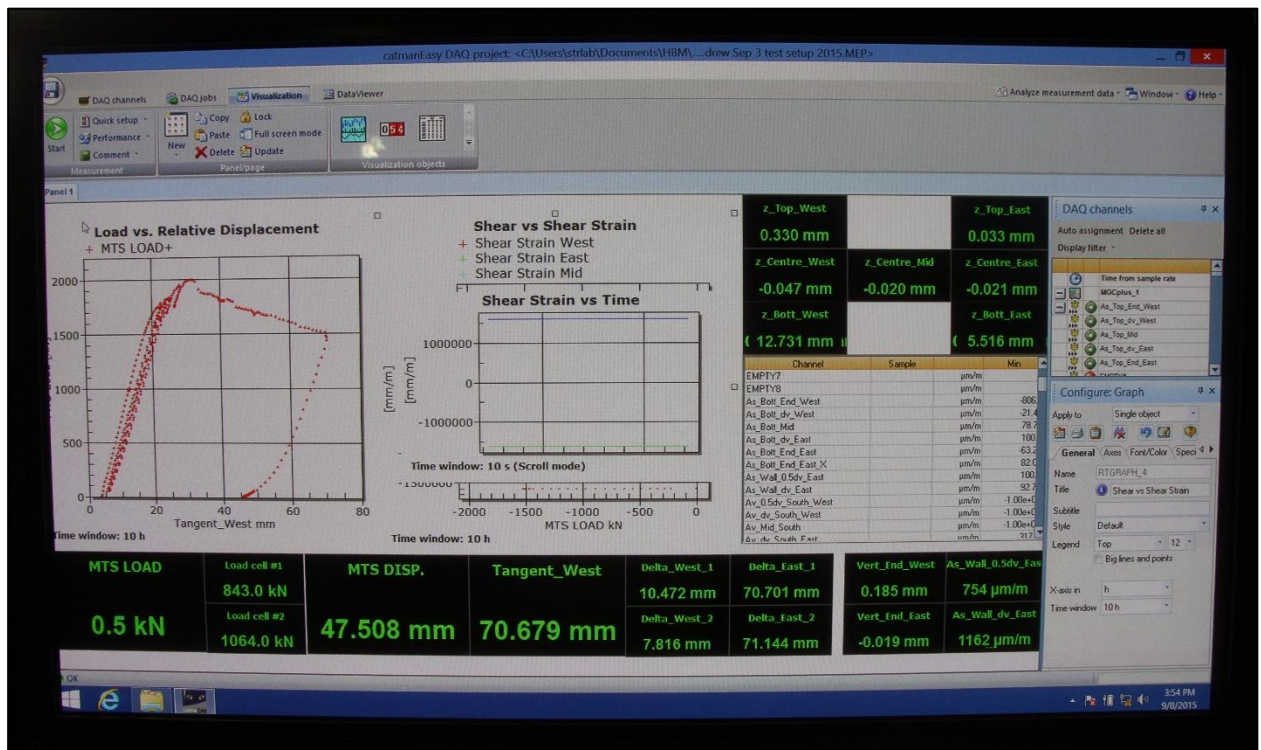


Figure 4-20: Real-time Visualization of Data Channels for Test of CBF2

A high resolution 18-megapixel digital camera and 1080p HD camcorder were set up on the south side of the specimen in order to document the tests. At this stage, the test was ready to commence. A full view of the test setup is shown in Figure 4-21.



*Figure 4-21: Experimental Test Setup*

Due to the complexity of the test procedure, each experiment took several days. At the end of each test day, the applied load was removed and the test assembly was lowered back onto the temporary supports. The following day, the initiation process outlined earlier was repeated. The only difference is that the instrumentation was not zeroed so that any permanent deformations and creep that occurred between test days was still captured.

#### 4.3.2 Loading Protocol

All of the test specimens were loaded to failure under monotonic loading. The load was paused at various load stages in order to inspect the specimen, take photos, mark crack propagation, and manually measure crack widths. Scaffolding and ladders were used to access the coupling beam. During a load stage, the machine operator removed 10% of the load for the safety of those performing the inspections. With the load removed, the LED camera system was paused, however the LVDTs, linear pots, and strain gauges continuously measured throughout the test.

In order to mimic the cyclic wind loading experienced by coupling beams, the load was cycled at the second last, and last load stages before the predicted failure. The machine load was reduced to a value between 0 kN and 50 kN, then loaded back up to the load stage value. This was repeated once more in order to create three peaks at the load stage value. After reaching the third peak, and pausing to inspect the specimen, the load was increased to the next load stage or to failure.

All tests had a loading rate of 0.03 mm/sec when loading for the first time, 0.05 mm/sec when unloading and reloading a load stage, and 0.08 mm/sec when unloading and reloading the cycles.

Once peak load was reached, the displacement of the loading jack was increased until the applied load was less than 80% of the failure load and the specimen had achieved significant displacements. This was done to ensure there was adequate data for the post-peak analysis of the coupling beams.

#### 4.3.3 Test Overview

The testing of specimens CBF1 to CBF4 occurred throughout the months of August and September, 2015. The final testing schedule based on when each load stage was completed is presented in Table 4-1.

*Table 4-1: Testing Schedule for CBF1-4*

Specimen	LS1	LS2	LS3	LS4	LS5	LS6	LS7
CBF1	Friday Aug. 7		Monday Aug. 10		Tuesday Aug. 11*		
CBF2		Friday Sept. 4			Tuesday Sept. 8*		
CBF3			Wednesday Sept. 16		Thursday Sept. 17*		
CBF4				Wednesday Sept. 23*			

\*failure occurred on this date

Each of the specimens had their own predetermined load stages based on the predicted failure loads. During the tests, the load stages were modified based on the observed behavior of the specimens. The applied machine load associated with each of the load stages, the failure load, and the end of post-peak loading are presented in Table 4-2.

Table 4-2: Machine Load,  $P$ , at Load Stages, Peak Load, and End of Post-Peak [kN]

Specimen	LS1	LS2	LS3	LS4	LS5	LS6	LS7	Peak	Post-Peak
CBF1	253	502	1002	1501	1751*	1875*	-	1918	1217
CBF2	252	501	1002	1501	1801*	1827*	1950	1992	1503
CBF3	257	503	1000	1500	1752*	1827*	-	1830 <sup>+</sup>	1138
CBF4	251	502	1003*	1130*	1251	1381	-	1481	1076

\*load cycled three times    +peaked during second cycle

During loading, the sum of the load cells under the pin-support was compared to that of the machine load. It was observed that as the machine load increased, the difference between these two values grew apart, with the machine load reading a higher value. This difference was primarily caused by friction in the self-weight jacks but also involved friction on the bearing pads that provided the lateral restraint. The frictions resisted the displacement of the test assembly, causing an increase in machine load. In order to mitigate some of the friction, the load maintainer for the self-weight jacks was adjusted periodically such that the load cell readings matched that of the machine load. Even with these periodic adjustments, there was still a variation in machine load,  $\Delta P$ . Figure 4-22 plots these variations against the machine load.

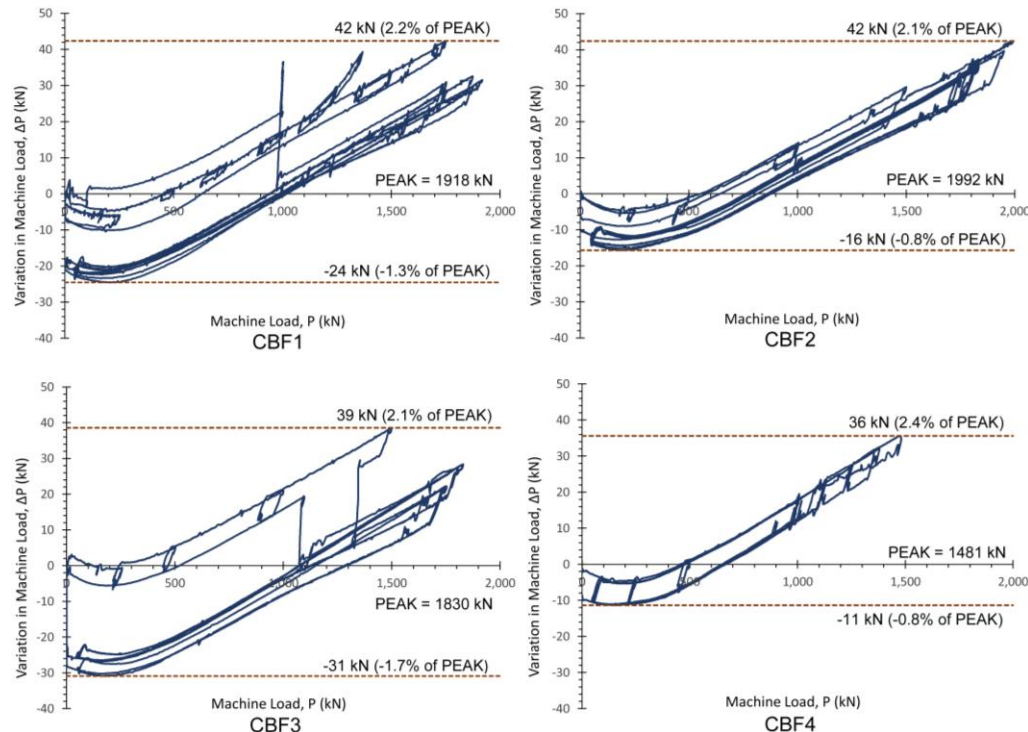
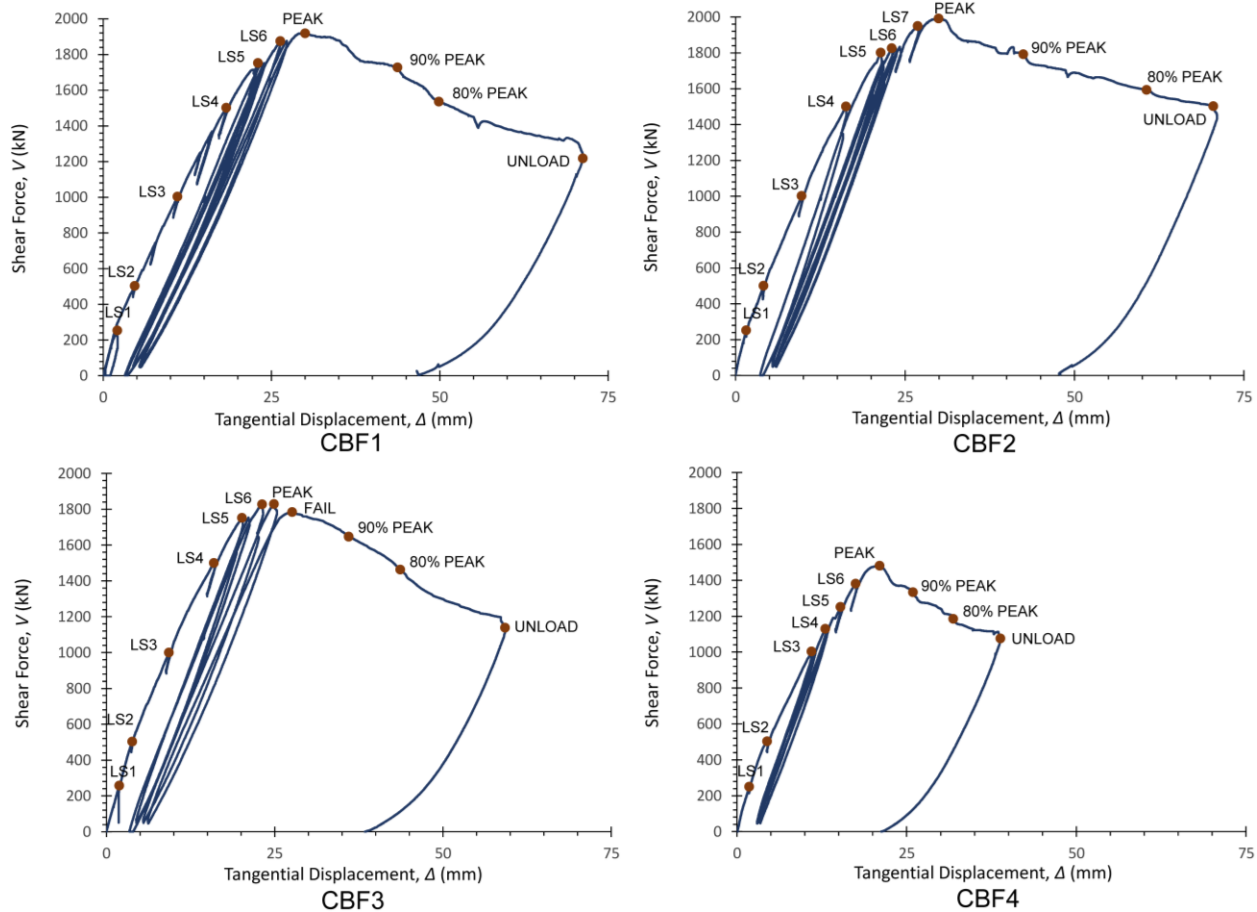


Figure 4-22: Machine Load Variation due to Self-Weight Jack Friction

From the graphs, the maximum variation was 2.4% of the peak load. This variation is not considered significant for these tests and will be neglected. The machine load will be used as the applied load for the remainder of the analysis.

The tangential displacement measurement was also influenced by other factors during the test. It was observed that at higher loads, the interface between the cantilever shear wall components and the end blocks of the specimens started to open up on the tension face of the shear wall. This was due to the elongation of the post-tensioning bars. The expansion at the interface, measured with LDVTs on the shear wall, caused an extra rotation of the test assembly that artificially increased the tangential displacement. This was easily corrected for during the analysis stage.

Since the machine load,  $P$ , is equal to the shear force in the beam,  $V$ , the shear force will be used as the primary variable for the remainder of the analysis. The shear force versus displacement plots for CBF1 to CBF4 with labelled load stages are presented in Figure 4-23.



*Figure 4-23: Shear Force vs. Tangential Displacement for CBF1 to CBF4*

#### 4.3.4 Test Observations for Specimen CBF1

Specimen CBF1 was designed with a concrete side cover of 3 mm and a shear reinforcement ratio of 2.11% which was 18 times the required CSA Code minimum. CBF1 had a test day concrete strength of 80.3 MPa. The coupling beam reached an ultimate shear capacity of 1918 kN, resulting in an average sectional shear stress of 13.8 MPa. The shear force versus tangential displacement plot with labelled load stages is presented in Figure 4-24.

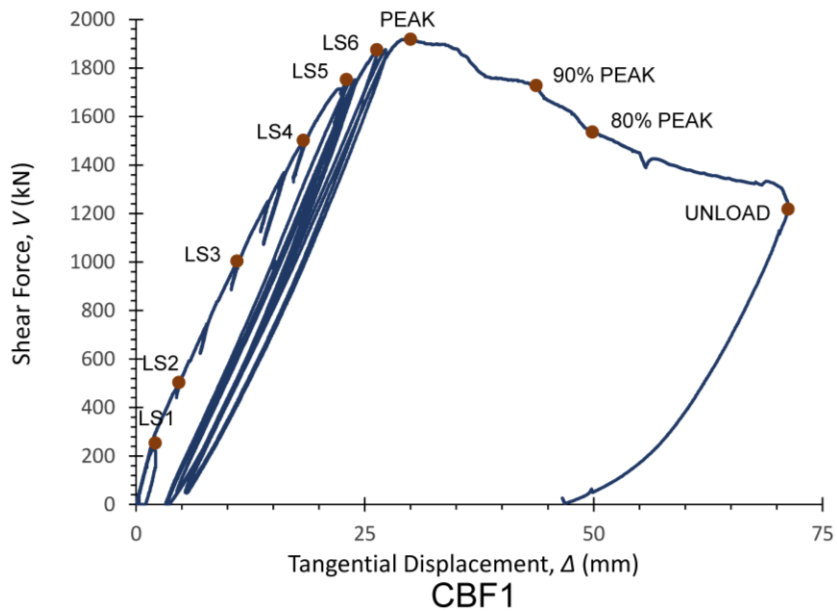


Figure 4-24: Shear Force vs. Tangential Displacement for CBF1 (repeat of Fig. 4-23)

During loading to the first load stage, a noise was heard at 80 kN. Pausing at 125 kN revealed the first flexural crack had formed at the face of the east shear wall. Being the only observable crack, loading continued with real-time readouts of the sectional strains showing a crack forming on the west end of the specimen at 200 kN, followed by a crack forming on the east end at 220 kN. At the first load stage of 253 kN, three flexural cracks had formed on each end of the beam; the largest propagating to three quarters of the beam depth. The first shear crack had also formed on the east end at an angle of approximately 45 degrees. Figure 4-25 shows a photograph from load stage one. The numbers shown in Figure 4-25 are the crack widths in mm, manually measured with an accuracy of 0.05 mm.



Figure 4-25: Photograph of CBF1 at Load Stage 1

During loading to the second load stage, the shear strains for the east and west ends of the beam converged around 300 kN, meaning both sides of the beam were equally cracked. Reaching the second load stage at 502 kN, shear cracks had formed  $d_v$  (439 mm) away from the shear wall faces on both ends of the beam at angles of approximately 35 degrees. The flexural cracks at the wall interfaces had begun to widen. At 750 kN, halfway through loading to the third load stage, the specimen was unloaded to 625 kN in order to remove the locks on the pin-support. This step was missed during the test preparations, but was not considered to have a significant impact on the initial test data since there was no change in slope on the load versus displacement graph before and after the pin was released. At the third load stage of 1002 kN, shear cracks had formed at midspan at an angle of approximately 30 degrees, as shown in Figure 4-26.

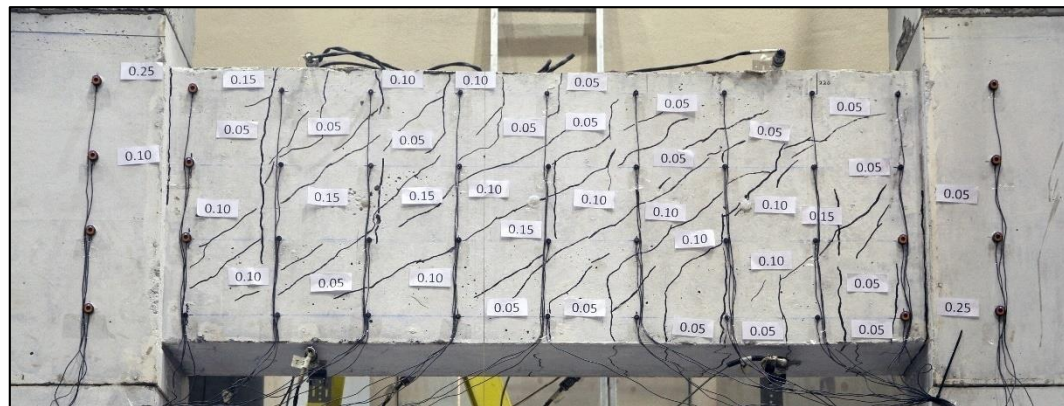


Figure 4-26: Photograph of CBF1 at Load Stage 3

At 1250 kN, the test was paused and unloaded to 1125 kN in order to investigate a loud bang. No significant change in the cracking pattern was observed and none of the real time data was affected. It was determined that the noise was caused by the slipping of the lateral bracing pads. There was enough friction between the bolts and the pads that the bolts were able to deform with the movement of the pad. Once the friction was overcome by the elastic resistance of the bending bolt, the pads slipped and the bolts returned to their original position causing a loud bang. This stick-slip friction noise was heard repeatedly throughout all four tests.

At 1370 kN it was observed that the east end of the test assembly had started bearing on the temporary wood block underneath it. The test was paused and unloaded to 1080 kN to ensure enough of the data was recaptured without the effects of the wood block.

Between load stage four and five at 1720 kN, the pump for the loading jack reached its set limit, causing the load to plateau. Real time creep on the load versus displacement plot was observed. The pump limit was quickly adjusted and the loading recommenced to 1751 kN for load stage five. The load was cycled three times at 1750 kN causing an additional tangential displacement of 1.2 mm.

During load stage six at 1875 kN, it was observed that there was significant cracking in the shear wall end blocks of the specimen. See Figure 4-27. It was decided that these cracks should be marked for the remaining duration of the test in order to better visualize the coupling beam shear wall interaction. The widths of these “shear wall” cracks were not measured for CBF1, however they were marked and measured during the other three tests. More shear cracks had formed in the region located  $d_v$  from the shear walls with a maximum width of 0.3 mm. Propagations of existing cracks had reduced their inclinations to approximately 25 degrees. The flexural cracks at the wall interface had expanded to 0.65 mm. A crack of 1.2 mm was observed at mid-depth of the beam at the face of the east shear wall. This crack was an artifact of the shear wall edge beginning to spall off. The cracks in the shear wall end blocks had propagated approximately 75% into the shear wall shown in Figure 4-27. A photograph of load stage six is presented in Figure 4-28.



Figure 4-27: Crack Propagation in East Shear Wall End Block for CBF1

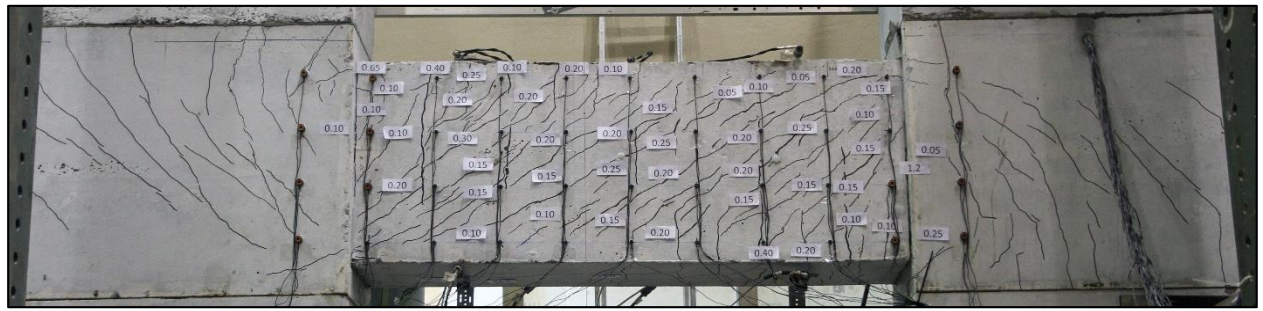


Figure 4-28: Photograph of CBF1 at Load Stage 6

It was also observed that all of the flexural cracks were forming at stirrup locations. This was apparent due to an offset of the flexural cracks between the north and south faces. This was best observed from the top and bottom surfaces as shown in Figure 4-29. This occurred for all four specimens.

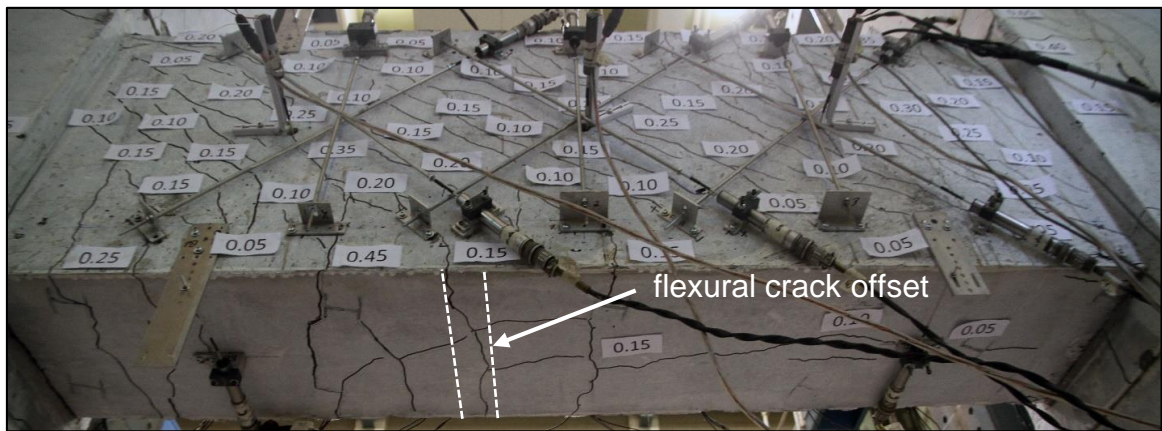
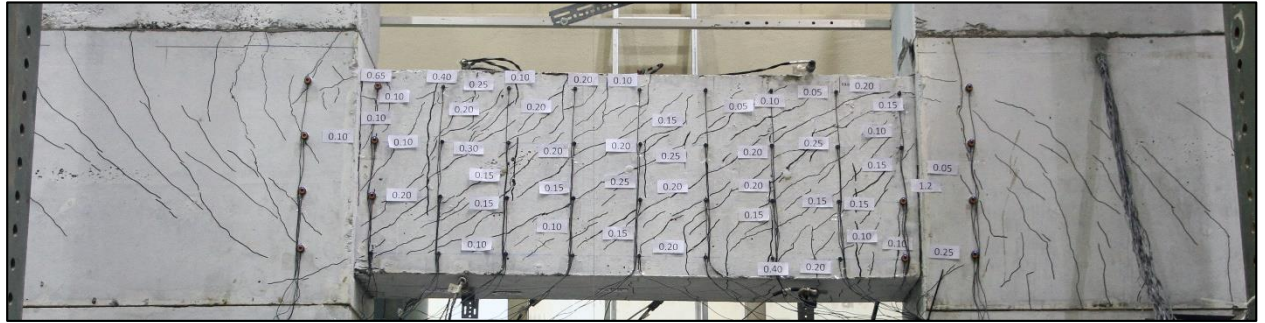


Figure 4-29: Flexural Crack Offset Observed from Bottom Surface of CBF1

The load was cycled three times at 1875 kN causing an additional tangential displacement of only 1.6 mm. Peak load occurred at 1918 kN with a tangential displacement of 30.0 mm. The failure was gradual and with no immediate drop in strength. Figure 4-30 shows the specimen at the peak load.



*Figure 4-30: Photograph of CBF1 at Peak Load*

The post-peak response was very ductile. The tangential displacement increased to 71.2 mm yet the beam was still able to hold 1217 kN; 63% of the peak load. There was visible deterioration of the concrete surface during the post-peak response. Upon closer inspection, the 3 mm side cover had spalled off. A photo of the beam at the end of post-peak loading is presented in Figure 4-31.



*Figure 4-31: Photograph of CBF1 at end of Post-Peak*

After the specimen had been unloaded and placed onto its temporary supports, the loose concrete cover was removed from the surface of the coupling beam. A majority of the concrete side cover outside the compression fan region had spalled off, including the cover on the top and bottom faces of the beam. A portion of the edge of the east shear wall had also spalled off. A photo of the beam with the loose cover removed is presented in Figure 4-32. The substantial displacement of the coupling beam is clearly evident in this figure.



*Figure 4-32: Loose Concrete Cover Removed for CBF1*

A full set of photographs from each of the loads stages for the north and south faces of CBF1 are presented in Appendix D.1.

#### 4.3.5 Test Observations for Specimen CBF2

Specimen CBF2 was designed with a concrete side cover of 45 mm and a shear reinforcement ratio of 1.67% which was 14 times the required CSA minimum. CBF2 had a test day concrete strength of 80.3 MPa. The coupling beam reached an ultimate shear capacity of 1992 kN, resulting in an average sectional shear stress of 11.4 MPa. The shear force versus tangential displacement plot with labelled load stages is presented in Figure 4-33.

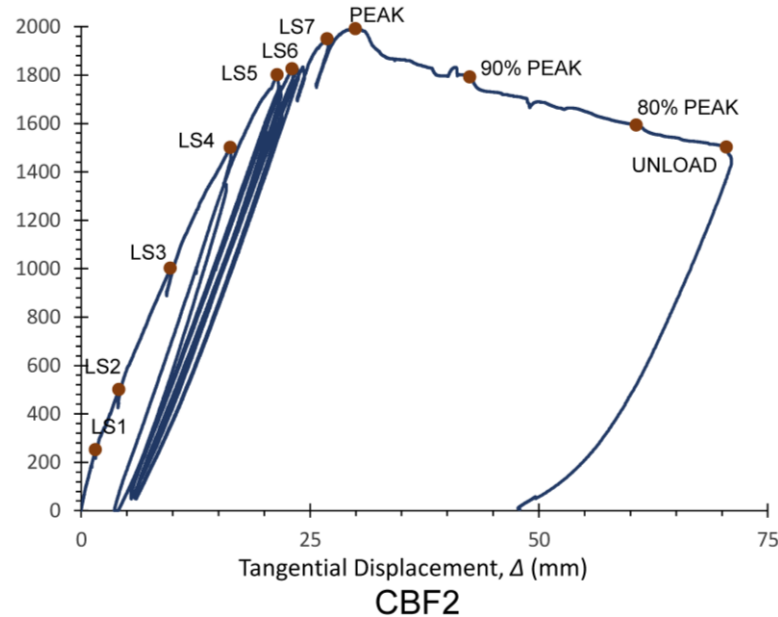


*Figure 4-33: Shear Force vs. Tangential Displacement for CBF2 (repeat of Fig. 4-23)*

The first flexural cracked occurred around 90 kN based on a change in the real-time strain measurements. At the first load stage at 252 kN, two flexural cracks had formed on each end of the beam. The largest crack occurred in the shear wall of the specimen and propagated to half of the beam depth. This was a different observation than CBF1 where the flexural crack occurred at the wall interface. Since CBF2 had full 45 mm side cover, the strains were able to transfer into the wall and form a crack at the edge of the shear wall reinforcement. The first crack in the shear wall end blocks also occurred at this load. Figure 4-34 shows the photograph for load stage one.

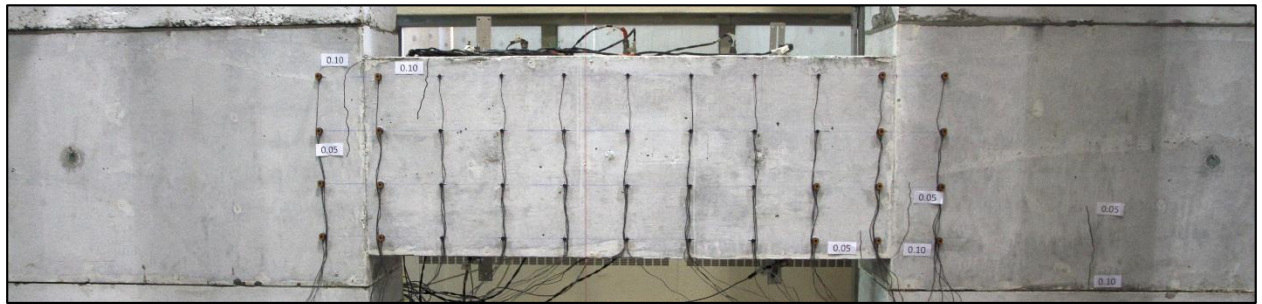


*Figure 4-34: Photograph of CBF2 at Load Stage 1*

At 502 kN for the second load stage, shear cracks had formed  $d_v$  away from the shear wall face on both ends of the beam at an angle of approximately 45 degrees. Shear cracks also began to form in the shear wall end blocks. At the third load stage at 1002 kN, shear cracks had formed at midspan and at an angle of approximately 35 degrees, as shown in Figure 4-35.



*Figure 4-35: Photograph of CBF2 at Load Stage 3*

Between load stage four and five, the pump for the loading jack had reached its set limit. The pump limit was adjusted, however there was a significant jump in the load since the jack control had not been paused. The load jumped to 1801 kN before it was paused, overshooting the specified target of 1750 kN for load stage five. A load stage was taken at this value, however during the

cycling phase, the load was cycled at 1750 kN rather than 1801 kN to be consistent with what was done for CBF1. During these cycles the tangential displacement increased by 0.6 mm.

At 1827 kN for load stage six, larger shear cracks had formed in the region  $d_v$  from the shear walls, having a maximum width of 0.5 mm. This width was much larger than the 0.3 mm seen at 1875 kN for CBF1 due to fewer cracks for the strains to distribute across. The propagations of existing cracks had reduced inclinations of about 25 degrees. The flexural cracks at the edge of the shear wall had expanded to 0.65 mm. The photo for load stage six is shown in Figure 4-36.

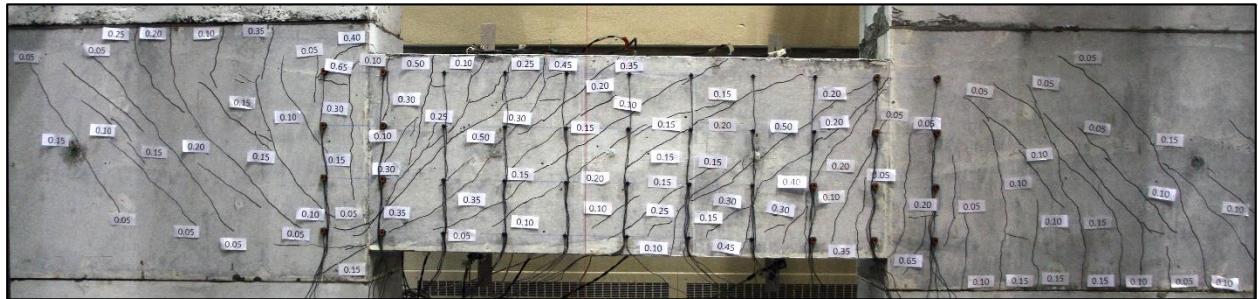


*Figure 4-36: Photograph of CBF2 at Load Stage 6*

The load was cycled three times at 1827 kN causing an additional tangential displacement of only 1.2 mm. A seventh load stage was taken at 1950 kN, however the load was not cycled at this stage so that there would be a consistent number of cycles performed on each specimen. Shear cracks continued to propagate with a maximum width of 0.8 mm located  $d_v$  from the east shear wall face. The flexural cracks at the edge of the shear wall had expanded to a maximum width of 0.85 mm. The cracks in the shear wall end blocks had propagated approximately 75% of the way into the shear wall shown in Figure 4-37. A photograph of load stage seven is presented in Figure 4-38.

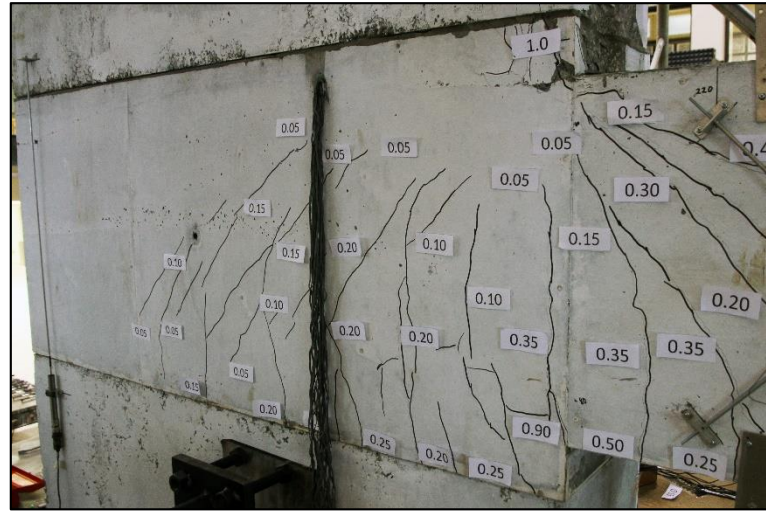


*Figure 4-37: Crack Propagation in East Shear Wall End Block for CBF2*

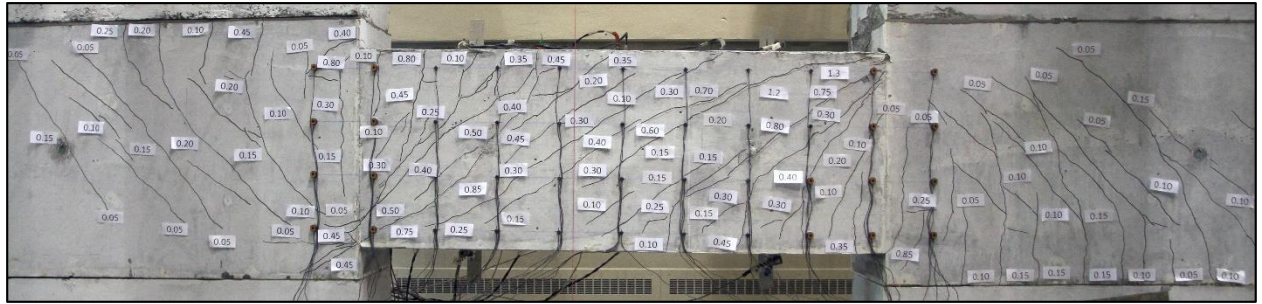


*Figure 4-38: Photograph of CBF2 at Load Stage 7*

The peak load occurred at 1992 kN with a tangential displacement of 30.0 mm. This was similar to the displacement experienced by CBF1 at peak load. There was a steeper loss of strength after the peak which then levelled off at a displacement similar to that of CBF1. Figure 4-39 shows the specimen at the peak load.

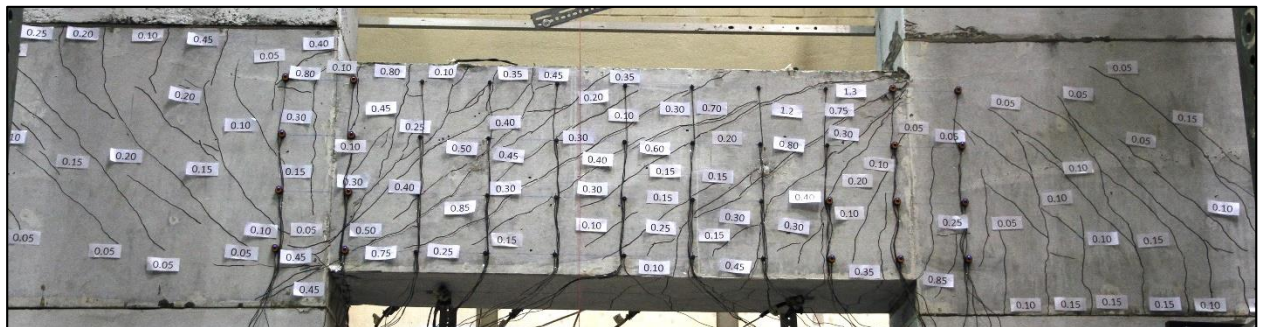


*Figure 4-39: Photograph of CBF2 at Peak Load*

The post-peak response was very ductile. The tangential displacement increased to 70.5 mm yet the beam was still able to hold 1503 kN; 75% of the peak load. There was visible deterioration of the concrete surface during the post-peak response due to concrete side cover spalling. A photo of the beam at the end of post-peak is presented in Figure 4-40.

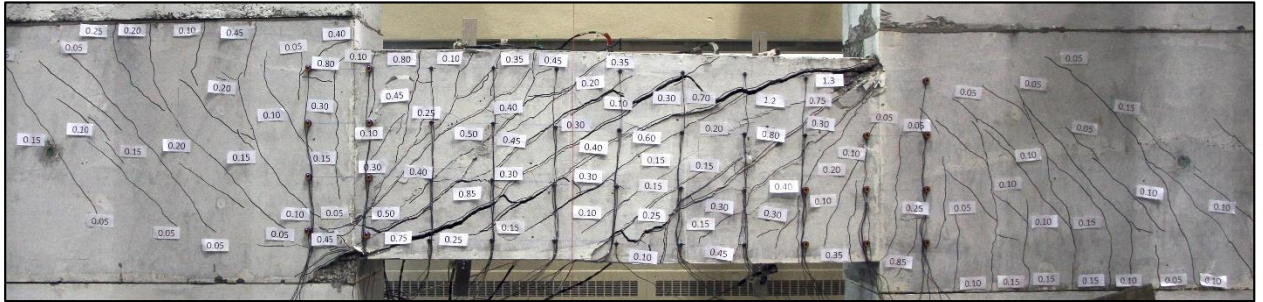


*Figure 4-40: Photograph of CBF2 at end of Post-Peak*

After the specimen had been unloaded and placed onto its temporary supports, the loose concrete cover was removed from the surface of the coupling beam. All of the concrete side cover outside of the compression fan region was able to be removed. A photo of CBF2 with the loose cover removed is presented in Figure 4-41.



*Figure 4-41: Loose Concrete Cover Removed for CBF2*

A full set of photographs from each of the loads stages for the north and south faces of CBF2 are presented in Appendix D.2.

#### 4.3.6 Test Observations for Specimen CBF3

Specimen CBF3 was designed with a concrete side cover of 45 mm and a shear reinforcement ratio of 1.67 % which was 15 times the required CSA minimum. CBF3 had a test day concrete strength of 66.5 MPa. The coupling beam reached an ultimate shear capacity of 1830 kN,

resulting in an average sectional shear stress of 13.3 MPa. The shear force versus tangential displacement plot with labelled load stages is presented in Figure 4-42.

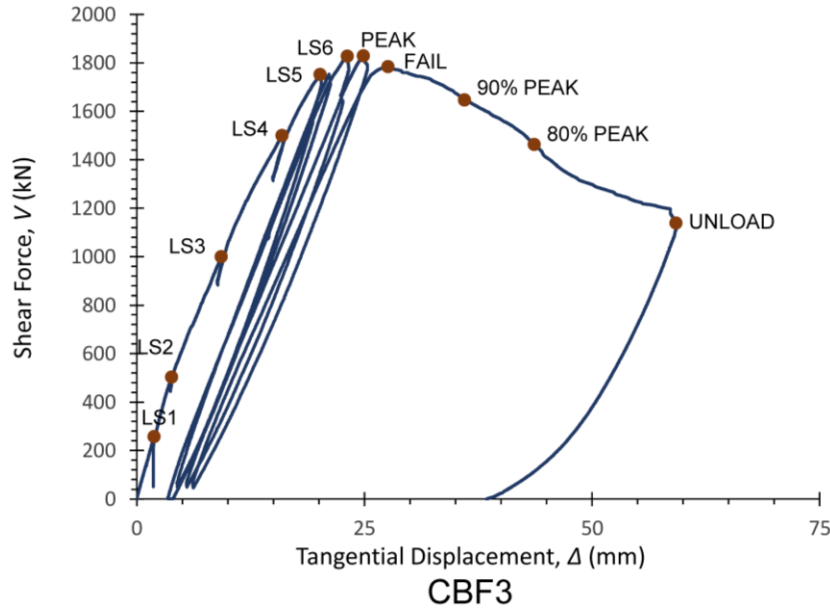


Figure 4-42: Shear Force vs. Tangential Displacement for CBF3 (repeat of Fig. 4-23)

At 257 kN for the first load stage, very few cracks were observed. Despite having a weaker concrete strength than CBF1 and CBF2, only three flexural cracks approximately 30 to 50 mm long had formed. Figure 4-43 shows the photograph for load stage one.



Figure 4-43: Photograph of CBF3 at Load Stage 1

At 503 kN for the second load stage, a single shear crack had formed at midspan at approximately 45 degrees, and the largest flexural crack propagated to three quarters of the beam depth. No cracks were observed in the shear wall end blocks. Loading continued, with real-time readouts of the sectional strains showing a crack forming at the east end and midspan at 620 kN,

followed by a crack forming at the west end at 720 kN. At 1000 kN for the third load stage, shear cracks had formed  $d_v$  away from the shear walls at angles of approximately 35 degrees, with a maximum width of 0.15 mm. Flexural crack widths had expanded to a maximum of 0.20 mm. Cracks had started to form in the shear wall end blocks. There were significantly fewer cracks at this load than exhibited by CBF1 and CBF2. A photo of load stage three is shown in Figure 4-44.



*Figure 4-44: Photograph of CBF3 at Load Stage 3*

At load stage five, the load was cycled three times at 1752 kN. During these cycles the tangential displacement increased by 1.5 mm. During load stage six at 1827 kN, significant shear cracks had formed over the entire beam. The maximum width was 0.9 mm located  $d_v$  away from the east shear wall, which was almost double the width experienced by CBF2 at the same load. The propagations of existing cracks were inclined at about 25 degrees. The flexural cracks at the edge of the shear wall had expanded to a maximum width of 0.80 mm at the west shear wall face. The cracks in the shear wall end blocks had propagated approximately 75% into the wall as shown in Figure 4-45. The photo for load stage six is shown in Figure 4-46.

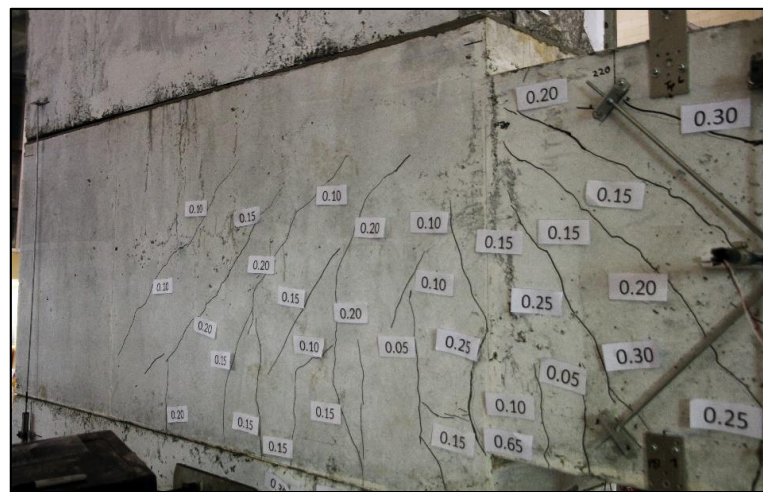


*Figure 4-45: Crack Propagation in East Shear Wall End Block for CBF3*

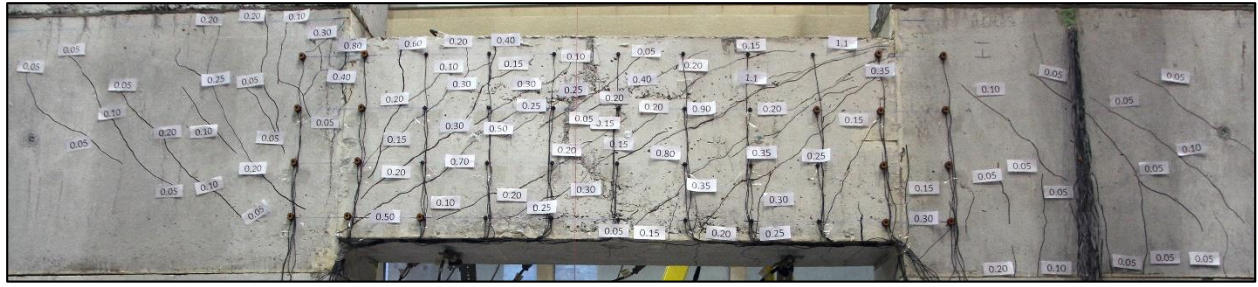


*Figure 4-46: Photograph of CBF3 at Load Stage 6*

The load was cycled at 1827 kN. The tangential displacement had increased by 1.8 mm after only the first cycle which was significant compared to the cycles from the previous tests. This cycle finished at a load of 1830 kN which ended up being the peak load for the test. A photograph of the specimen at the peak load is presented in Figure 4-47.



*Figure 4-47: Photograph of CBF3 at Peak Load*

The load was paused at this cycle in order to determine if any concrete side cover had begun to spall. A metal rod was used to tap the concrete surface, with any change in sound pitch signifying side cover spalling. It was observed that the side cover had started to spall at the flexural compression corners, with the east side having more spalled concrete than the west. On the second cycle the specimen peaked at a load of 1785 kN. The tangential displacement increased an additional 2.7 mm for a total of 27.6 mm. This was 2.4 mm smaller than the peak displacements of CBF1 and CBF2. Failure was gradual with no immediate loss of strength.

The post-peak response was ductile, but less ductile than CBF1 and CBF2. The tangential displacement was increased to 59.2 mm and the beam was able to hold 1183 kN; 65% of the peak load. There was visible deterioration of the concrete surface during the post-peak response due to concrete side cover spalling. A photo of the beam at the end of post-peak response is presented in Figure 4-48.



*Figure 4-48: Photograph of CBF3 at end of Post-Peak*

After the specimen had been unloaded and placed onto its temporary supports, the loose concrete cover was removed from the surface of the coupling beam. The concrete side cover had spalled outside the compression fan region except for at mid-depth of the beam. A photo of CBF3 with the loose cover removed is presented in Figure 4-49.



*Figure 4-49: Loose Concrete Cover Removed for CBF3*

A full set of photographs from each of the loads stages for the north and south faces of CBF3 are presented in Appendix D.3.

#### 4.3.7 Test Observations for Specimen CBF4

Specimen CBF4 was designed with a concrete side cover of 45 mm and a shear reinforcement ratio of 0.83% which was eight times the required CSA minimum. CBF4 had a test day concrete strength of 66.5 MPa. The coupling beam reached an ultimate shear capacity of 1481 kN, resulting in an average sectional shear stress of 8.4 MPa. The shear force versus tangential displacement plot with labelled load stages is presented in Figure 4-50.

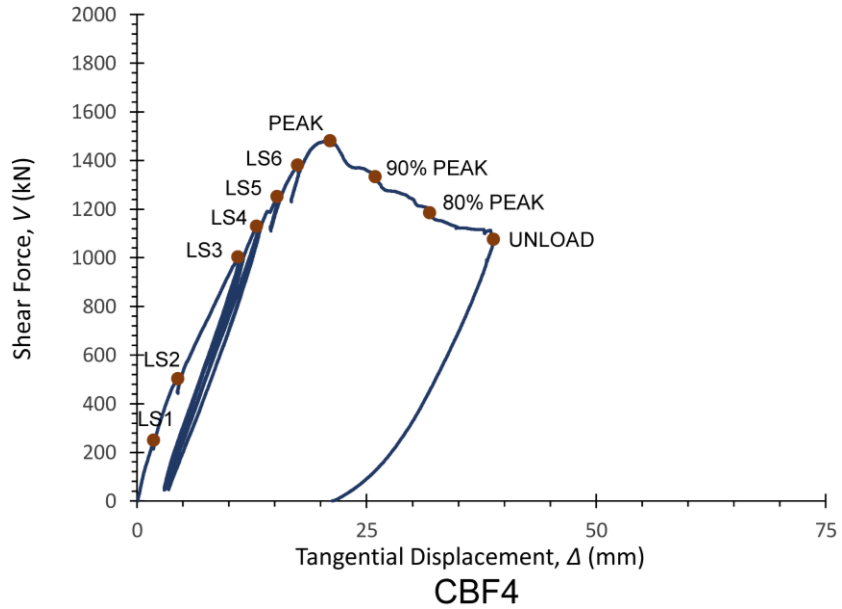


*Figure 4-50: Shear Force vs. Tangential Displacement for CBF4 (repeat of Fig. 4-23)*

At the first load stage of 251 kN no cracks were observed, similar to CBF3. The test proceeded to load stage two at 502 kN where three flexural cracks had formed at each end of the beam. Shear cracks had formed at midspan and  $d_v$  away from the shear walls, at 45 degree angles, but only on the north face of the beam shown in Figure 4-51. The south face had no shear cracks shown in Figure 4-52. This was presumed to be caused by some torsional effects, however once the beam was fully cracked, these effects would become negligible. There were no cracks in the shear wall end blocks.

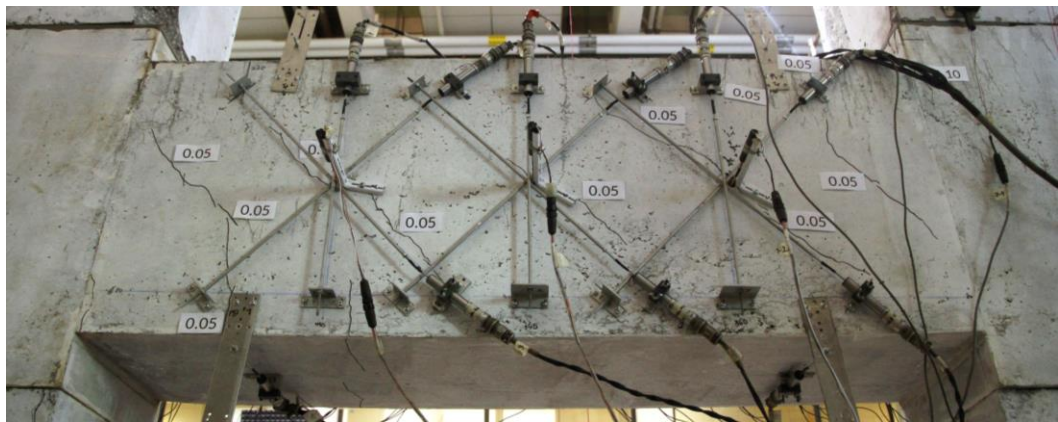


*Figure 4-51: Photograph of Shear Cracks on North Face of CBF4 at Load Stage 2*

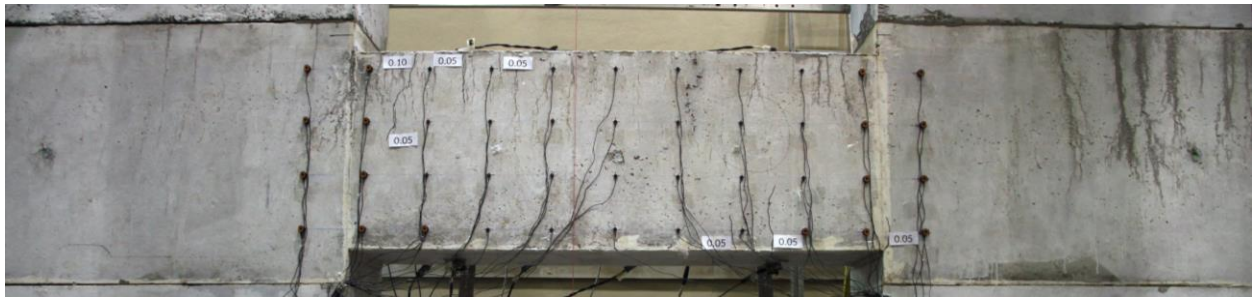


*Figure 4-52: Photograph of South Face of CBF4 at Load Stage 2*

At 1003 kN for the third load stage, shear cracks had formed on the north face of the beam at angles of approximately 30 degrees located  $d_v$  away from the shear wall faces, and 25 degrees at midspan. The maximum shear crack width was 0.25 mm near midspan of the beam. There were significantly fewer flexural cracks than previous tests, with the largest having a width of 0.25 mm. Cracks had started to form in the shear wall end blocks at this load. A photo of load stage three is presented in Figure 4-53.

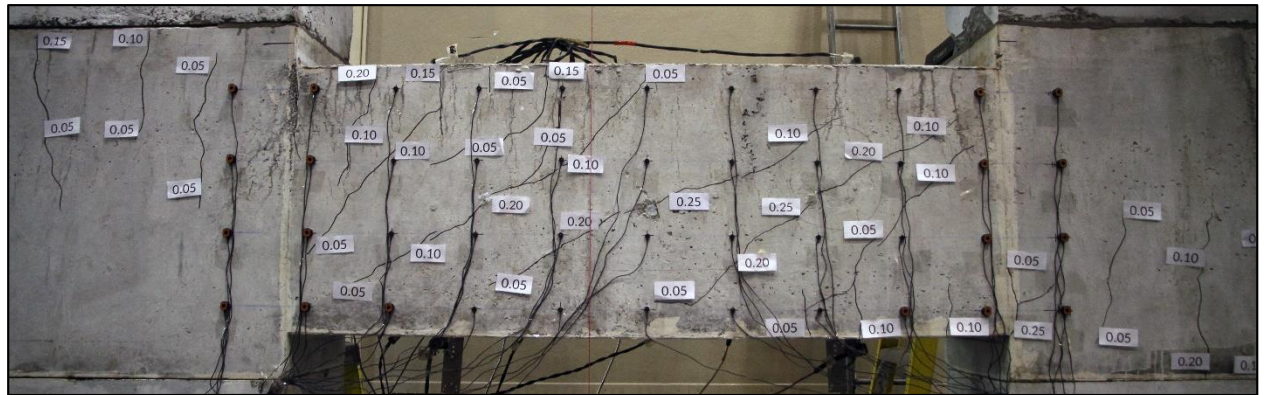


*Figure 4-53: Photograph of CBF4 at Load Stage 3*

The load was cycled three times at 1003 kN, and again at 1130 kN for load stage 4, causing an increase in the tangential displacement by 0.5 mm and 0.4 mm respectively. These load stages were chosen to be cycled based on a predicted failure load of 1200 kN, however this was not the case. Load stage five and six occurred at 1251 kN and 1381 kN respectively. Cycles were not performed at these load stages in order to maintain the same number of cycles for the test series. At load stage six, the maximum shear crack width had reached 0.45 mm at  $d_v$  away from the shear walls. The propagations of existing cracks occurred at about 25 degrees. The flexural cracks at the edge of the shear wall had expanded to a width of 0.45 mm. There were fewer

cracks marked on the south side of the shear walls, with the cracks propagating about 30% into the wall. Cracks marked on the north side of the shear walls propagated into 75% of the shear wall as shown in Figure 4-54. The discrepancy was likely due to difficulties marking the cracks on the south side. The photo for load stage six is shown in Figure 4-55.



*Figure 4-54: Crack Propagation in East Shear Wall End Block for CBF4*

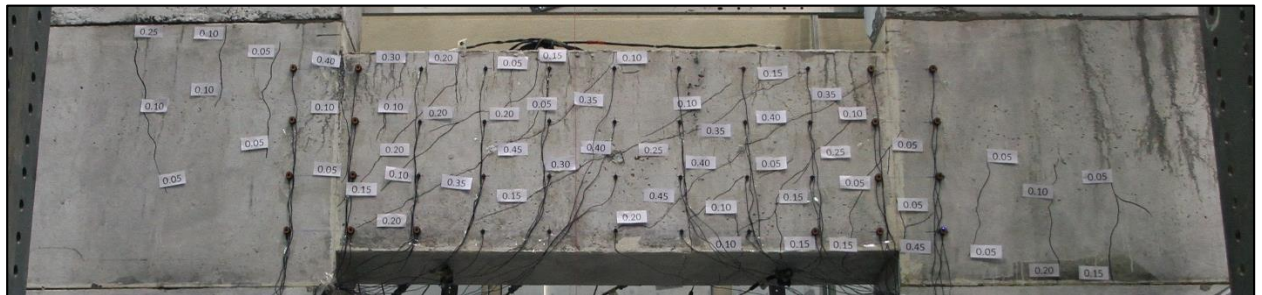


*Figure 4-55: Photograph of CBF4 at Load Stage 6*

Peak load occurred at 1481 kN with a tangential displacement of 21.1 mm. Figure 4-56 shows the specimen at the peak load.

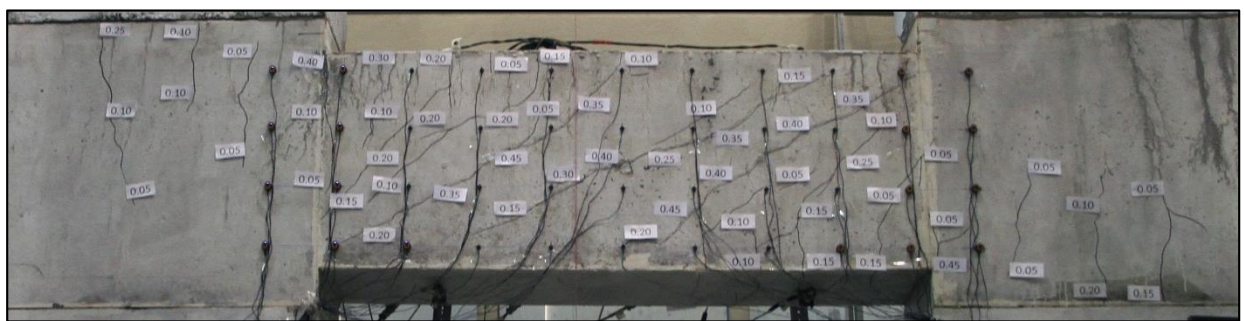


*Figure 4-56: Photograph of CBF4 at Peak Load*

The post-peak response had a similar ductility to CBF3. The tangential displacement was increased to 38.8 mm and the beam was still able to hold 1076 kN; 73% of the peak load. There was visible deterioration of the concrete surface during the post-peak response due to concrete side cover spalling. A photo of the beam at the end of post-peak is presented in Figure 4-57.



Figure 4-57: Photograph of CBF4 at end of Post-Peak

After the specimen had been unloaded and placed onto its temporary supports, the loose concrete cover was removed from the surface of the coupling beam. The concrete side cover had spalled outside the compression fan region. A photo of CBF4 with the loose cover removed is presented in Figure 4-58.



Figure 4-58: Loose Concrete Cover Removed for CBF4

A full set of photographs from each of the loads stages for the north and south faces of CBF3 are presented in Appendix D.4.

## Chapter 5: Discussion of Experimental Results

The failure mechanics for the coupling beam specimens were characterized by yielding of the stirrups followed closely by slip on the crack, and then concrete crushing. It was observed that spalling of the concrete side cover occurred prior to reaching the peak load. The full response of the specimens will be elaborated in the section including evaluation of the collected data. A summary of the experimental observations is presented in Table 5-1.

*Table 5-1: Summary of Experimental Observations*

Specimen	Beam Section	Yielding of Stirrups			Peak Load					
		V (kN)	v (MPa)	$\varepsilon_z$ (mm/m)	V (kN)	$\Delta$ (mm)	v (MPa)	$\gamma_{xz}$ (mm/m)	$\varepsilon_z$ (mm/m)	$\Delta_{oop}$ (mm)
CBF1	West	1747	12.6	2.11	1918	30.0	13.8	6.44	3.35	0.48
	Midspan	1750	12.6					6.50	3.49	0.41
	East	1696	12.2					7.33	5.66	1.34
CBF2	West	1755	10.0	2.11	1992	30.0	11.3	5.99	6.70	1.54
	Midspan	1867	10.6					4.89	4.19	0.74
	East	1769	10.1					3.96	4.65	1.51
CBF3	West	1700	9.7	2.11	1830	27.6	10.4	4.67	6.67	1.03
	Midspan	1757	10.0					3.31	7.90	1.05
	East	1734	9.9					4.19	8.95	0.28
CBF4	West	1353	7.7	2.11	1481	21.1	8.4	4.03	3.72	0.11
	Midspan	1351	7.7					4.77	4.56	0.03
	East	1308	7.4					4.27	5.43	0.26

The primary variables that were altered between the four specimens were the concrete side cover thickness between CBF1 and CBF2, the concrete strength between CBF2 and CBF3, and the shear reinforcement ratio between CBF3 and CBF4. This section will also focus on how these variables influenced the failure of each specimen and how it relates to the concrete side cover spalling phenomenon. Other interesting conclusions from the data will also be presented.

For the purposes of data presentation, all cyclic data collected below 10% of the load stage value has been removed from the data plots in order to better visualize the data envelope. The only exception is for CBF 3 where the last cycle in which the specimen failed is plotted.

## 5.1 Sectional Strains

The sectional strains for the coupling beam specimens were calculated using the LVDTs attached to the north face. The strains are calculated for three beam sections:  $d_v$  (439 mm) from the shear wall faces and at midspan. The sectional strains are all plotted with the sectional shear stress taken as  $\nu = V/(b_w d_v)$  where  $b_w$  is the unspalled width.

### 5.1.1 LVDT Shear Strains

The shear strains were calculated using the LVDTs crossed at 45 degrees and 135 degrees on the north face of the coupling beam specimens. The sectional shear stress versus shear strain plots for each coupling beam are presented in Figure 5-1.

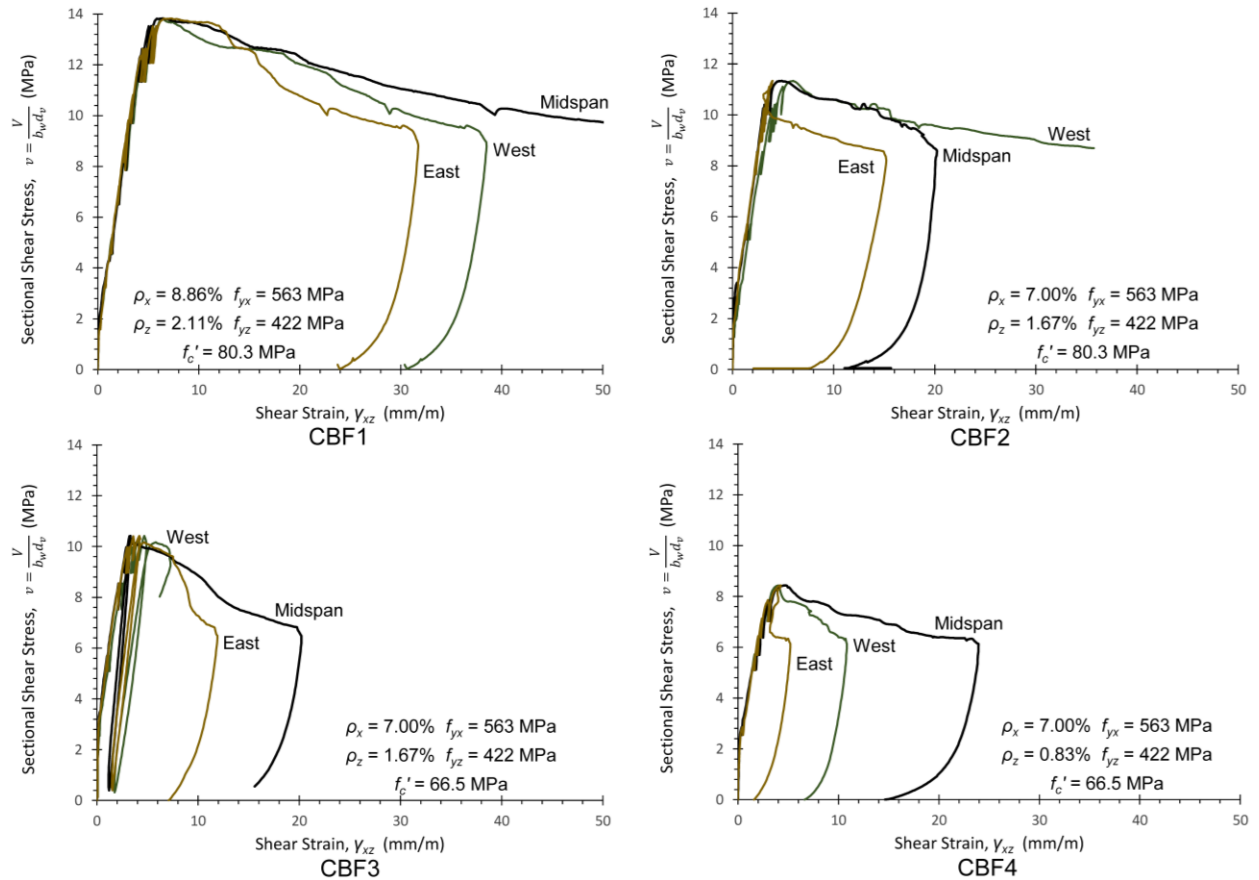


Figure 5-1: Sectional Shear Stress vs. Shear Strain for CBF1 to CBF4

The end of the post-peak response for the midspan strain of CBF1, and the west strains of CBF2 and CBF3, were truncated due to erroneous readings by the LVDTs. This was due to the spalled concrete interfering with the strain measurements. The east strain for CBF2 shows odd behavior

just after the peak due to a crack forming directly through the mounting screws of the LVDT, causing it to come loose. The east strain for CBF4 shows odd behavior also due to an LVDT coming loose as a result of poor installation.

The shear strains had a significant contribution to tangential displacement of the coupling beams. Since the moment at midspan is zero, it can be assumed that the midspan shear strain is representative of an element undergoing pure shear. If this strain is assumed to act over the 1600 mm coupling beam length plus  $0.5d_v$  extensions into the walls at each end, giving a 2039 mm effective shear length, the shear strain contribution to the tangential displacement at peak load can be calculated as shown in Table 5-2 below.

*Table 5-2: Tangential Displacement due to Pure Shear at Peak Load*

Specimen	Midspan Shear Strain $\gamma_{xz}$ (mm/m)	Shear Displacement $\Delta_v$ (mm)	Total Displacement $\Delta$ (mm)	Contribution of Shear Displacement (%)
CBF1	6.50	13.25	30.0	44.2
CBF2	4.89	9.97	30.0	33.2
CBF3	3.31	6.74	27.6	24.4
CBF4	4.77	9.73	21.1	46.0

It can be seen that the shear strain deformations of the coupling beam contributed between 25% and 50% of the total tangential displacement at the peak load. In addition to the shear strain deformations, the diagonal compression due to shear increases the coupling beam curvature which also contributes to the tangential displacement. The values in Table 5-2 therefore underestimate the total impact of shear on the deformations of the coupling beams. It is clear that shear deformations play a significant role in the behavior of coupling beams and should be taken into account when determining a building's stiffness. If the shear deformations are ignored during the analysis, the total stiffness of the building could be significantly overestimated. To illustrate this, the load versus tangential displacement curve for CBF1 up to the peak load is plotted in Figure 5-2. The uncracked and cracked elastic response of the coupling beams with the applied shear force defined as  $12EI\Delta/L^3$  are also plotted. The variation in total displacement is substantial, with the cracked response predicting 3.6 mm while the experimental results reached 30.0 mm at the peak load.

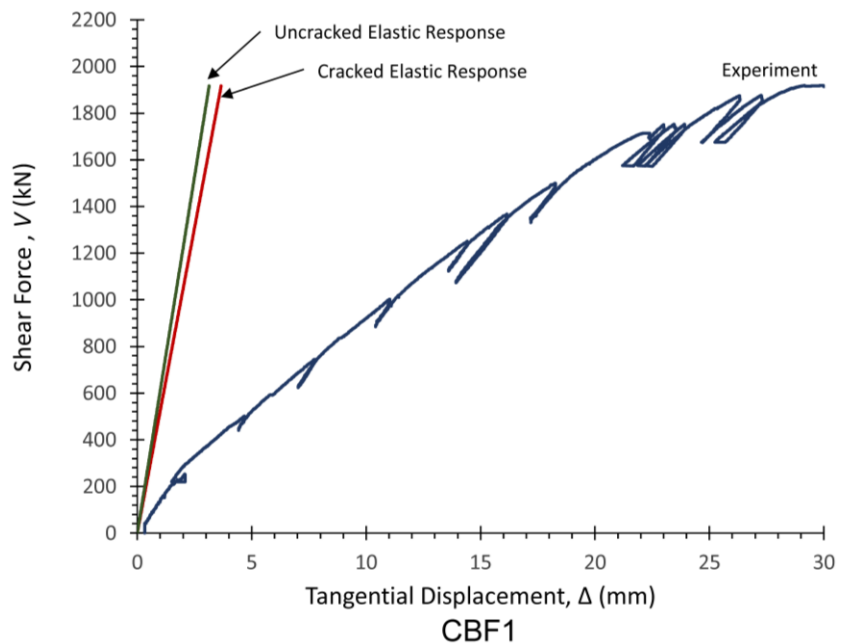


*Figure 5-2: Evaluation of Elastic Stiffness for CBF1*

### 5.1.2 LVDT z-Direction Strains

The z-direction strains were calculated using the vertical LVDTs on the north face of the coupling beam specimens. The sectional shear stress versus z-direction strain plots for each coupling beam are presented in Figure 5-3.

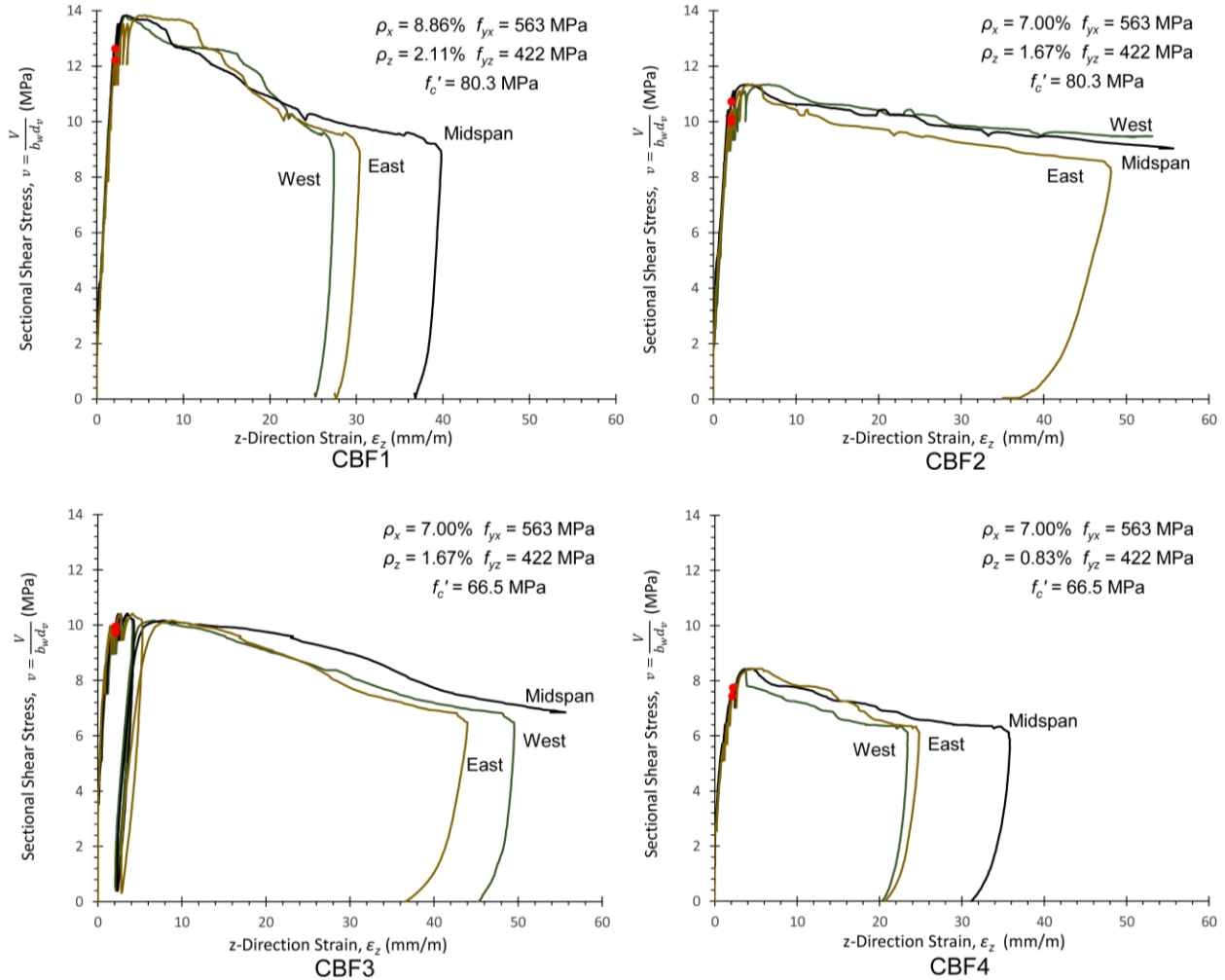


Figure 5-3: Sectional Shear Stress vs. z-Direction Strain for CBF1 to CBF4

The end of the post-peak response for the west and midspan strains in CBF2, and the west strain in CBF3, were truncated due to erroneous readings by the LVDTs. This was due to the spalled concrete interfering with the strain measurements.

The red data points in Figure 5-3 indicate when the z-direction strain, averaged over the 440 mm base length of the vertical LVDTs, reached a value of 2.11 mm/m which corresponds to the yield strain of the stirrups. The data points indicate that the stirrups yielded before the peak load was reached. A zoomed in view of these data points is presented in Figure 5-4.

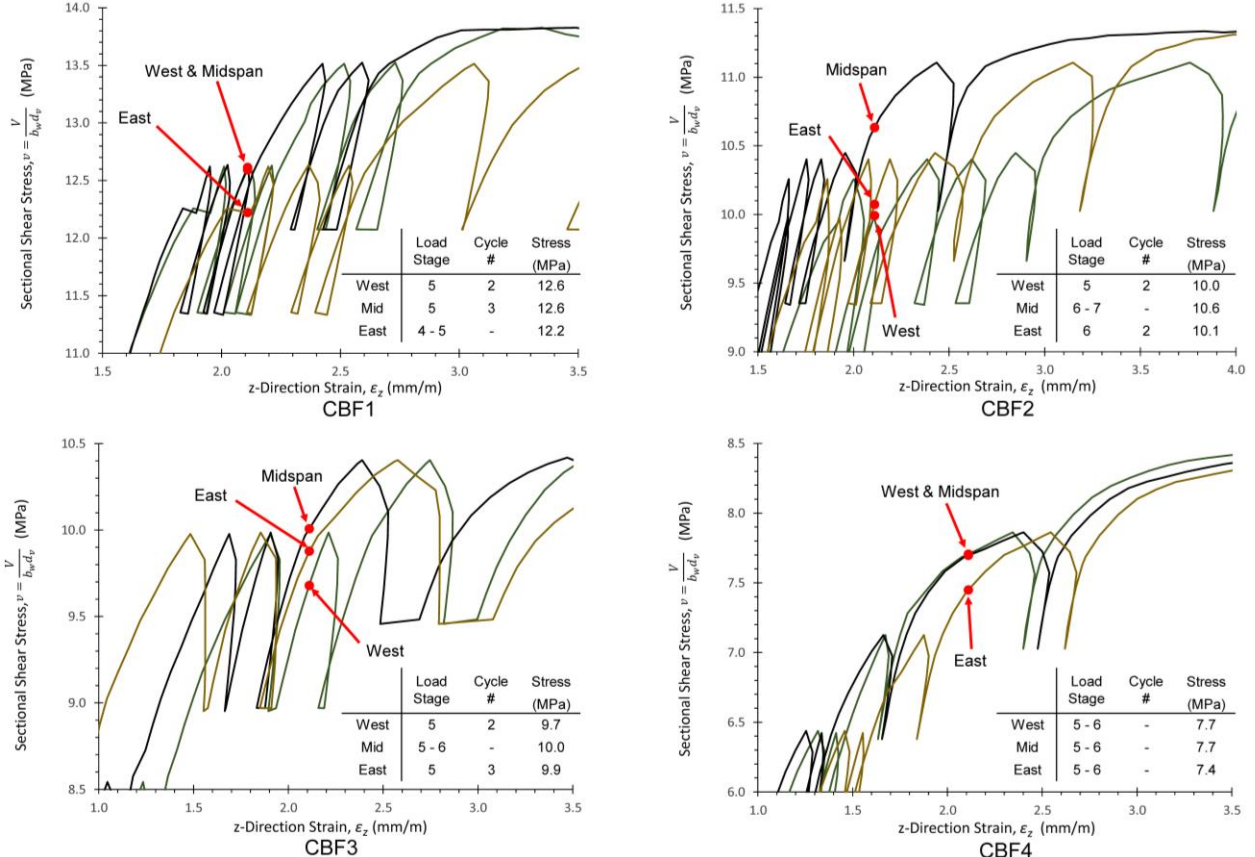


Figure 5-4: Zoomed in Stirrup Yield Points on Stress-Strain Plots for CBF1 to CBF4

From the zoomed in plots it can be seen that for each specimen, the stirrups reached yield at relatively similar sectional shear stresses. It is important to note that the z-direction strains reached the yield strain at different times during the test. The tables in Figure 5-4 identify at what load stage the strain was reached, and if it occurred during one of the load stage cycles. The loading cycles had a significant role in increasing the sectional strains without increasing the sectional stress.

## 5.2 Local Reinforcement Strains

The local reinforcement strains were measured using strain gauges attached directly to the reinforcing bars. Strain gauge measurements during the post-peak loading were very unreliable due to large reinforcement strains and deterioration of the concrete around the strain gauges causing many to malfunction or wires to break. Post-peak strains presented in this section are for visual purposes only in order to demonstrate the variation that occurred after the peak load. A full set of data plots for the strain gauges are available in Appendix E.

### 5.2.1 Transverse Reinforcement Strains

Local stirrup strains were obtained from strain gauges affixed mid-height on the stirrup legs. The gauges were installed on north and south facing stirrups legs in order to detect any torsional effects caused by the test setup. The measured strains at each load stage are plotted with respect to the strain gauge location in Figure 5-5. The horizontal axis on the top of the plots identifies which side of the beam the stirrup leg was located.

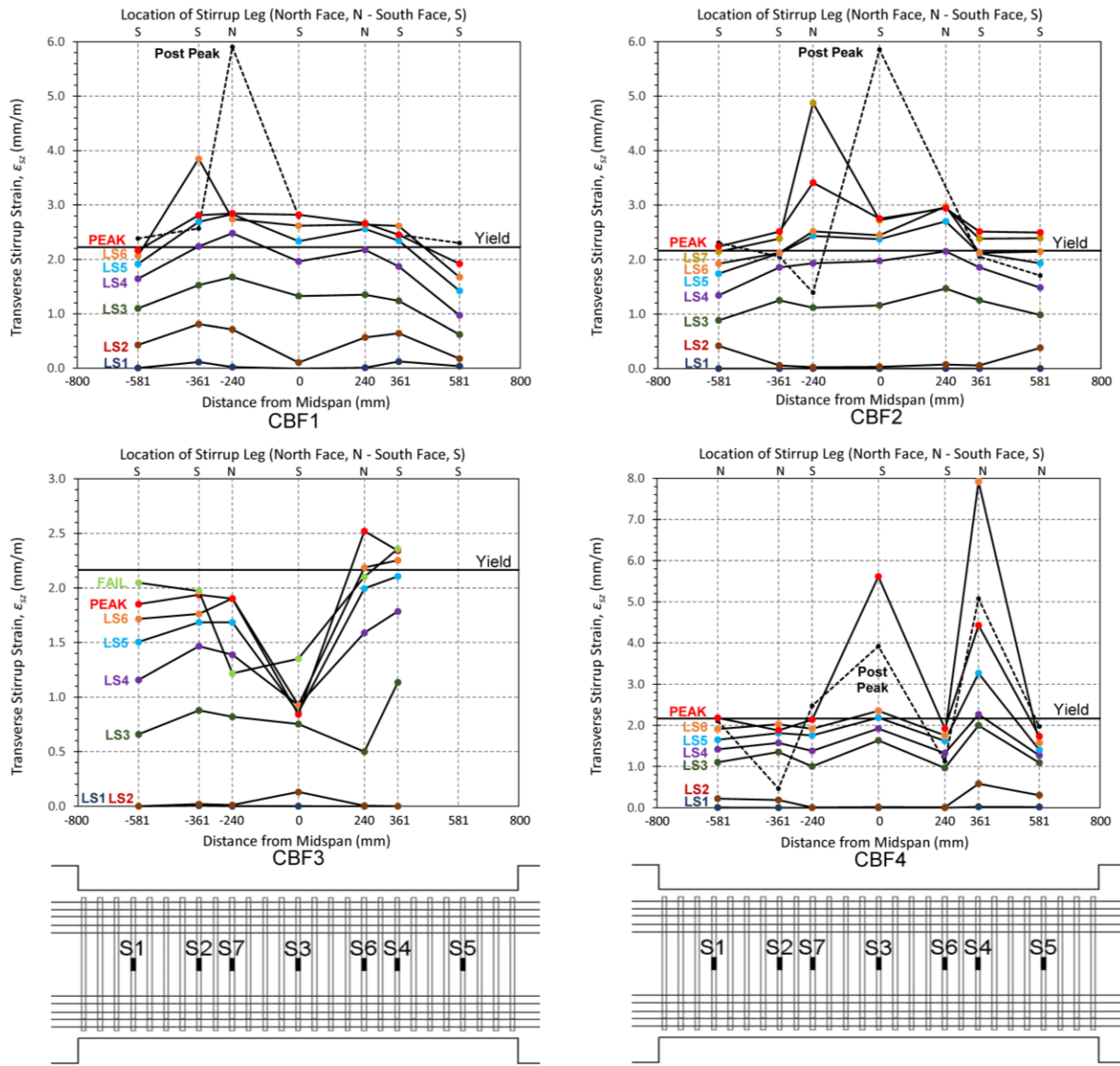


Figure 5-5: Local Transverse Reinforcement Strains for CBF1 to CBF4

The measured strains from gauge S5 in CBF3 were erroneous in nature and were removed from the analysis. The measured strains from gauge S3 in CBF3 appear to have stagnated after the third load stage. The gauge should have been showing strains closer to yield at the peak load based on the measurements from S4 and S6. All strains to the west of midspan for CBF3 also show odd behavior, with none of the strains surpassing the yield strain despite LVDT data indicating they should have.

Outside of these anomalies, it was observed that the stirrups yielded prior to reaching the peak load. When compared to the LVDT z-direction strains, the strain gauges showed the stirrups yielding at lower shear stresses, with most stirrups yielding between load stages four, five and six for all specimens. Yielding primarily occurred in stirrups located a distance  $d_v$  (439 mm) from the shear wall faces to midspan, with stirrups located at  $d_v$  yielding first. When comparing strains on the north and south stirrup legs, there seem to be no significant variations that would indicate torsional effects occurred.

The strain measurements for gauge S4 in CBF4 show much higher strains than the other gauges in the beam. This phenomenon is due to a crack forming at the strain gauge location. At this crack location, the tensile strain in the concrete drops to zero, causing the stirrup strain to increase [14].

### 5.2.2 Longitudinal Reinforcement Strains

Local longitudinal strains were obtained from strain gauges affixed on the outermost top and bottom layers of reinforcing bars. The strain gauges were affixed to the sides of the bars and aligned with their centreline to ensure the average bar strain was measured. The strains at each load stage are plotted with respect to the strain gauge location in Figure 5-6.

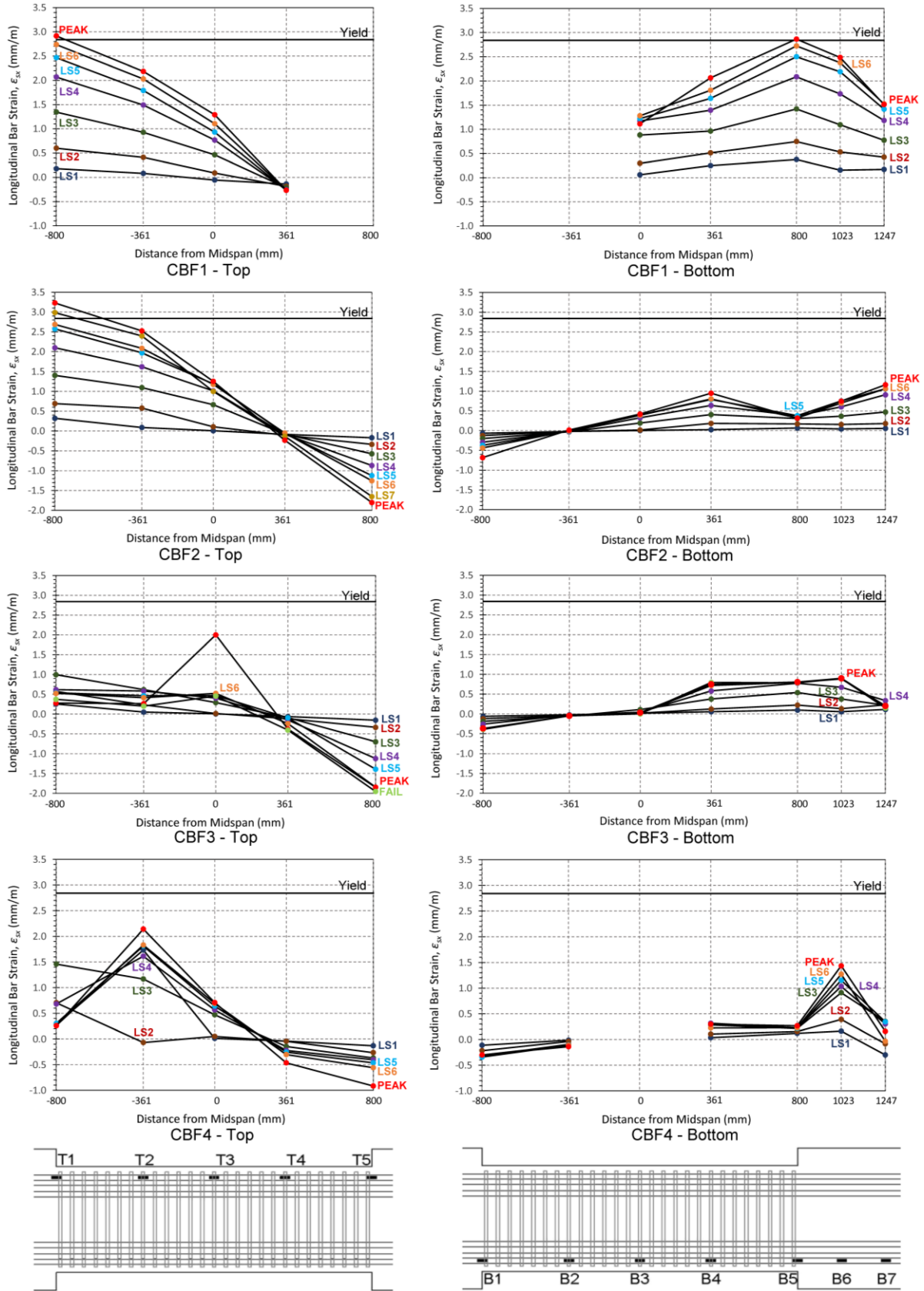


Figure 5-6: Local Longitudinal Reinforcement Strains for CBF1 to CBF4

The measured strains from gauges T5, B1, and B2 in CBF1, and B3 in CBF4 were erroneous in nature and were removed from the analysis. The measured strains for a significant number of gauges, specifically for the bottom layers of reinforcement in CBF3 and CBF4, appear to be measuring lower strains than expected when compared to the top layers of reinforcement. This could be a result of the strain gauges being damaged during casting or wires breaking as the beams deformed. These strains will be verified using the LED targets in Section 5.3.

Outside of these anomalies, it was observed that the longitudinal reinforcement at the flexural tension faces of the shear walls just began to yield at the peak load for CBF1 and CBF2. This indicates that the flexural reinforcement design was adequate in preventing a flexural failure from occurring. The location of zero longitudinal strain was consistent for all four tests, being located approximately  $d_v$  (439 mm) from the flexural compression faces of the shear walls. The shear in the coupling beams causes tension in the top and bottom longitudinal reinforcement, and hence the longitudinal bars are not zero at midspan (800 mm from each end). The location of zero longitudinal strain in the reinforcing bars will be at the location where the flexural compression cancels out the tension due to shear.

Strain gauges B6 and B7 were installed in all specimens to measure the tensile strain penetration of the longitudinal reinforcement into the shear wall end blocks. For CBF1, gauge B7 located 447 mm into the shear wall measured 1.51 mm/m at the peak load which was about 50% of the strain at the shear wall face. This indicates the strains penetrated even further than the 447 mm. Cracking in the shear wall end blocks was observed during all tests, with cracks propagating approximately 75% (1390 mm) into the shear walls. It is reasonable to assume the strains penetrated the same distance as the crack propagation. Industry designs often calculate the tensile strain penetration length using Equation 5.1, where  $d_b$  is the longitudinal bar diameter, and  $f_y$  is the yield strength of the reinforcement [30].

$$l_{yp} = 0.022d_b f_y \text{ mm} \quad (5-1)$$

From Equation 5.1, the penetration length is calculated to be 370 mm into shear wall end blocks. This calculation significantly underestimates the tensile strain penetration seen during the tests. This discrepancy is further discussed in Chapter 6.

### 5.3 Element Strains

LED targets installed in an 11x4 grid were used to calculate local surface strains on the south face of the coupling beam specimens. The program Timeline written by Ruggiero [31] was used to determine the Mohr's circle of strains for each LED element bound by four LED targets. Figure 5-7 illustrates the element labelling scheme that will be used to identify elements in this section.

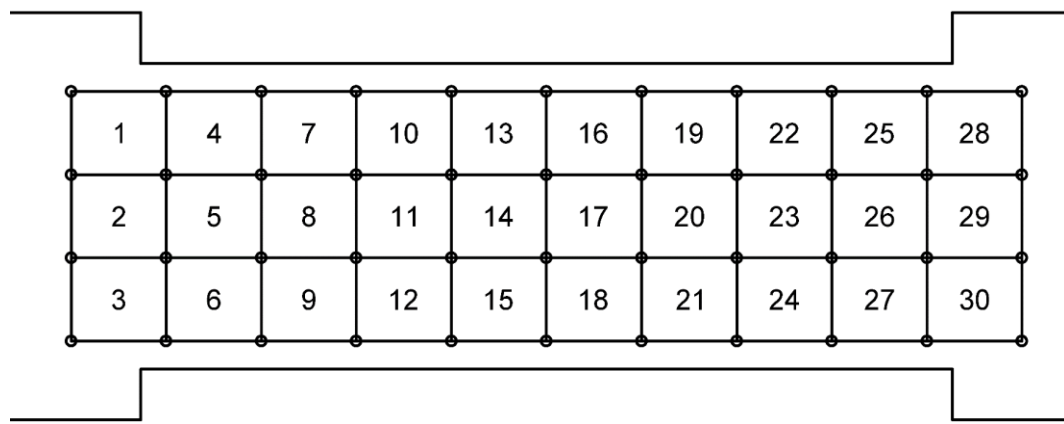


Figure 5-7: LED Element Labelling Scheme

The deflected shape, shear strains, x-direction and z-direction strains, principle tensile and compressive strains, and angle of principle compression are presented in Figure 5-8 to Figure 5-11 at the peak load for CBF1 to CBF4 respectively. The deflected shape was determined using a dynamic reference frame aligned with the LEDs attached to the shear walls. This allowed the shape to be oriented to what a typical coupling beam would experience rather than the test orientation. A full set of LED element strains for each load stage are presented in Appendix F.

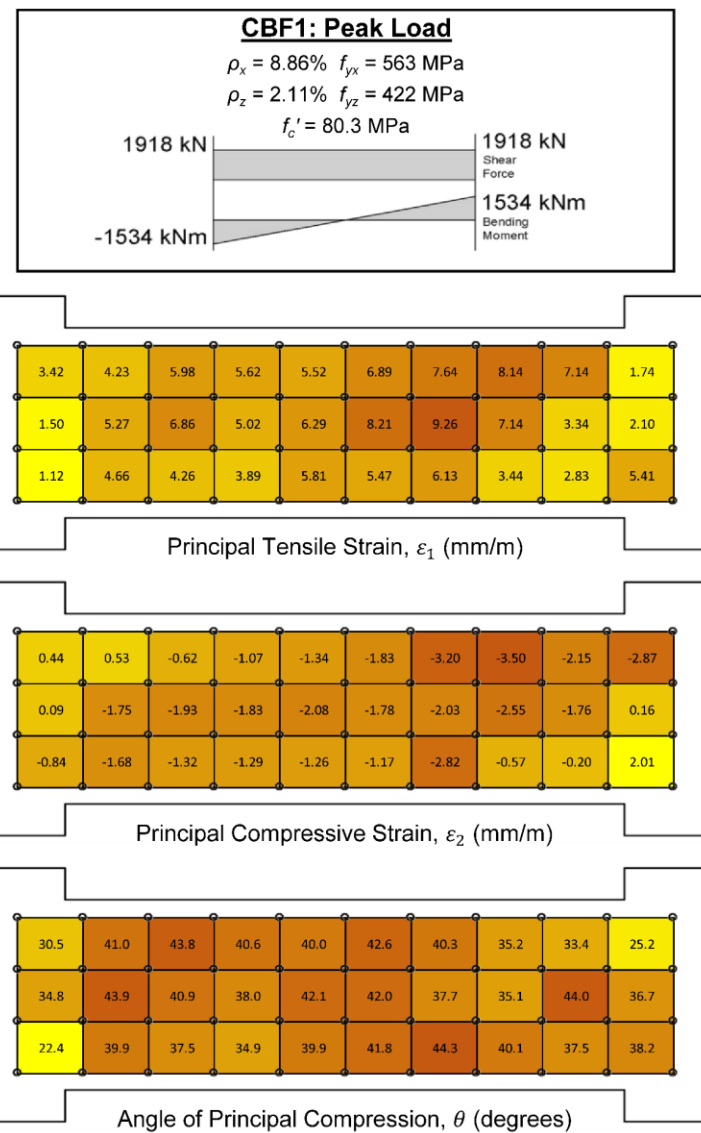
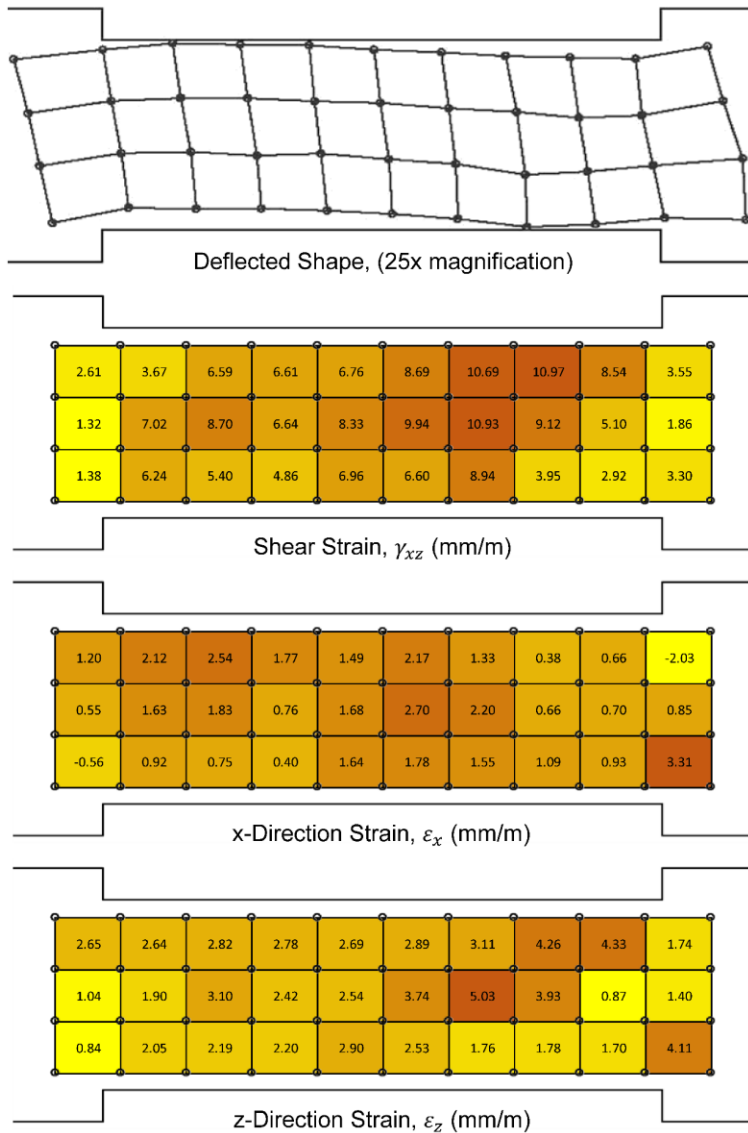


Figure 5-8: LED Elements at Peak Load for CBF1

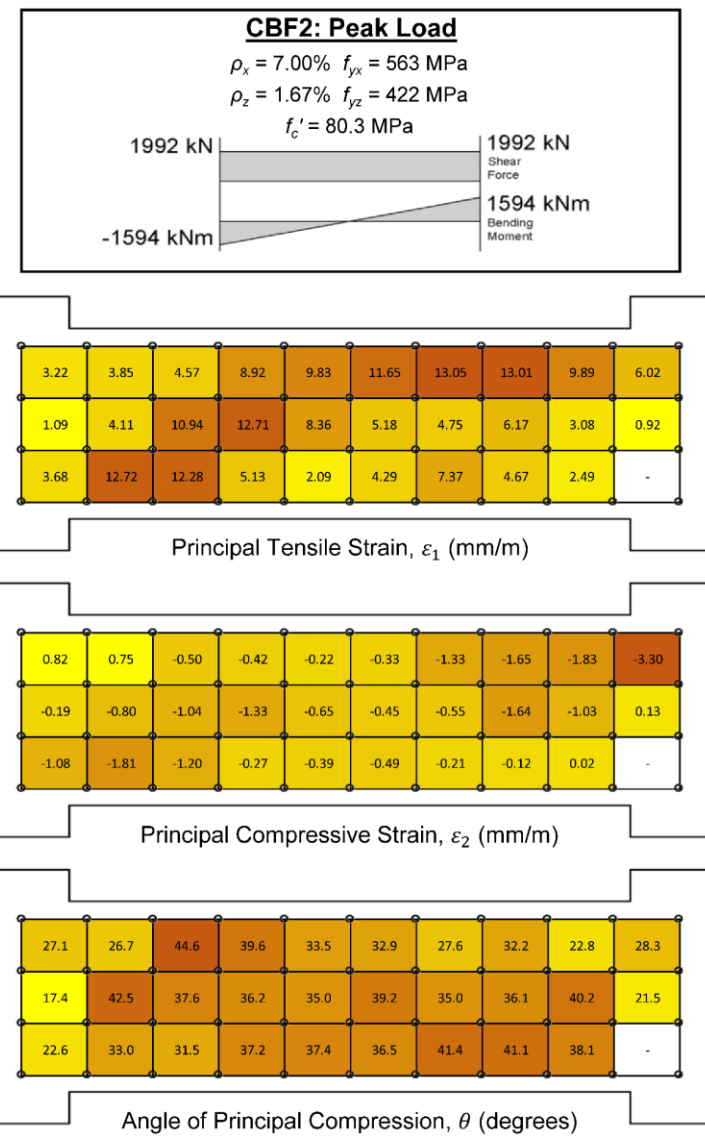
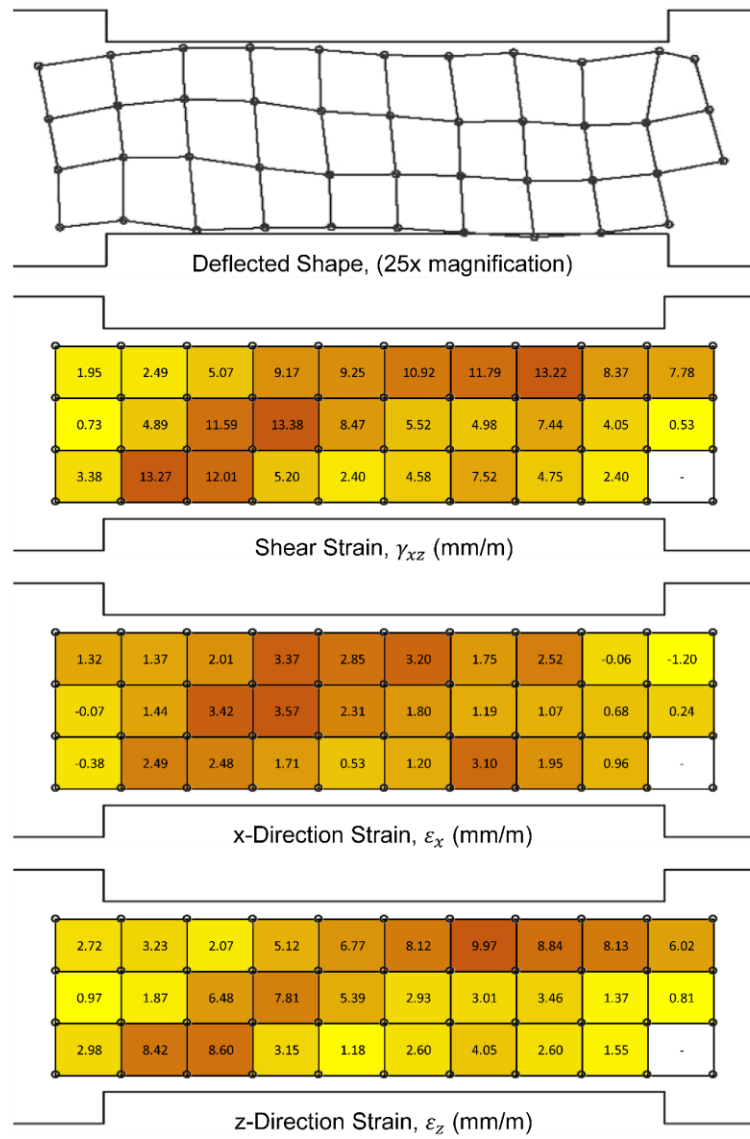


Figure 5-9: LED Elements at Peak Load for CBF2

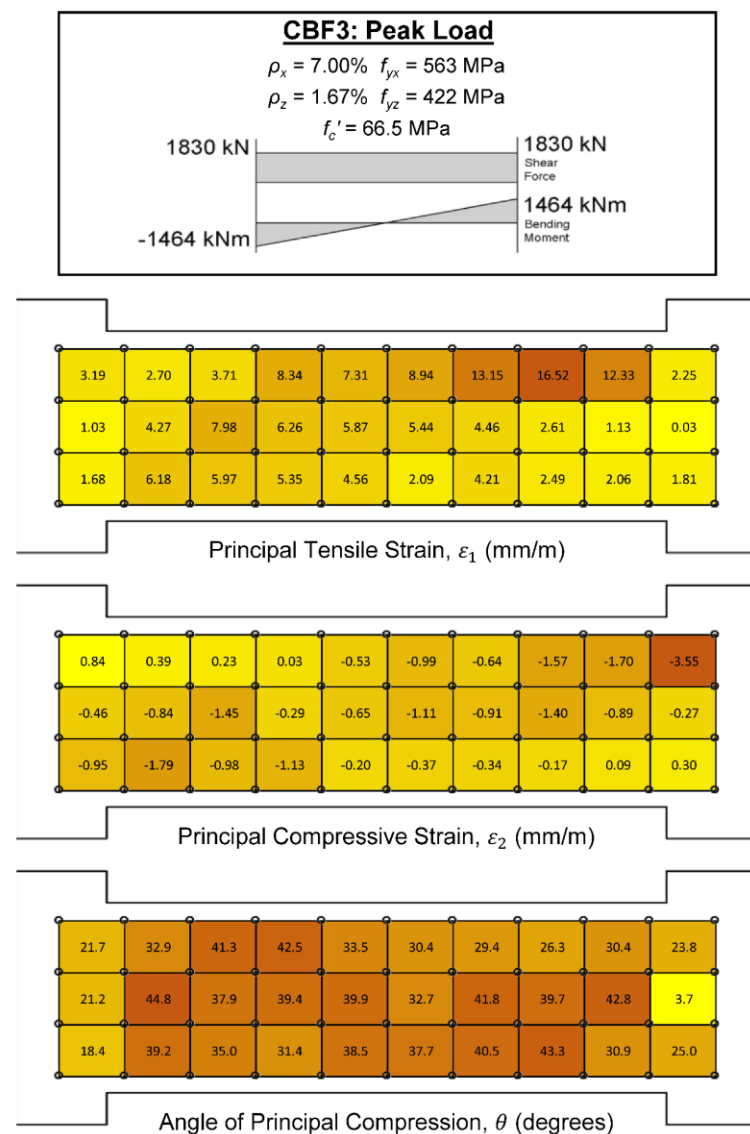
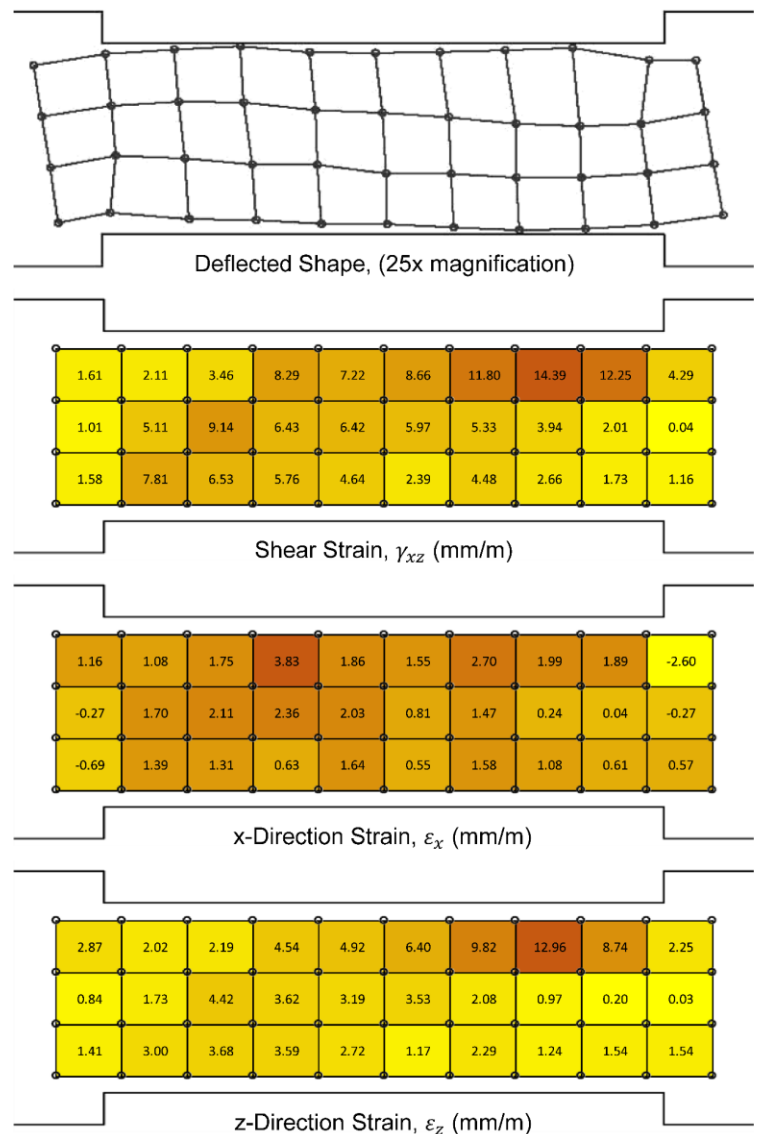


Figure 5-10: LED Elements at Peak Load for CBF3

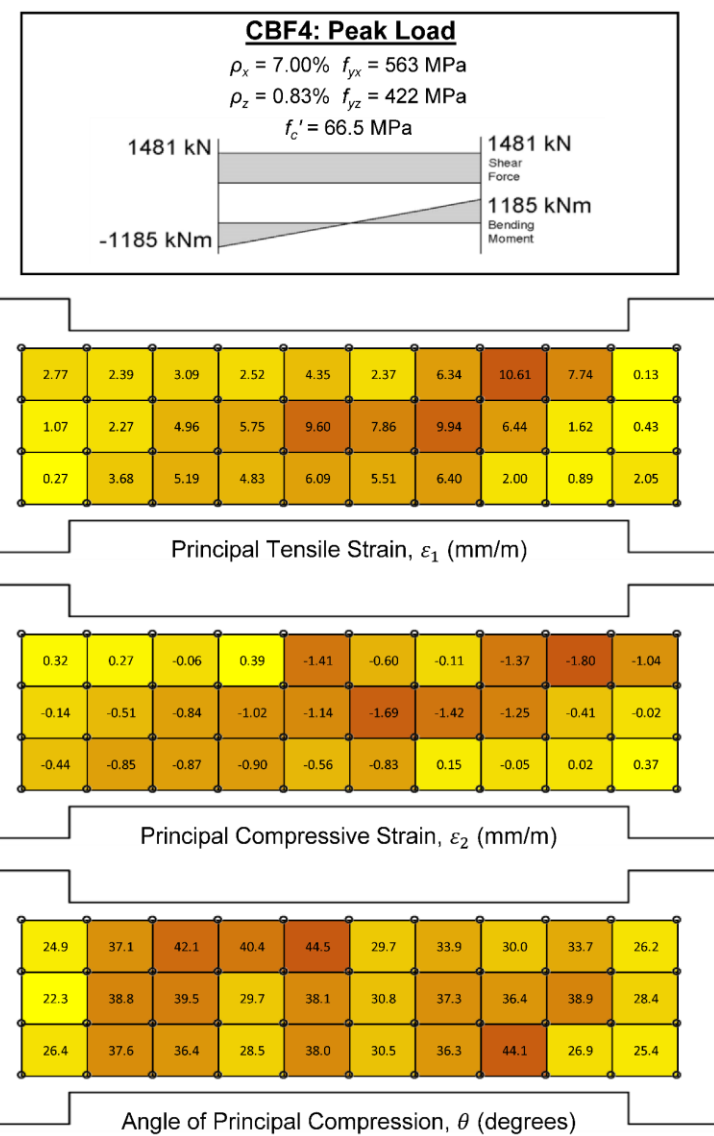
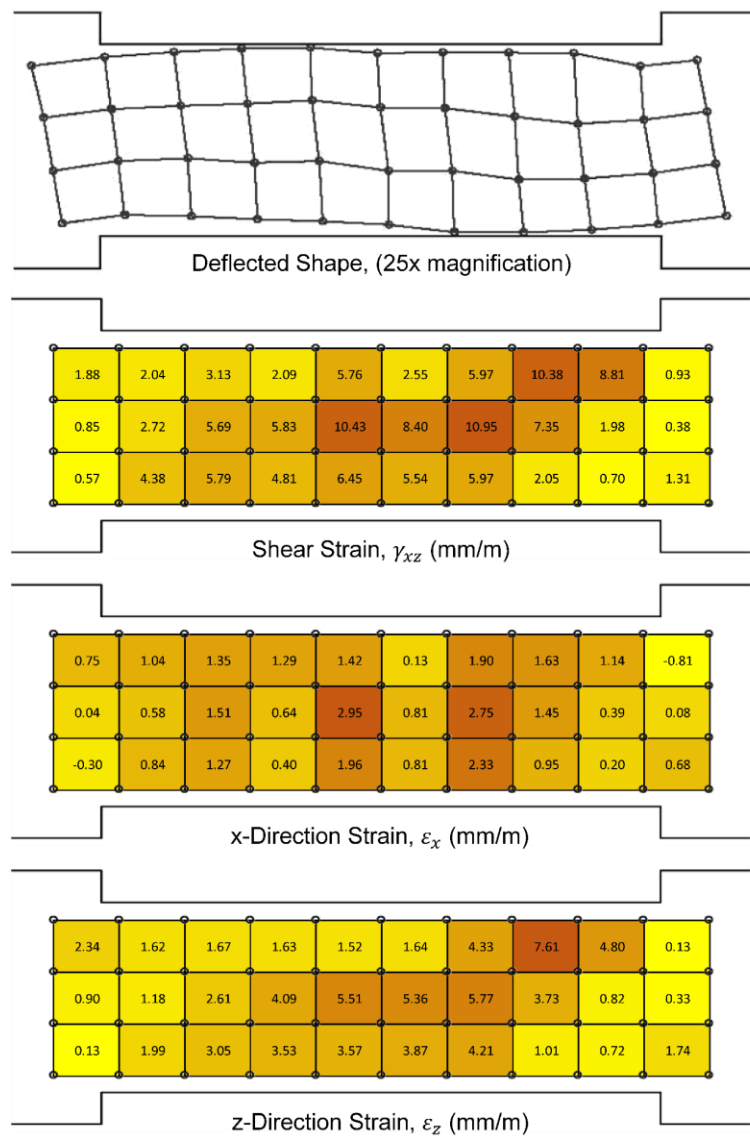


Figure 5-11: LED Elements at Peak Load for CBF4

### 5.3.1 LED Shear Strains

The LED elements show significantly higher local shear strains,  $\gamma_{xz}$ , at the peak load than the average sectional shear strains obtained by the three sets of LVDTs. In order to compare these values, the element shear strains were averaged over an area equivalent to that of the three LVDT measurements. These values are compared in Table 5-3 at the peak load and at the load stage just when the stirrups began to yield.

*Table 5-3: LVDT and LED Average Shear Strain Comparison for CBF1 to CBF4*

Specimen	Load Stage	LVDT $\gamma_{xz}$ (mm/m)	LED $\gamma_{xz}$ (mm/m)	Variation (%)
CBF1	Yield (1751 kN)	4.49	4.81	7.2
	Peak (1918 kN)	6.76	7.50	11.1
CBF2	Yield (1801 kN)	3.33	3.75	13.5
	Peak (1992 kN)	4.95	7.66	58.0
CBF3	Yield (1752 kN)	3.11	3.61	16.4
	Peak (1830 kN)	4.06	6.28	58.5
CBF4	Yield (1251 kN)	2.45	2.52	2.8
	Peak (1481 kN)	4.36	5.68	30.2

For specimen CBF1 which had only 3 mm of side cover, the variation between the LVDT and LED shear strains at stirrup yield was 7%. For specimens CBF2 to CBF4 which had 45 mm of side cover, the variation was between 3% and 16%. Since all specimens showed similar variation between the LEDs and LVDTs at stirrup yield, it can be concluded that the variation at stirrup yielding was not affected by cover spalling. Note that there are significant variations in the shear strains measured in the six LED elements corresponding to the central set of LVDT readings.

At the peak load for CBF1, the variation increased to 11%, whereas CBF2 and CB3 increased to 58% and CBF4 to 30%. As the concrete side cover begins to spall, it causes localized strain changes. This localized variation would directly affect the LED and LVDT measurements causing the observed variation. LED and LVDT measurements recorded after stirrup yielding should therefore be used carefully when making conclusions about the coupling beam behavior since they were influenced by the side cover spalling phenomena.

### 5.3.2 LED x-Direction and z-Direction Strains

The yield strain for the longitudinal reinforcement was 2.82 mm/m. The strain gauges indicated that the top layer of longitudinal steel just started to yield at the tension face of the shear walls at the peak load. Since the concrete side cover was not observed to spall in these regions, the LED x-direction strains,  $\varepsilon_x$ , can be used to directly evaluate the strain state of the longitudinal reinforcement. For all four specimens, the x-direction strains for elements 4, 7, 24, and 27, see Figure 5-7, were below the reinforcement yield strain, indicating that the beams did not experience flexural yielding at the peak load.

The yield strain for the transverse reinforcement was 2.11 mm/m. The strain gauges and LVDTs indicated that the stirrup steel yielded before the peak load in the regions of the coupling beam that were at least  $d_v$  (439 mm) from the shear wall faces. The z-direction element strains,  $\varepsilon_z$ , in this region indicate that the stirrups had yielded at the peak load. All four specimens showed element z-direction strains at or near yield around load stage five.

### 5.3.3 LED Principal Compressive Strains

Based on concrete cylinder test data, the crushing strain of the concrete was -2.55 mm/m for CBF1 and CBF2, and -2.19 mm/m for CBF3 and CBF4. Once the principal compressive strains,  $\varepsilon_2$ , surpass this strain then the concrete is considered to have started crushing. For CBF1, the elements located  $d_v$  (439 mm) from the east shear wall had reached and surpassed the crushing strain of the concrete at the peak load. The elements ranged from -2.55 mm/m to -3.50 mm/m. See Figure 5-8. The average strain outside the compression fan region was -1.93 mm/m. The surface compressive strains for CBF2 were significantly lower, having a maximum strain of -1.83 mm/m and an average strain outside the compression fan region of -0.73 mm/m. See Figure 5-9. The only strain that surpassed the crushing strain was in element 28, which is an artifact of the disturbed region at the shear wall face. This variation in measured principal compression strains indicates that spalling of the concrete side cover occurred prior to the peak load. As the concrete side cover delaminates from the coupling beam core, it is no longer able to transfer the same levels of compression, resulting in smaller strains. CBF3 and CBF4 showed similar behavior, having maximum strains of -1.79 mm/m and -1.80 mm/m, and average strains of -0.98 mm/m and -1.04 mm/m respectively. See Figure 5-10 and Figure 5-11. Despite having twice the shear reinforcement, CBF3 transmitted the same amount of compressive strain in the

concrete side cover as CBF4, indicating that once the side cover spalls, there is a limit to the amount of strain able to be transmitted between the concrete side cover and core.

## 5.4 Shear on the Crack

The failure mechanism for the coupling beam specimens was initiated by yielding of the stirrups, followed closely by slip on the cracks, and then concrete crushing. The ability for cracks to transmit shear stresses,  $v_{ci}$ , is a function of the crack width,  $w$ , and the aggregate size,  $a_g$ , as shown in Equation 5-2 [12] [32].

$$v_{ci} \leq \frac{0.18\sqrt{f'_c}}{0.31 + \frac{24w}{a_g + 16}} \text{ where } \sqrt{f'_c} \leq 8 \text{ MPa} \quad (5-2)$$

Cracks widths were measured up to the last load stage before failure. The maximum crack width,  $w_{max}$ , and average crack width,  $w_{avg}$ , measured at each load stage for all four specimens are presented in Figure 5-12. Flexural crack widths or abnormally large widths due to side cover spalling were not included in this data set.

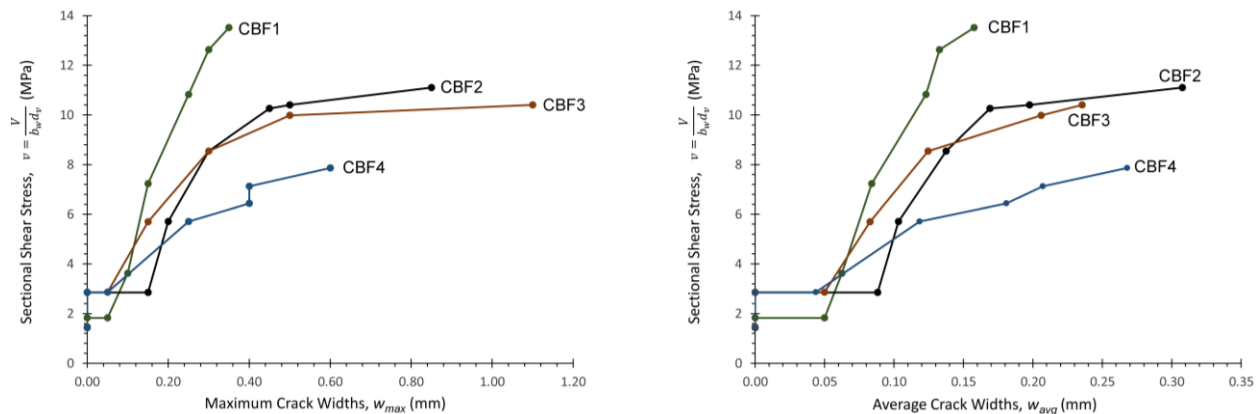
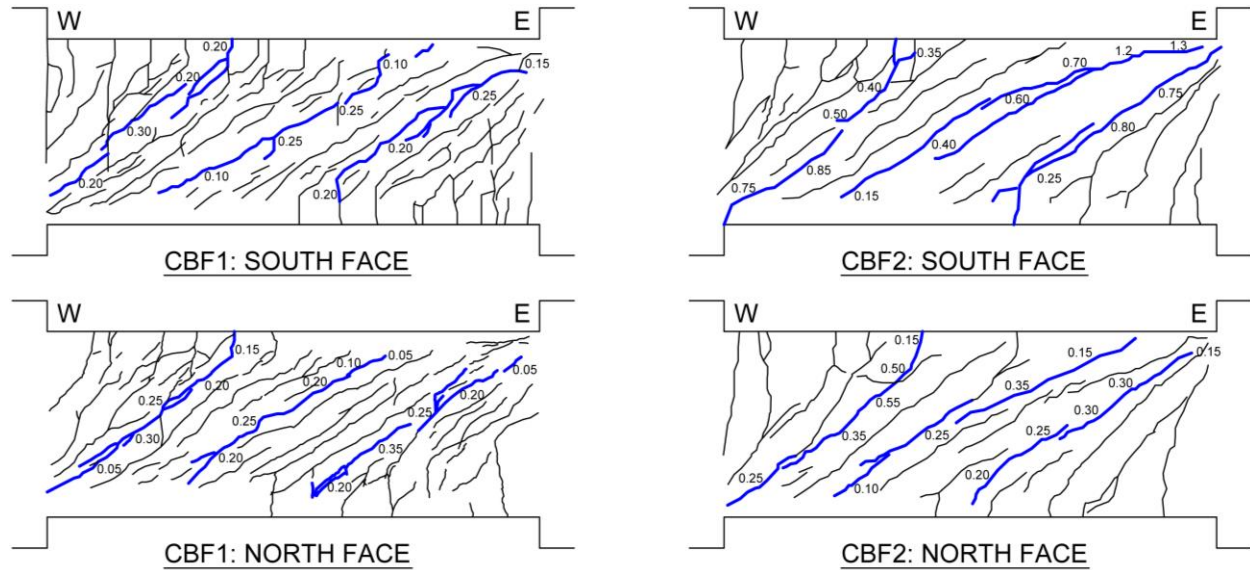


Figure 5-12: Crack Widths for CBF1 to CBF4

On average, the maximum crack widths were 2.1 times larger than the average crack widths. Since CBF1 had more cracks spaced closer together, the average and maximum crack widths were much smaller than the other specimens. Concrete side cover thickness is the primary reason for this variation. The further away the concrete surface is from a reinforcing bar, the less ability it has to control the width of the crack, resulting in wider cracks spaced further apart. Since

CBF2 to CBF4 had 45 mm of side cover, the widths in these specimens were much larger than in CBF1 which only had 3 mm of side cover.

The crack widths measured during the final load stage before failure are a good indicator of how much shear was transferred across the crack. The largest cracks crossing  $d_v$  (439 mm) away from the shear wall faces and midspan are identified in Figure 5-13 and Figure 5-14.



*Figure 5-13: Widths and Angles of Largest Cracks at Final Load Stage for CBF1&2*

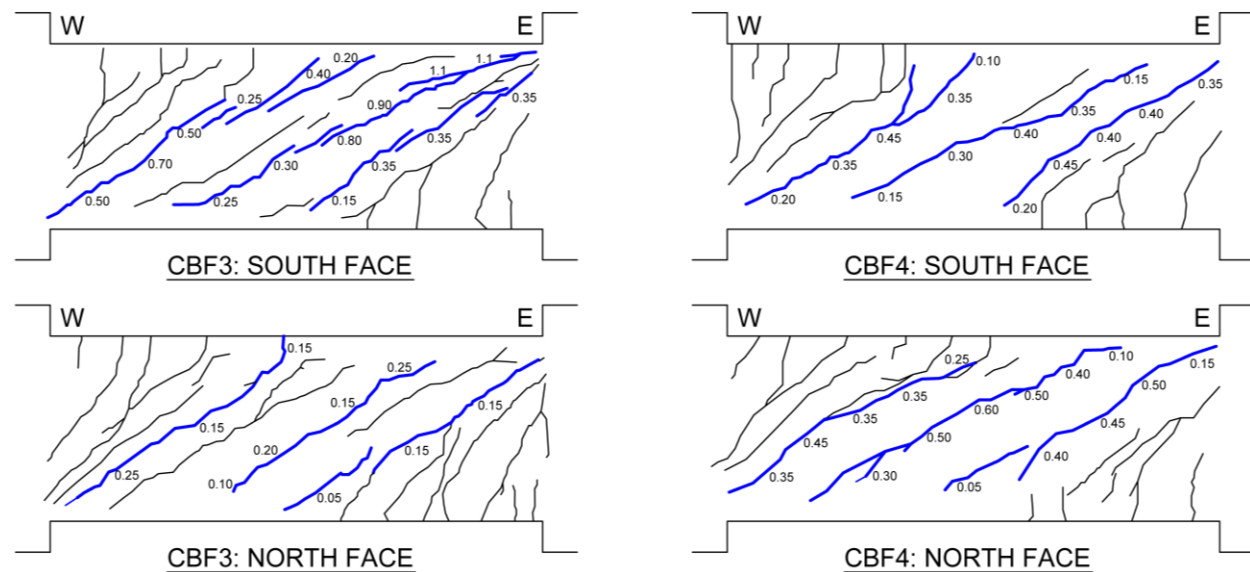


*Figure 5-14: Widths and Angles of Largest Cracks at Final Load Stage for CBF3&4*

The crack capacity in combination with the yield strength of the transverse reinforcement provides the overall shear capacity at the crack, shown in Equation 5-3 [12].

$$v = v_{ci} + \frac{f_{yz}\rho_z}{\tan \theta} \quad (5-3)$$

Since the stirrups were first to yield, the shear reinforcement contributes a maximum bar stress of 422 MPa at the crack. From the LED analysis, the angle of principal compression,  $\theta$ , is obtained. The LED diagrams are overlaid with the crack patterns in Figure 5-15 and Figure 5-16 to show how the angles calculated by the LED targets compare to the actual crack pattern.

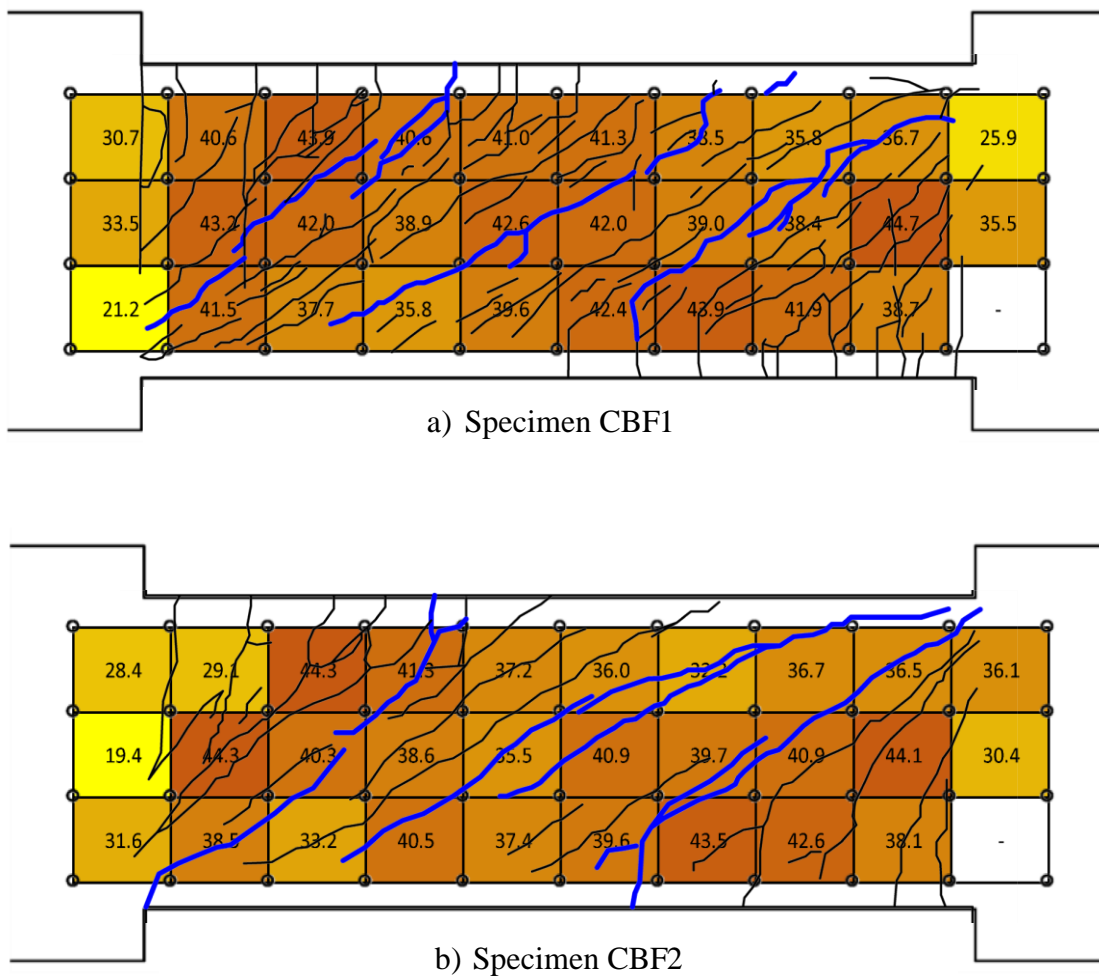


*Figure 5-15: Crack Widths and Angles at Final Stage for CBF1 and CBF2*

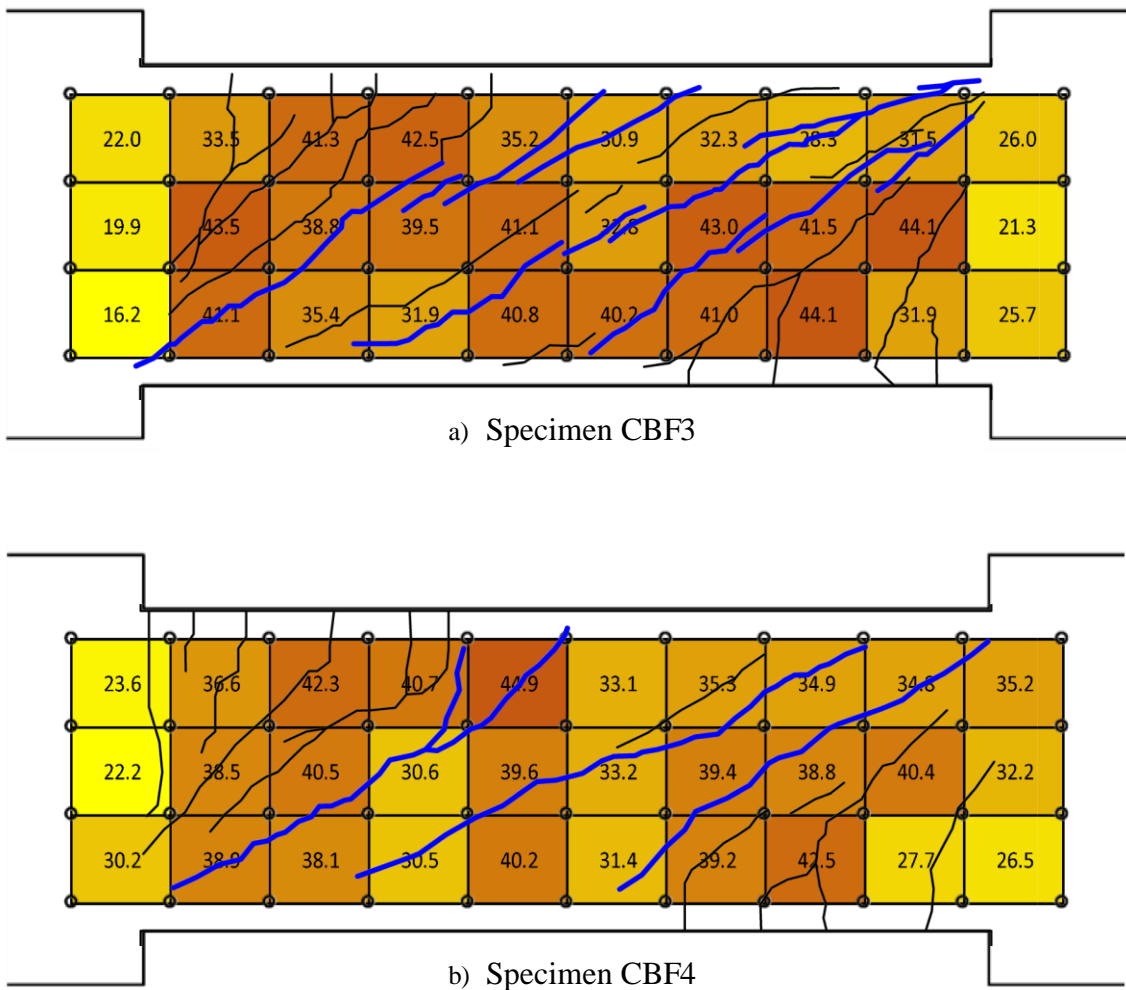


Figure 5-16: Crack Widths and Angles at Final Stage for CBF3 and CBF4

The maximum shear stress the concrete could carry at the crack,  $\nu_{ci,max}$ , was calculated using Equation 5-2. The crack width,  $w$ , in Equation 5-2 was taken as the average width,  $w_{avg}$ , for each of the three largest cracks. The crack angle,  $\theta$ , was taken as the average element angle,  $\theta_{avg}$ , that each of the three cracks crossed. This was used to calculate the steel contribution of the crack capacity. The maximum concrete contribution and the steel contribution were used in Equation 5-3 to calculate the maximum shear capacity at the crack,  $\nu_{max}$ . This maximum capacity is compared to the applied shear stress,  $\nu$ , in Table 5-4 in order to identify if slip on the crack occurred.

Table 5-4: Shear Capacity at the Crack for CBF1 to CBF4

Specimen	Location	$f'_c$ (MPa)	$a_g$ (mm)	$f_{yz}\rho_z$ (MPa)	$w_{avg}$ (mm)	$\theta_{avg}$ (degrees)	$f_{yz}\rho_z/\tan \theta$ (MPa)	$v_{ci,max}$ (MPa)	$v_{max}$ (MPa)	$v$ (MPa)
CBF1	West	80.3	0	8.90	0.23	42.2	9.80	2.22	12.03	13.52
	Midspan				0.18	40.0	10.59	2.52	13.11	
	East				0.20	38.5	11.20	2.36	13.57	
CBF2	West	80.3	0	7.04	0.56	40.0	8.38	1.25	9.63	10.40
	Midspan				0.46	37.0	9.34	1.43	10.77	
	East				0.60	40.4	8.26	1.19	9.45	
CBF3	West	66.5	4.9	7.04	0.43	39.4	8.56	1.80	10.37	10.40
	Midspan				0.67	37.0	9.35	1.33	10.68	
	East				0.30	39.3	8.60	2.20	10.80	
CBF4	West	66.5	4.9	3.50	0.29	39.0	4.32	2.24	6.56	7.86
	Midspan				0.27	35.3	4.94	2.32	7.26	
	East				0.36	36.6	4.72	1.99	6.71	

The maximum aggregate size for all four specimens was 14 mm. However, the CSA Code specifies that for concrete strengths between 60 MPa and 70 MPa, the aggregate size is to be linearly reduced, with concrete strengths exceeding 70 MPa using an aggregate size of zero.

Comparing the maximum crack capacity,  $v_{max}$ , with the applied shear stress,  $v$ , indicates that slip on the crack did occur in all four specimens after the stirrups began to yield. Since this shear is calculated at the load stage prior to failure, it indicates that the shear slip occurred prior to concrete crushing.

## 5.5 Out-of-Plane Expansion

### 5.5.1 Out-of-Plane Linear Pot Displacements

Out-of-plane displacements were measured using linear pots located  $d_v$  (439 mm) from the shear wall faces and at midspan. The LVDT rods were installed through plastic ducts that were located mid height and ran the entire width of the coupling beams measuring the total out-of-plane expansion of the section. The sectional shear stress versus out-of-plane displacement plots for each coupling beam are presented in Figure 5-17.

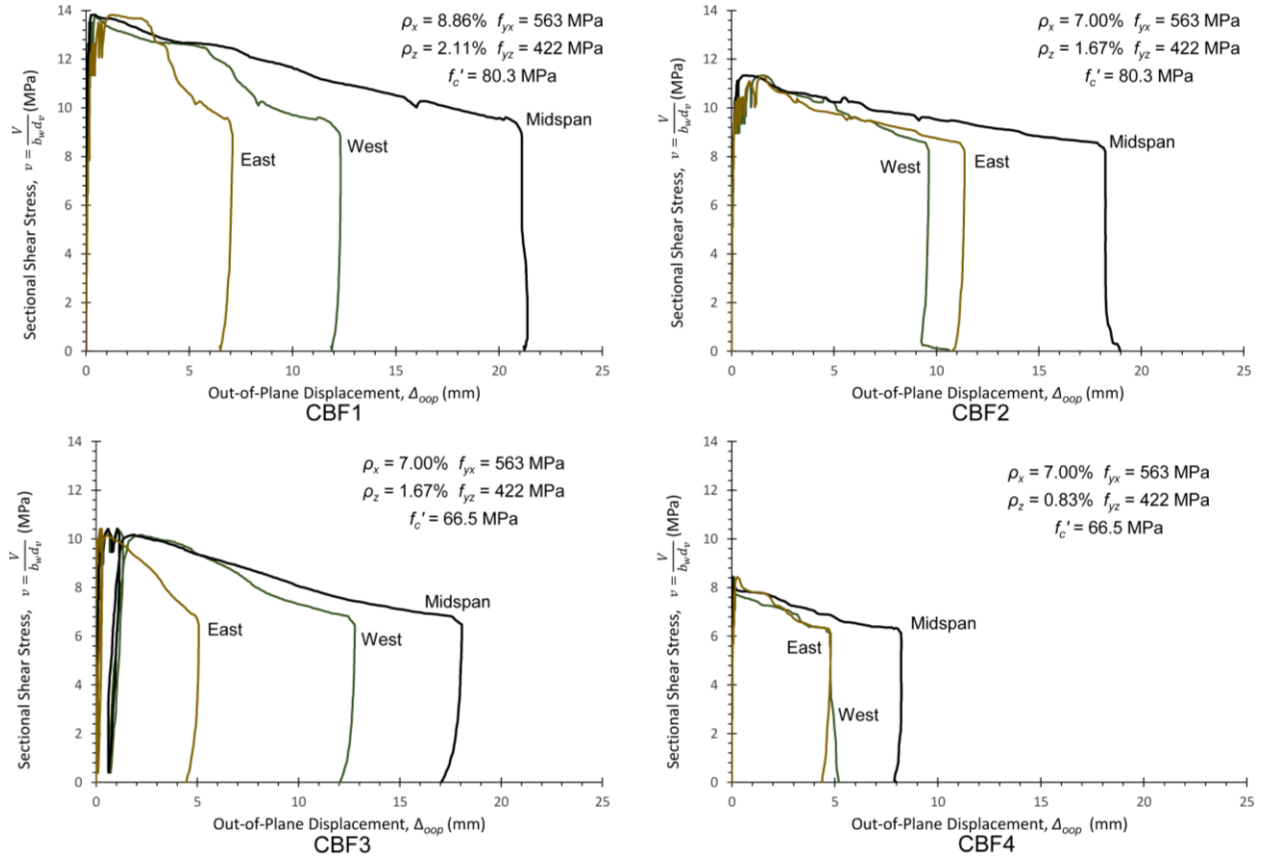


Figure 5-17: Sectional Shear Stress vs. Shear Strain for CBF1 to CBF4

Most of the out-of-plane expansion measured at mid height occurred after the peak load, with the midspan of the beam showing the largest expansion. On average, the coupling beams experienced 92.8% of their total mid-height expansion during the post-peak response. This expansion was due to the spalled concrete side cover delaminating from the coupling beam core. The small amount of recovery that occurred during unloading was due to a small amount of elastic rebound in the stirrups.

Prior to the peak load, it was observed that the out-of-plane expansion at mid-height was very minimal up until the stirrups began to yield, at which point the rate of expansion began to increase. On average, 72.5% of the expansion at peak stress occurred after the stirrups began to yield. A summary of the out-of-plan expansion based on load stages is presented in Table 5-5.

Table 5-5: Summary of Out-of-Plane Mid-Height Expansion for CBF1 to CBF4

Specimen	Location	Out-of-Plane Expansion, $\Delta_{oop}$ (mm)						
		Stirrup Yield	LS4	LS5	LS6	LS7	PEAK	END of POST PEAK
CBF1	West $d_v$	0.23	0.14	0.2	0.32	-	0.48	12.3
	Midspan	0.13	0.06	0.1	0.16	-	0.41	21.4
	East $d_v$	0.27	0.18	0.29	0.60	-	1.34	7.1
CBF2	West $d_v$	0.34	0.07	0.25	0.49	0.87	1.54	10.6
	Midspan	0.24	0.09	0.16	0.18	0.28	0.74	19.0
	East $d_v$	0.38	0.10	0.20	0.31	0.87	1.51	11.4
CBF3	West $d_v$	0.25	0.05	0.17	0.62	-	1.03	12.8
	Midspan	0.39	0.12	0.26	0.57	-	1.05	18.1
	East $d_v$	0.10	0.00	0.04	0.19	-	0.28	5.1
CBF4	West $d_v$	0.00	0.03	0.04	0.07	-	0.11	5.2
	Midspan	0.00	0.02	0.01	0.02	-	0.03	8.2
	East $d_v$	0.11	0.06	0.11	0.13	-	0.26	4.8

### 5.5.2 Out-of-Plane Reinforcement Strains

Local out-of-plane reinforcement strains were obtained from a strain gauge affixed to the top leg of a stirrup located  $d_v$  (439 mm) from the east shear wall face. The strain gauge was installed for CBF1 and CBF2 only. The strain measurements have been plotted with the sectional shear stress in Figure 5-18.

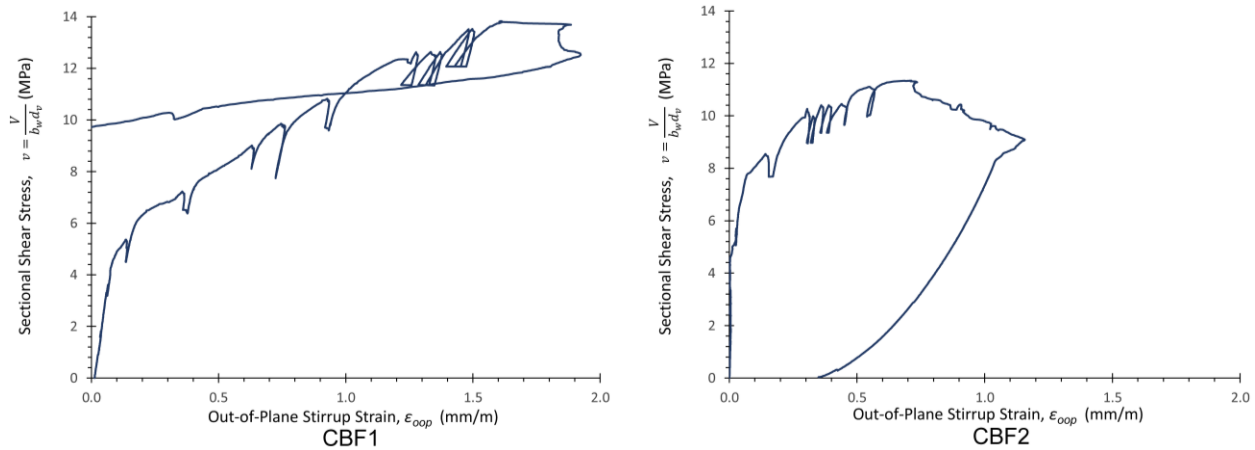
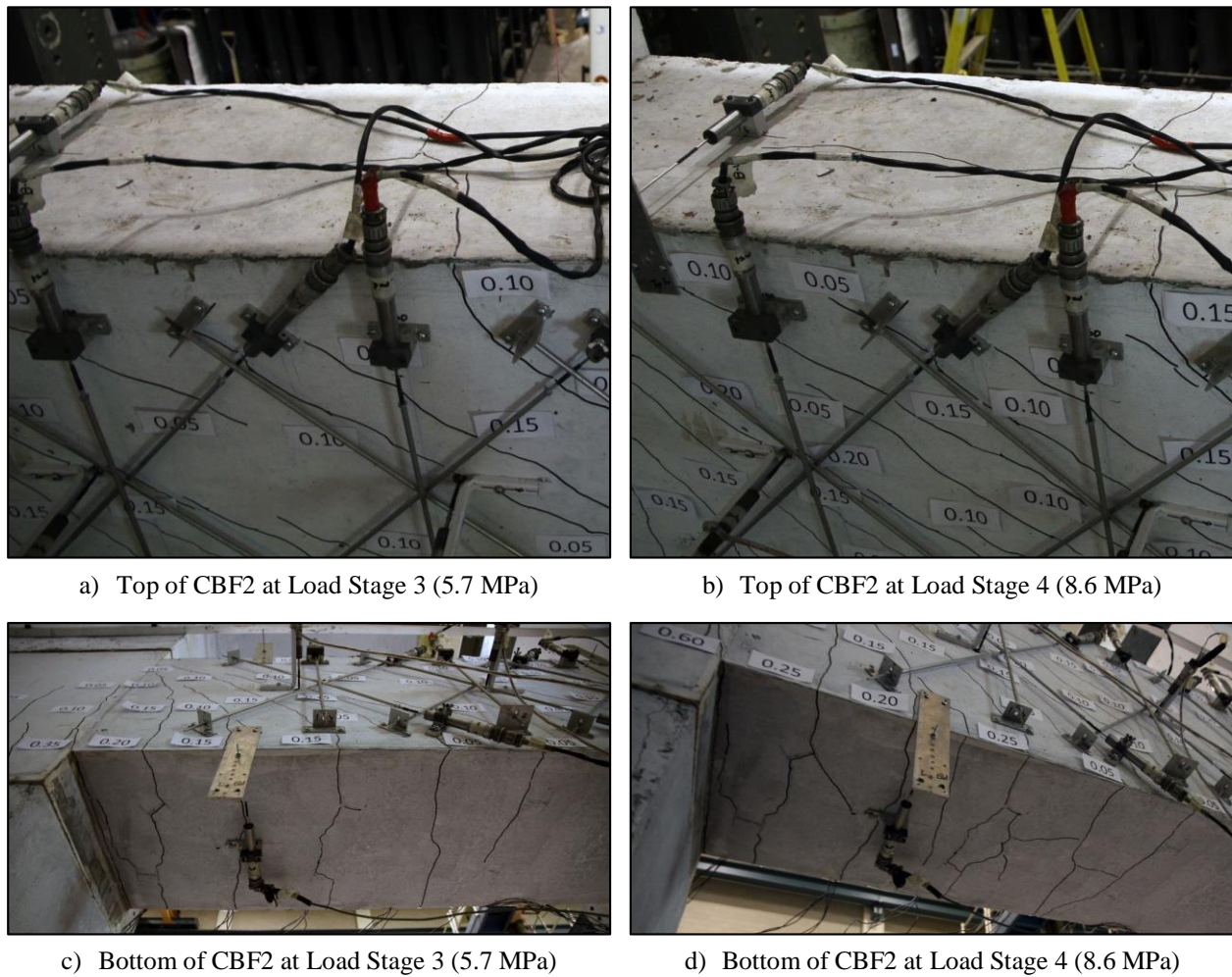


Figure 5-18: Out-of-Plane Reinforcement Strains for CBF1 and CBF2

The top stirrup legs reached a strain of 1.61 mm/m and 0.71 mm/m at the peak stress for CBF1 and CBF2 respectively. Assuming an effective leg length of 148 mm, these strains translate to an elongation of approximately 0.238 mm and 0.105 mm. The LVDT located  $d_v$  (439 mm) from the

east shear wall face at mid depth measured 1.34 mm and 1.51 mm at the peak stress, indicating the horizontal expansion due to the elongation of the top (and bottom) stirrup legs played a very small role in the total out-of-plane expansion. This elongation is what caused some of the elastic rebound during unloading. Prior to the peak load, the slope of the stress-strain plots shows a significant decrease around 6.3 MPa for CBF1 and 7.8 MPa for CBF2. Photos of CBF2 in Figure 5-19, show that longitudinal splitting cracks formed between load stage three (5.7 MPa) and load stage four (8.6 MPa). This indicates the change in slope was due to longitudinal splitting of the coupling beam. The slope decrease, and therefore longitudinal splitting, of CBF1 occurred at a lower stress than CBF2, indicating that the thicker concrete side cover of CBF2 played a role in increasing the out-of-plane cracking strength of the coupling beam.



*Figure 5-19: Longitudinal Cracking along Length of CBF2*

### 5.5.3 Out-of-Plane LED Displacements

Using the program Timeline written by Ruggiero [31], the out-of-plane strains were calculated for each LED element. These strains were used to show the progression of side cover spalling. Figure 5-20 to Figure 5-23 shows the variation in out-of-plane strain as a colour gradient, where the colour grey is zero strain, the darkest blue is strains below -1.0 mm/m, and the brightest red is strains above +1.0 mm/m. Positive is considered to be expansion of the coupling beam. The gradient is the same for all four specimens so that the colour states could be directly compared.

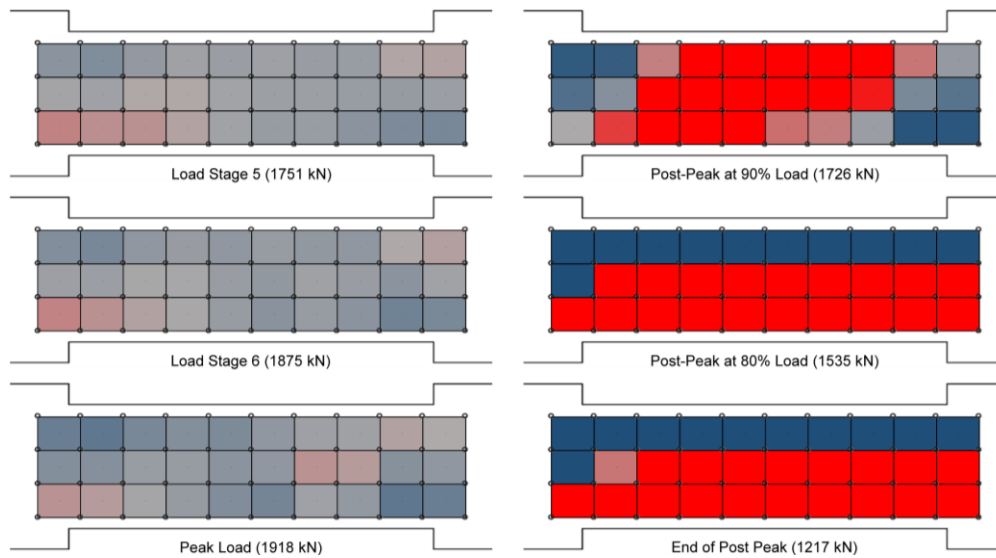


*Figure 5-20: Visualization of LED Element Out-of-Plane Strains for CBF1*

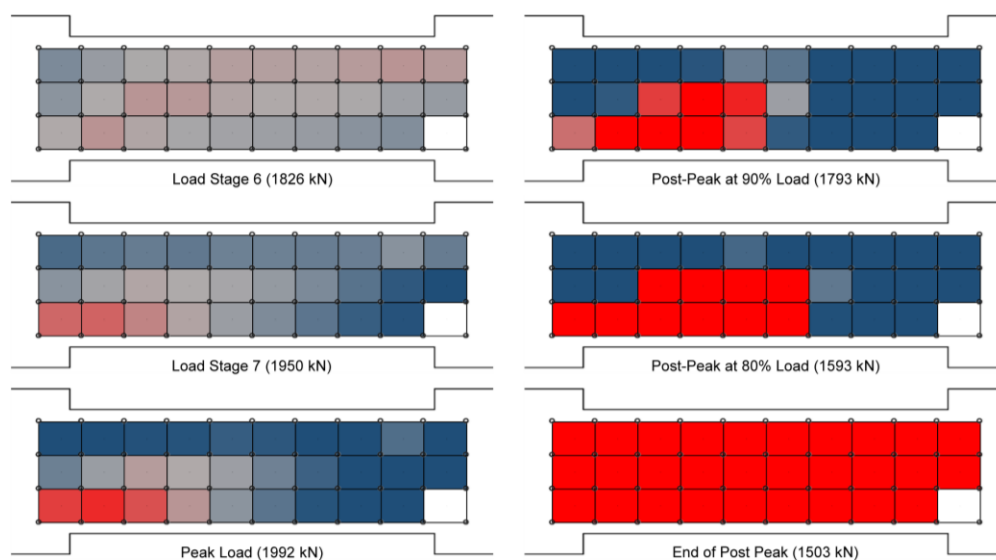


*Figure 5-21: Visualization of LED Element Out-of-Plane Strains for CBF2*

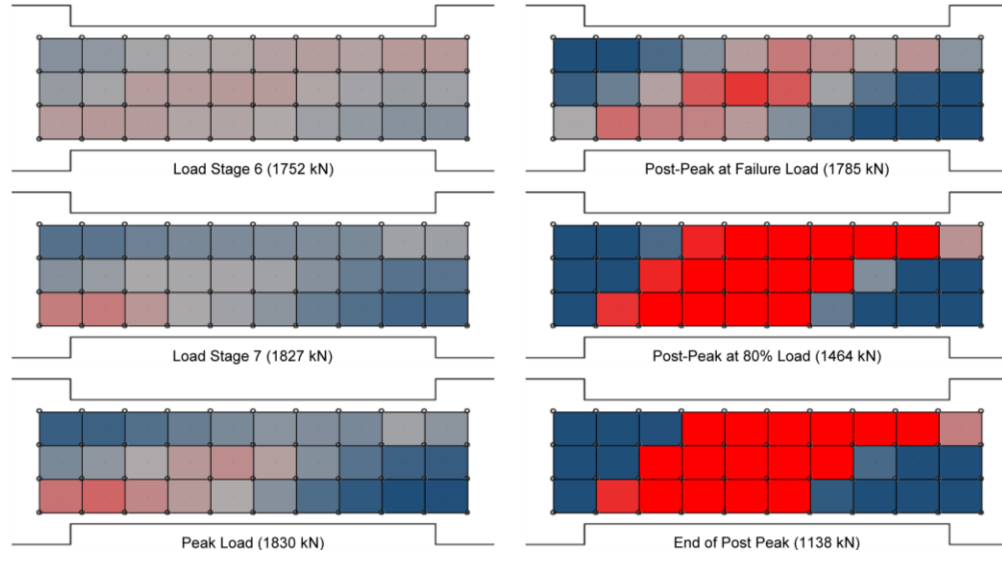


*Figure 5-22: Visualization of LED Element Out-of-Plane Strains for CBF3*

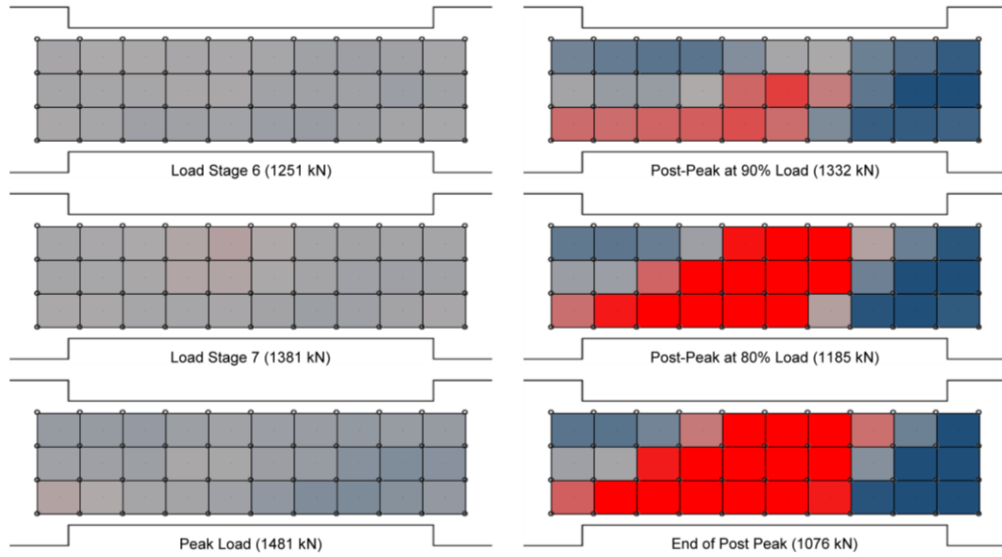


*Figure 5-23: Visualization of LED Element Out-of-Plane Strains for CBF4*

Specimen CBF1, shown in Figure 5-20, showed small amounts of expansion at the corners of flexural compression at load stage five, which is when the stirrups began to yield. At the peak load, expansion started to progress towards the midspan of the beam. After the peak load, significant expansion occurred outside of the compression fan region. This corresponds with where the side cover was observed to spall. The out-of-plane expansion for CBF2 to CBF4, shown in the remaining figures, all progressed in a similar manner. The expansion started in the west flexural compression corner when the stirrups began to yield. Approaching the peak load, the expansion progressed to the east, reaching midspan at the peak load. During the post-peak

response, the out-of-plane expansions significantly increased causing cover spalling outside of the compression fan region. From these figures, it's clear that cover spalling begins in the flexural compression corners of the coupling beams and progresses towards midspan. Most of the expansion occurs in the post-peak response which verifies the mid-height liner pot expansion measurements explained in earlier sections.

#### 5.5.4 Influence of Concrete Side Cover Thickness

The primary variable altered between specimens CBF1 and CBF2 was the concrete side cover thickness. CBF1 had a thickness of 3 mm and CBF2 had a thickness of 45 mm. The intention of this variation was to see if CBF2 would behave similarly to CBF1 once the side cover spalled. For comparison, the shear force versus tangential displacement for specimens CBF1 and CBF2 are plotted together in Figure 5-24.

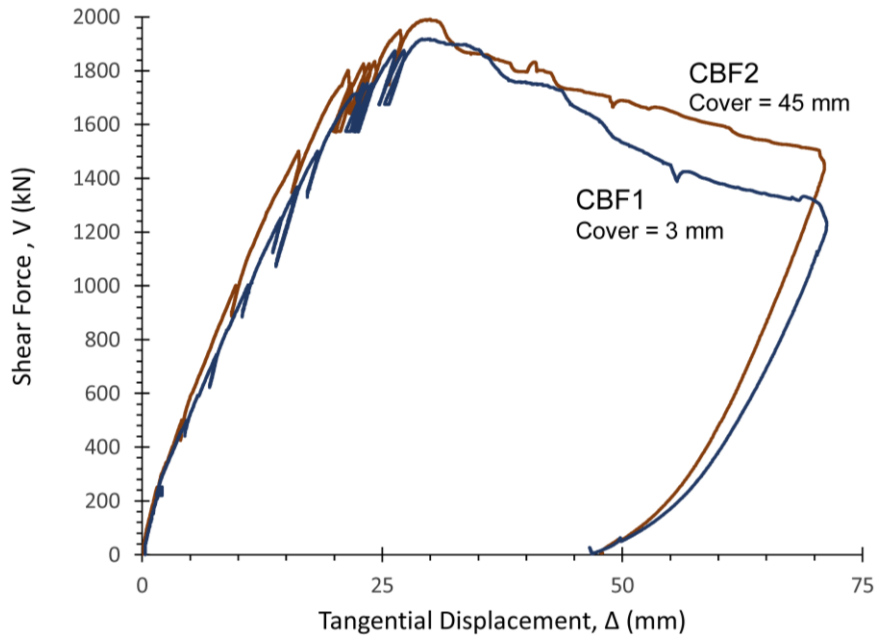


Figure 5-24: Shear Force vs. Tangential Displacement for CBF1 and CBF2

CBF2 was noticeably stiffer than CBF1 in the pre-peak response. This is predictable since CBF2 has the larger concrete cross section. CBF1 and CBF2 both failed at the same tangential displacement of 30.0 mm, indicating they had similar strain states throughout the test. The failure load of 1992 kN for CBF2 was 3.9% higher than CBF1, which is considered small. Concrete spalling occurred for CBF2 but surprisingly CBF1 as well. The 3 mm of side cover on CBF1 was observed to spall to the centerline of the stirrups. Even though spalling started to occur prior to

the peak load, the entire surface of the beam had not fully spalled off until into the post-peak response. From the LED analysis, it was observed that the concrete side cover for CBF2 was still able to hold some compressive strains after it began to spall. This may be a possible reason why CBF2 had a slightly higher failure load than CBF1. During the post peak response, the applied load on CBF2 reduces at 32 mm of displacement to a value similar to CBF1, at which point, both post-peak responses follow a similar path. This moment in the test is likely the point where all the concrete side cover had fully delaminated from specimen CBF2.

### 5.5.5 Influence of Concrete Strength

The primary variable altered between specimens CBF2 and CBF3 was the concrete strength. CBF2 had a test-day strength of 80.3 MPa and CBF3 had a test-day strength of 66.5 MPa. The original intention of CBF3 was to have 40 MPa concrete in order to observe how coupling beams close to crushing capacity behave when the side cover spalls. Unfortunately, CBF3 was far enough away from the crushing capacity that there was no significant loss in strength when the side cover spalled. For comparison, the shear force versus tangential displacement for specimens CBF3 and CBF4 are plotted together in Figure 5-25.

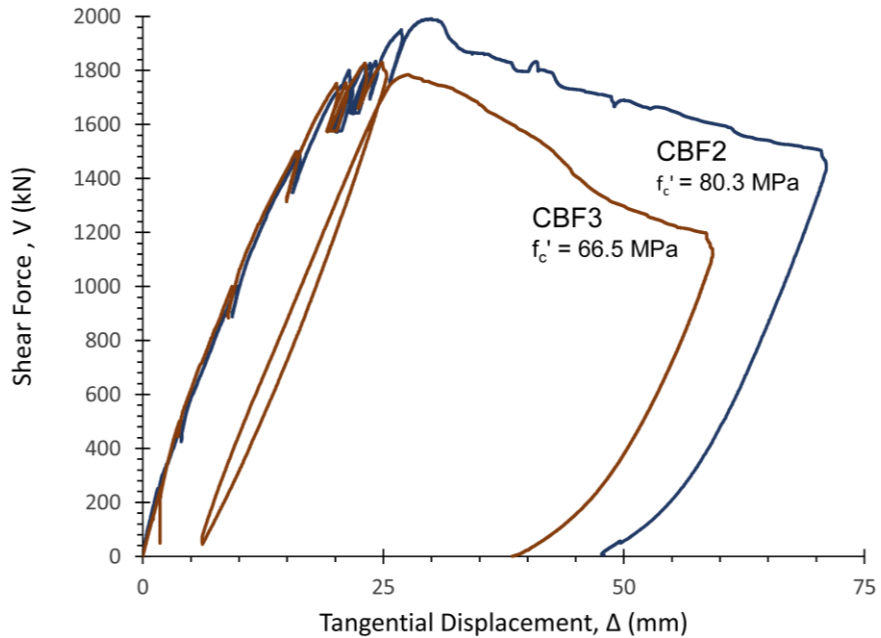


Figure 5-25: Shear Force vs. Tangential Displacement for CBF2 and CBF3

The pre-peak response for both specimens were essentially identical in stiffness. Each specimen followed the same load deformation path until the last set of cycles in which CBF3 failed. It was

observed that stirrup yielding had already begun in CBF3 prior to reaching these cycles. It is likely that the cycles increased the z-direction strains enough to cause failure at a slightly lower load than predicted. Both specimens showed similar behavior during the post-peak response with each having visible side cover spalling. For both CBF1 and CBF2, there was observable shearing of the aggregate. This is a phenomenon that primarily occurs in high-strength concrete and results in smoother cracks, causing a reduction in the shear capacity at the crack. Overall the variation in concrete didn't play a significant role in the failure mechanisms of the coupling beams, with both showing similar behaviors in the pre-peak and post-peak responses.

### 5.5.6 Influence of Transverse Reinforcement Ratios

The primary variable altered between specimens CBF3 and CBF4 was the shear reinforcement ratios. CBF3 had ratio of 1.67% and CBF4 had a ratio of 0.83%. The area of shear reinforcement was 15 times the minimum for CBF3, and eight times the minimum for CBF4. The intention of this variation was to see if side cover spalling would occur for CBF4. The CSA Code currently states that concrete side cover is assumed to spall when the shear reinforcement area is eleven times the required minimum. For comparison, the shear force versus tangential displacement for specimens CBF3 and CBF4 are plotted together in Figure 5-26.

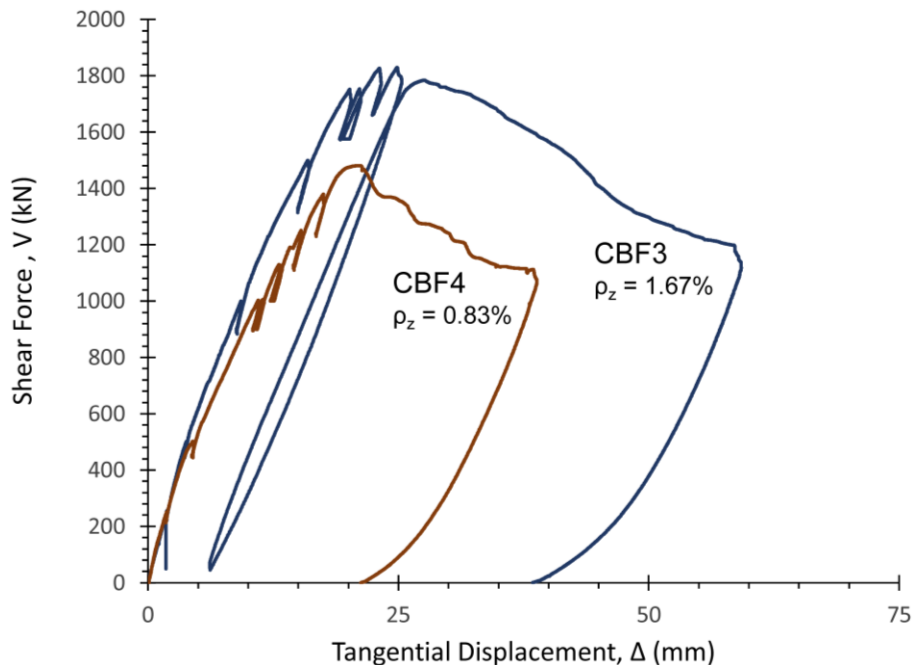


Figure 5-26: Shear Force vs. Tangential Displacement for CBF3 and CBF4

Specimen CBF3 and CBF4 showed similar behaviors throughout the test, with each specimen experiencing yielding of stirrups, followed quickly by slip on the crack. Despite having half the amount of shear reinforcement, CBF4 was still able to carry 81% of CBF3's peak strength. During the post-peak response, both specimens had visible concrete side cover spalling. This is especially important for CBF4 which was assumed to not be affected by this phenomenon. However, the negative effects of the spalling phenomenon were not observable since the specimen had a capacity well above its predicted strength.

# Chapter 6: Comparison of Observed Response to MCFT and Code Predictions

## 6.1 MCFT Predictions using Program Membrane

The MCFT uses equations of equilibrium, compatibility, and stress-strain relationships to predict the full load deformation response of members subjected to shear and axial stresses. These equations are implemented into the program Membrane-2012 [33] which is used to generate the full load-deformation response for a reinforced concrete element in pure shear. Membrane was used to predict the response of an element at the midspan of the coupling beam. The longitudinal reinforcement ratios used in Membrane were calculated using a shear depth  $d_v$ , resulting in values higher than those used for the gross sectional properties. For a more accurate prediction, the parabolic concrete stress-strain relationship used in the traditional MCFT analysis was substituted with the generalized Popovics curves defined earlier in section 3.4.2.

An additional MCFT element analysis was performed to show how confinement and side cover spalling impact the capacity of the specimens. The Mander model for confined concrete of rectangular members [34] was used for the concrete stress-strain relationships instead of the generalized Popovics curve. A full explanation of the Mander model is provided in Appendix G. The Mander concrete stress-strain relationships are plotted with the generalized Popovics curves in Figure 6-1.

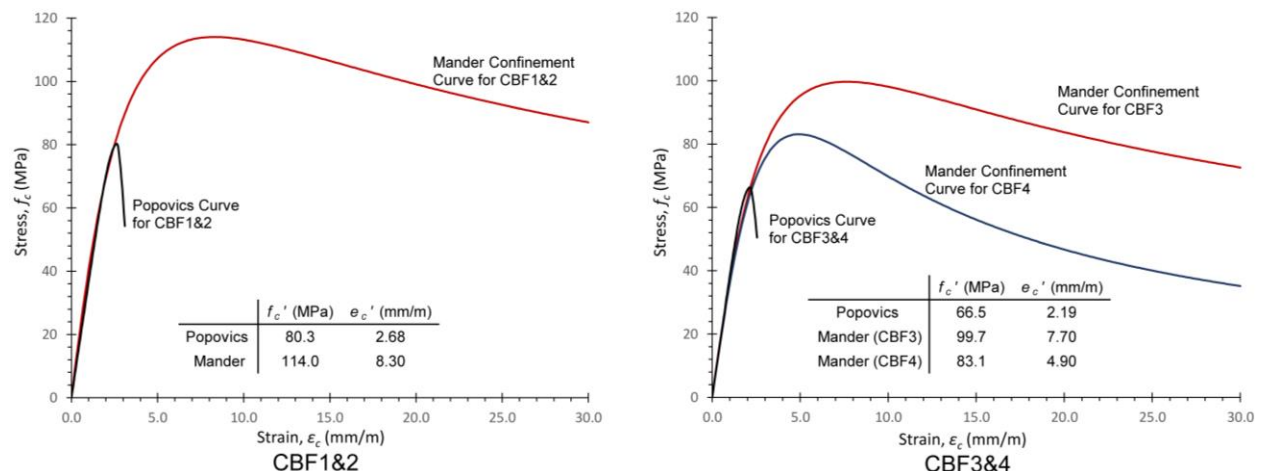


Figure 6-1: Stress-Strain Curve for Confined Concrete of Rectangular Members

Since the Mander model calculates confinement assuming the side cover will spall, the Membrane element was designed with a thickness of 295 mm. This assumes the side cover spalls to the stirrup centerlines. In order to better compare these results with the experimental data, the predicted stresses for the spalled elements were converted for a beam width of 316 mm for CBF1 and 400 mm for CBF2 to CBF4. Figure 6-2 shows the experimental data for specimens CBF1 to CBF4 with both the standard MCFT-Popovics prediction, and the spalled and confined MCFT-Mander prediction.

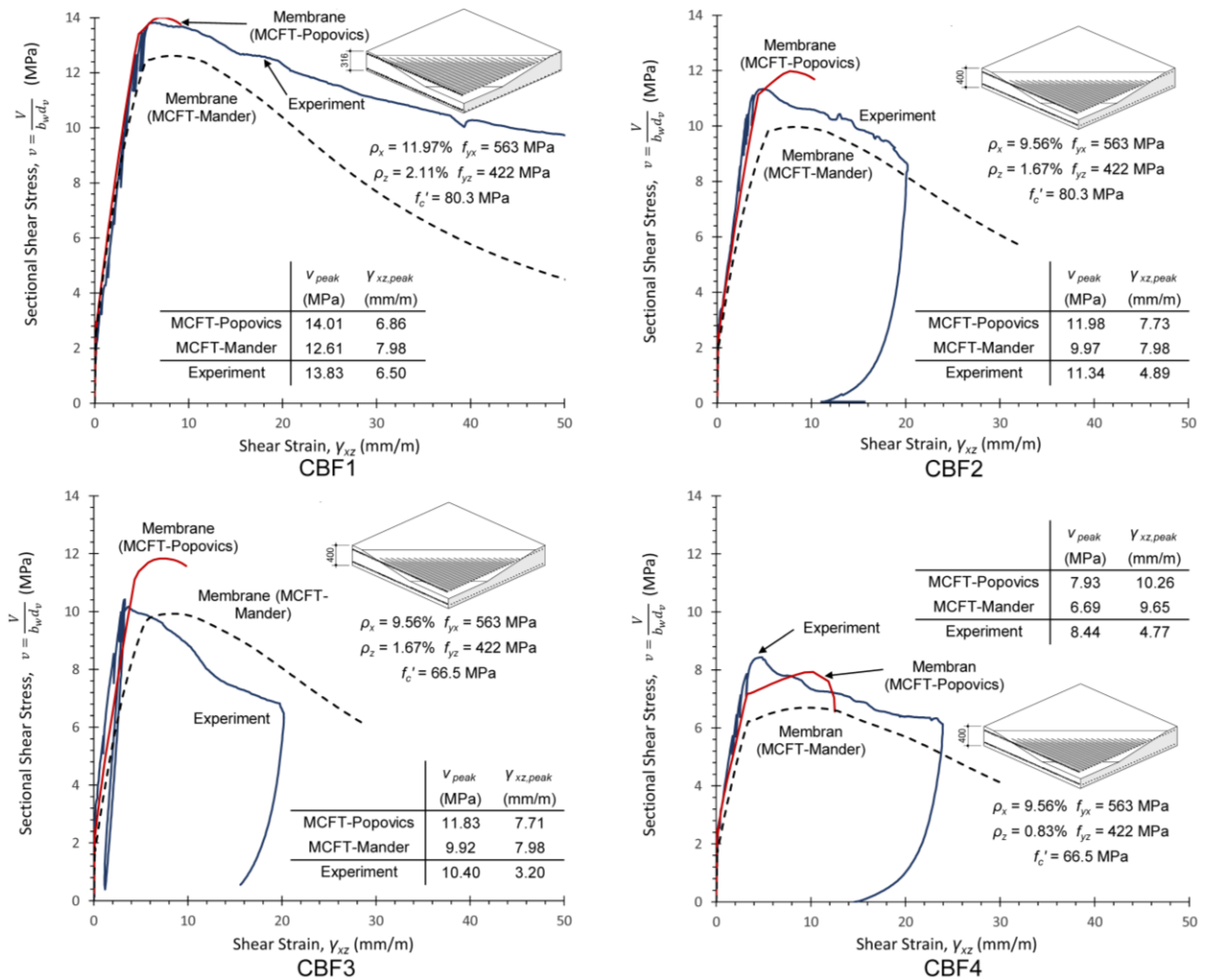


Figure 6-2: MCFT Predictions for Midspan Elements of CBF1 to CBF4

The MCFT-Popovics model accurately predicts the midspan response of specimen CBF1 up to the peak load. This indicates that confinement of the member doesn't play a significant role in the pre-peak response, and is entirely a post-peak phenomenon. Since CBF1 had only 3 mm of

side cover, the small amount of side cover that did spall had little impact on the beam capacity, resulting in an accurate prediction by the MCFT with the full beam width of 316 mm.

In contrast, the MCFT-Popovics model over predicts the strengths of CBF2 and CBF3 whereas the MCFT-Mander model under predicts these strengths. This indicates that side cover spalling does influence the strength predictions, but should only be accounted for when the spalling actually occurs. If a spalled width is assumed from the start of the analysis, the model will under predict the capacity. The MCFT-Popovics model is therefore representative of the coupling beams prior to yielding of the stirrups. After the stirrups yield and the side cover spalls, the beams begin to behave like the MCFT-Mander model. The MCFT Mander model adequately predicted the post-peak response of the coupling beams. From the LED analysis it was observed that the concrete side cover was still able to carry some compressive strains up to the peak load, giving the beams a residual capacity after the side cover began to spall. The predicted response should therefore be a combination of the two models with a transition period to account for the residual stresses in the concrete side cover.

CBF4 was under predicted by both models, indicating there was some other factor which improved the strength of the coupling beam during the test. From photos of the test, there appears to have been a shear key that developed near  $d_v$ , from the east shear wall along the failure crack. Figure 6-3 identifies this shear key at the end of the post-peak response. This shear key likely improved the capacity of the failure crack. Since failure was characterized by yielding of stirrups followed by slip on the crack, the increased crack capacity would have resisted the crack slip and resulted in a higher peak load. This phenomenon is not captured in the Membrane program, as it assumes the worst case crack pattern involving smooth cracks.

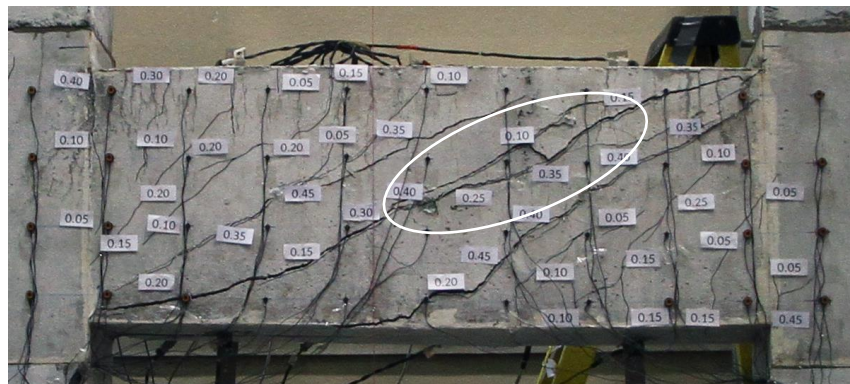


Figure 6-3: Shear Key Developed along Failure Crack of CBF4

## 6.2 MCFT Predictions using Program Response

As an extension to the program Membrane, the program Response-2012 written by Bentz [35] is a sectional analysis program that uses the MCFT to generate the load-deformation response for a reinforced concrete member subjected to shear, moment, and axial load. For this analysis, the 1986 compression softening model [8] was used as it better predicted the capacities of the coupling beams. The Mander confinement model was not used since the higher concrete strength in the pre-peak response resulted in large over-predictions. Since the program Response does not model the post-peak, and from the Membrane analysis confinement did not play a significant role in the pre-peak strength, the effects of confinement were modelled using the standard Popovics-Mander model [34] for confined concrete, an extension of the generalized Popovics curve. This stress-strain curve is described using Equation 6-1.

$$\frac{f_c}{f'_c} = \frac{n(e_{cf}/e'_c)}{n-1+(e_{cf}/e'_c)^n} \quad (6-1)$$

$$n = \frac{E_c}{E_c - E_{sec}}, E_{sec} = \frac{f'_c}{e'_c} \text{ MPa}$$

The Popovics-Mander confined concrete curves plotted in Figure 6-4 utilize the same concrete properties as the original generalized Popovics curves from section 3.4.2.

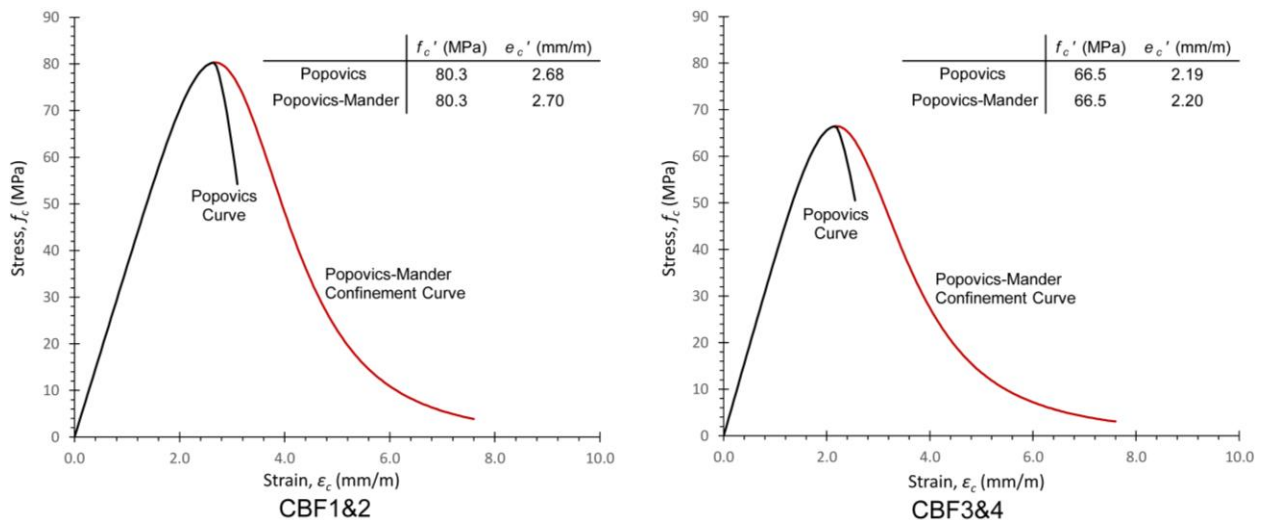


Figure 6-4: Stress-Strain of Confined Concrete using Popovics-Mander Model

The initial predictions made by Response were much stiffer than the actual tests, showing a peak displacement that was close to half the test value. This discrepancy was a result of the yield penetration of the longitudinal reinforcement into the shear wall end blocks. By default, this phenomenon is not accounted for in the program Response. When selected, the default value for the yield penetration length is  $0.022d_b f_y$  mm. From the observations described in section 5.2.2, it was determined that this formula under predicts the actual length of penetration seen during the tests. Based on crack patterns shown in Figure 6-5, the actual yield penetration length can be estimated as 1390 mm, whereas the default formula only predicts a value of 370 mm.



*Figure 6-5: Crack Patterns in Shear Wall End Blocks (repeat of figures)*

The load-deflection plots for the four coupling beam specimens are presented in Figure 6-6. The dashed lines are the Response predictions before yield penetration was accounted for, and the solid lines are the predictions for an assumed 1390 mm yield penetration (YP) length, equaling  $0.082d_b f_y$  mm.

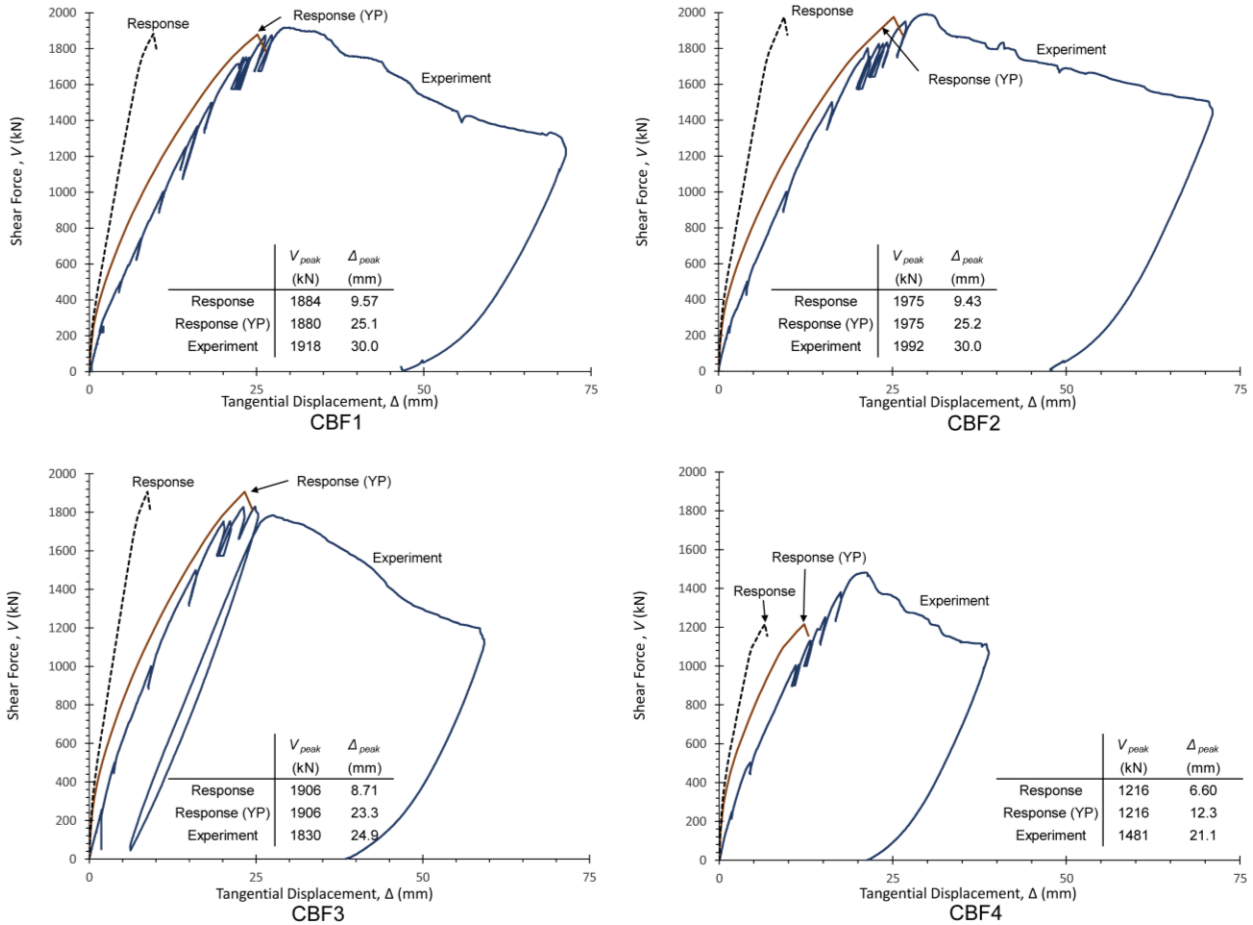


Figure 6-6: Shear Force vs. Tangential Displacement Predictions for CBF1 to CBF4

Response accurately predicts strength and displacement of specimens CBF1 and CBF2.

Specimen CBF1 had a test-to-prediction ratio of 0.98 and CBF2 had a test-to-prediction ratio of 0.99 for the ultimate strength. The prediction for CBF3 slightly overestimated the strength, similar to the Membrane prediction, having a test-to-prediction ratio of 1.04. This is likely as a result of the failure load occurring during a set of cycles, causing a premature failure. The ultimate strength for specimen CBF4 was under predicted by Response, having a test-to-prediction ratio of 1.22. This low prediction follows the same trend as the Membrane analysis, and is likely due to the shear key which developed along the failure crack.

### 6.3 Code Predictions for the Strength of Coupling Beams

The CSA and ACI Codes described earlier in Chapter 2 were used to predict the overall strength of the coupling beam specimens. Table 6-1 summarizes these predictions including those made by the program Response.

*Table 6-1: Code Predictions for Strengths of Coupling Beams*

Specimen	Experimental Values							MCFT (Response)		CSA	ACI
	$f'_c$ (MPa)	$\rho_x$ (%)	$f_{yx}$ (MPa)	$\rho_z f_{yz}$ (MPa)	$V_u$ (kN)	$v_u$ (MPa)	$\Delta$ (mm)	$V_u$ (kN)	$\Delta$ (mm)	$V_u$ (kN)	$V_u$ (kN)
CBF1	80.3	8.86	563	8.9	1918	13.8	30.0	1880	25.1	1871	1063
CBF2	80.3	7.00	563	7.0	1992	11.3	30.0	1975	25.2	1907	1346
CBF3	66.5	7.00	563	7.0	1830	10.4	24.9	1906	23.3	1907	1322
CBF4	66.5	7.00	563	3.5	1481	8.4	21.1	1216	12.3	1213	951
CBF1 exp/pred							1.02	1.17	1.02	1.45	
CBF2 exp/pred							1.01	1.16	1.04	1.32	
CBF3 exp/pred							0.96	1.06	0.96	1.28	
CBF4 exp/pred							1.22	1.46	1.22	1.36	
<b>Average exp/pred</b>							1.04	1.21	1.05	1.35	
<b>Coefficient of Variation exp/pred %</b>							8.6	18.9	8.5	9.7	

The above results indicate that the CSA code is able to accurately predict the ultimate shear capacity of the coupling beams with an average test-to-prediction ratio of 1.05 and a coefficient of variation of 8.5%. The CSA code prediction for CBF4 is very close to the predictions made by Response, further suggesting that the shear key developing along the failure crack improved the beam capacity.

The predicted strengths calculated using the ACI code were much less accurate with a test-to-prediction ratio of 1.35 and a coefficient of variation of 9.7%. The primary cause for these low predictions are the upper limit on the steel contribution,  $v_s$ , of  $0.66\sqrt{f'_c}$  MPa and upper limit on the total shear capacity,  $v_u$ , of  $0.83\sqrt{f'_c}$  MPa. Each of these artificially limit the capacity of heavily reinforced members that utilize high-strength concrete.

The inadequacy of the ACI limits can be demonstrated by designing a coupling beam with a predicted capacity equal to the tested capacity of specimen CBF2. To recall, the ACI predicted strength for CBF2 is 1346 kN. In order to reach a capacity of around 2000 kN, the width of the

beam would need to increase to 600 mm, or the depth increased to 850 mm. In order to increase the coupling beam width, the shear walls would also need to increase by 200 mm which would be a costly use of material if the building is hundreds of meters tall. Increasing the beam depth is the more logical solution. If this example was applied to the Burj Khalifa which has 148 occupied stories with an average floor-to-floor height of 3.75 m, the number of stories would be reduced by ten to fit a 4.0 m story-to-storey height into the same building elevation.

## 6.4 Influence of Cover Spalling on Predicated Shear Strength

The strengths of the two concretes used for the CBF test series turned out to be considerably higher than the intended strengths, and therefore side cover spalling had a minimal impact on the observed shear strengths. Side cover spalling will significantly reduce shear strength only if spalling of the concrete cover causes the remaining concrete to crush in diagonal compression prior to yielding of the shear reinforcement, or prior to the expected reduction in angle  $\theta$ . Thus if coupling beams have predicted strengths somewhat less than the  $0.25f'_c$  crushing limit if spalling is ignored, they will then have predicted strengths higher than the  $0.25f'_c$  if the reduction in width  $b_w$  due to side cover spalling is taken into account. In such cases the beams would fail in shear at unexpectedly low loads if cover spalling was not taken into account.

In order to demonstrate this phenomenon, two coupling beams are designed using the same reinforcement layout as CBF3 but with 40 MPa and 30 MPa concrete strengths rather than the 66.5 MPa value that CBF3 actually had. These designs will be named CBFx40 and CBFx30. Using the program Response and assuming a spalled width of 295 mm, CBFx40 and CBFx30 have predicted strengths of 1442 kN and 1142 kN respectively compared to the predicted 1906 kN strength for CBF3. Because Response gave such accurate predictions for the three very heavily reinforced sections, CBF1, CBF2, and CBF3, it will be assumed that the Response predicted failure loads for CBFx40 and CBFx30 are the loads at which these beams will fail. These strengths are plotted in Figure 6-7, along with the experimental and predicted strengths of CBF1 to CBF4. In order to compare all data points, the shear strengths are normalized by the concrete strength and are plotted with respect to the amount of shear reinforcement. The CSA and ACI prediction curves are also included in Figure 6-7. If cover spalling is accounted for and a spalled width of 295 mm is used, the CSA code will somewhat under predict the strength, resulting in a conservative but safe design. However, if a width of 400 mm is used for CBFx30

and CBFx40, the CSA code over predicts the shear strengths, resulting in an unsafe coupling beam design. These data points are also plotted in Figure 6-7. It can therefore be concluded that accounting for the side cover spalling phenomenon in the design codes is especially important for designs that approach the  $0.25f'_c$  CSA limit.

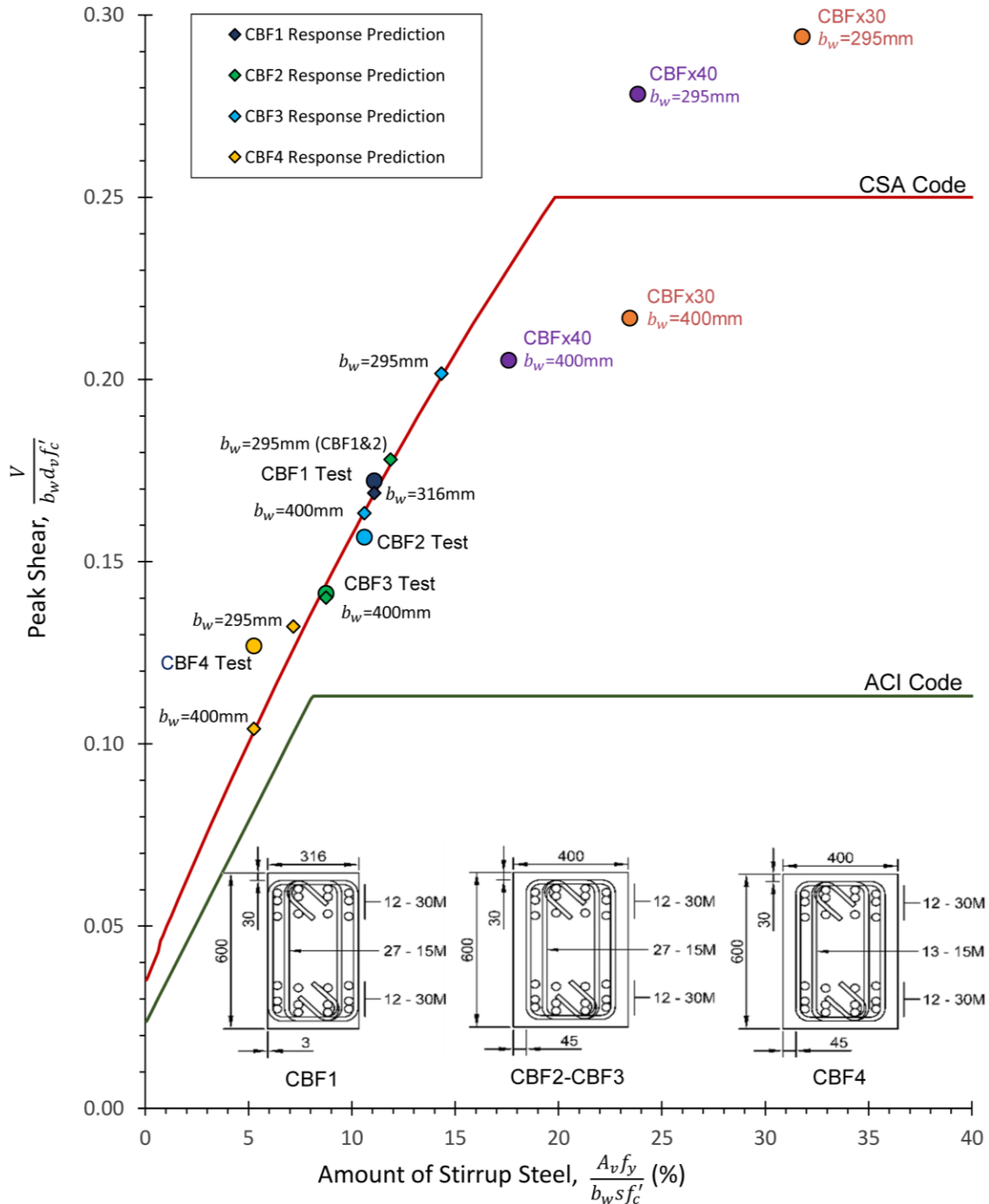


Figure 6-7: Influence of Side Cover Spalling on the Code Predicted Shear Strength

## Chapter 7: Conclusions and Recommendations

Concrete side cover spalling is a serious problem for heavily reinforced members with design strengths that approach the diagonal concrete crushing limit of  $0.25f'_c$  MPa. The reduction in cross-sectional area can result in a dangerous crushing failure prior to yielding of the stirrups. Results of this thesis indicate that concrete side cover spalling does occur for heavily reinforced high-strength coupling beams that are typical to industry design, and therefore should be accounted for in the design process.

When yielding of the stirrups governs failure, the concrete side cover is expected to spall after yielding begins. The side cover is expected to start spalling in the corners of flexural compression and progress to the midspan of the member. Concrete side cover spalling can occur with any side cover thickness, with tests showing side cover as thin as 3 mm spalling off. If neglecting the effects of the concrete side cover, test results showed that it is appropriate to assume the side cover spalls to the centerline of the outermost reinforcement.

It was observed that side cover spalling is a gradual process that occurs after the stirrups yield and continues into the post-peak response. From the analysis, it was observed that the concrete side cover was still able to hold compressive strains during the pre-peak response even after the side cover began to spall. Designing a concrete beam assuming the concrete side cover spalls entirely at will result in slightly conservative values as a result.

Neglecting the concrete side cover based on the area of shear reinforcement is an adequate method to account for the spalling phenomenon in design codes. However, the threshold of eleven times the required minimum outlined in CSA Code Clause 11.2.10.5 needs to be revisited as spalling was observed to occur with reinforcement levels at only eight times the minimum.

Due to the monotonic loading protocol, side cover spalling occurred outside the compression fan region of all four coupling beams. In order better document the real world behavior of this phenomenon, it is recommended that further tests be performed using a reverse-cyclic loading protocol to observe the behaviour of a fully spalled coupling beam under realistic loading scenarios.

Due to the  $0.66\sqrt{f'_c}$  MPa limit on the steel contribution,  $v_s$ , and the  $0.83\sqrt{f'_c}$  MPa limit on the total strength,  $v_u$ , the ACI Code significantly under predicts the shear strength of members that are heavily reinforced and use high-strength concrete. The average test-to-prediction ratio was 1.35 for the four coupling beam specimens. The CSA Code, which is based on the MCFT, was able to predict the peak loads with an average test-to-prediction ratio of 1.05.

The MCFT, with the use of program Response, was able to accurately predict the load-deformation response of the four coupling beams, with an average test-to-prediction ratio for the peak load of 1.04.

In order to accurately model the stiffness of coupling beams, it is important to account for confinement in the concrete stress-strain relationship due to the high levels of shear reinforcement present. By using the Mander model for rectangular concrete sections, the MCFT was able to adequately predict the ductile post-peak response of midspan elements in all four beams. The yield penetration of the longitudinal bars into the shear walls must also be accounted for so as to not overestimate the stiffness of the coupled shear wall system. The experimental results showed that the longitudinal bars had a yield penetration length of  $0.082f_y d_b$  mm, which is more than three times larger than the recommended approximation of  $0.022f_y d_b$  mm.

Coupling beams are critical to the lateral stiffness of a high rise structure and as such, the ability to accurately predict their load deformation response is essential to an efficient and economic design. While concrete side cover spalling, yield penetration, and confinement all play important roles in these predictions, having a rational approach for the basic design of these members as demonstrated by the MCFT, is critical to the economics of building development.

## References

- [1] PwC and the Urban Land Institute, "Emerging Trends in Real Estate 2016," PwC and the Urban Land Institute, Washington, D.C., 2015.
- [2] Council on Tall Buildings and Urban Habitat, "The Skyscraper Center," Council on Tall Buildings and Urban Habitat, 2016. [Online]. Available: <http://www.skyscrapercenter.com/>. [Accessed 12 January 2016].
- [3] World Floor Plans, "Floorplans," 2016. [Online]. Available: <http://www.worldfloorplans.com/floorplans/Armani-Hotel-Typical-Floor-Plan.shtml>. [Accessed 12 January 2016].
- [4] ACI Code Committee 318, Building Code Requirements for Structural Concrete (ACI 318-14) and Commentary, Farmington Hills, Michigan: American Concrete Institute, 2014, p. 519.
- [5] CSA A23.3-14, Design of Concrete Structures, Mississauga, Ontario: Canadian Standards Association, 2014.
- [6] ACI-ASCE Committee 326, "Shear and Diagonal Tension," *Journal of the American Concrete Institute*, vol. 59, no. 2, pp. 277-334, 1962.
- [7] ACI Code Committee 318, Building Code Requirements for Structural Concrete (ACI 318-63), Detroit, Michigan: American Concrete Institute, 1963, p. 144.
- [8] F. J. Vecchio and M. P. Collins, "The Modified Compression Field Theory for Reinforced Concrete Elements Subjected to Shear," *ACI Journal*, vol. 83, no. 2, pp. 219-231, March 1986.

- [9] E. C. Bentz and M. P. Collins, "Development of the 2004 Canadian Standards Association (CSA) A23.3 Shear Provisions for Reinforced Concrete," *Canadian Journal of Civil Engineering*, vol. 33, no. 5, pp. 521-534, 2006.
- [10] J.-Y. Lee and H.-B. Hwang, "Maximum Shear Reinforcement of Reinforced Concrete Beams," *ACI Structural Journal*, vol. 107, no. 5, pp. 580-588, 2010.
- [11] M. P. Collins and D. Mitchell, *Prestressed Concrete Basics*, Ottawa: Canadian Prestressed Concrete Institute, 1987.
- [12] M. P. Collins, "Towards a Rational Theory for Reinforced Concrete Members in Shear," *Journal of the Structural Division*, vol. 104, no. 4, pp. 649-666, 1978.
- [13] M. P. Collins, "Improving Analytical Models for Shear Design and Evaluation of Reinforced Concrete Structures," *fib (federation International du beton) Bulletin 57*, pp. 77-92, October 2010.
- [14] M. P. Collins and D. Mitchell, *Prestressed Concrete Structures*, Toronto, Ontario: Response Publications, 1997.
- [15] D. Mitchell and M. P. Collins, "Diagonal Compression Theory - A Rational Model for Concrete in Pure Torsion," *Journal of the American Concrete Institute*, vol. 71, no. 8, pp. 396-408, 1974.
- [16] W. Ritter, "Die bauweise hennebique," *Schweizerische Bauzeitung*, vol. 33, no. 7, pp. 59-61, 1899.
- [17] E. Morsch, *Concrete-Steel Construction*, New York: McGraw-Hill Book Company, 1909, (translated by E.p. Goodrich of 3rd edition of Der Eisenbetonbau, 1st edition 1902), p. 368.
- [18] H. Wagner, "Ebene Blechwandtrager mit sehr dunnem Stegblech," *Zeitschrift fur Flugtechnik und Motorluftschiffahr*, vol. 20, no. 18-21, 1929.

- [19] F. Vecchio and M. P. Collins, "The Response of Reinforced Concrete to In-Plane Shear and Normal Stresses," Publication No. 82-03, Toronto: Department of Civil Engineering, University of Toronto, March 1982.
- [20] S. B. Bhide and M. P. Collins, "Influence of Axial Tension on the Shear Capacity of Reinforced Concrete Members," *ACI Structural Journal*, vol. 86, no. 5, pp. 570-581, September-October 1989.
- [21] C. Sadler, "Investigating Shear Design Criteria for Prestressed Concrete Girders," M.A.Sc. Thesis: Department of Civil Engineering, University of Toronto, 1978.
- [22] M. Montgomery, "Fork Configuration Dampers (FCDs) for Enhanced Dynamic Performance of High-Rise Buildings," Ph.D. Thesis: Department of Civil Engineering, University of Toronto, 2011.
- [23] CSA A23.3-04, Design of Concrete Structures, Mississauga, Ontario: Canadian Standards Association, 2004.
- [24] A. Pauw, "Static Modulus of Elasticity of Concrete as Affected by Density," *ACI Journal*, vol. 57, no. 6, pp. 679-688, December 1960.
- [25] R. L. Carrasquillo, A. H. Nilson and F. O. Slate, "Properties of High Strength Concrete Subject to Short-Term Loads," *ACI Journal*, vol. 78, no. 3, pp. 171-178, May-June 1981.
- [26] S. Popovics, "A Numerical Approach to the Complete Stress-Strain Curve of Concrete," *Cement and Concrete Research*, vol. 3, no. 5, pp. 483-599, May 1973.
- [27] E. Thorenfeldt, A. Tomaszewicz and J. J. Jensen, "Mechanical Properties of High-Strength Concrete and Application in Design," in *Proceedings of the Symposium "Utilization of High Strength Concrete"*, Stavanger, Norway, June, 1987.
- [28] M. P. Collins and A. Porasz, "Shear Strength for High Strength Concrete," *Bulletin No. 193-Design Aspects of High Strength Concrete*, pp. 75-83, 1989.

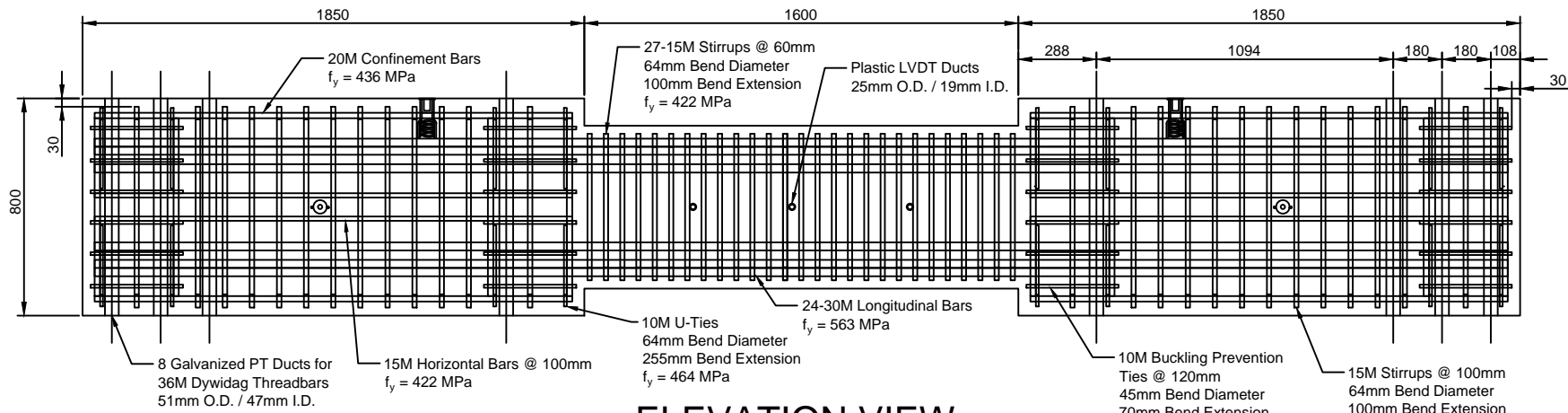
- [29] Y. J. Kim, "The Shear Response of Circular Concrete Columns Reinforced with High Strength Steel Spirals," M.A.Sc. Thesis: Department of Civil Engineering, University of Toronto, 2000.
- [30] T. Paulay and M. J. N. Priestley, Seismic Design of Reinforced Concrete and Masonry Buildings, New York: John Wiley & Sons, Inc., 1992, pp. 140-142.
- [31] D. Ruggiero, *Timeline, Version 1.5*, University of Toronto, 2014.
- [32] J. C. Walraven, "Fundamental Analysis of Aggregate Interlock," *Journal of Structural Division*, vol. 107, no. ST11, pp. 2245-2270, November 1981.
- [33] E. C. Bentz, "Membrane-2012," University of Toronto, 2012. [Online]. Available: <http://www.ecf.utoronto.ca/~bentz/m2k.htm>. [Accessed 30 January 2016].
- [34] J. Mander, M. Priestley and R. Park, "Theoretical Stress-Strain Model for Confined Concrete," *Journal of Structural Engineering*, vol. 114, no. 8, pp. 1804-1826, September 1988.
- [35] E. C. Bentz, "Response-2012," University of Toronto, 2012.

# Appendix A: Digital Drawings for Experimental Program

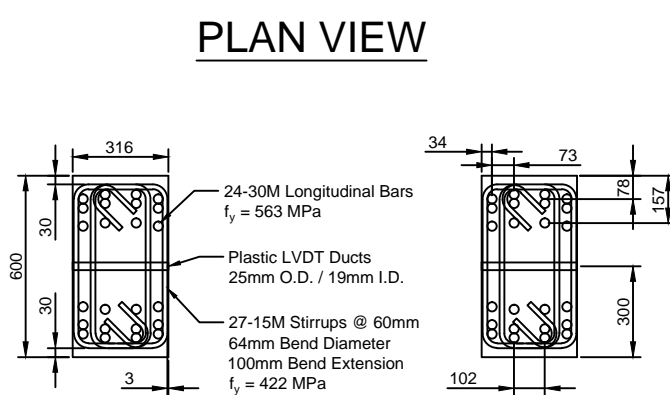
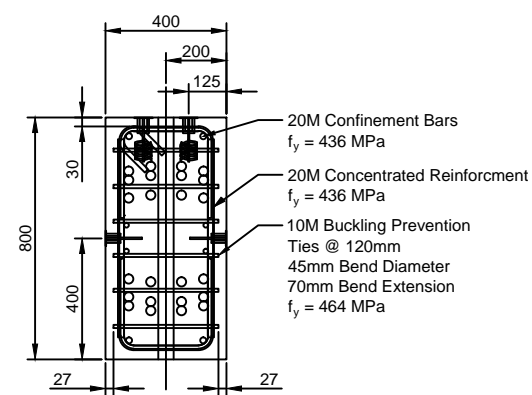
The following drawings were created using AutoCAD and accurately depict the final specimen designs and experimental setup. The drawings were last updated on January 15, 2016.

*Table A-1: List of Drawings*

Drawing #	Drawing Title	Page #
001	CBF1 Specimen and Shear Wall End Block Design	125
002	CBF1 Strain Gauge Layout	126
003	CBF2 Specimen and Shear Wall End Block Design	127
004	CBF2 Strain Gauge Layout	128
005	CBF3 Specimen and Shear Wall End Block Design	129
006	CBF3 Strain Gauge Layout	130
007	CBF4 Specimen and Shear Wall End Block Design	131
008	CBF4 Strain Gauge Layout	132
009	Cantilever Shear Wall Component Design	133
010	Rectangular Shear Wall Component Design	134
011	Coupling Beam Test Assembly	135
012	Rebar Stirrup and Tie Dimensions	136
013	Formwork Design for Coupling Beam Specimens	137
014	Formwork Design for Cantilever Shear Wall Component	138
015	Formwork Design for Rectangle Shear Wall Component	139
016	Meccano Frame Experimental Setup – Facing North	140
017	Experimental Setup without Frame – Facing North	141
018	Meccano Frame Experimental Setup – Facing East	142
019	Meccano Frame Experimental Setup – Loading Plane	143
020	Meccano Frame Experimental Setup – Facing West	144
021	LVDT and Linear Pot Instrumentation Setup	145
022	LED Target Instrumentation Setup	146
023	Metris K610 Camera System Placement	147
024	Metris K610 Camera System Field of View Dimensions	148



**ELEVATION VIEW**



**NOTES:**

- 1) Test day 6" cylinder compressive strength = 80.3 MPa
- 2)  $A_v = 18$  times the minimum

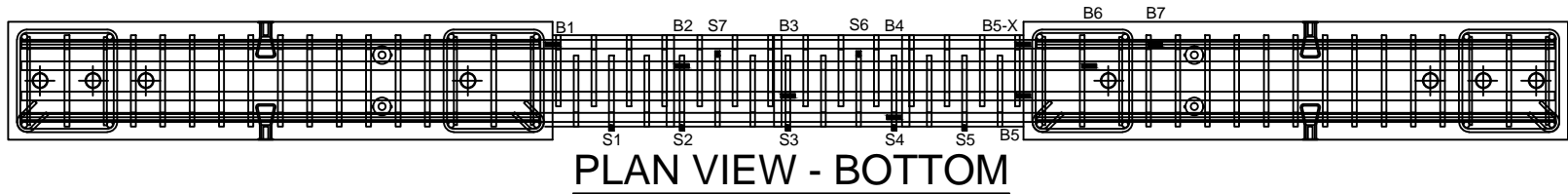
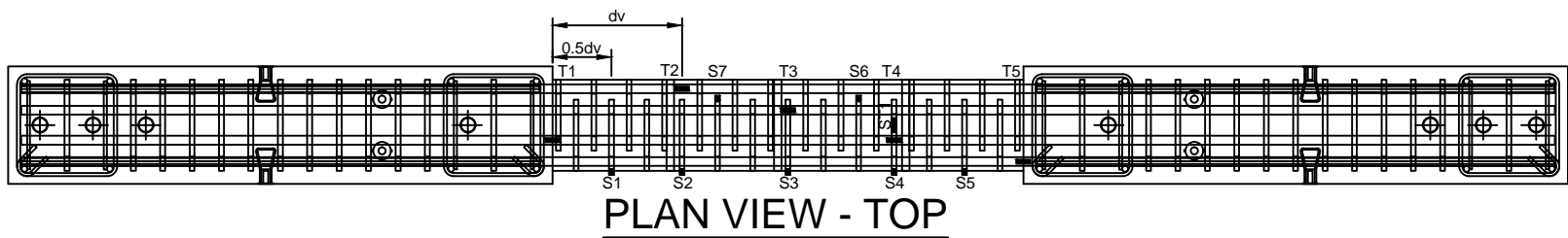
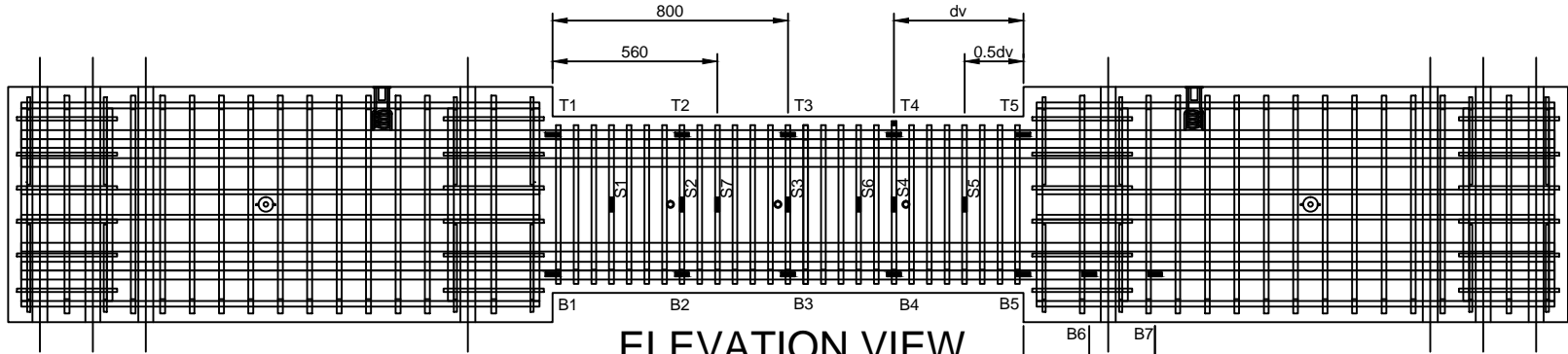
1) 5/8" (M16) Type LF-W  
2) 1" (M24) Type EC-2FW

Scale = 1:25

**University of Toronto**  
**Department of Civil Engineering**

Title:  
**CBF1 Specimen and Shear Wall End Block Design**

Date: 2016-01-15	DWG No: 001	Designed: AWF	Rev: 11
------------------	-------------	---------------	---------



### Strain Gauge Naming System

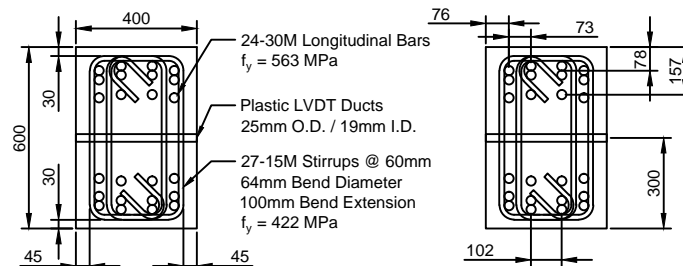
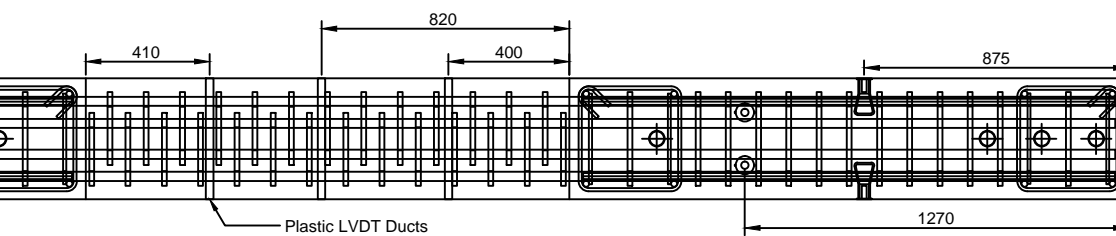
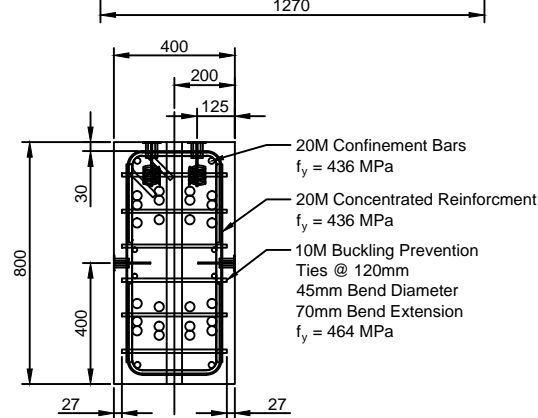
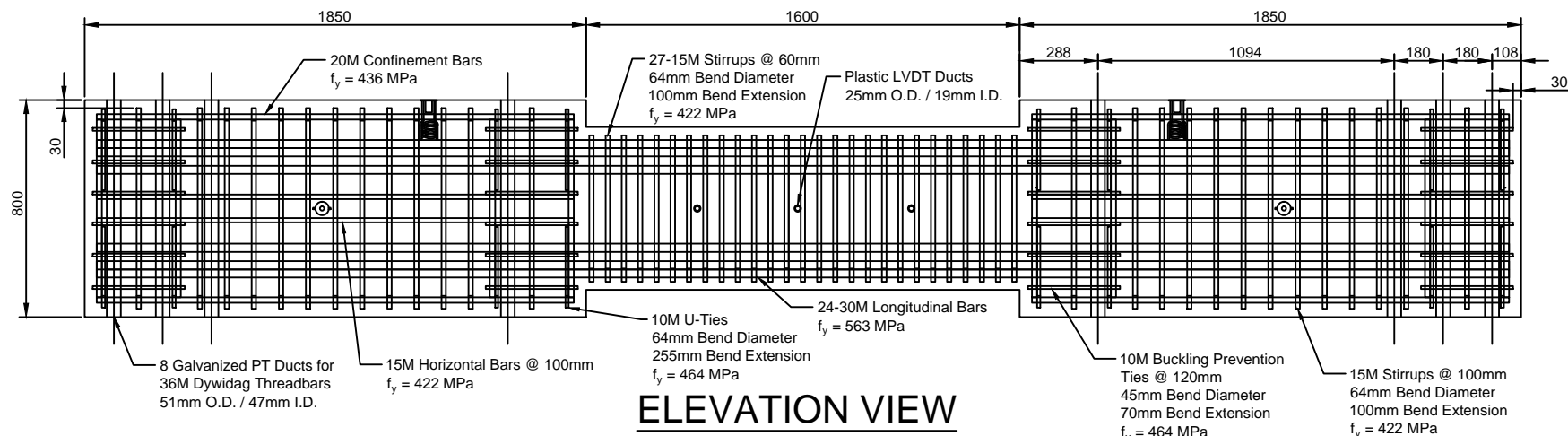
T1 = As_Top_End_West	B1 = As_Bot_End_West	S1 = Av_0.5dv_South_West
T2 = As_Top_dv_West	B2 = As_Bot_dv_West	S2 = Av_dv_South_West
T3 = As_Top_Mid	B3 = As_Bot_Mid	S3 = Av_Mid_South
T4 = As_Top_dv_East	B4 = As_Bot_dv_East	S4 = Av_dv_South_East
T5 = As_Top_End_West	B5 = As_Bot_End_East	S5 = Av_End_South_East
	B5-X = As_Bot_End_East_X	S6 = Av_dv_North_East
	B6 = As_Wall_0.5dv_East	S7 = Av_dv_North_West
	B7 = As_Wall_dv_East	ST1 = Av_dv_Top_East

Scale = 1:25

University of Toronto  
Department of Civil Engineering

Title:  
**CBF1 Strain Gauge  
Instrumentation Layout**

Date: 2016-01-15	DWG No: 002	Designed: AWF	Rev: 11
------------------	-------------	---------------	---------



**NOTES:**  
 1) Test day 6" cylinder compressive strength = 80.3 MPa  
 2)  $A_v = 14$  times the minimum

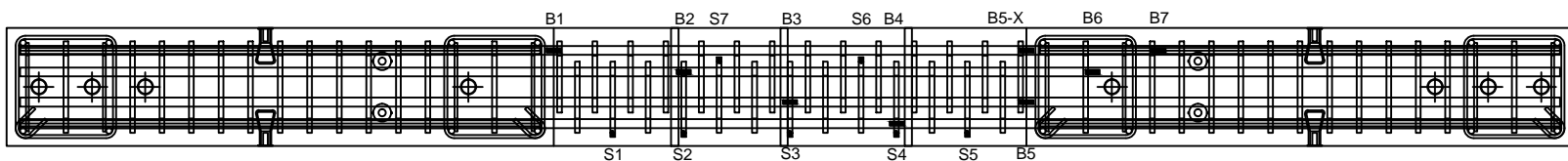
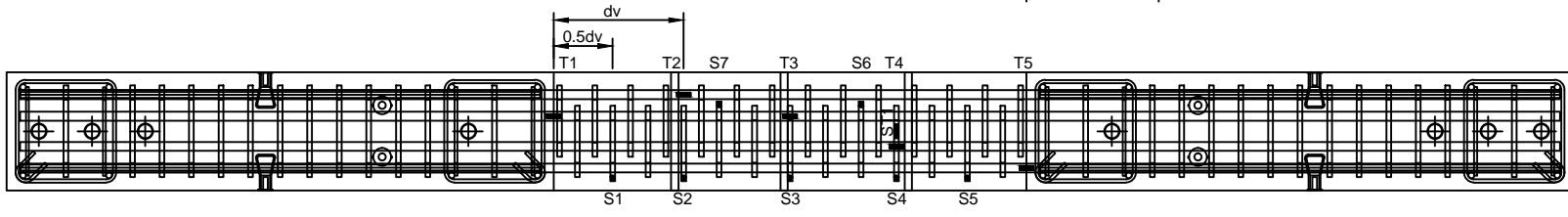
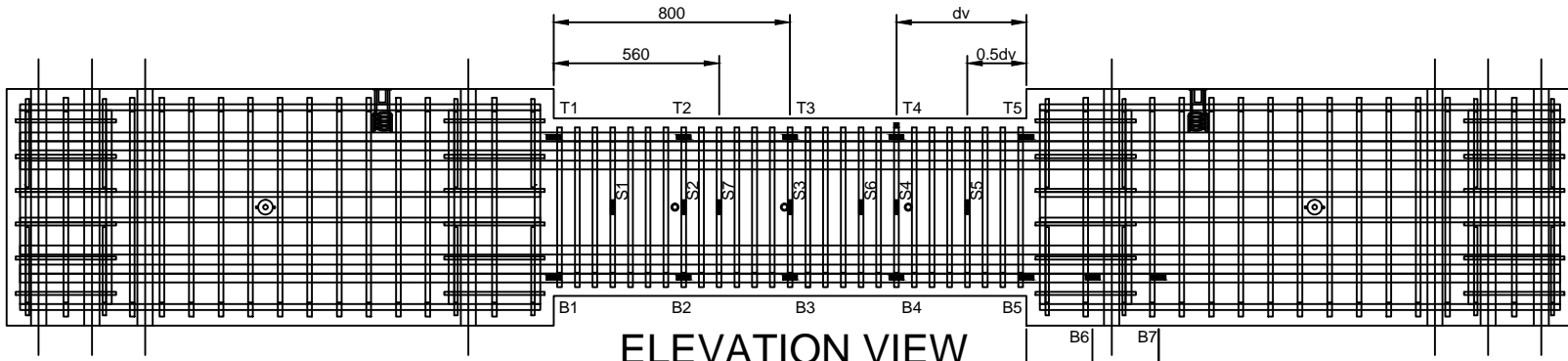
- 1) 5/8" (M16) Type LF-W  
 2) 1" (M24) Type EC-2FW

Scale = 1:25

**University of Toronto**  
**Department of Civil Engineering**

Title:  
**CBF2 Specimen and Shear Wall End Block Design**

Date: 2016-01-15	DWG No: 003	Designed: AWF	Rev: 11
------------------	-------------	---------------	---------



### Strain Gauge Naming System

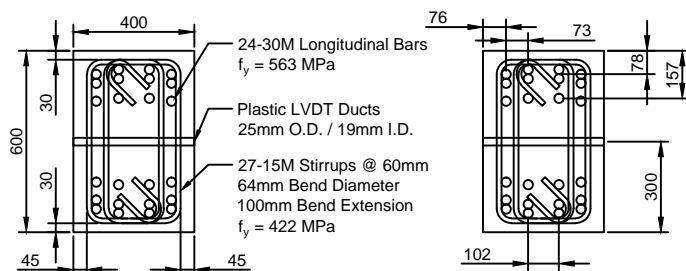
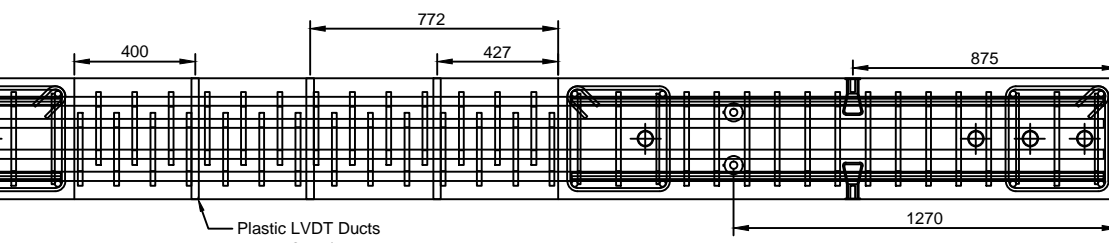
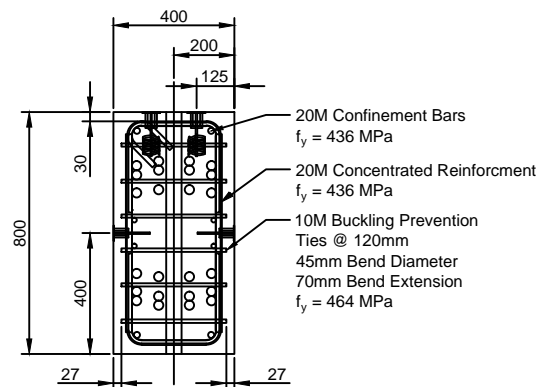
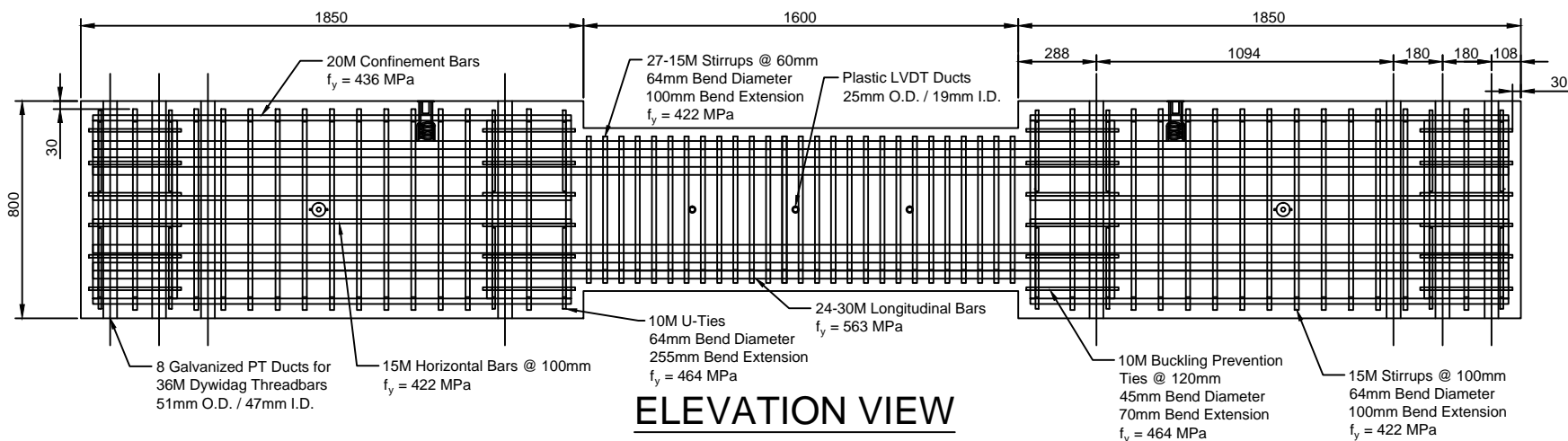
T1 = As_Top_End_West	B1 = As_Bot_End_West	S1 = Av_0.5dv_South_West
T2 = As_Top_dv_West	B2 = As_Bot_dv_West	S2 = Av_dv_South_West
T3 = As_Top_Mid	B3 = As_Bot_Mid	S3 = Av_Mid_South
T4 = As_Top_dv_East	B4 = As_Bot_dv_East	S4 = Av_dv_South_East
T5 = As_Top_End_West	B5 = As_Bot_End_East	S5 = Av_End_South_East
	B5-X = As_Bot_End_East_X	S6 = Av_dv_North_East
	B6 = As_Wall_0.5dv_East	S7 = Av_dv_North_West
	B7 = As_Wall_dv_East	ST1 = Av_dv_Top_East

Scale = 1:25

University of Toronto  
Department of Civil Engineering

Title:  
CBF2 Strain Gauge  
Instrumentation Layout

Date: 2016-01-15	DWG No: 004	Designed: AWF	Rev: 11
------------------	-------------	---------------	---------



**NOTES:**

- 1) Test day 6" cylinder compressive strength = 66.5 MPa
- 2)  $A_v = 15$  times the minimum

1 2

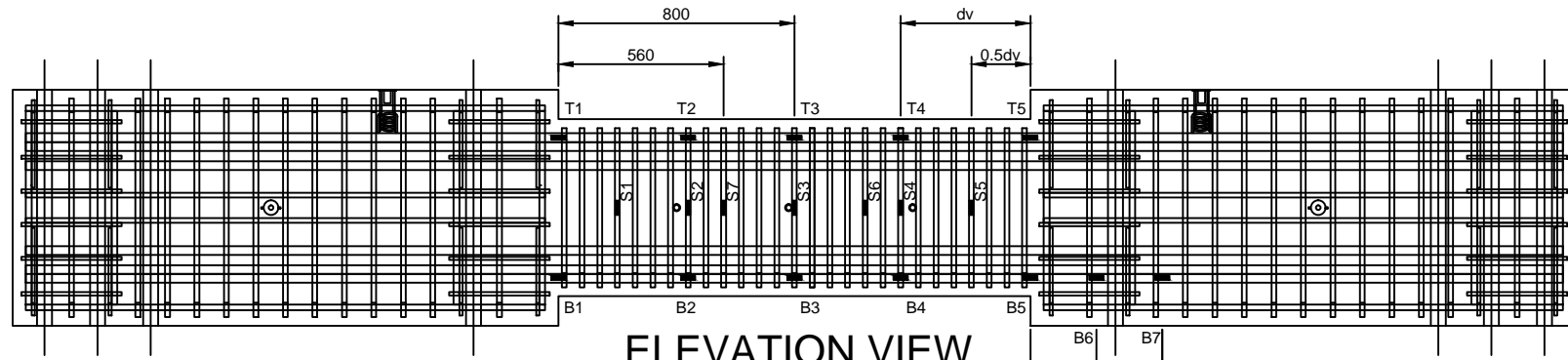
1) 5/8" (M16) Type LF-W  
2) 1" (M24) Type EC-2FW

Scale = 1:25

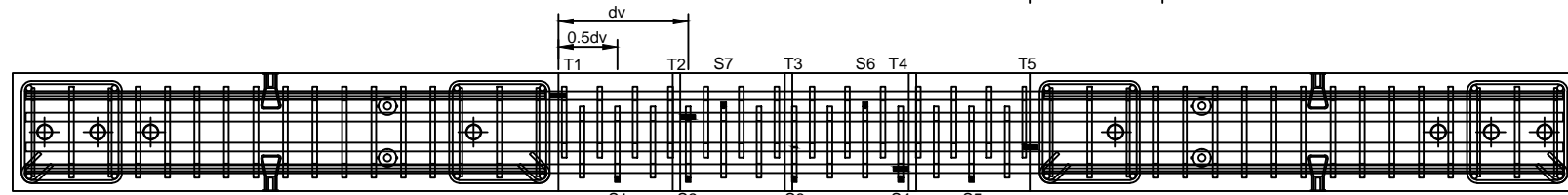
**University of Toronto**  
**Department of Civil Engineering**

Title:  
**CBF3 Specimen and Shear Wall End Block Design**

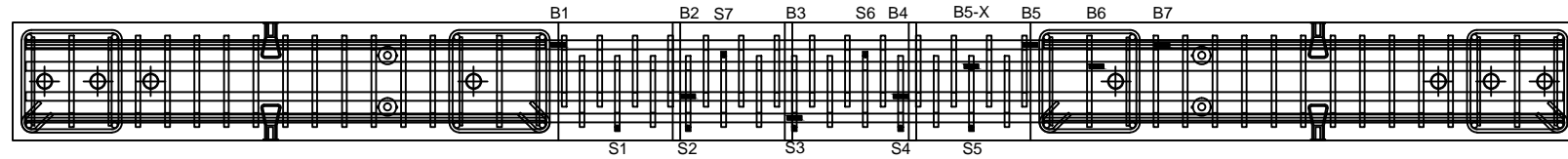
Date: 2016-01-15	DWG No: 005	Designed: AWF	Rev: 11
------------------	-------------	---------------	---------



**ELEVATION VIEW**



**PLAN VIEW - TOP**



**PLAN VIEW - BOTTOM**

### Strain Gauge Naming System

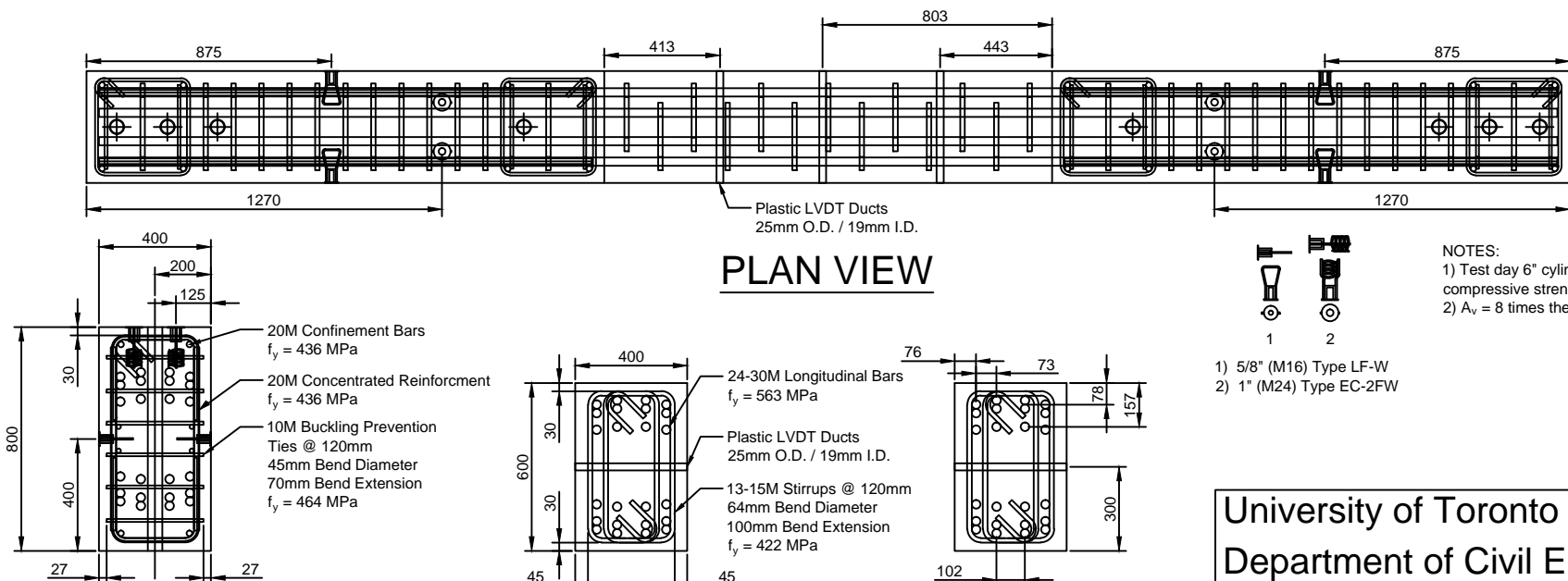
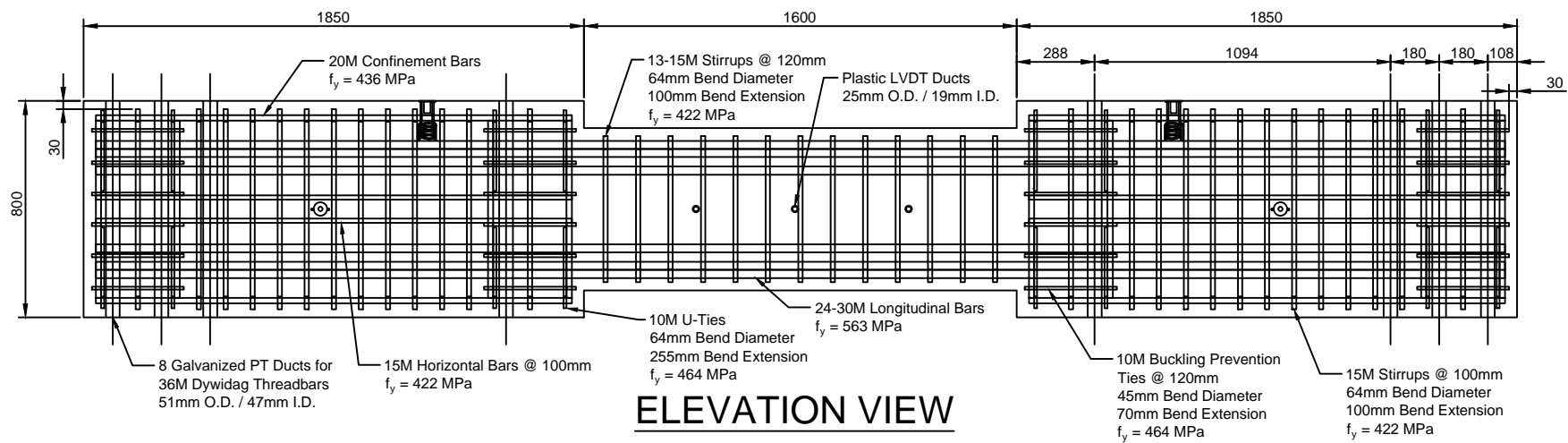
T1 = As_Top_End_West	B1 = As_Bot_End_West	S1 = Av_0.5dv_South_West
T2 = As_Top_dv_West	B2 = As_Bot_dv_West	S2 = Av_dv_South_West
T3 = As_Top_Mid	B3 = As_Bot_Mid	S3 = Av_Mid_South
T4 = As_Top_dv_East	B4 = As_Bot_dv_East	S4 = Av_dv_South_East
T5 = As_Top_End_West	B5 = As_Bot_End_East	S5 = Av_End_South_East
	B6 = As_Wall_0.5dv_East	S6 = Av_dv_North_East
	B7 = As_Wall_dv_East	S7 = Av_dv_North_West

Scale = 1:25

University of Toronto  
Department of Civil Engineering

Title:  
**CBF3 Strain Gauge  
Instrumentation Layout**

Date: 2016-01-15	DWG No: 006	Designed: AWF	Rev: 11
------------------	-------------	---------------	---------



**NOTES:**

- 1) Test day 6" cylinder compressive strength = 66.5 MPa
- 2)  $A_v = 8$  times the minimum

- 1) 5/8" (M16) Type LF-W  
2) 1" (M24) Type EC-2FW

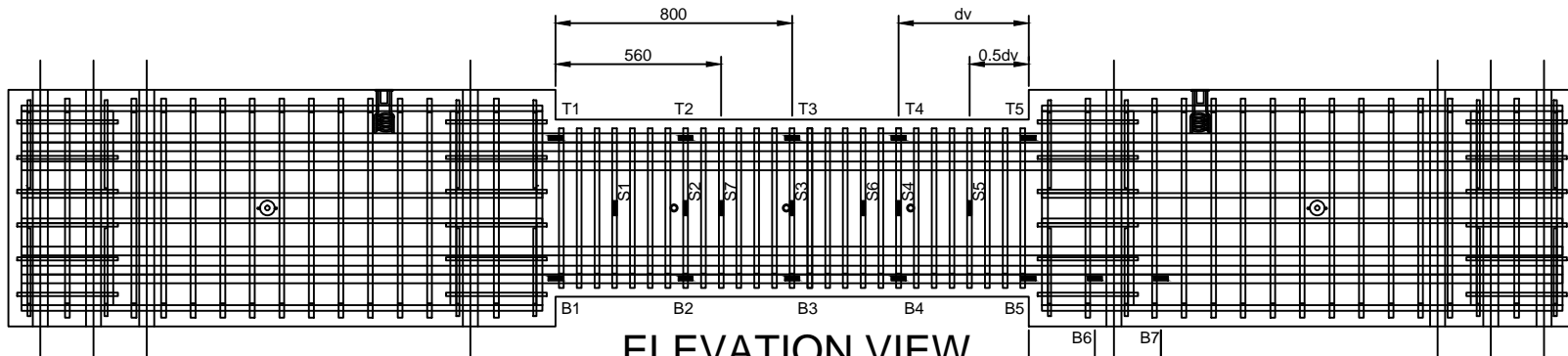
Scale = 1:25

**WALL CROSS SECTION**

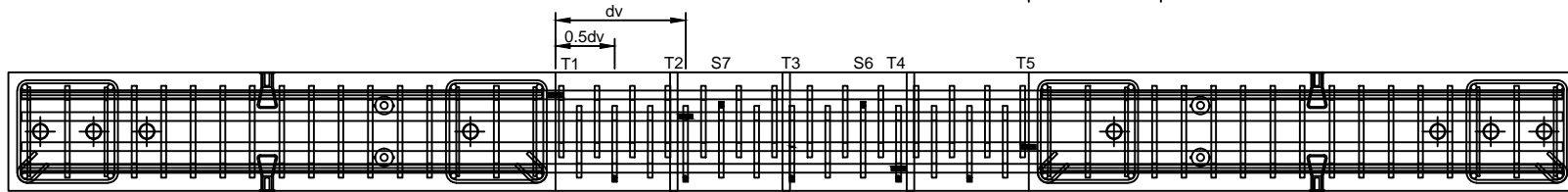
University of Toronto  
Department of Civil Engineering

Title:  
**CBF4 Specimen and Shear Wall End Block Design**

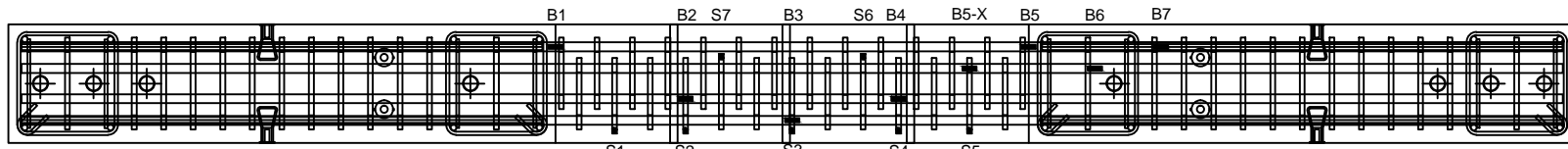
Date: 2016-01-15	DWG No: 007	Designed: AWF	Rev: 11
------------------	-------------	---------------	---------



ELEVATION VIEW



PLAN VIEW - TOP



PLAN VIEW - BOTTOM

### Strain Gauge Naming System

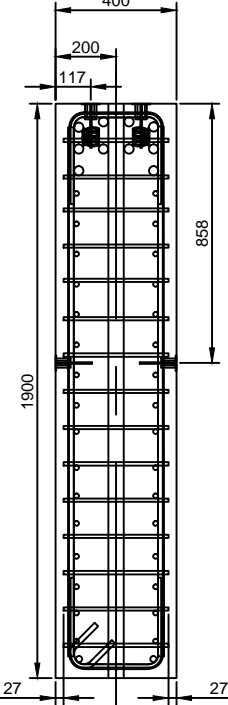
T1 = As_Top_End_West	B1 = As_Bot_End_West	S1 = Av_0.5dv_South_West
T2 = As_Top_dv_West	B2 = As_Bot_dv_West	S2 = Av_dv_South_West
T3 = As_Top_Mid	B3 = As_Bot_Mid	S3 = Av_Mid_South
T4 = As_Top_dv_East	B4 = As_Bot_dv_East	S4 = Av_dv_South_East
T5 = As_Top_End_West	B5-X = As_Bot_0.5dv_East	S5 = Av_End_South_East
	B5 = As_Bot_End_East	S6 = Av_dv_North_East
	B6 = As_Wall_0.5dv_East	S7 = Av_dv_North_West
	B7 = As_Wall_dv_East	

Scale = 1:25

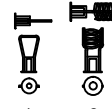
University of Toronto  
Department of Civil Engineering

Title:  
CBF4 Strain Gauge  
Instrumentation Layout

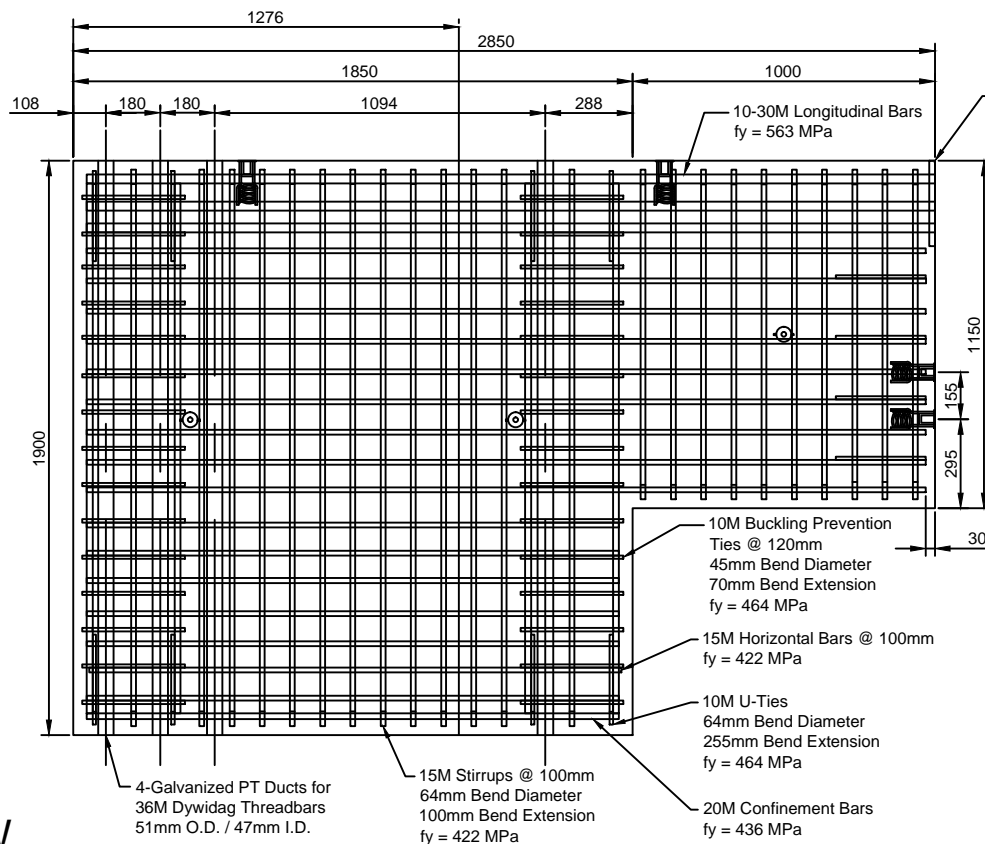
Date:	DWG No:	Designed:	Rev:
2016-01-15	008	AWF	11



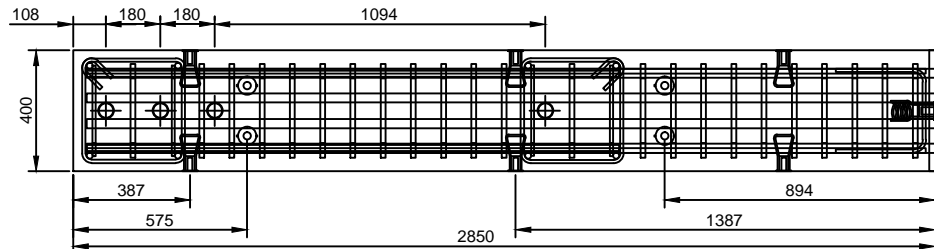
LEFT SIDE VIEW



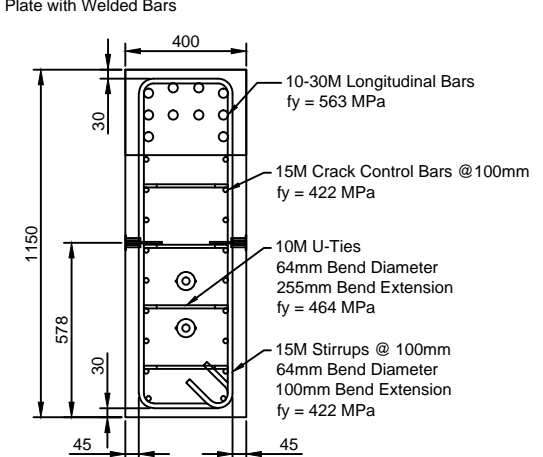
1) 5/8" (M16) Type LF-W  
2) 1" (M24) Type EC-2FW



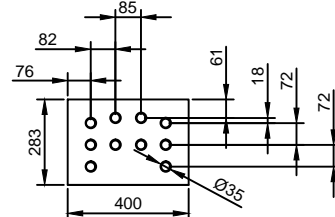
ELEVATION VIEW



PLAN VIEW



RIGHT SIDE VIEW

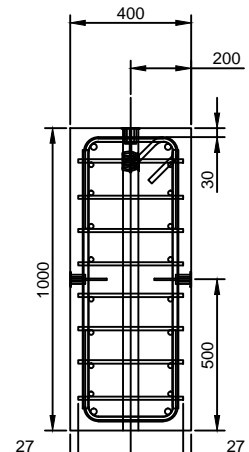


3/4" End Plate with Welded Bars

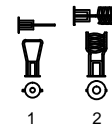
Scale = 1:25

University of Toronto  
Department of Civil Engineering

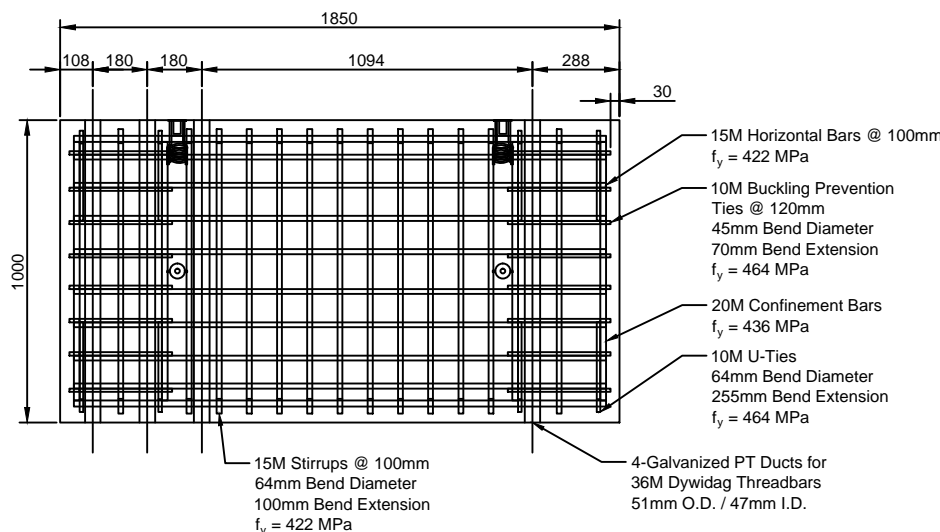
Title:	Cantilever Shear Wall Component Design
Date:	DWG No:
Designed:	Rev:
2016-01-15	009
AWF	11



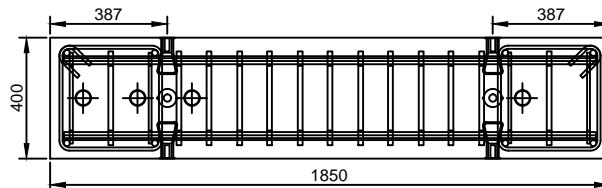
SIDE VIEW



- 1) 5/8" (M16) Type LF-W  
2) 1" (M24) Type EC-2FW



ELEVATION VIEW



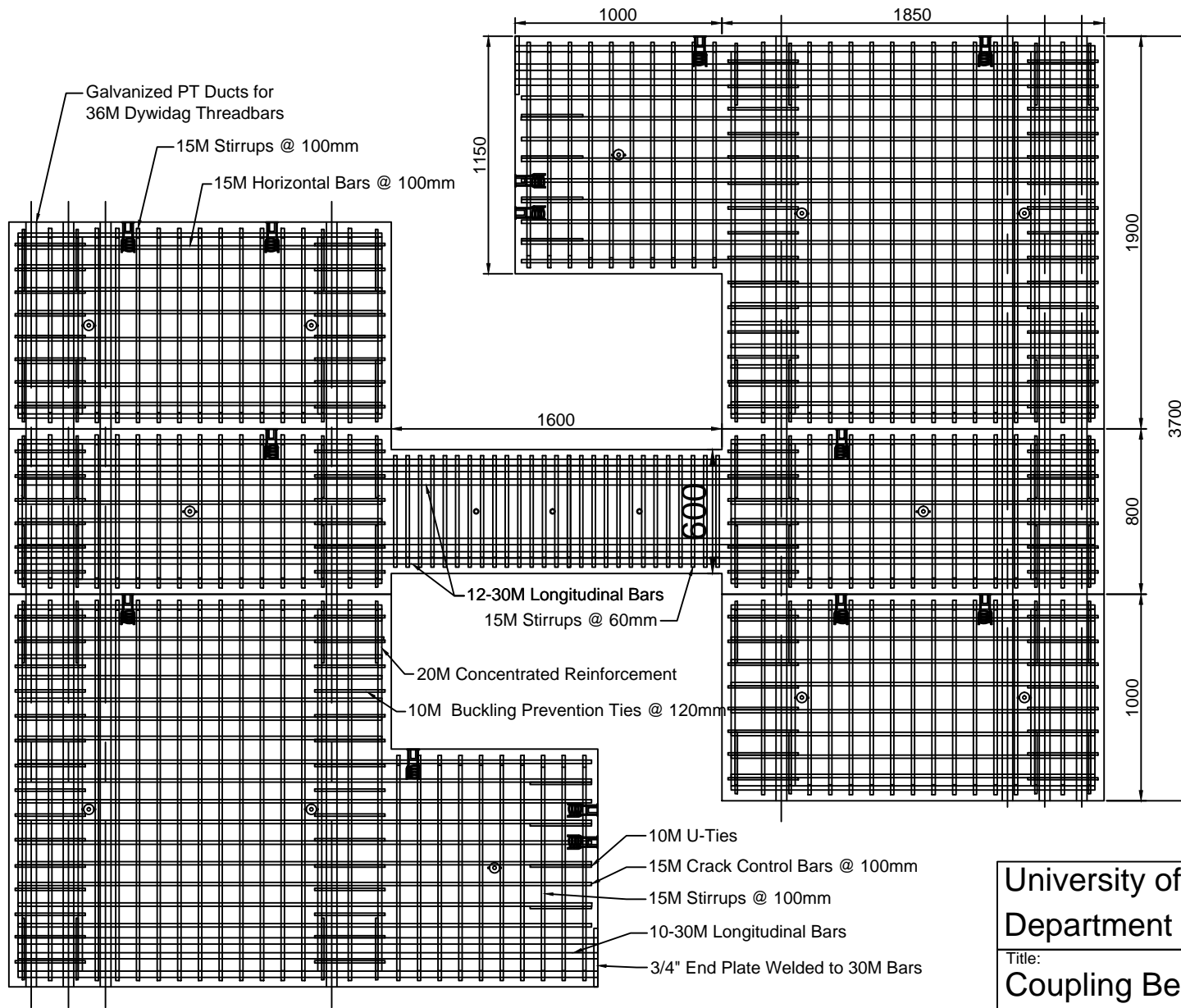
PLAN VIEW

Scale = 1:25

University of Toronto  
Department of Civil Engineering

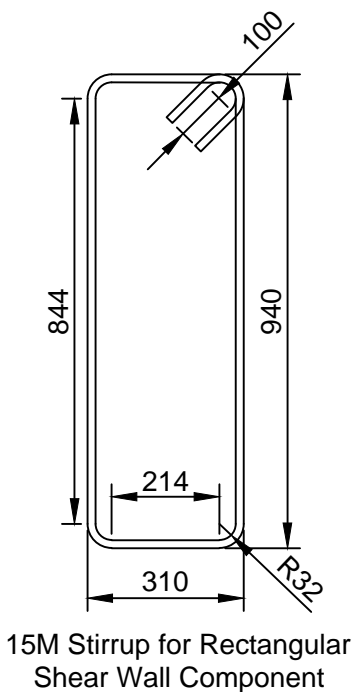
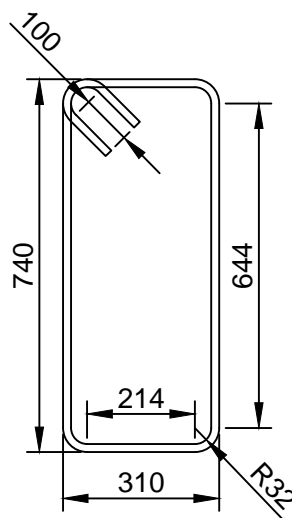
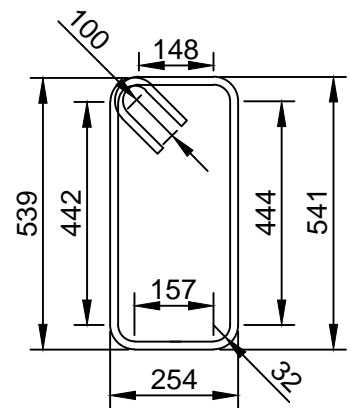
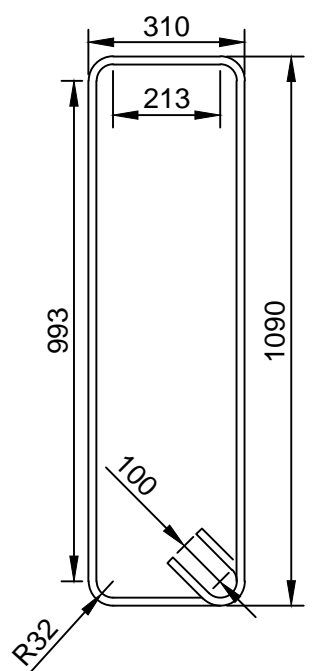
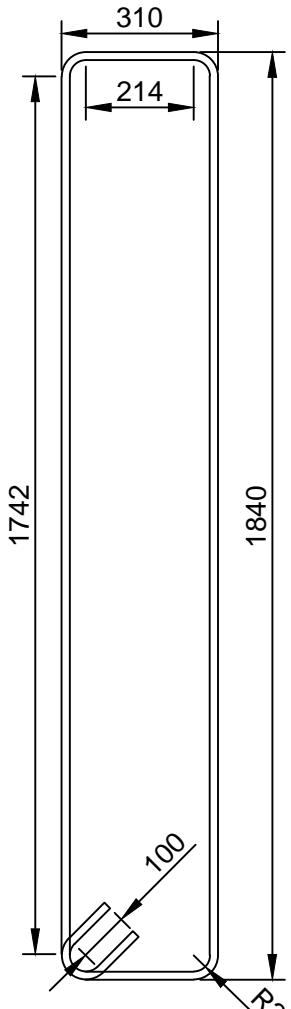
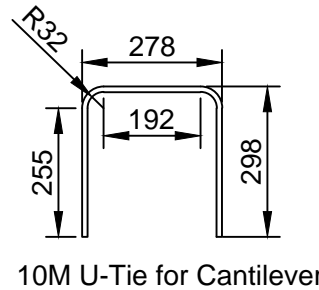
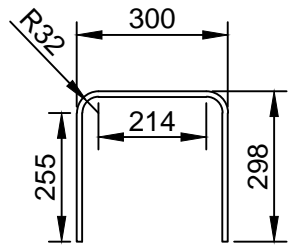
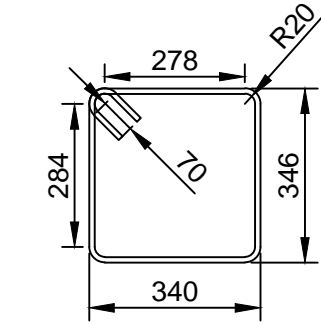
Title:  
Rectangular Shear Wall  
Component Design

Date:	DWG No:	Designed:	Rev:
2016-01-15	010	AWF	11



University of Toronto  
Department of Civil Engineering  
Title:  
Coupling Beam Test Assembly

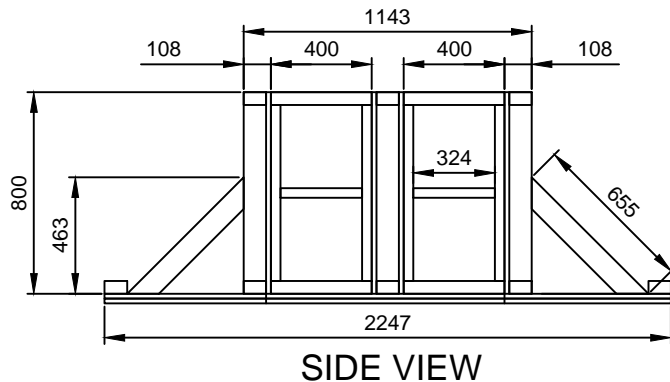
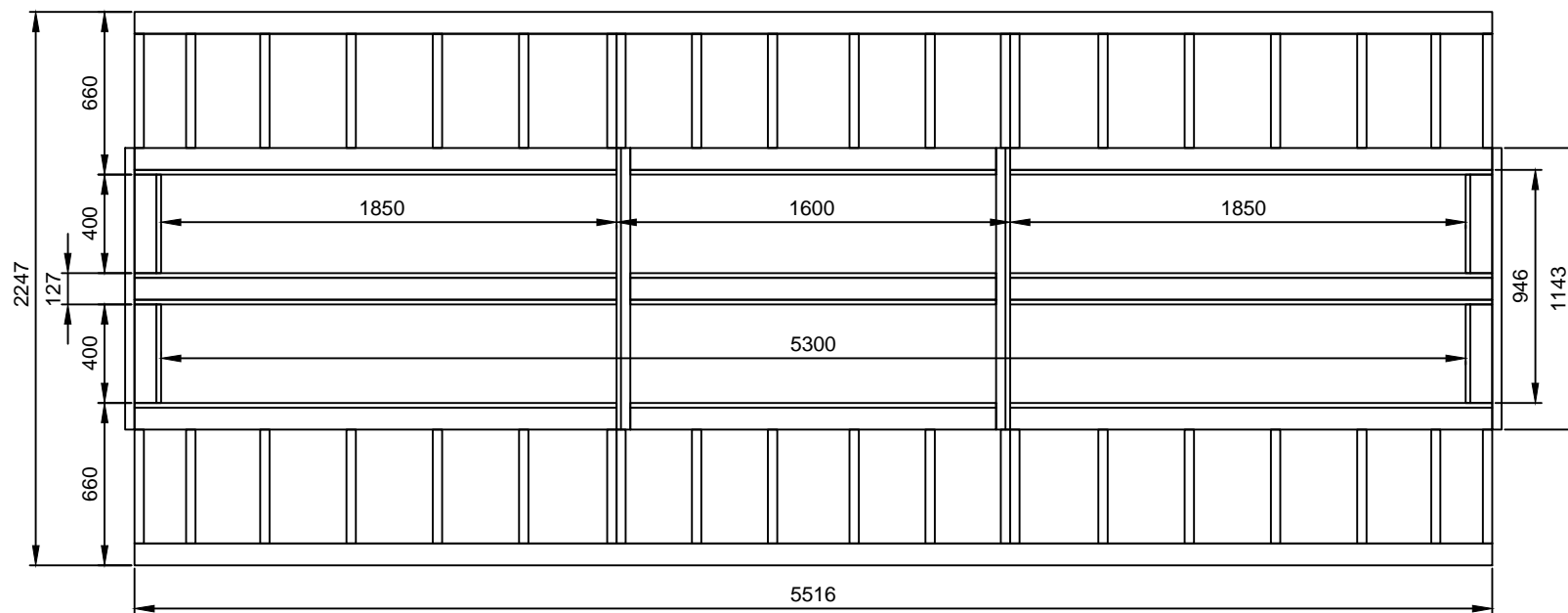
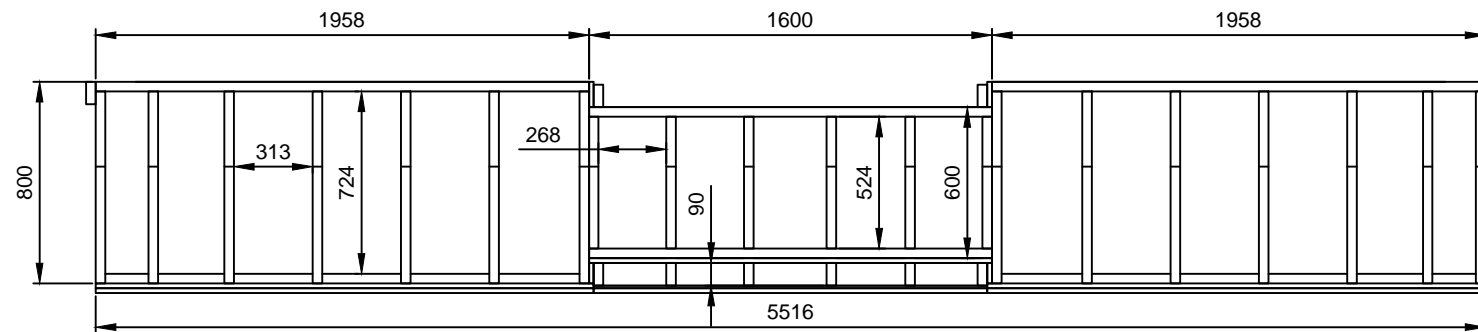
Date:	DWG No:	Designed:	Rev:
2016-01-15	011	AWF	11



Scale = 1:15

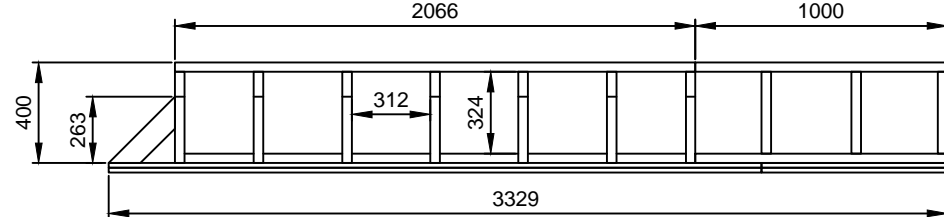
University of Toronto  
Department of Civil Engineering

Title:	Rebar Stirrup and Tie Dimensions		
Date:	DWG No:	Designed:	Rev:
2016-01-15	012	AWF	11

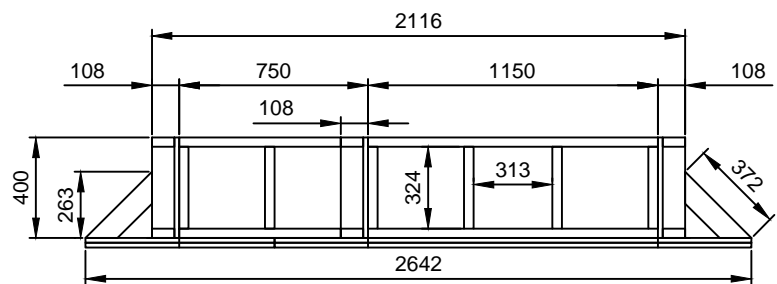


Scale = 1:30

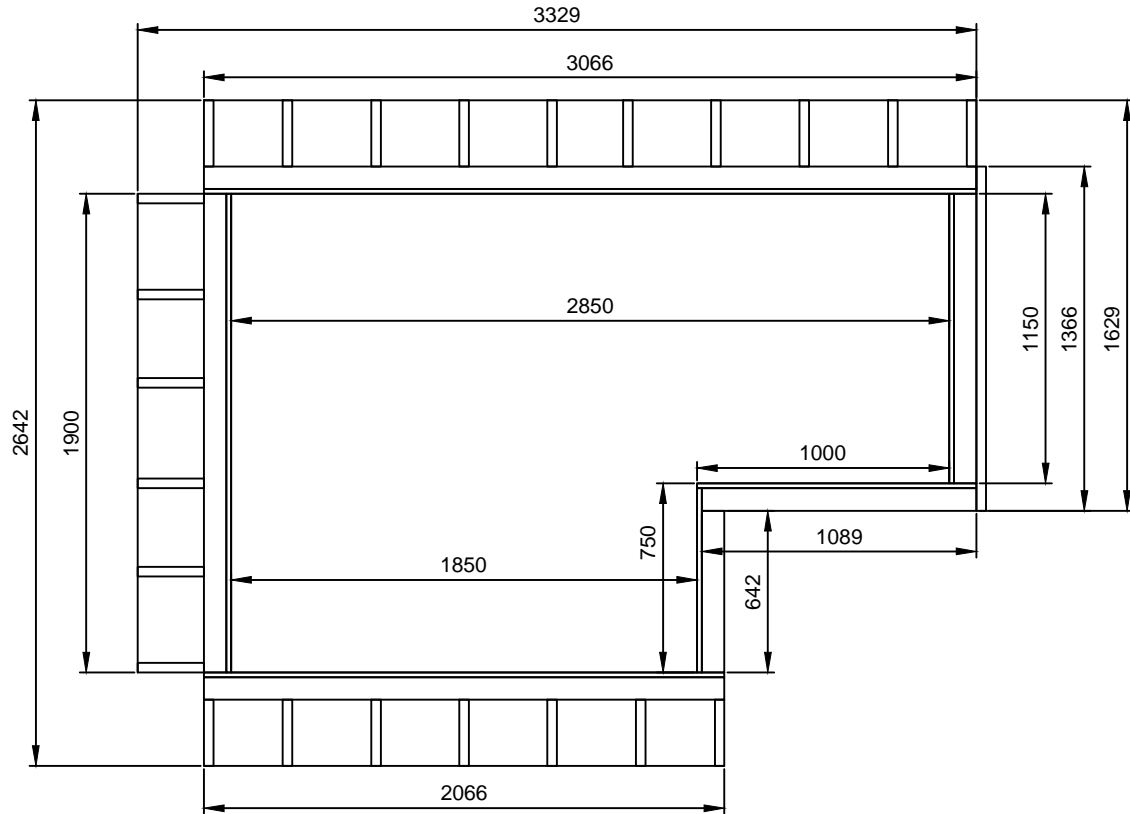
University of Toronto	
Department of Civil Engineering	
Title:	
Formwork Design for Coupling Beam Specimens	
Date:	DWG No:
2016-01-15	013
Designed:	Rev:
AWF	11



ELEVATION VIEW



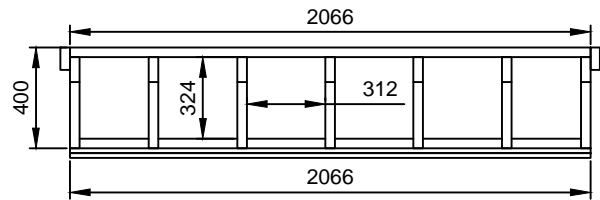
SIDE VIEW



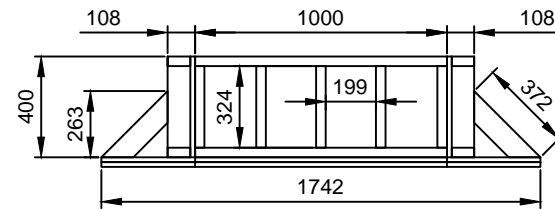
PLAN VIEW

Scale = 1:30

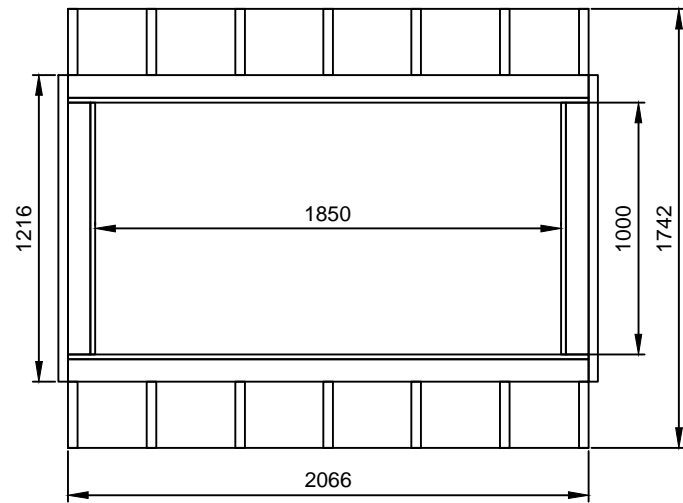
University of Toronto Department of Civil Engineering			
Title: Formwork Design for Cantilever Shear Wall Component			
Date: 2016-01-15	DWG No: 014	Designed: AWF	Rev: 11



ELEVATION VIEW



SIDE VIEW



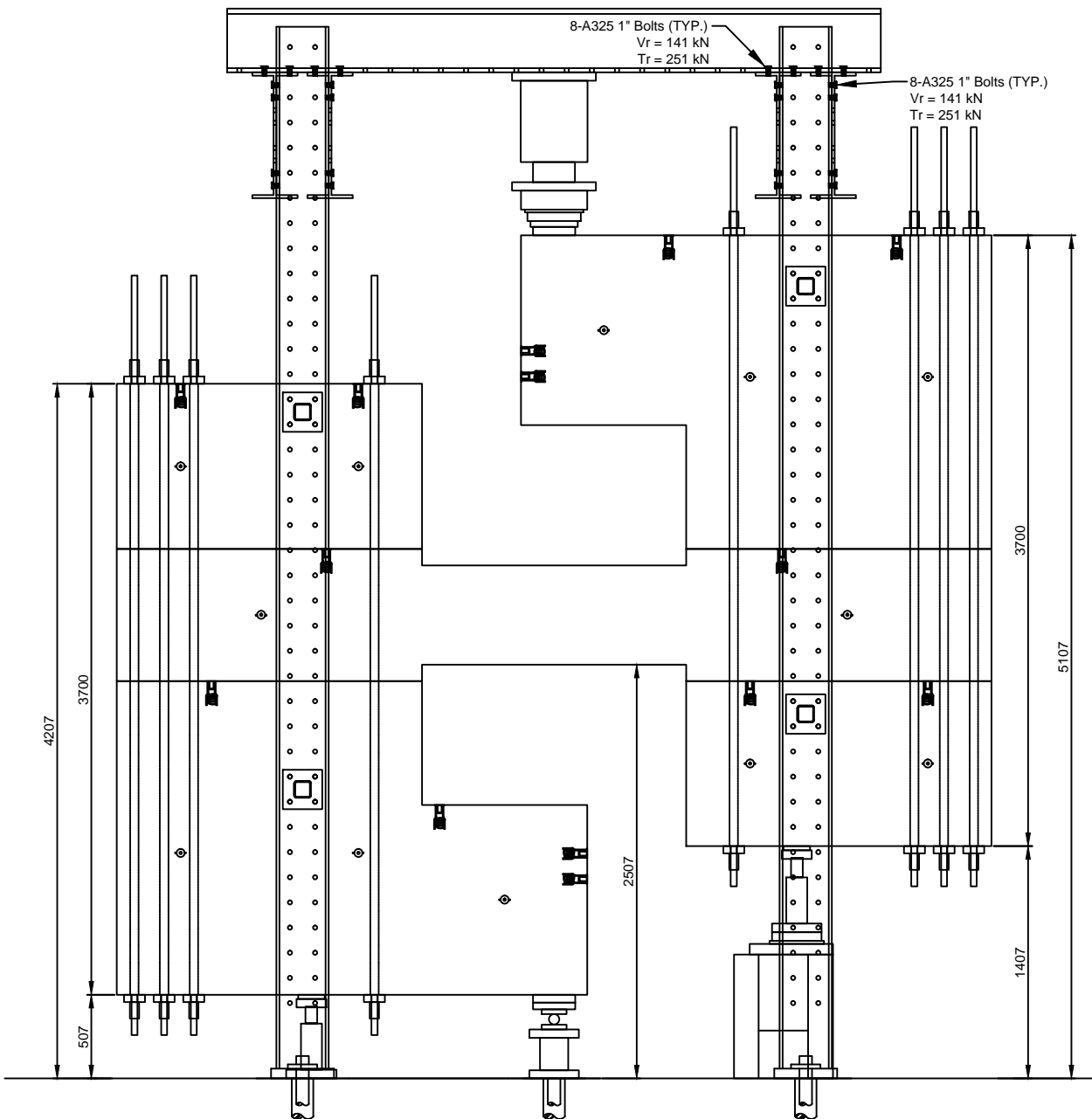
PLAN VIEW

Scale = 1:30

University of Toronto  
Department of Civil Engineering

Title:  
Formwork Design for Rectangle  
Shear Wall Component

Date:	DWG No:	Designed:	Rev:
2016-01-15	015	AWF	11

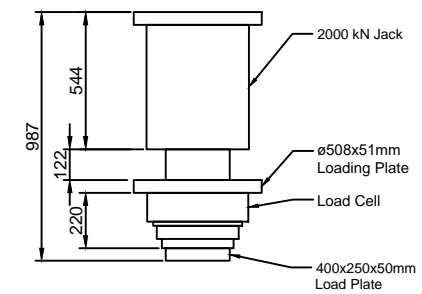
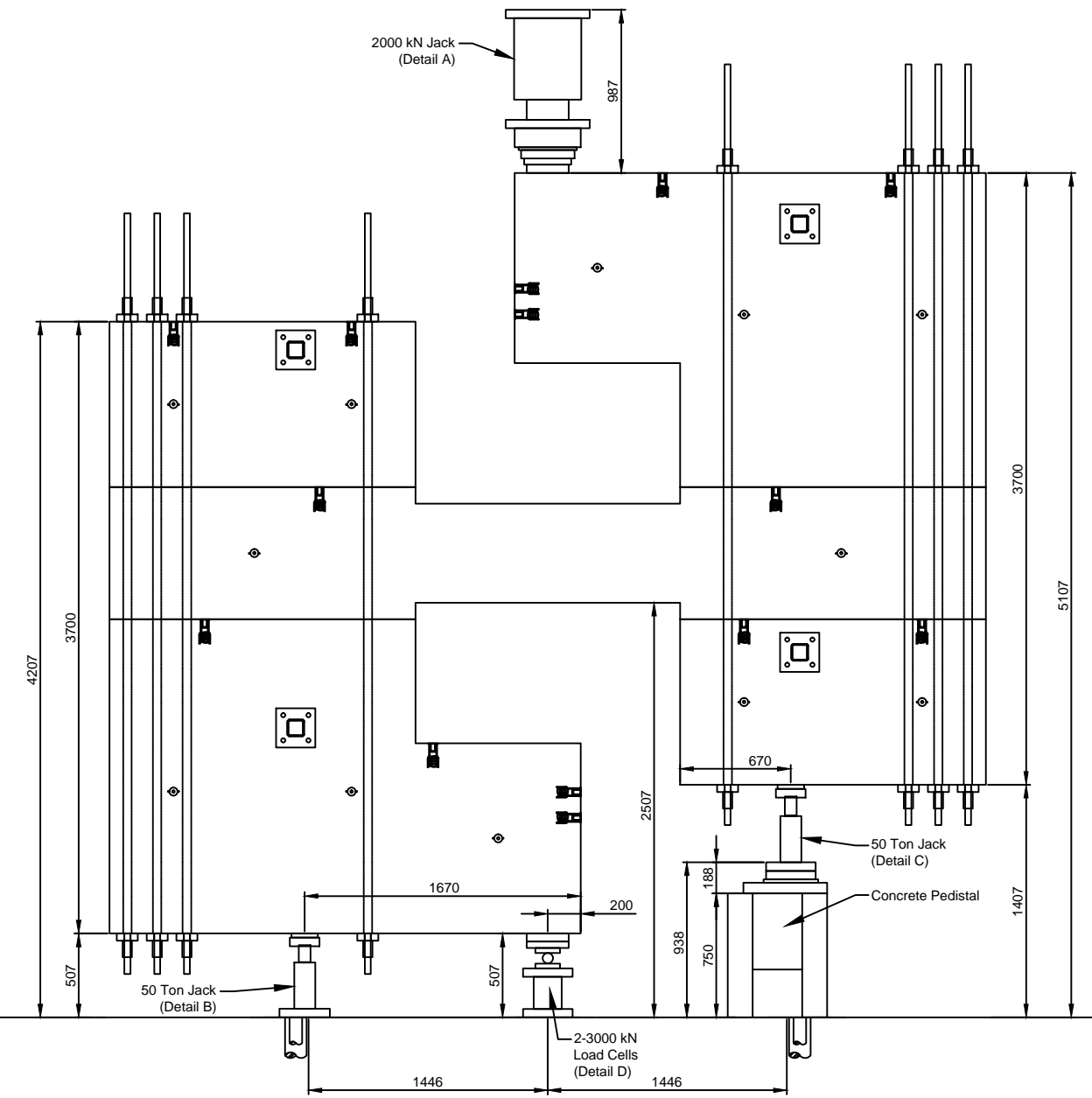


Scale = 1:40

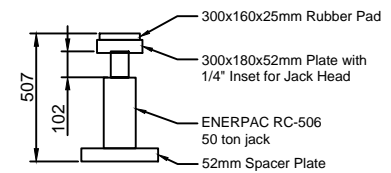
University of Toronto  
Department of Civil Engineering

Title:  
Meccano Frame Experimental  
Setup - Facing North

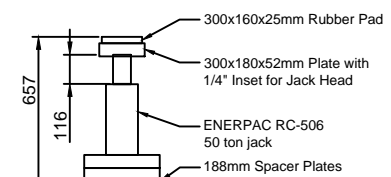
Date:	DWG No:	Designed:	Rev:
2016-01-15	016	AWF	11



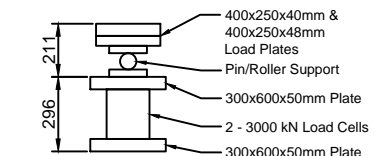
**DETAIL A**



**DETAIL B**



**DETAIL C**



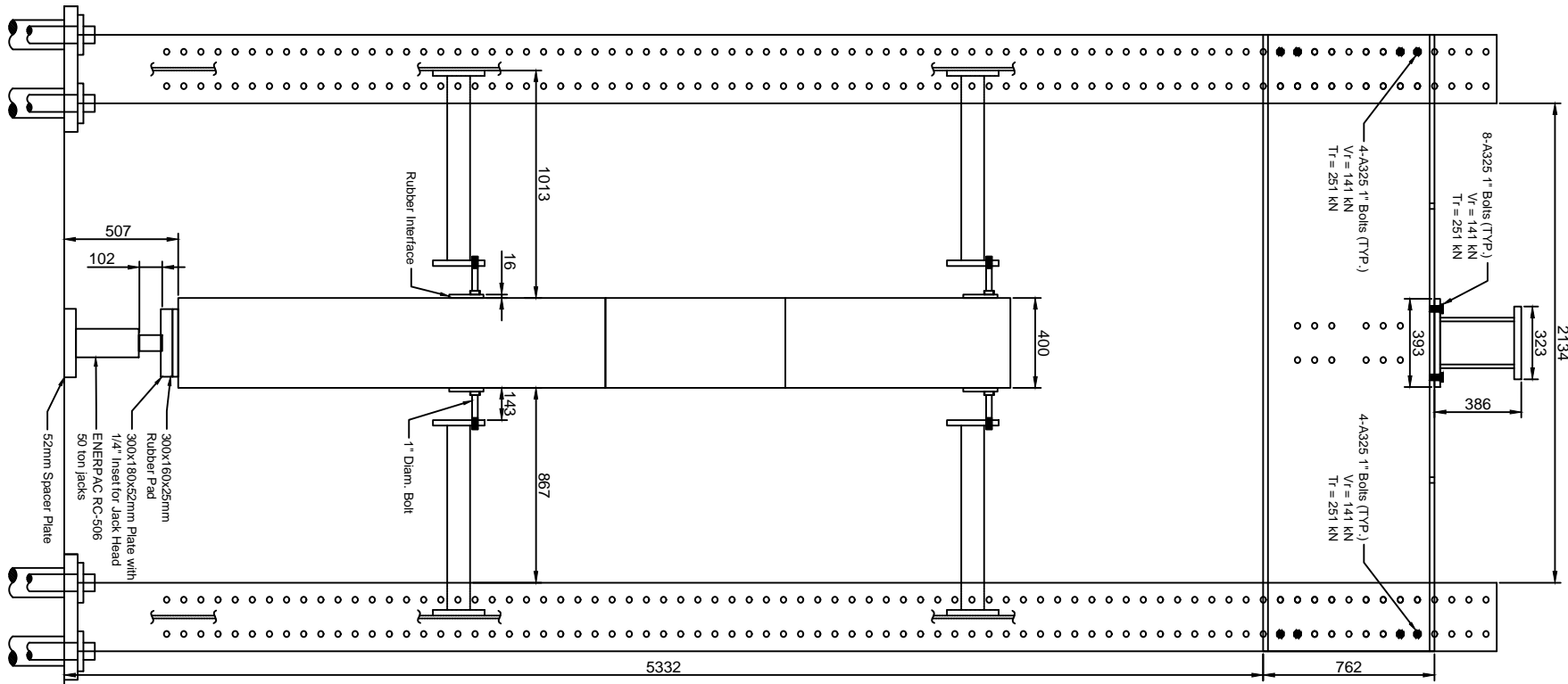
**DETAIL D**

Scale = 1:30

University of Toronto  
Department of Civil Engineering

Title:  
Experimental Setup without  
Frame - Facing North

Date:	DWG No:	Designed:	Rev:
2016-01-15	017	AWF	11

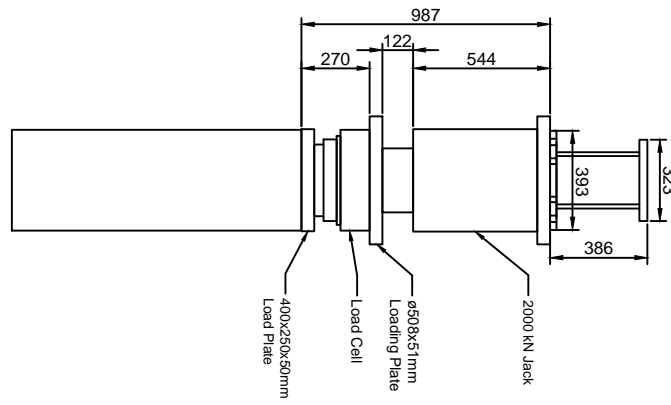
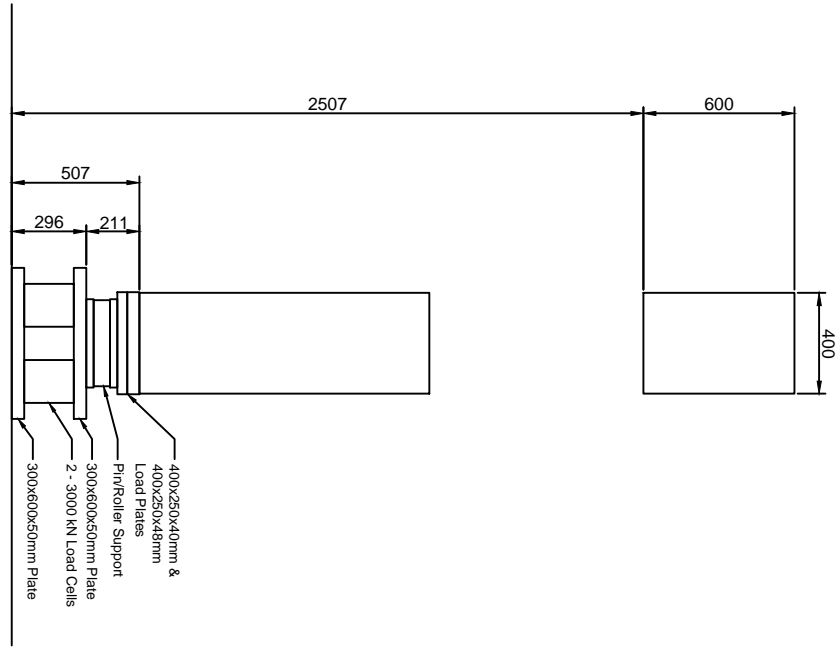


Scale = 1:30

University of Toronto  
Department of Civil Engineering

Title:  
Meccano Frame Experimental  
Setup - Facing East

Date:	DWG No:	Designed:	Rev:
2016-01-15	018	AWF	11

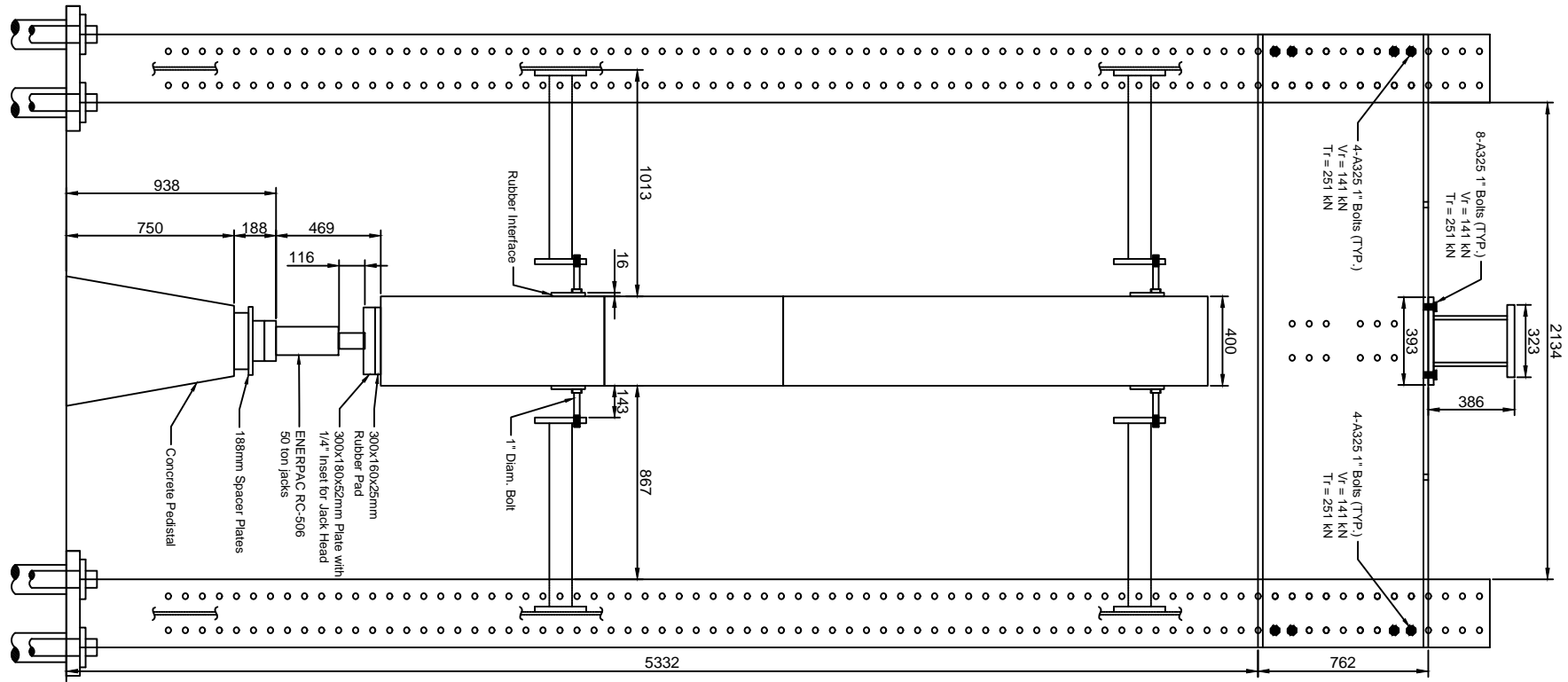


Scale = 1:30

University of Toronto  
Department of Civil Engineering

Title:  
Meccano Frame Experimental  
Setup - Loading Plane

Date:	DWG No:	Designed:	Rev:
2016-01-15	019	AWF	11

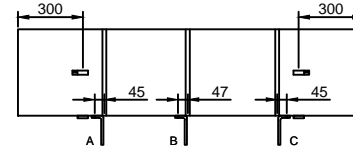
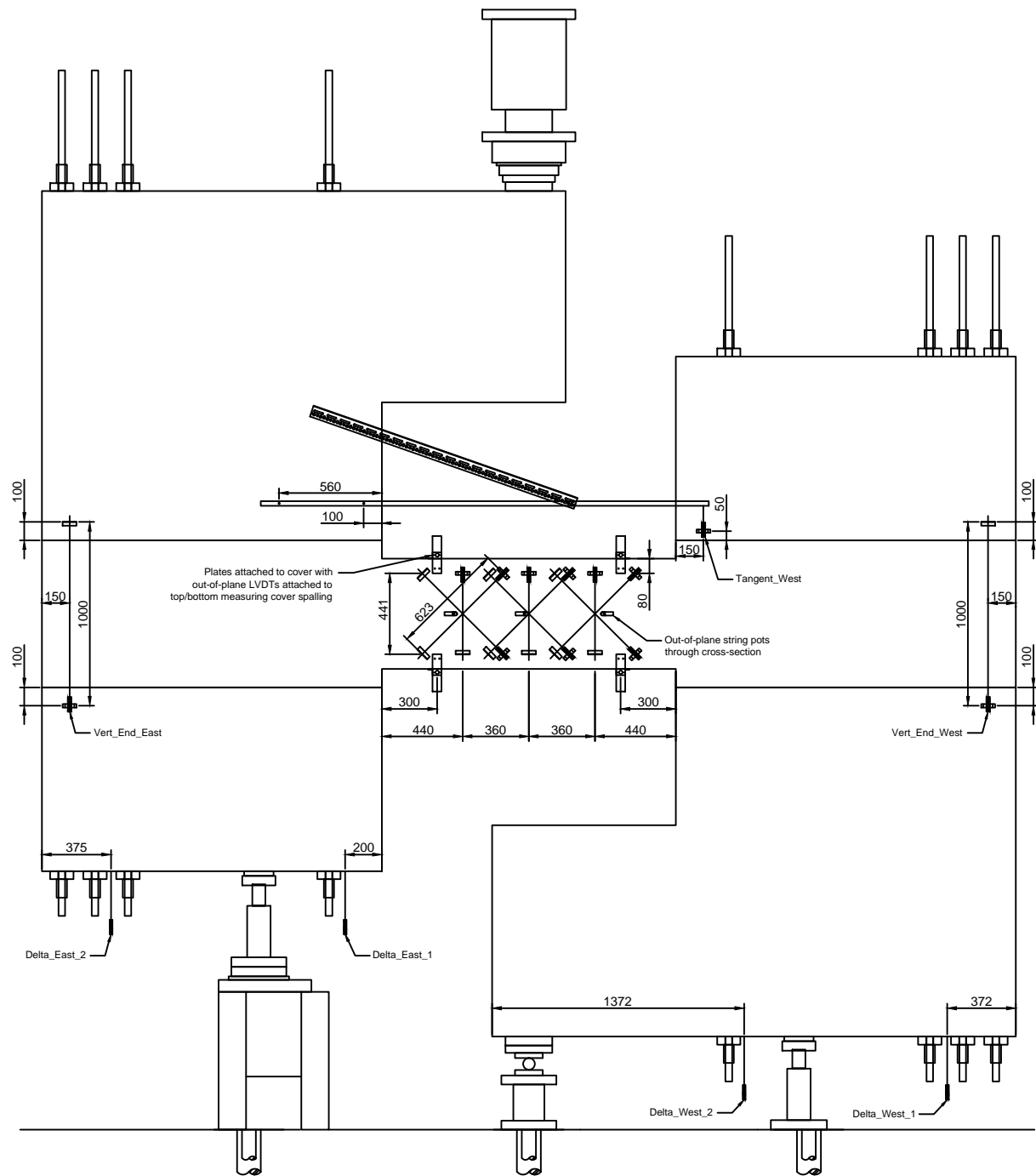


Scale = 1:30

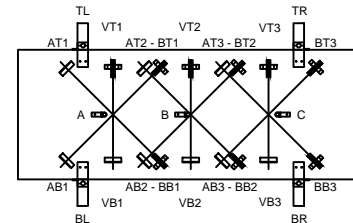
University of Toronto  
Department of Civil Engineering

Title:  
Meccano Frame Experimental  
Setup - Facing West

Date:	DWG No:	Designed:	Rev:
2016-01-15	020	AWF	11



TOP VIEW



LVDT MOUNT LABELS

VT1/VB1 = Vert\_dv\_East  
AB1/BT1 = Cross\_dv\_East\_1  
AT1/BB1 = Cross\_dv\_East\_2

VT2/VB2 = Vert\_Mid  
AB2/BT2 = Cross\_Mid\_1  
AT2/BB2 = Cross\_Mid\_2

VT3/VB3 = Vert\_dv\_West  
AB3/BT3 = Cross\_dv\_West\_1  
AT3/BB3 = Cross\_dv\_West\_2

TL = z\_Centre\_East  
TR = z\_Centre\_West  
BL = z\_Bot\_East  
BR = z\_Bot\_West

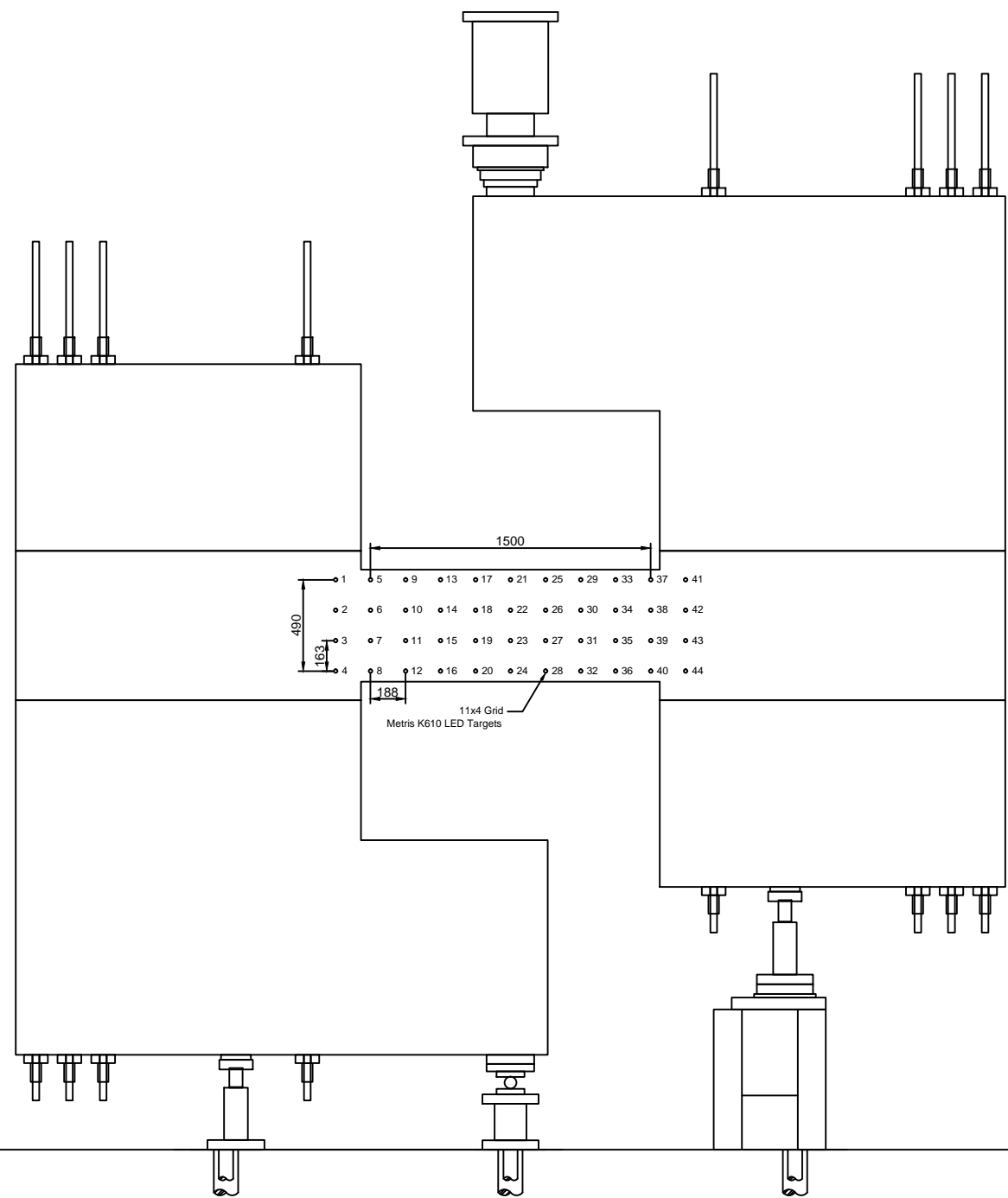
A = z\_Centre\_East  
B = z\_Centre\_Mid  
C = z\_Centre\_West

Scale = 1:35

University of Toronto  
Department of Civil Engineering

Title:  
**LVDT and Linear Pot  
Instrumentation Setup**

Date: 2016-01-15	DWG No: 021	Designed: AWF	Rev: 11
------------------	-------------	---------------	---------

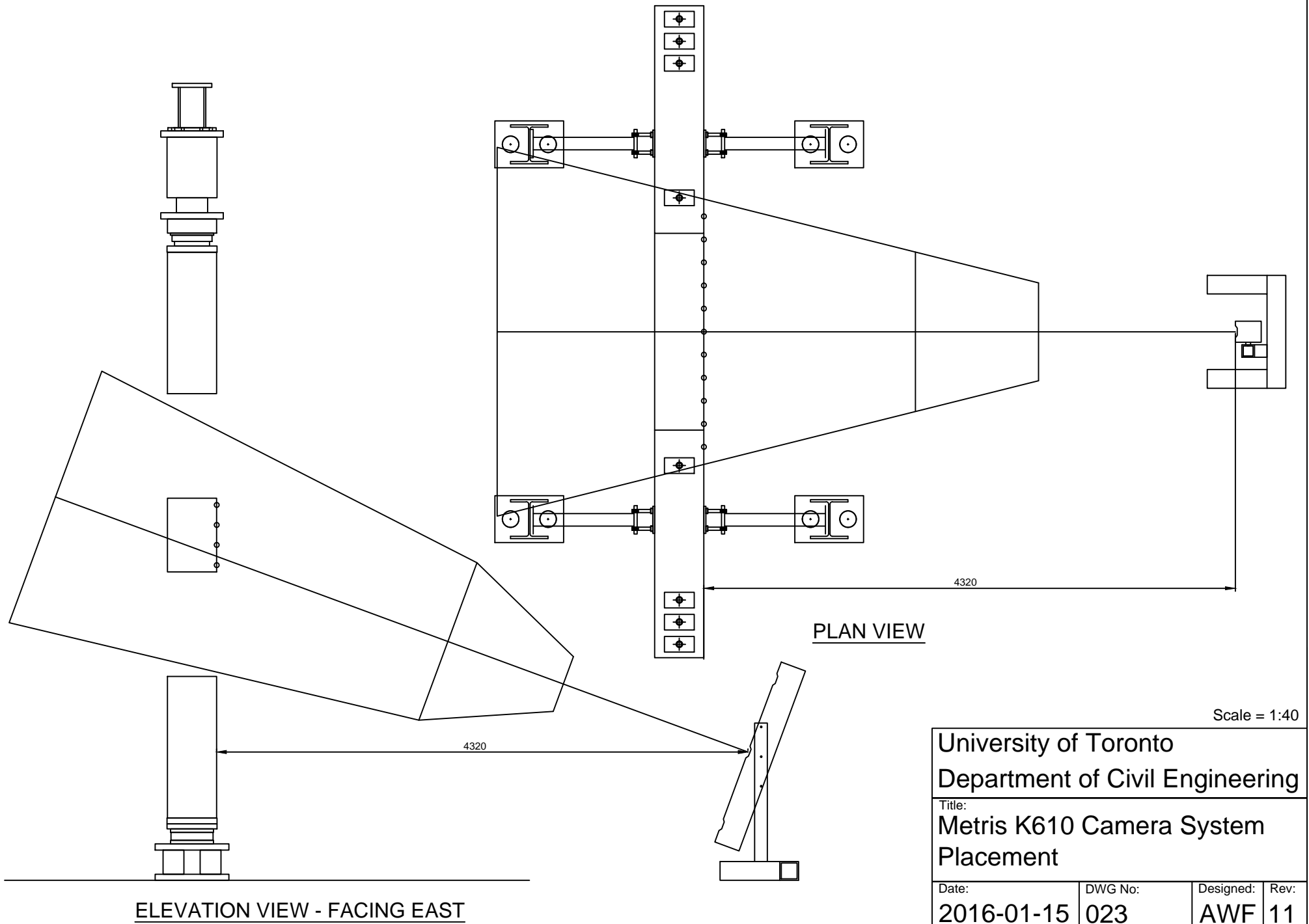


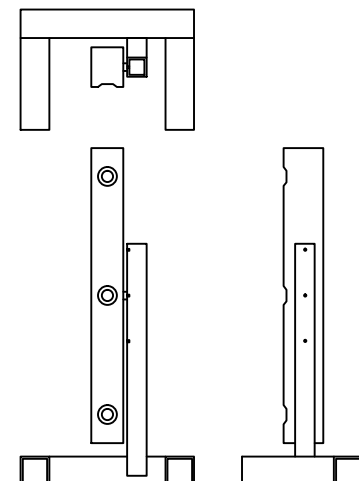
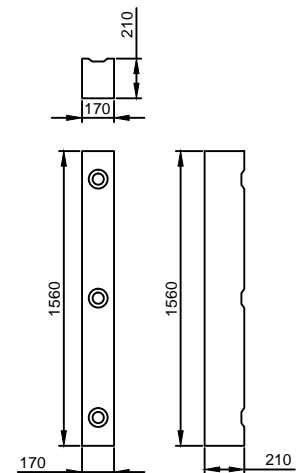
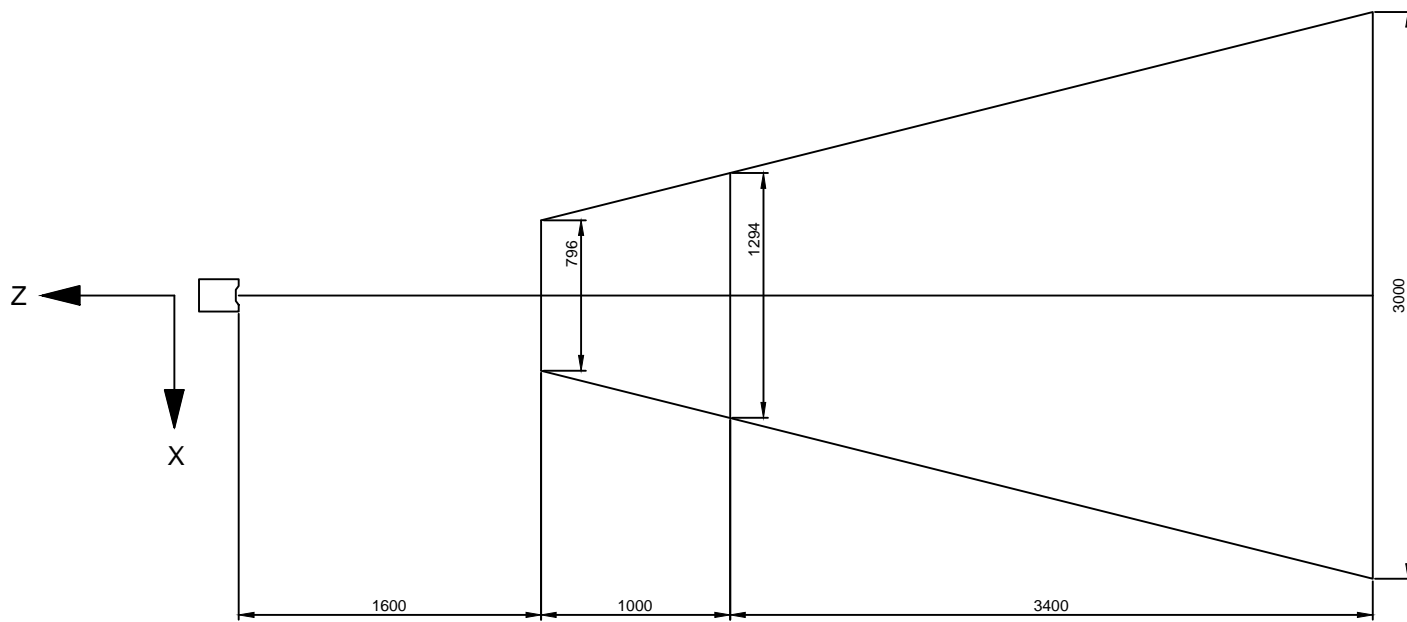
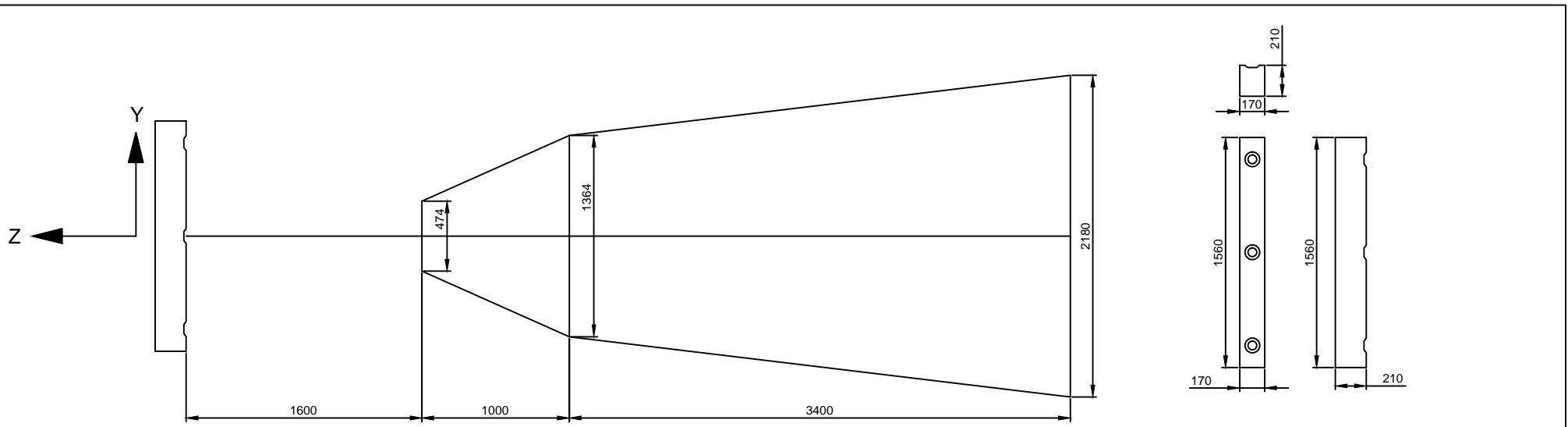
Scale = 1:35

University of Toronto  
Department of Civil Engineering

Title:  
LED Target Instrumentation  
Setup

Date: 2016-01-15	DWG No: 022	Designed: AWF	Rev: 11
---------------------	----------------	------------------	------------



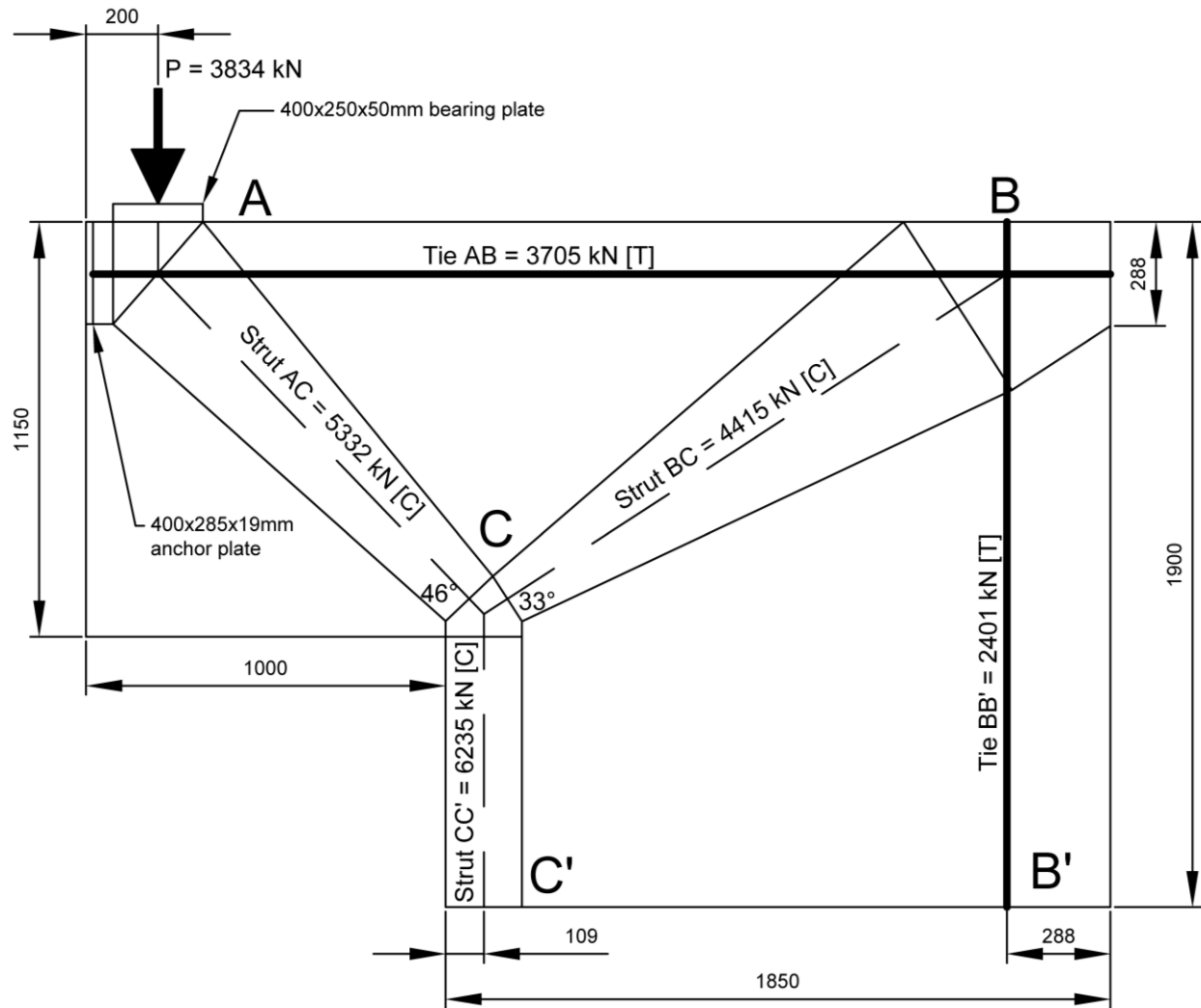


Scale = 1:40

University of Toronto Department of Civil Engineering			
Title: Metris K610 Camera System Field of View Dimensions			
Date:	DWG No:	Designed:	Rev:
2016-01-15	024	AWF	11

## Appendix B: Design Calculations for Test Assembly

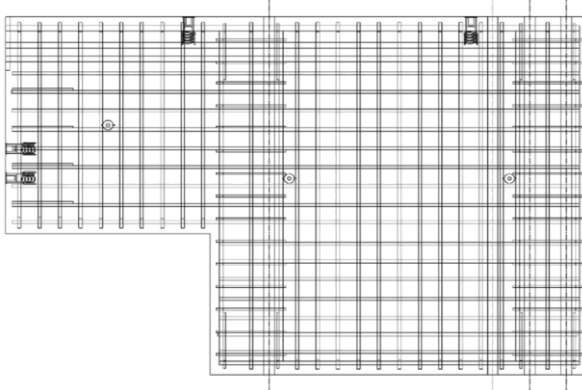
The cantilever shear wall components were designed using the CSA A23.3-04 Chapter 11.4: Strut and Tie Method [23]. The design load used was 1.5 times the flexural capacity of the strongest coupling beam, resulting in a design capacity of 3834 kN. Figure B illustrates the final strut and tie design. The full set of calculations are provided on pages 150 to 154.



## Cantilever Beam and Shear Wall Component Design

Designed According to CSA A23.3-04

The design was an iterative process, with the final calculated values presented below



### Material Properties

Concrete Properties:

Concrete Strength

$$f_c' = 83.8 \text{ MPa}$$

Steel Properties:

Steel Modulus of Elasticity

$$E = 200000 \text{ MPa}$$

30M Longitudinal Steel Yield Strength

$$f_y = 563 \text{ MPa}$$

15M Stirrup Steel Yield Strength

$$f_{y,v} = 422 \text{ MPa}$$

Area of 15M Shear Reinforcement (2 legs)

$$A_v = 400 \text{ mm}^2$$

36 mm DYWIDAG Post-Tension Bar Yield Strength (provided by DS)

$$f_{y,PT} = 960 \text{ MPa}$$

### Shear Wall Geometry

Length of the shear wall

$$l_{wall} = 1850 \text{ mm}$$

Length of loaded cantilever section

$$l_{cant} = 800 \text{ mm}$$

Height of cantilever beam

$$h_{cant} = 1150 \text{ mm}$$

Width of cantilever beam and shear wall

$$b_w = 400 \text{ mm}$$

Clear cover on top of cantilever beam

$$cc = 30 \text{ mm}$$

### Bearing Plate Geometry

Length of plate

$$l_{plate} = 250 \text{ mm}$$

Width of plate

$$b_{plate} = 400 \text{ mm}$$

Thickness of plate

$$t_{plate} = 50 \text{ mm}$$

### Design Loads

Load to cause flexural failure of strongest coupling beam

$$P_{max} = 2556 \text{ kN}$$

Design load with 1.5 safety factor

$$P_f = 3834 \text{ kN}$$

## STEP 1 - GEOMETRY OF STRUT CC'

### Notes

Compressive force at Node C' resists the overturning moment caused by load at Node A

The sum of moments about Node B was used to solve for the length of Node C'

A stress limit factor of 0.85 is applied to the concrete strength at Node C' (CCC Node)

### Calculations

Moment due to applied load at Node A taken about Node B

Length of Node C' (iterate variable to solve)

Width of Node C'

Concrete strength of Node C'

Compressive force at Node C'

Resisting moment at Node C' taken about Node B ( $M_r$  must equal  $M_f$ )

Location of Strut CC', taken as centerline of Node C'

$M_f$	9056	kNm
$l_C'$	219	mm
$b_w$	400	mm
$f_c'$	71.2	MPa
$C_{C'}$	6234	kN
$M_r$	9056	kNm
$x_{CC'}$	109	mm

OKAY

## STEP 2 - INITIAL GEOMETRY OF NODE C

### Notes

Initial location of Node C is based on the maximum lever arm between Node C and Tie AB

A stress limit factor of 0.85 is applied to the concrete strength at Node C (CCC Node)

A stress limit factor of 0.75 is applied to the concrete strength at Node A (CCT Node)

The depth of the tension tie reinforcement ABC is assumed to be a conservative 1.13 (0.85/0.75) times the depth of the compressive stress block at Node C

### Calculations

Moment due to applied load at Node A taken about Node C

Height of compression stress block at Node C (iterate variable to solve)

Width of Node C

Concrete strength of Node C

Compressive force at Node C

Lever arm between Node C and Tie AB

Resisting moment of Tie AB and Node C ( $M_r$  must equal  $M_f$ )

Location of Node C, taken as centerline of compression stress block

$M_f$	3487	kNm
$a$	120	mm
$b_w$	400	mm
$f_c'$	71.2	MPa
$C_c$	3410	kN
$jd$	1022	mm
$M_r$	3487	kNm
$x_c$	60	mm

OKAY

## STEP 3 - GEOMETRY OF TIE AB

### Notes

The tensile force in Tie AB must equal the compressive force resisted by Node C

A stress limit factor of 0.85 is applied to the concrete strength at Node C (CCC Node)

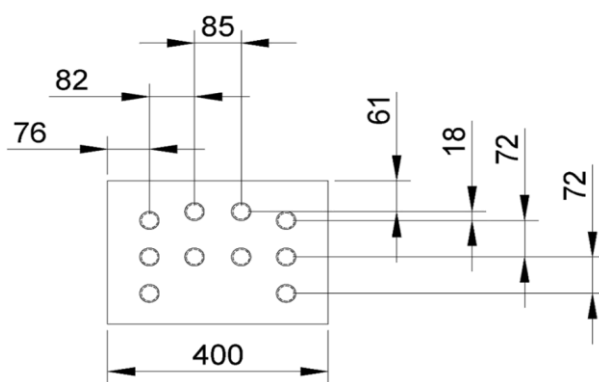
### Calculations

Tensile Force in Tie AB

Area of longitudinal steel required

Number of 30M bars required

The following reinforcement layout was selected, using 10 bars instead of 9:



$T_{AB}$	3410	kN
$A_s$	6058	mm <sup>2</sup>
$n_{bars}$	9	

Location of steel centroid, and depth of Tie AB

$x_{AB}$  144 mm

## STEP 4 - NEW GEOMETRY OF NODE C

### Notes

Height of compression stress block at Node C is recalculated with new location of Tie AB

A stress limit factor of 0.85 is applied to the concrete strength at Node C (CCC Node)

### Calculations

Assume lever arm between Node D and Tie ABC (iterate variable to solve)

Compressive force at Node D due to moment caused by applied load at Node A

Check individual bar stress in Tie AB ( $f_s \leq f_y$ )

Height of compression stress block at Node C

Check length of lever arm

Location of Node C, taken as centerline of compression stress block

$jd_{initial}$	941	mm
$C_c$	3705	kN
$f_{s,AB}$	529	MPa
$a$	130	mm
$jd_{final}$	941	mm
$x_c$	65	mm

## STEP 5 - GEOMETRY OF TIE BB'

### Notes

The tensile force in Tie BB' must resist the vertical compressive force in Strut BD

The location of the post-tensioning bars is based on predetermined spacing due to post-tensioning plates

Location of Tie BB' is at the centerline of the post-tensioning bars

### Calculations

Assume a location of Tie BB' measured from left edge of wall (iterate variable to solve)

Angle of strut BC

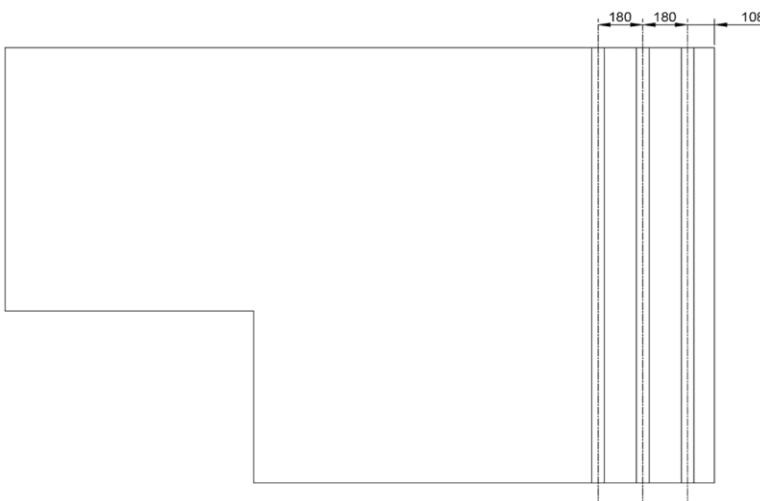
Tensile force in Tie BB'

Area of post-tensioning bars required

Number of post-tensioning bars required

The following post-tensioning layout was selected:

$x'_{BB',initial}$	1562	mm
$\vartheta_{BC}$	33	degrees
$T_{BB'}$	2401	kN
$A_{PT}$	2501	mm <sup>2</sup>
$n_{PT}$	3.00	



Check location of Tie BB'

Location of Tie BB' measured from right edge of shear wall

$x'_{BB',final}$	1562	mm	OKAY
$x_{BB'}$	288	mm	

## STEP 6 - STRUT AND TIE FORCES

### Design Notes

All forces are calculated using sum of forces at each node

### Calculations

Tensile force in Tie AB (previously calculated)

$T_{AB}$	3705	kN
$T_{BB'}$	2401	kN

Tensile force in Tie BB' (previously calculated)

Compressive force in Strut CC'

$C_{CC'}$	6235	kN
$\vartheta_{BC}$	33	degrees
$C_{BC}$	4415	kN

Angle of Strut BC (previously calculated)

Compressive force in Strut BC

Angle of Strut AC

$\vartheta_{AC}$	46	degrees
$C_{AC}$	5332	kN

Compressive force in Strut AC

## STEP 7 - NODE CAPACITY CHECKS

### Notes

Checks performed according to Clause 11.4.2.3

A stress limit factor of 0.85 is applied to the concrete strength at Node C (CCC Node)

A stress limit factor of 0.75 is applied to the concrete strength at Node A (CCT Node)

A stress limit factor of 0.65 is applied to the concrete strength at Node B (CTT Nodes)

### Calculations

#### *Node C Checks:*

Height of Node C

$h_a$	130	mm
$l_{b,CC'}$	219	mm
$l_{o,AC}$	187	mm
$l_{o,BC}$	155	mm
$C_{r,CC'}$	6234	kN
$C_{r,AC}$	5332	kN
$C_{r,BC}$	4415	kN

Length of Strut CC' into Node C

Length of Strut AC into Node C

Length of Strut BC into Node C

Compressive resistance of Strut CC' into Node C

Compressive resistance of combined Strut AC into Node C

Compressive resistance of Strut BC into Node C

#### *Node A Checks:*

Strain in Tie AB

$\varepsilon_{s,AB}$	0.003	mm/mm
$\varepsilon_{t,AC}$	0.007	mm/mm
$f_{cu,AC}$	42	MPa
$l_b$	250	mm
$h_a$	283	mm
$l_{o,AC}$	376	mm
$C_{r,AB}$	6046	kN
$C_{r,b}$	6285	kN
$C_{r,AC}$	6347	kN

Tensile strain in strut AC

Compressive strength of strut AC

Length of bearing plate

Height of Node A

Length of Strut AC into Node A

Compressive resistance of concrete in Tie AB

Compressive resistance of concrete under bearing plate

Compressive resistance of Strut AC

#### *Node B Checks:*

Strain in Tie AB

$\varepsilon_{s,AB}$	0.003	mm/mm
$\varepsilon_{t,BC}$	0.014	mm/mm
$f_{cu,BC}$	27	MPa
$l_b$	576	mm

Tensile strain in strut BC

Compressive strength of strut BC

Length of effective cross-section of Tie BB' into Node B

Height of Node B	$h_a$	288	mm
Length of Strut BC into Node B	$l_{a,BC}$	555	mm
Compressive resistance of concrete in Tie BB'	$C_{r,BB'}$	7561	kN OKAY
Compressive resistance of concrete in Tie AB	$C_{r,AB}$	6267	kN OKAY
Compressive resistance of Strut BC	$C_{r,BC}$	5936	kN OKAY

## STEP 9 - CODE DESIGN REQUIREMENTS

### Calculations

*Horizontal skin reinforcement in cantilever:*

Minimum area of 15M horizontal skin reinforcement (Clause 10.6.2)

$A_{s,min}$

368

mm<sup>2</sup>

Minimum spacing for 15M skin reinforcement

$s_{min}$

144

mm

Spacing of 15M horizontal crack reinforcement (previously selected)

$s$

100

mm

OKAY

*Development of longitudinal steel in cantilever:*

Required development length for 30M reinforcement (Clause 12.2.3)

$l_d$

1263

mm

Modified development length for excess 30M reinforcement (Clause 12.2.5)

$l_{d,mod}$

1093

mm

Length of 30M longitudinal bar of embedment

$l$

2480

mm

*Concentrated reinforcement in shear walls:*

Requirement to use four bars in two reinforcement layers (Clause 21.6.6.1)

$d_{b,max}$

40

mm

Maximum bar diameter to be used in shear wall (Clause 21.6.4.4)

$A_{s,min}$

740

mm<sup>2</sup>

Minimum area of concentrated reinforcement (Clause 21.6.6.4)

$A_{s,max}$

9600

mm<sup>2</sup>

Maximum area of concentrated reinforcement (Clause 21.6.4.3)

$A_s$

1200

mm<sup>2</sup>

OKAY

Area of 4-20M bars for concentrated reinforcement

$s_{min}$

117

mm

Minimum spacing of 10M buckling prevention ties (Clause 21.6.6.9)

$s$

120

mm

OKAY

Spacing of 10M buckling prevention ties

*Distributed shear wall reinforcement:*

Minimum spacing of 15M distributed reinforcement (Clause 21.6.5.1)

$s_{min}$

400

mm

Spacing of 15M distributed reinforcement

$s$

100

mm

OKAY

Two sheets of reinforcement required due to Clause 21.6.5.3

*Development of horizontal distributed reinforcement in shear wall:*

Confinement length into concentrated 20M reinforcement

$l_{confine}$

340

mm

Development length (Clause 21.6.5.5 & Clause 12.2.3)

$l_d$

303

mm

OKAY

*Development of coupling beam longitudinal reinforcement:*

Required development length for bundled 30M bars (Clause 12.2.3)

$l_d$

1389

mm

Length of 30M longitudinal bar of embedment

$l$

1805

mm

OKAY

## Appendix C: Material Test Data

### C.1 Steel Coupon Test Data

Three coupon tests were performed for all four reinforcing bar sizes in the University of Toronto Structures Laboratory. The coupon samples were each cut from a different bar length to ensure an adequate representation of data. Figure C-1 shows a coupon test being performed in an MTS universal testing machine. Figure C-2 presents all of the coupon test data for each bar size. The tables in Figure C-2 highlight the properties for the coupon tests including the stress,  $f_y$ , at which yielding occurred, the strain,  $\varepsilon_{sh}$ , at which strain hardening commenced, the maximum stress,  $f_u$ , which the coupon reached and associated strain,  $\varepsilon_u$ .

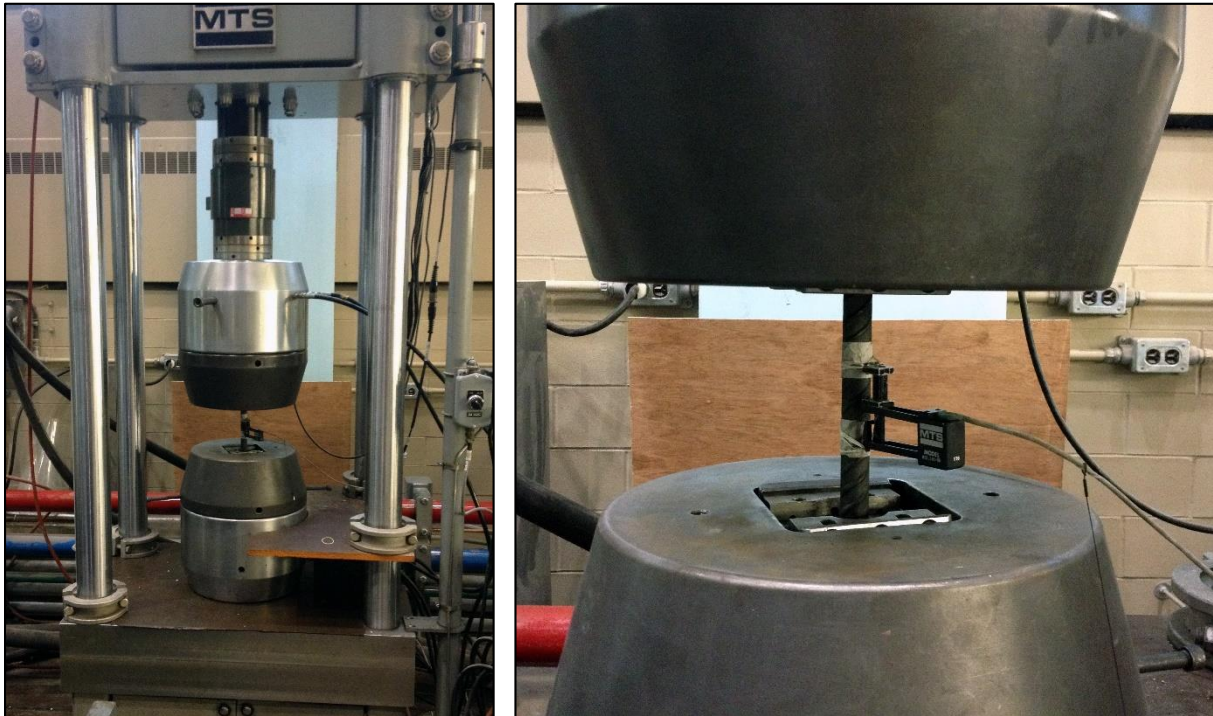
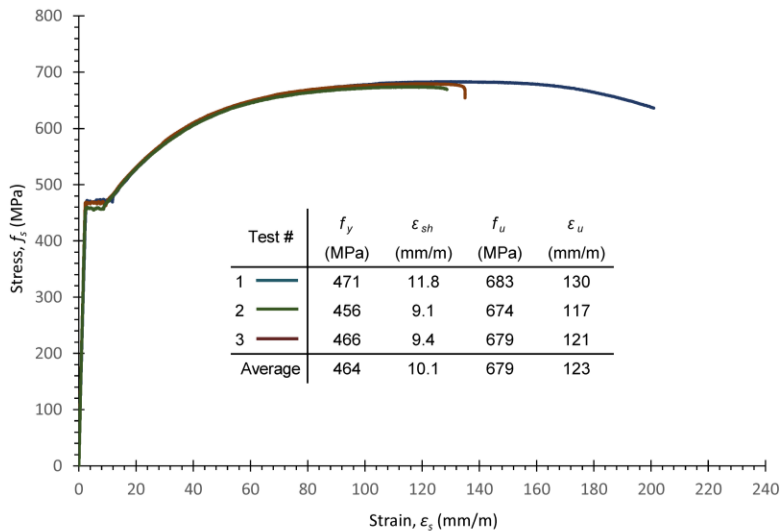
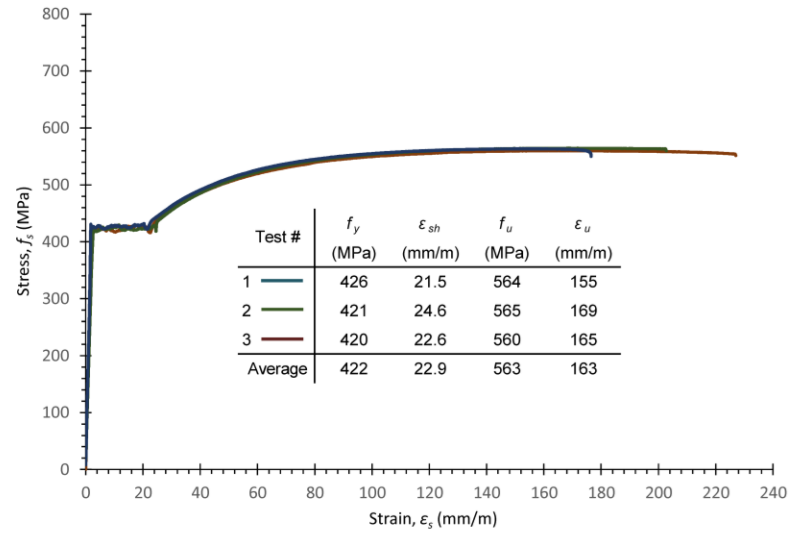


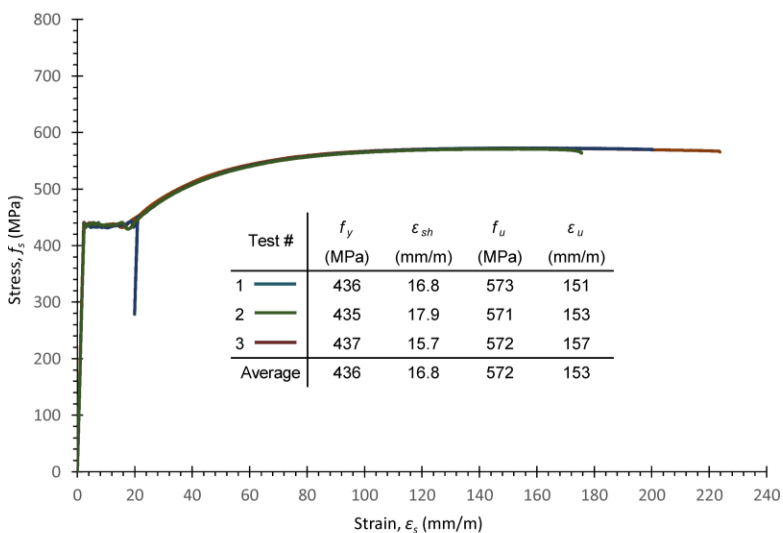
Figure C-1: 20M Coupon Test in 1000 kN MTS Universal Testing Machine



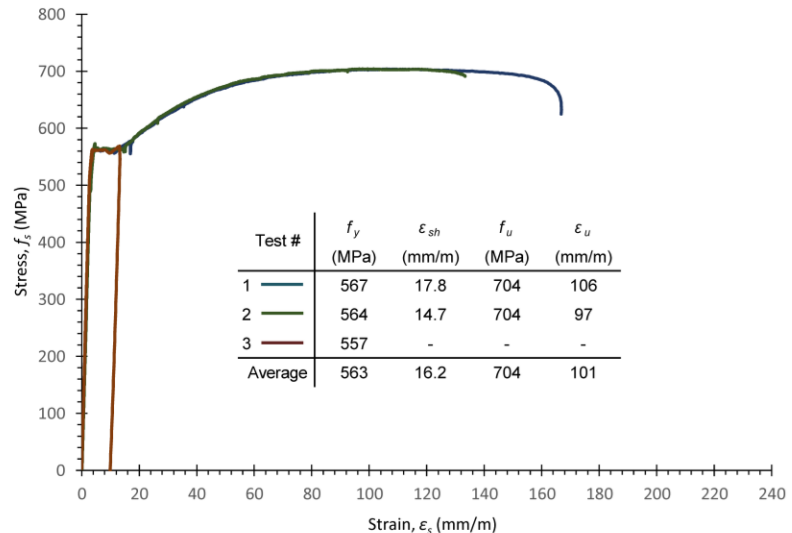
10M Coupon Test Data



15M Coupon Test Data



20M Coupon Test Data



30M Coupon Test Data

Figure C-2: Coupon Test Stress-Strain Plots

The third coupon test for the 30M reinforcing bars was only loaded to its yield capacity due to a malfunction with the MTS machine. Another coupon test was not performed in its place due to a limited number of coupon samples for the 30M bars.

Coupon samples were not tested in the structures laboratory for the 36 mm DYWIDAG THREADBARS used to post-tension the test assembly together. However, the mill certificate for the batch of steel was provided by DSI. The bars have an average yield strength,  $f_y$ , of 941 MPa and ultimate strength,  $f_u$ , of 1126 MPa. The full mill certificate is presented on pages 158 and 159.



**GERDAU**

US-ML-ST PAUL  
1678 RED ROCK ROAD  
SAINT PAUL, MN 55119  
USA

CERTIFIED MATERIAL TEST REPORT

Page 1/2

CUSTOMER SHIP TO DSI EASTERN CANADA 57 CARDICO DR GORMLEY, ON L0H 1G0 Canada	CUSTOMER BILL TO DYWIDAG SYSTEMS INTL USA INC 320 MARMON DR BOLINGBROOK IL 60440-3078 USA	GRADE D150	SHAPE / SIZE Stretched Thread Bar / 36MM
		LENGTH 60'00"	WEIGHT 6.023 LB
SALES ORDER 390646/000010	CUSTOMER MATERIAL N° 1332-000003429	SPECIFICATION / DATE or REVISION 1-ASTM A722/A722M-07 TYPE II 2-DYG D150 - CONFORMS TO DSI 3-USA / 4-INC.	

CUSTOMER PURCHASE ORDER NUMBER 207138367597		BILL OF LADING 1332-000003429	DATE 05/13/2013

CHEMICAL COMPOSITION													
C%	Mn%	P%	S%	Si%	Ch%	Ni%	Cr%	Mo%	Sn%	V%	Nb%	N%	
0.50	1.46	0.009	0.012	0.43	0.21	0.43	0.24	0.024	0.029	0.055	0.003	0.0214	

MECHANICAL PROPERTIES													
BrutTest	Elong.	GL Inch	UTS PkLd	UTS Psi	YS Psi								
OK	\$40	13.750	259	163500	139500								
	\$30	13.750	256	161500	132500								
	9.10	13.750	260	165000	137600								

MECHANICAL PROPERTIES													
YS Load Kib	221	210	218	215	214	213	212	211	210	209	208	207	206

GEOMETRIC CHARACTERISTICS													
CSA	RR												
Squa													
1.585	18.71												
1.586													
1.585													

HARDENABILITY													
DIN 5125	Inch												

The above figures are certified chemical and physical test records as contained in the permanent records of company. This material, including the billets, was melted and manufactured in the USA. We certify that these data are correct and in compliance with specified requirements. CMTR complies with EN 10204 3.1.

Bhaskar Yalamanchili

BHASKAR YALAMANCHILI  
QUALITY DIRECTOR

Alea Brandenburg  
ALEA BRANDENBURG  
QUALITY ASSURANCE MGR.



US-ML-ST PAUL  
1678 RED ROCK ROAD  
SAINT PAUL, MN 55119  
USA

## CERTIFIED MATERIAL TEST REPORT

CUSTOMER SHIP TO  DSI EASTERN CANADA 37 CARDICO DR GORMLEY,ON L0H 1G0 Canada	CUSTOMER BILL TO  DYWIDAG SYSTEMS INTL USA INC 520 MARMON DR BOLINGBROOK IL 60440-3078 USA	GRADE D150	SHAPE / SIZE Stretched Thread Bar / 36MM
		LENGTH 60'00"	WEIGHT 6.028 LB
SALES ORDER 390646/000010		CUSTOMER MATERIAL N° 1332-0000003429	SPECIFICATION / DATE or REVISION 1-ASTM A722/A722M-07 TYPE II 2-DYG D150 - CONFORMS TO DSI 3-USA / 4-INC.
CUSTOMER PURCHASE ORDER NUMBER 207138/367697	BILL OF LADING 1332-0000003429	DATE 05/13/2013	

## COMMENTS / NOTES

Material 100% melted and rolled in the USA. Manufacturing processes for this steel, which may include scrap melted in an electric arc furnace and hot rolling, have been performed at Gerdaud St. Paul Mill, 1678 Red Rock Rd, St. Paul, Minnesota, USA. All products produced from strand cast billets. Silicon killed (deoxidized) steel. No weld repairment performed. Steel not exposed to mercury or any liquid alloy which is liquid at ambient temperatures during processing or while in Gerdaud St. Paul Mill's possession. Any Modification to this certification as provided by Gerdaud # St. Paul Mill without the expressed written consent of Gerdaud St. Paul Mill negates the validity of this test report. This report shall not be reproduced except in full, without the expressed written consent of Gerdaud St. Paul Mill. Gerdaud St. Paul Mill is not responsible for the inability of this material to meet specific applications.

Roll Batch 6215046708 roll dat 4/24/2013

D150 Melted and MFG in the USA

D150-Conforms to DSI, USA, INC. Spec #2, Rev 6, 10/21/02

Steel not exposed to mercury, no weld repairment performed.

The above figures are certified chemical and physical test records as contained in the permanent records of company. This material, including the billets, was melted and manufactured in the USA. We certify that these data are correct and in compliance with specified requirements. CMTR complies with EN 10204 3.1.

BHASKAR YALAMANCHILI  
QUALITY DIRECTOR

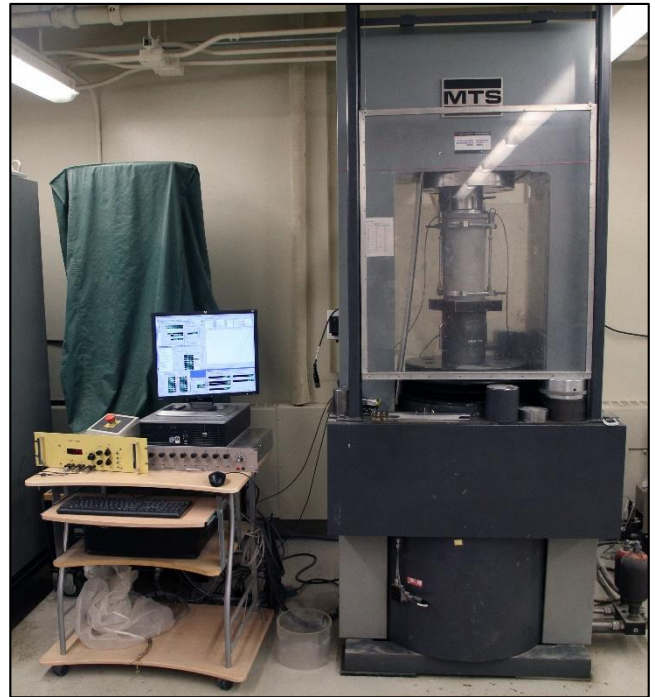
ALEA BRANDENBURG  
QUALITY ASSURANCE MGR.

## C.2 Concrete Cylinder Test Data

All of the 6-inch diameter concrete cylinders were tested in the University of Toronto Structures Laboratory. Cylinder tests were performed periodically during the 28-day curing period in order to obtain the progression of the cylinder strength gain. The Forney testing machine was used for this purpose, shown in Figure C-3a. The full stress-strain curves for the 28-day and test-day cylinders were obtained using an MTS Universal Testing Machine and LVDT instrumentation, shown in Figure C-3b.



a) Cylinder test using the Forney test machine



b) Cylinder test using the MTS universal test machine

*Figure C-3: Cylinder Tests in University of Toronto Structures Laboratory*

Three cylinders were tested for each day in order to ensure a representative data set. The full data set of the concrete strengths is presented in Figure C-4 and Figure C-5, while the full data set for the stress-strain curves is presented in Figure C-6 and Figure C-7.

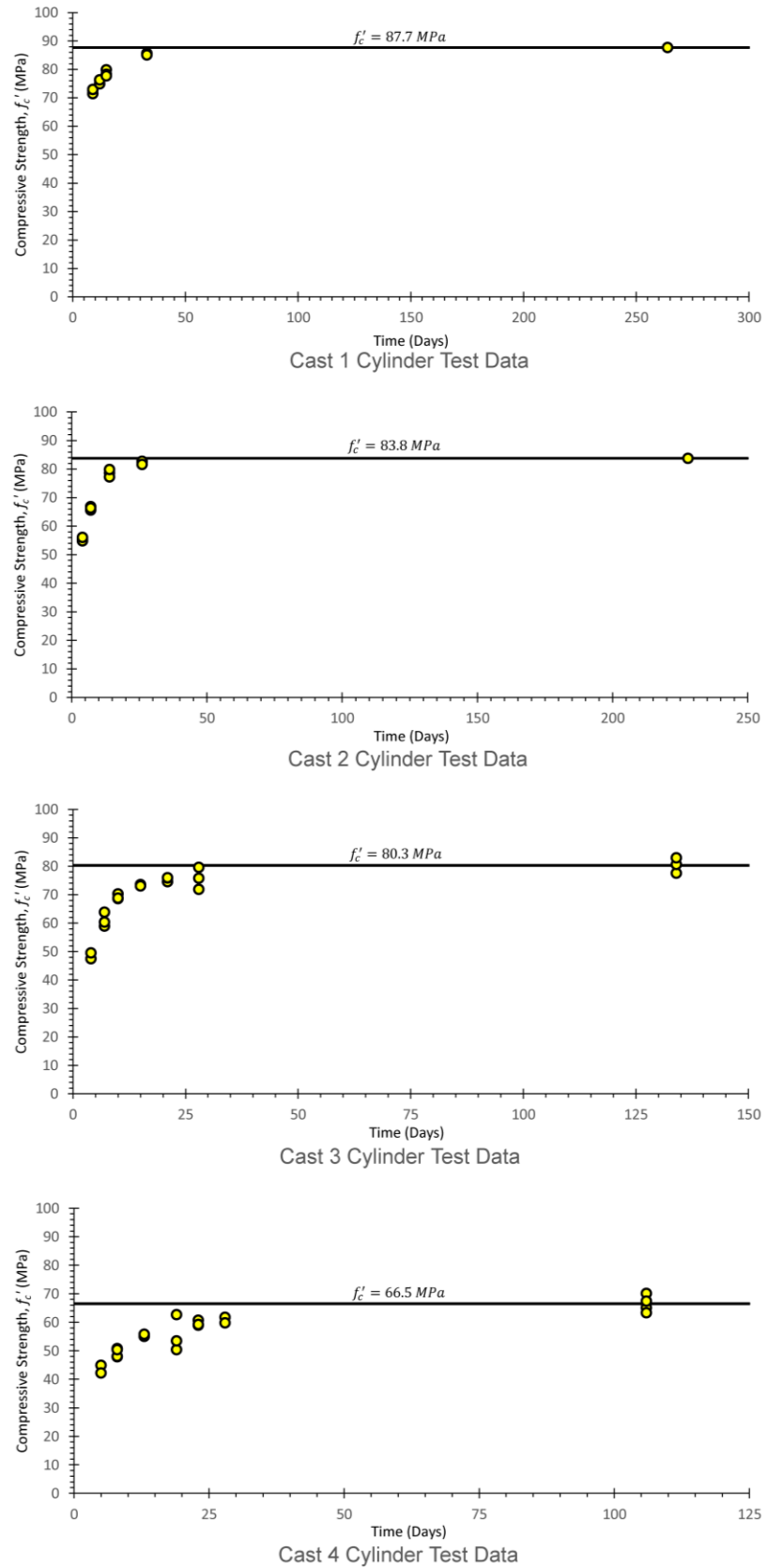


Figure C-4: Concrete Cylinder Strength Gain for all Casts

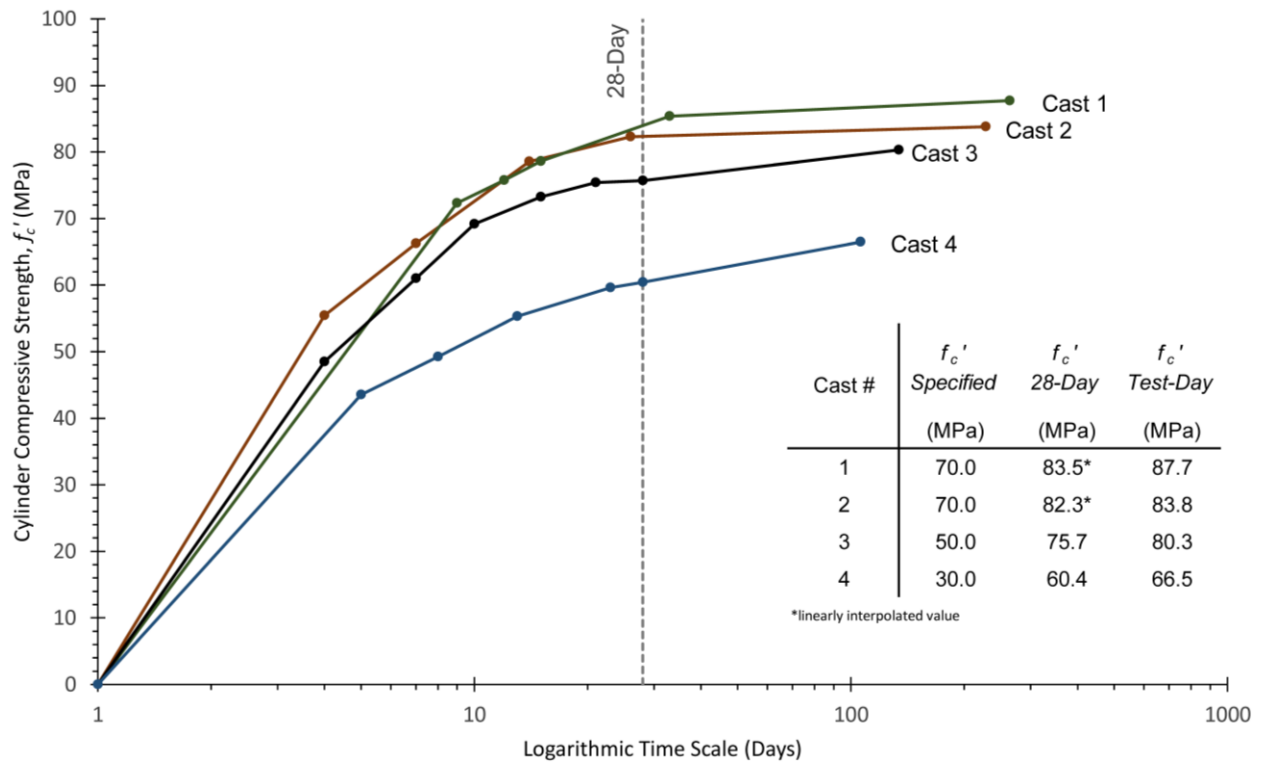
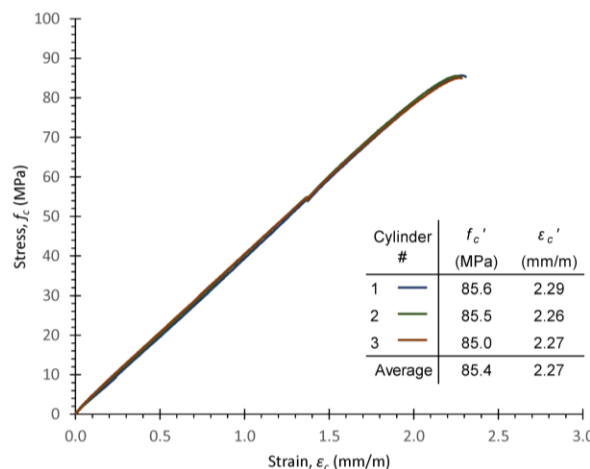
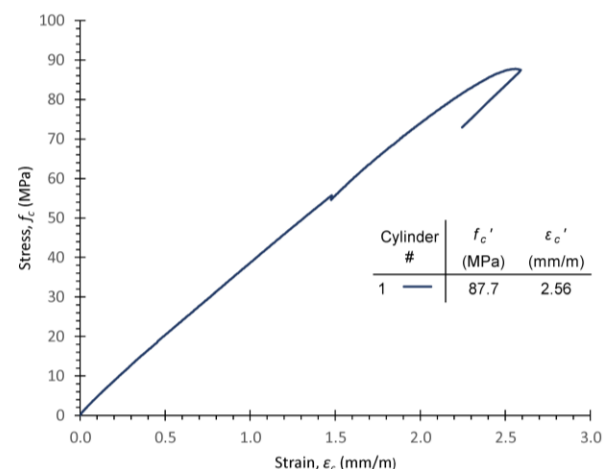


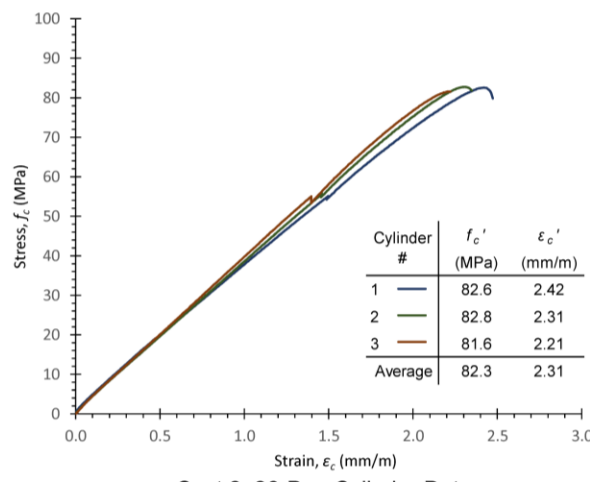
Figure C-5: Average Concrete Cylinder Strength Gain Plotted on Logarithmic Time Scale



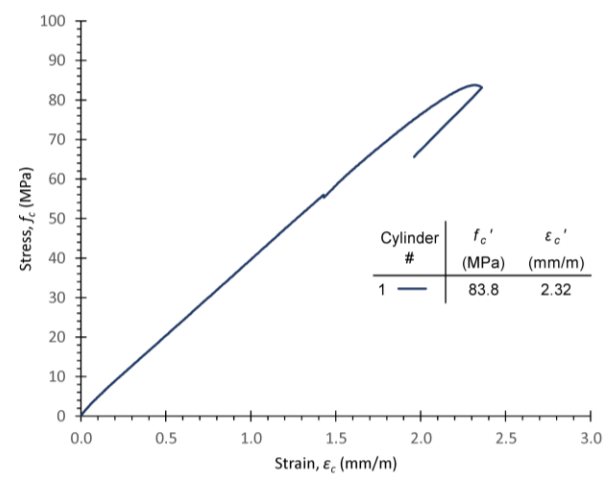
Cast 1: 33-Day Cylinder Data



Cast 1: 264-Day Cylinder Data

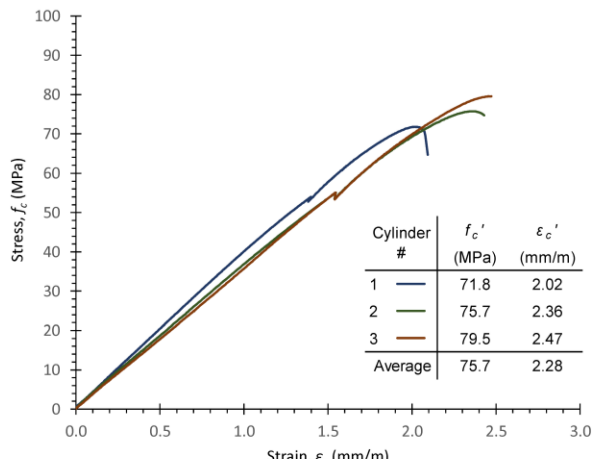


Cast 2: 26-Day Cylinder Data

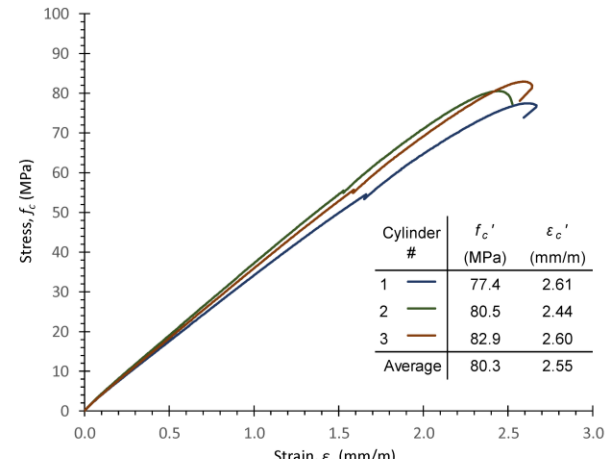


Cast 2: 228-Day Cylinder Data

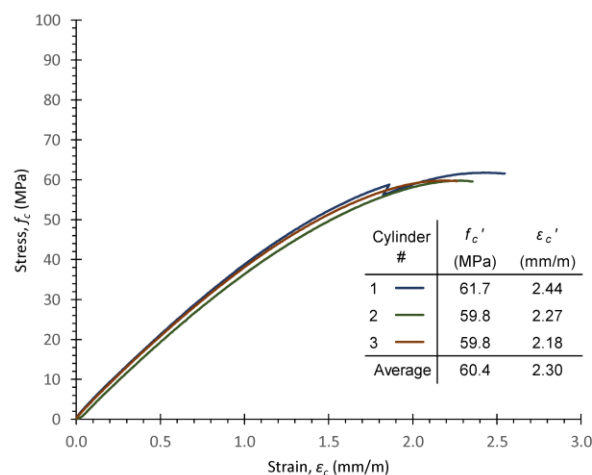
Figure C-5: Concrete Cylinder Stress-Strain Data for CBF1 and CBF2



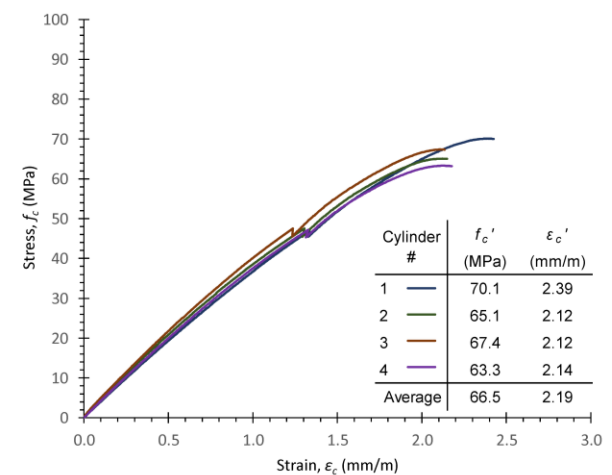
Cast 3: 28-Day Cylinder Data



Cast 3: 134-Day Cylinder Data



Cast 4: 28-Day Cylinder Data



Cast 4: 106-Day Cylinder Data

Figure C-6: Concrete Cylinder Stress-Strain Data for CBF3 and CBF4

## Appendix D: Photographs of Specimens

Photographs from each load stage for all four tests are presented in this appendix. Each load stage photo also includes the maximum widths for the flexural ( $w_{M,max}$ ) and shear ( $w_{V,max}$ ) cracks based on manual measurements during the load stage. Cracks were measured with an accuracy of 0.05 mm.

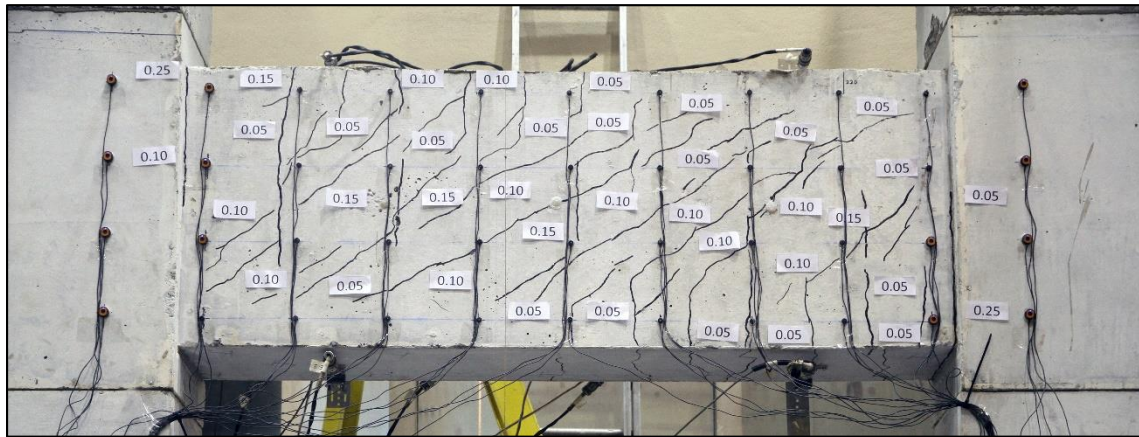
### D.1 Photographs of Specimen CBF1



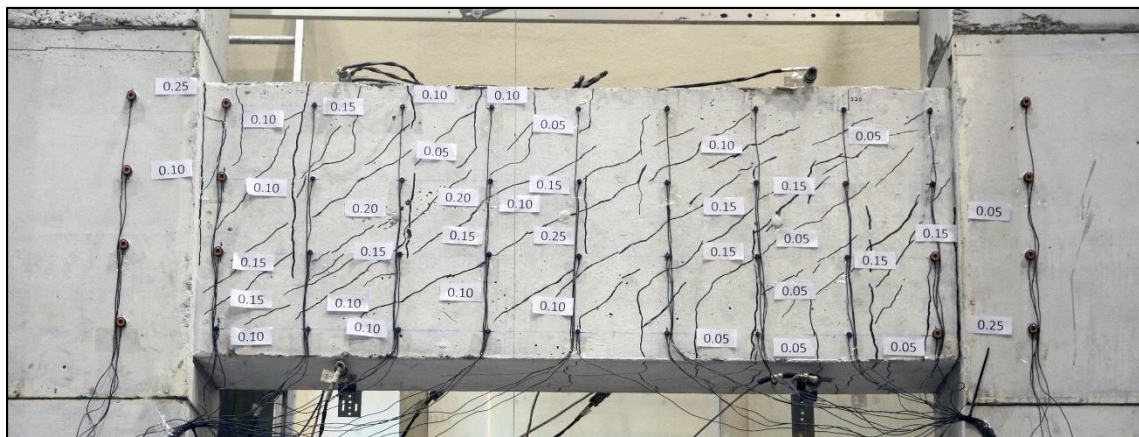
Figure D-1: South Face of CBF1 at Load Stage 1  
 $V = 253 \text{ kN}$   $w_{M,max} = 0.05 \text{ mm}$   $w_{V,max} = 0.05 \text{ mm}$



Figure D-2: South Face of CBF1 at Load Stage 2  
 $V = 502 \text{ kN}$   $w_{M,max} = 0.15 \text{ mm}$   $w_{V,max} = 0.10 \text{ mm}$



*Figure D-3: South Face of CBF1 at Load Stage 3*  
 $V = 1003 \text{ kN}$   $w_{M,\text{max}} = 0.25 \text{ mm}$   $w_{V,\text{max}} = 0.15 \text{ mm}$



*Figure D-4: South Face of CBF1 at Load Stage 4*  
 $V = 1501 \text{ kN}$   $w_{M,\text{max}} = 0.25 \text{ mm}$   $w_{V,\text{max}} = 0.20 \text{ mm}$

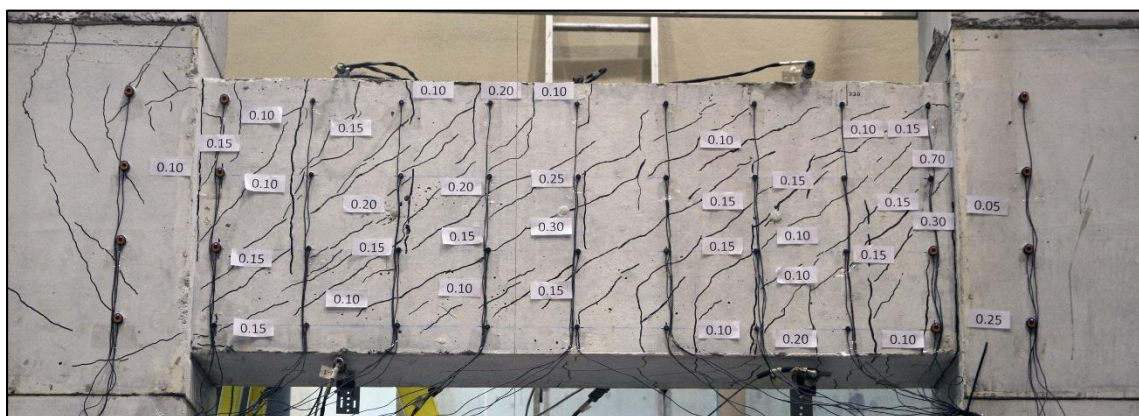


*Figure D-5: South Face of CBF1 at Load Stage 5*  
 $V = 1751 \text{ kN}$   $w_{M,\text{max}} = 0.25 \text{ mm}$   $w_{V,\text{max}} = 0.30 \text{ mm}$

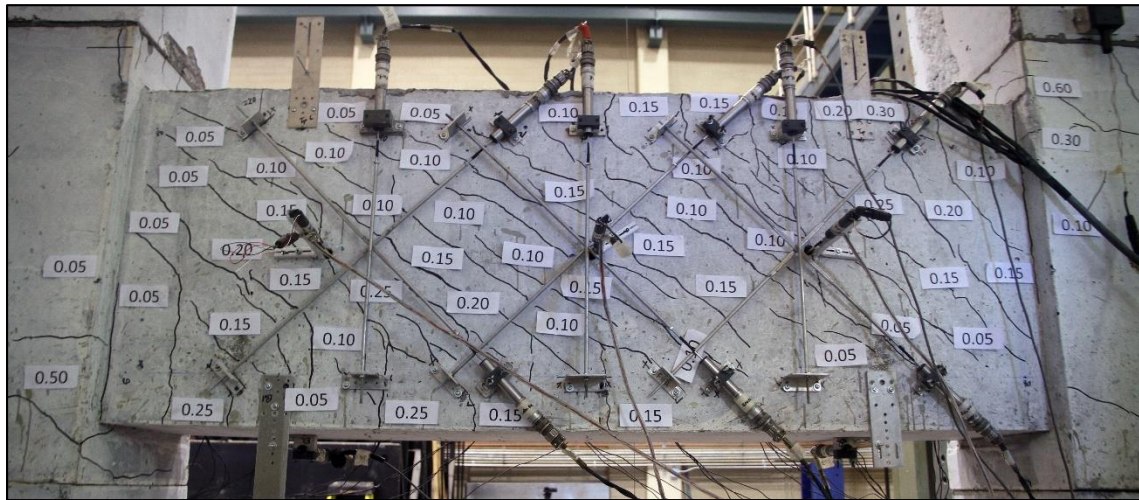


Figure D-6: North Face of CBF1 at Load Stage 5  
 $V = 1751 \text{ kN}$   $w_{M,max} = 0.60 \text{ mm}$   $w_{V,max} = 0.25 \text{ mm}$

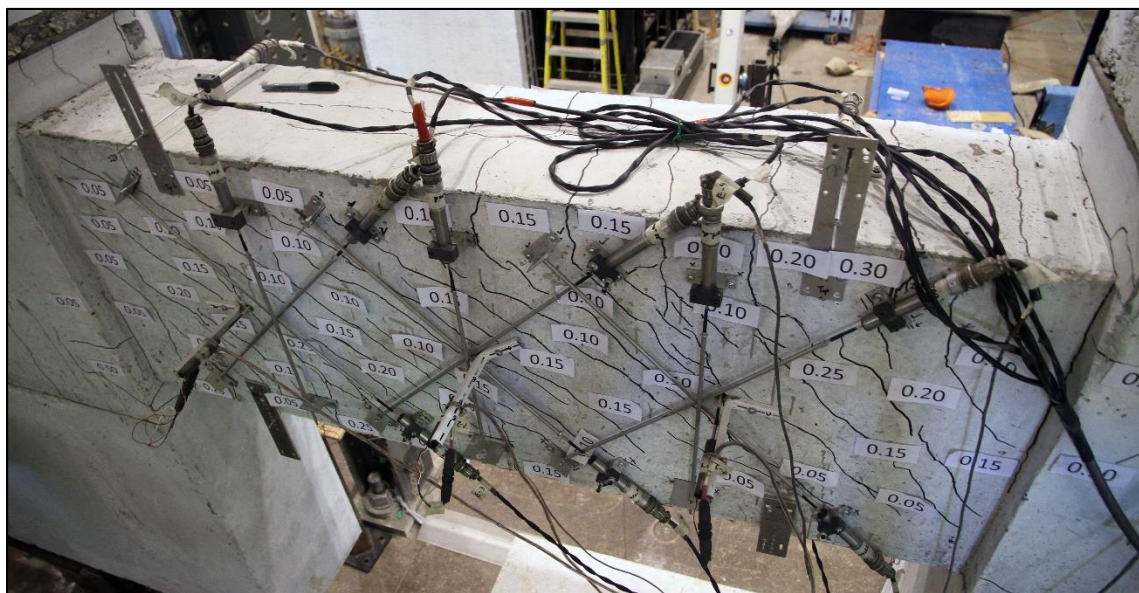


Figure D-7: Top Face of CBF1 at Load Stage 5  
 $V = 1751 \text{ kN}$

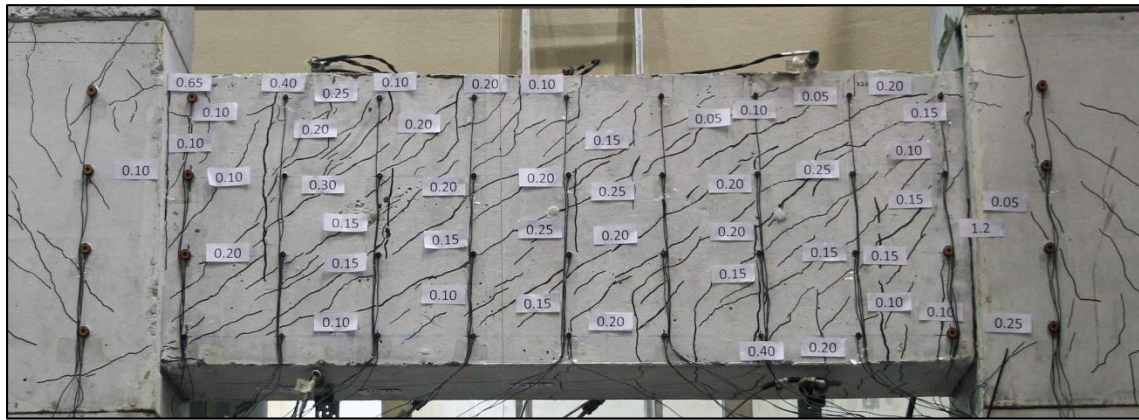


Figure D-8: South Face of CBF1 at Load Stage 6  
 $V = 1875 \text{ kN}$   $w_{M,max} = 0.65 \text{ mm}$   $w_{V,max} = 0.30 \text{ mm}$

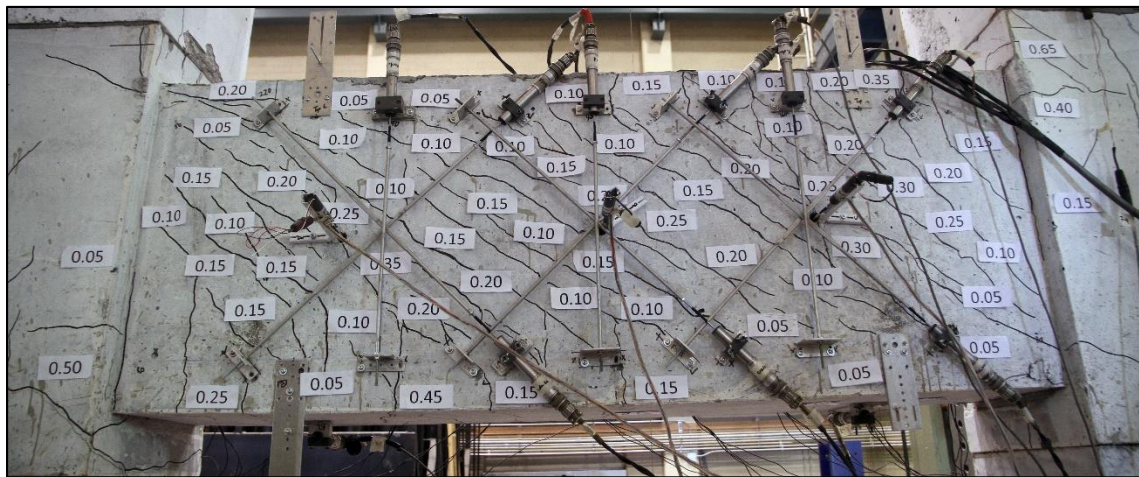


Figure D-9: North Face of CBF1 at Load Stage 6  
 $V = 1875 \text{ kN}$   $w_{M,max} = 0.65 \text{ mm}$   $w_{V,max} = 0.35 \text{ mm}$

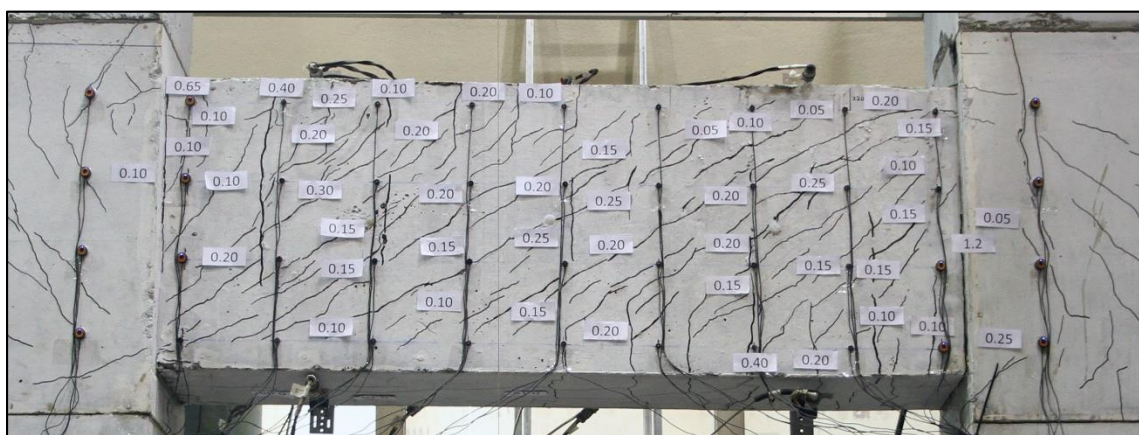


Figure D-10: South Face of CBF1 at Peak Load  
 $V_{peak} = 1918 \text{ kN}$



Figure D-11: South Face of CBF1 during Post-Peak at 90% of Load  
 $V = 1726 \text{ kN}$



Figure D-12: South Face of CBF1 during Post-Peak at 80% of Load  
 $V = 1534 \text{ kN}$



Figure D-13: South Face of CBF1 at End of Post Peak  
 $V = 1217 \text{ kN}$

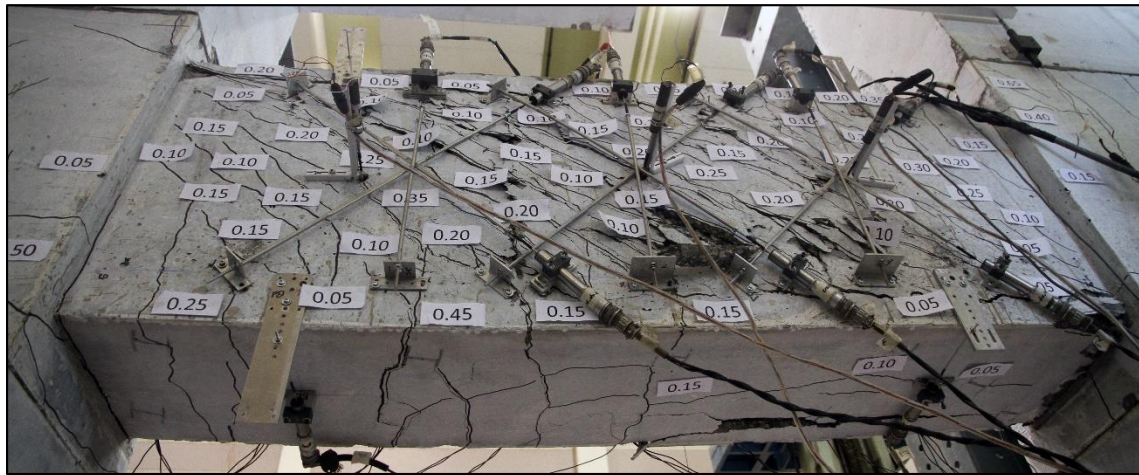


Figure D-14: North Face of CBF1 at End of Post Peak  
 $V = 1217 \text{ kN}$



Figure D-15: South Face of CBF1 with Loose Cover Removed



Figure D-16: North Face of CBF1 with Loose Cover Removed

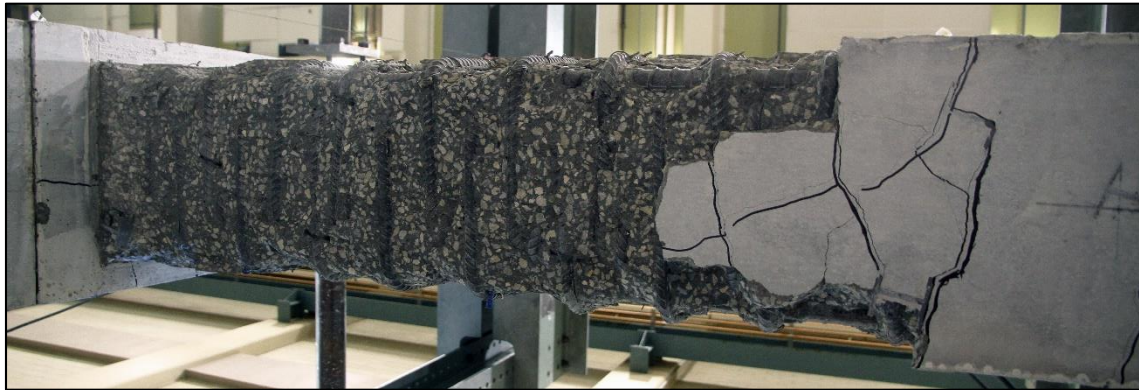


Figure D-17: Bottom Face of CBF1 with Loose Cover Removed



Figure D-18: South Face of CBF1 with Loose Cover Removed

## D.2 Photographs of Specimen CBF2

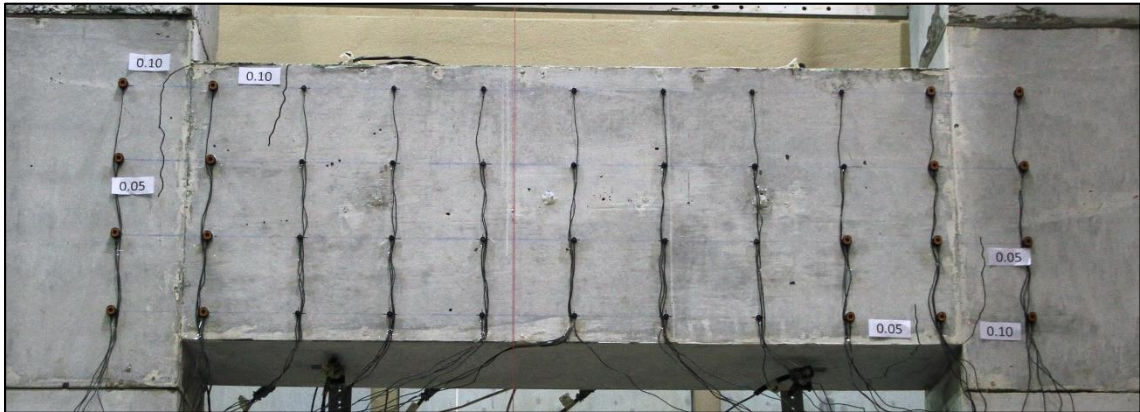


Figure D-19: South Face of CBF2 at Load Stage 1  
 $V = 252 \text{ kN}$   $w_{M,max} = 0.10 \text{ mm}$

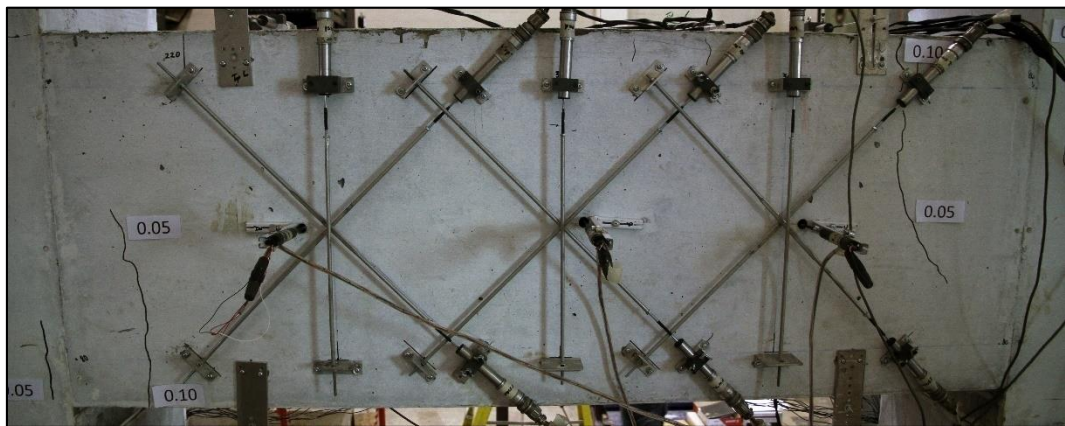


Figure D-20: North Face of CBF2 at Load Stage 1  
 $V = 252 \text{ kN}$   $w_{M,max} = 0.10 \text{ mm}$

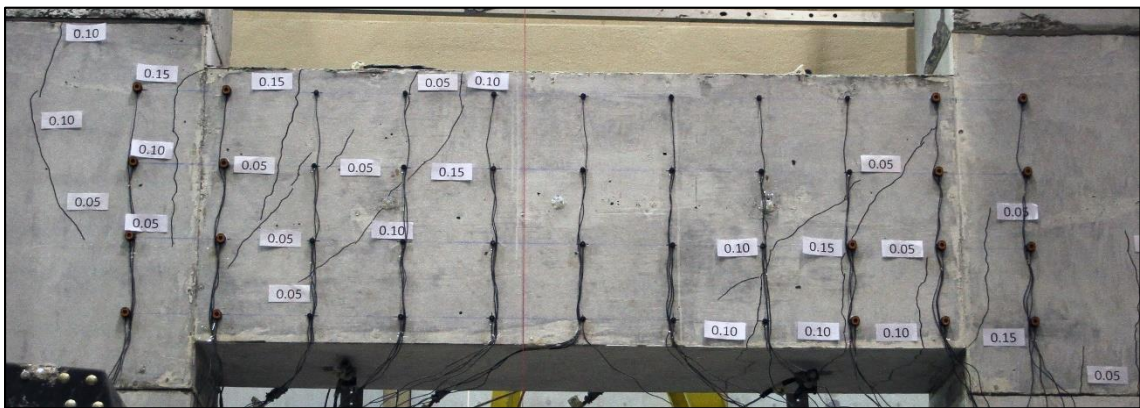


Figure D-21: South Face of CBF2 at Load Stage 2  
 $V = 501 \text{ kN}$   $w_{M,max} = 0.15 \text{ mm}$   $w_{V,max} = 0.15 \text{ mm}$

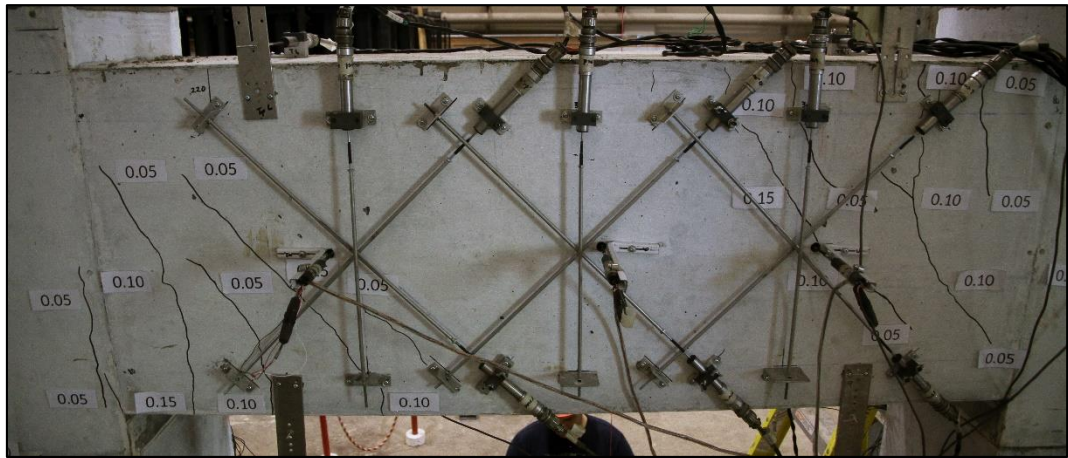


Figure D-22: North Face of CBF2 at Load Stage 2  
 $V = 501 \text{ kN}$   $w_{M,max} = 0.15 \text{ mm}$   $w_{V,max} = 0.15 \text{ mm}$



Figure D-23: South Face of CBF2 at Load Stage 3  
 $V = 1002 \text{ kN}$   $w_{M,max} = 0.35 \text{ mm}$   $w_{V,max} = 0.15 \text{ mm}$

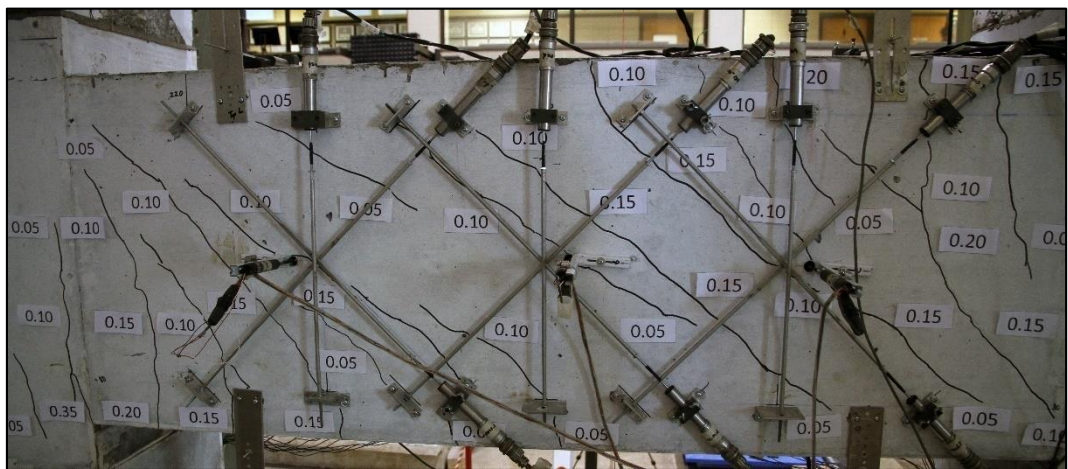
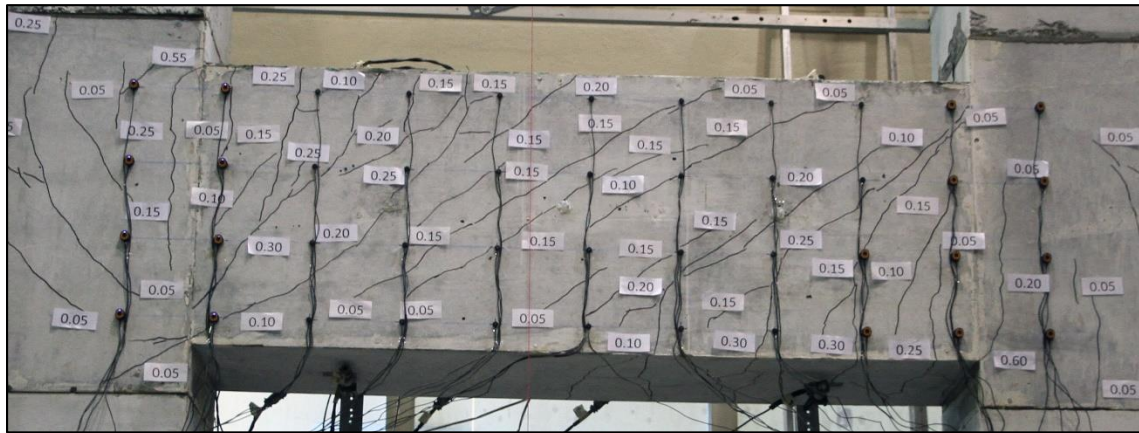
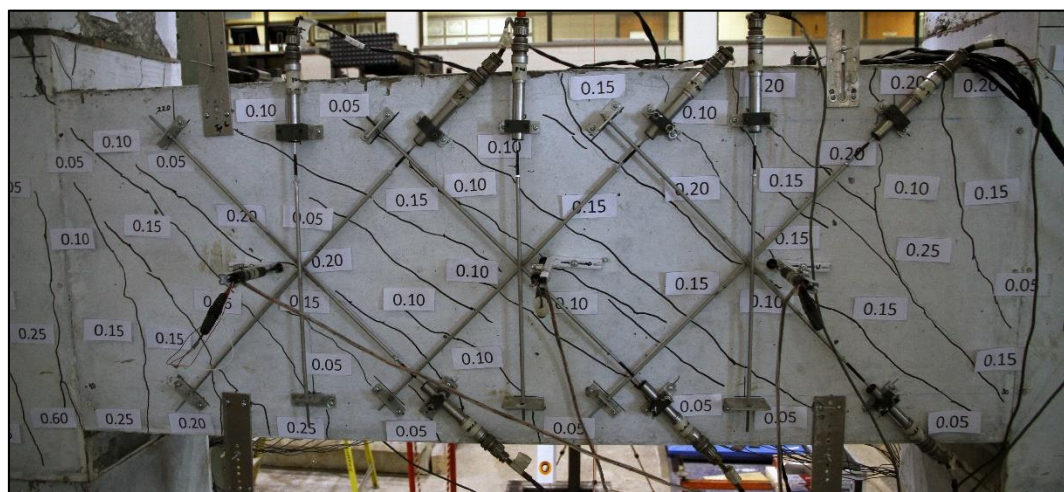


Figure D-24: North Face of CBF2 at Load Stage 3  
 $V = 1002 \text{ kN}$   $w_{M,max} = 0.35 \text{ mm}$   $w_{V,max} = 0.15 \text{ mm}$



*Figure D-25: South Face of CBF2 at Load Stage 4*  
 $V = 1501 \text{ kN}$   $w_{M,max} = 0.60 \text{ mm}$   $w_{V,max} = 0.30 \text{ mm}$



*Figure D-26: North Face of CBF2 at Load Stage 4*  
 $V = 1501 \text{ kN}$   $w_{M,max} = 0.60 \text{ mm}$   $w_{V,max} = 0.25 \text{ mm}$

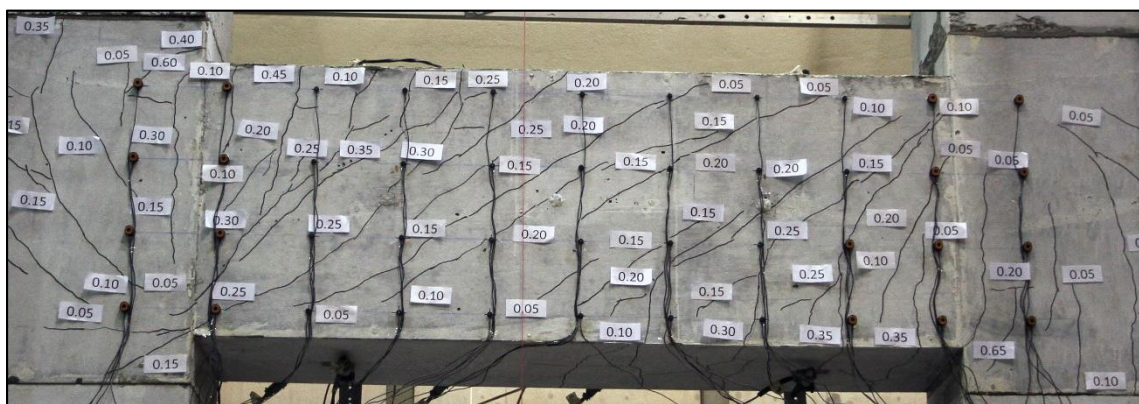


*Figure D-27: South Face of CBF2 at Load Stage 5*  
 $V = 1801 \text{ kN}$   $w_{M,max} = 0.65 \text{ mm}$   $w_{V,max} = 0.35 \text{ mm}$



Figure D-28: North Face of CBF2 at Load Stage 5  
 $V = 1801 \text{ kN}$   $w_{M,max} = 0.75 \text{ mm}$   $w_{V,max} = 0.45 \text{ mm}$

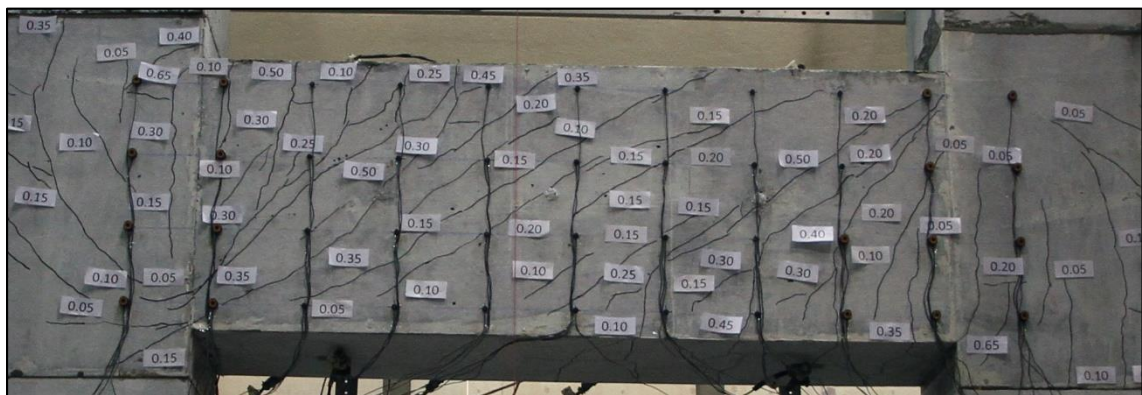


Figure D-29: South Face of CBF2 at Load Stage 6  
 $V = 1827 \text{ kN}$   $w_{M,max} = 0.65 \text{ mm}$   $w_{V,max} = 0.50 \text{ mm}$

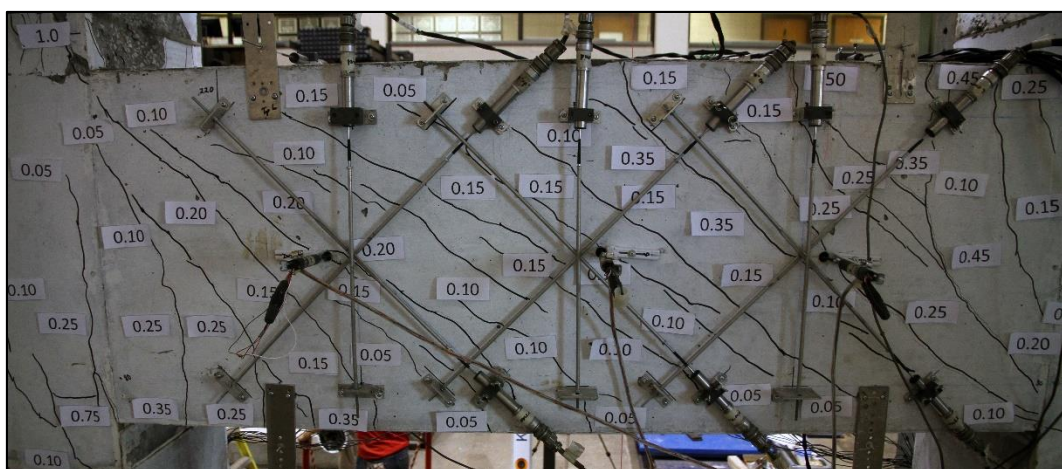
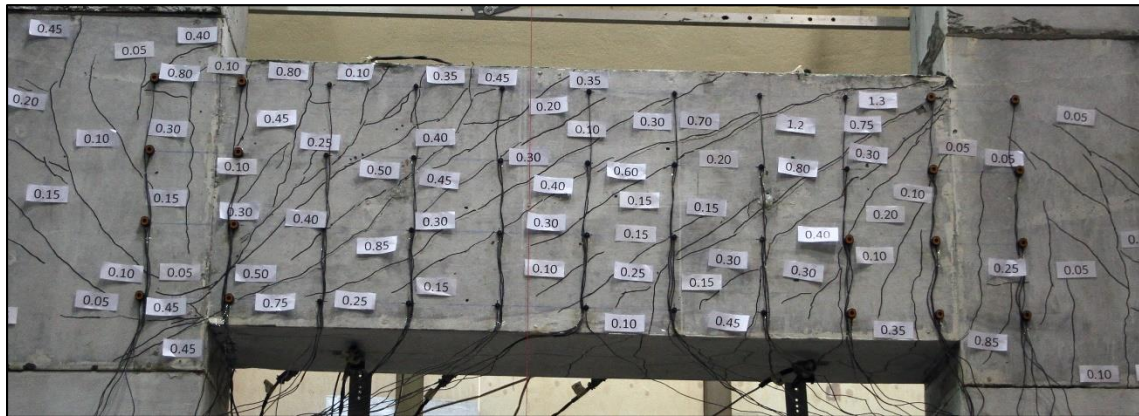


Figure D-30: North Face of CBF2 at Load Stage 6  
 $V = 1827 \text{ kN}$   $w_{M,max} = 0.75 \text{ mm}$   $w_{V,max} = 0.45 \text{ mm}$



*Figure D-31: South Face of CBF2 at Load Stage 7*  
 $V = 1950 \text{ kN}$   $w_{M,max} = 0.85 \text{ mm}$   $w_{V,max} = 0.85 \text{ mm}$



*Figure D-32: North Face of CBF2 at Load Stage 7*  
 $V = 1950 \text{ kN}$   $w_{M,max} = 0.90 \text{ mm}$   $w_{V,max} = 0.80 \text{ mm}$

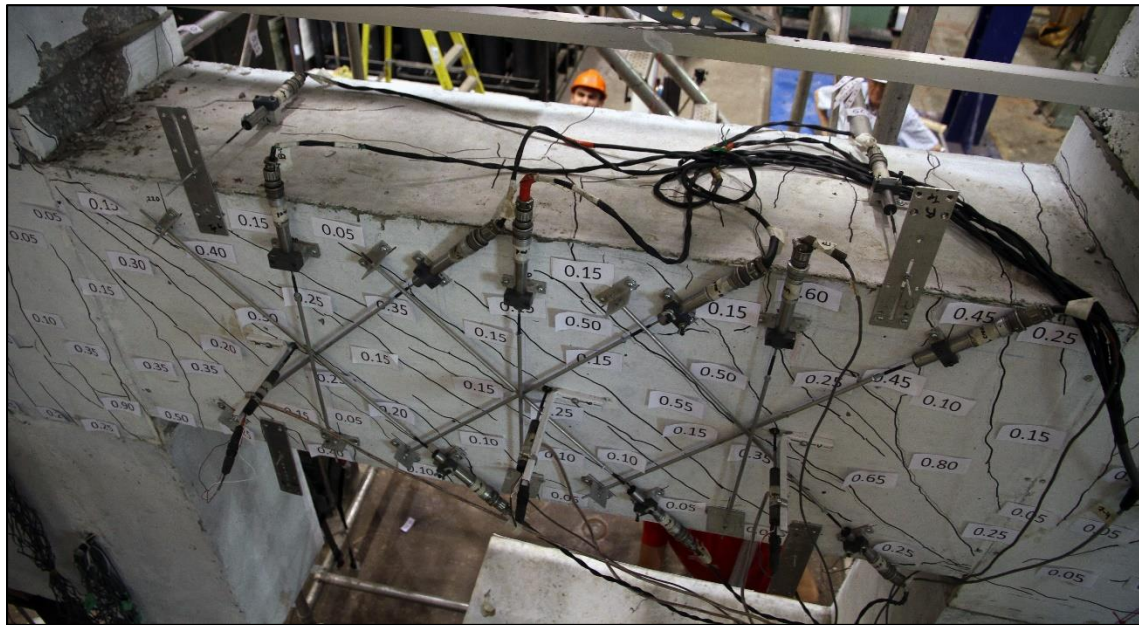


*Figure D-33: Top Face of CBF2 at Load Stage 7*  
 $V = 1950 \text{ kN}$

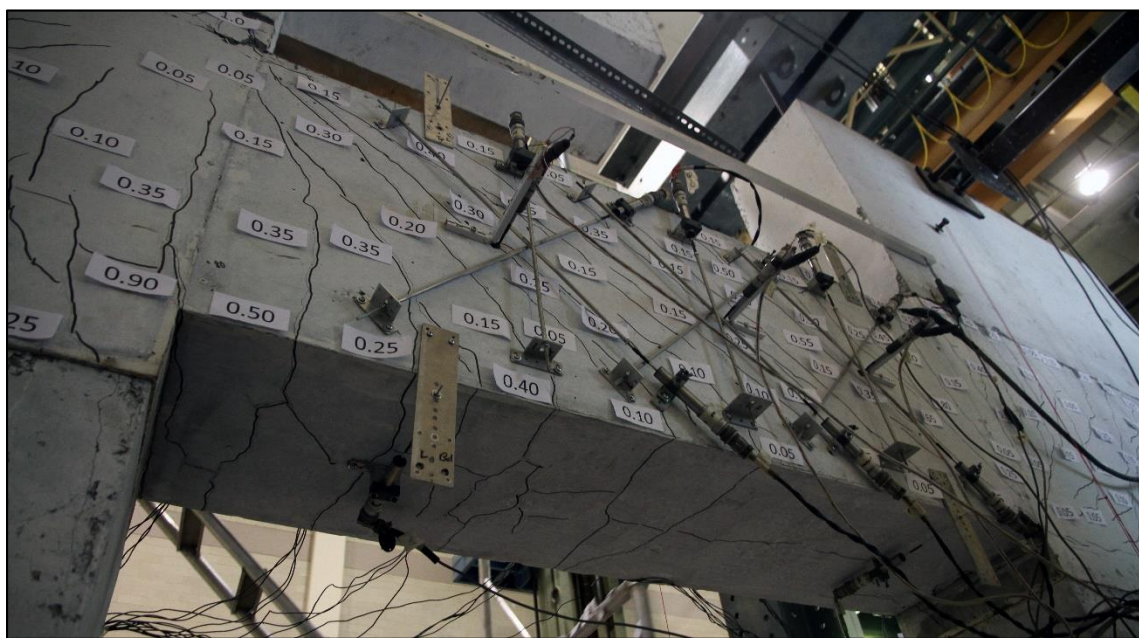


*Figure D-34: Bottom Face of CBF2 at Load Stage 7*  
 $V = 1950 \text{ kN}$

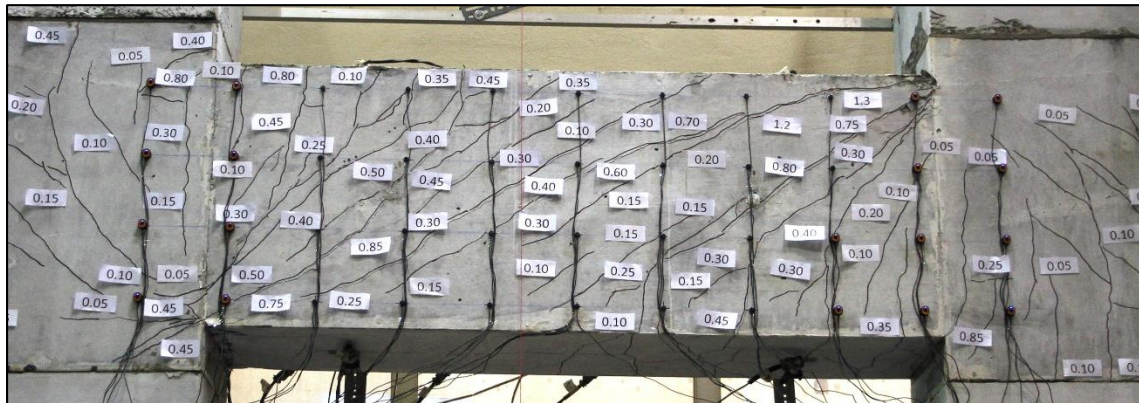


Figure D-35: South Face of CBF2 at Peak Load

$$V_{peak} = 1992 \text{ kN}$$



Figure D-36: South Face of CBF2 during Post-Peak at 90% of Load

$$V = 1793 \text{ kN}$$



Figure D-37: South Face of CBF2 during Post-Peak at 80% of Load

$$V = 1594 \text{ kN}$$



Figure D-38: South Face of CBF2 at End of Post-Peak  
 $V = 1503 \text{ kN}$

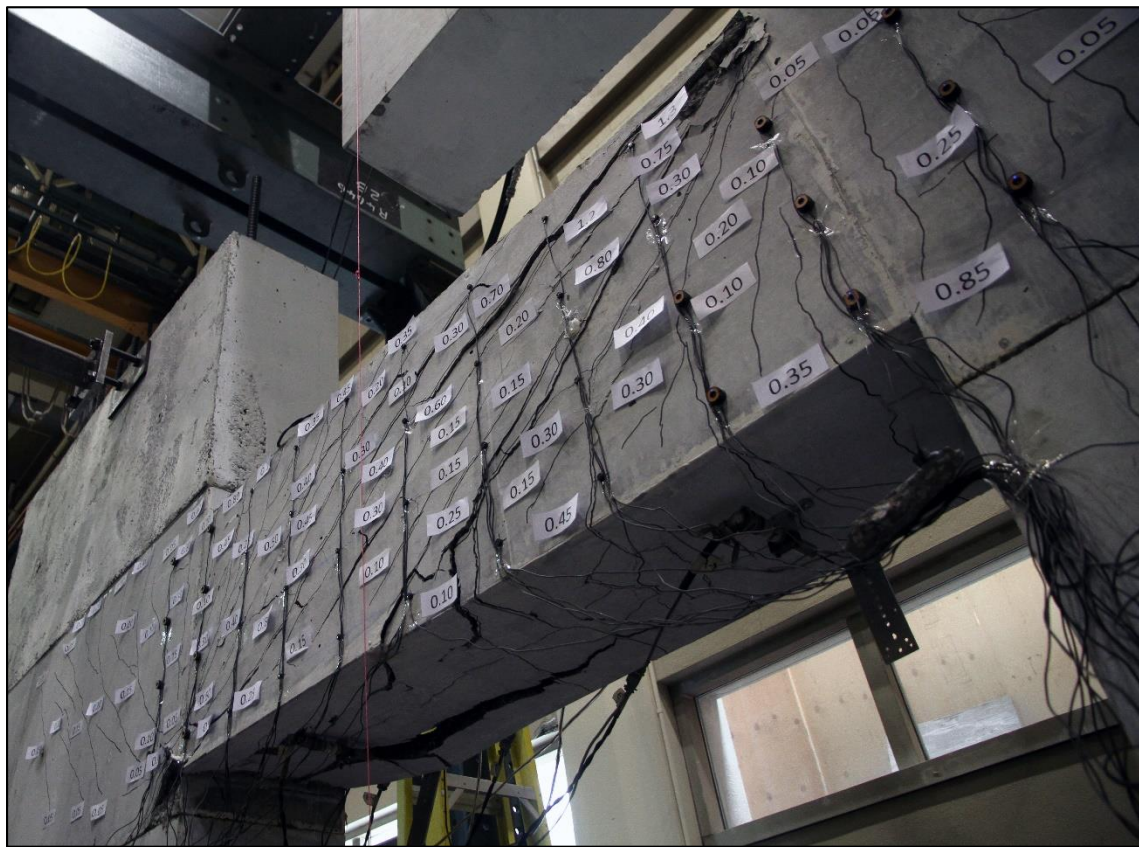


Figure D-39: South Face of CBF2 at End of Post-Peak  
 $V = 1503 \text{ kN}$

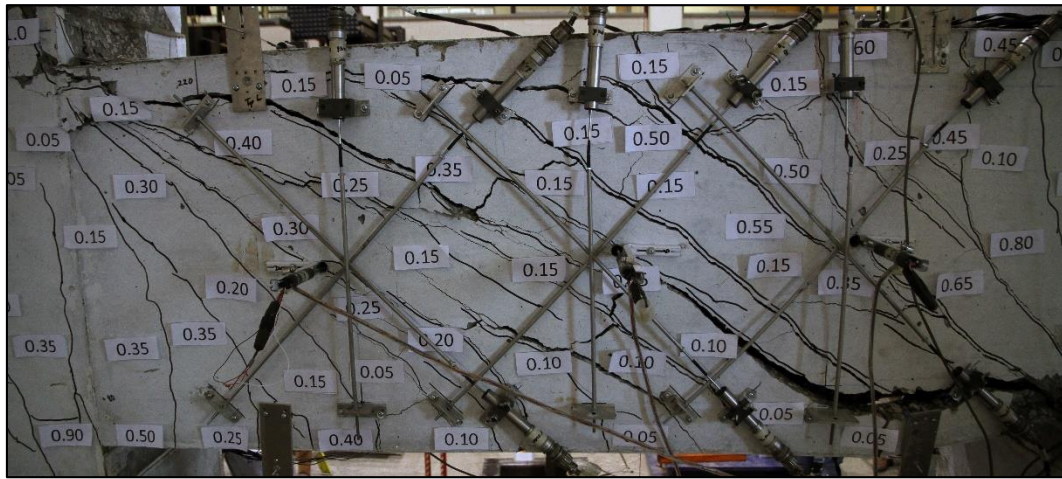


Figure D-40: North Face of CBF2 at End of Post-Peak  
 $V = 1503 \text{ kN}$

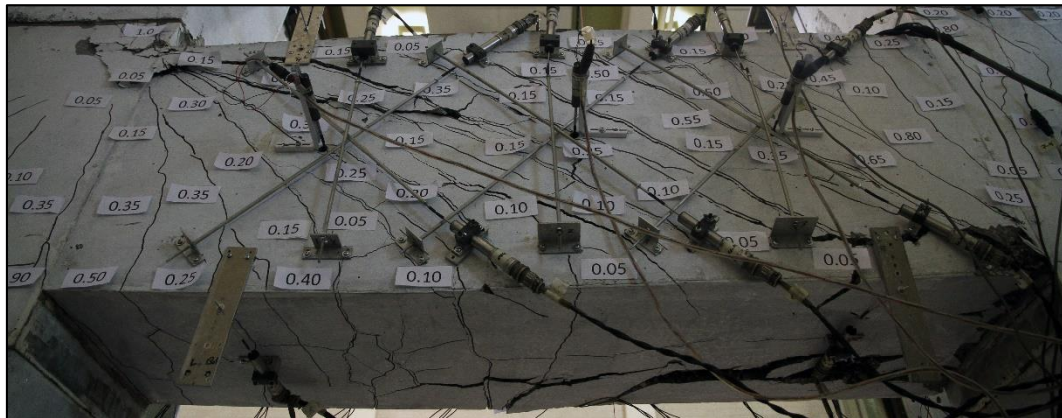


Figure D-41: North Face of CBF2 at End of Post-Peak  
 $V = 1503 \text{ kN}$



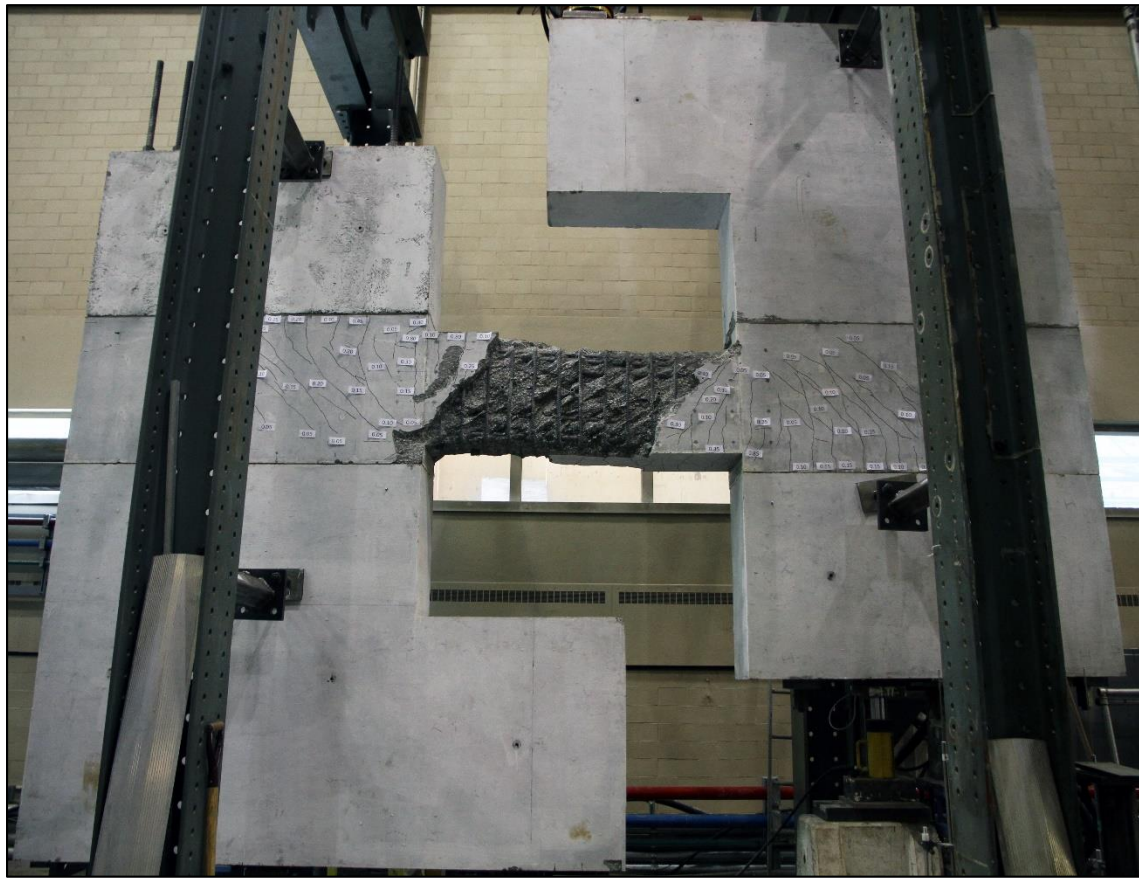
Figure D-42: South Face of CBF2 with Loose Cover Removed



Figure D-43: North Face of CBF2 with Loose Cover Removed



Figure D-44: North-Top Face of CBF2 with Loose Cover Removed



*Figure D-45: South Face of CBF2 with Loose Cover Removed*

### D.3 Photographs of Specimen CBF3

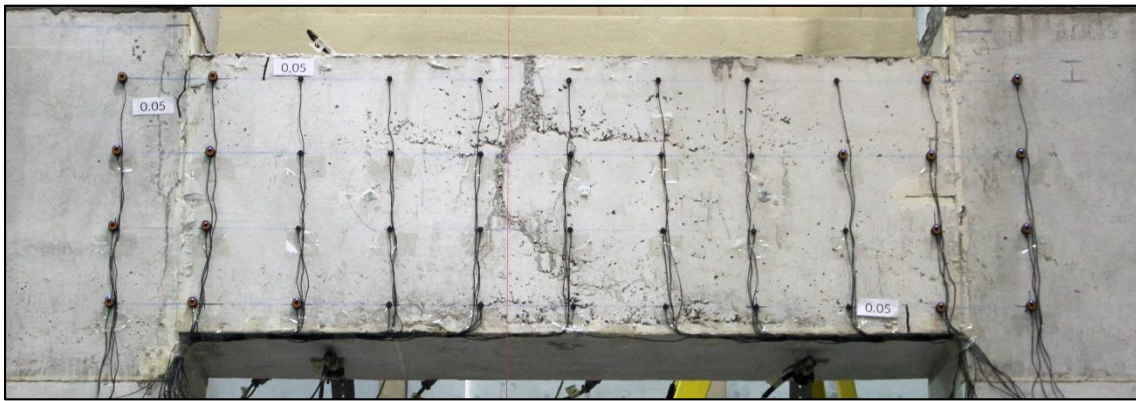


Figure D-46: South Face of CBF3 at Load Stage 1  
 $V = 257 \text{ kN}$   $w_{M,max} = 0.05 \text{ mm}$



Figure D-47: North Face of CBF3 at Load Stage 1  
 $V = 257 \text{ kN}$   $w_{M,max} = 0.05 \text{ mm}$

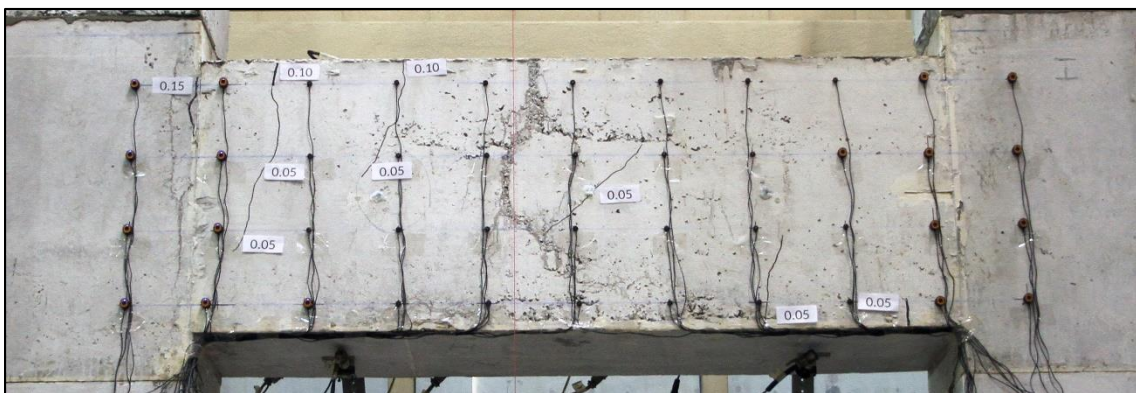


Figure D-48: South Face of CBF3 at Load Stage 2  
 $V = 503 \text{ kN}$   $w_{M,max} = 0.15 \text{ mm}$   $w_{V,max} = 0.05 \text{ mm}$

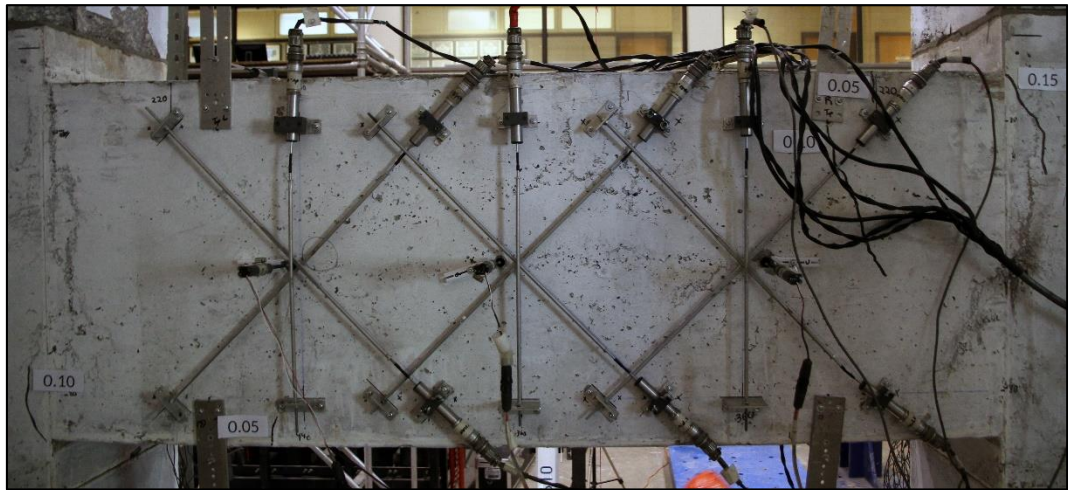


Figure D-49: North Face of CBF3 at Load Stage 2

$V = 503 \text{ kN}$   $w_{M,max} = 0.15 \text{ mm}$

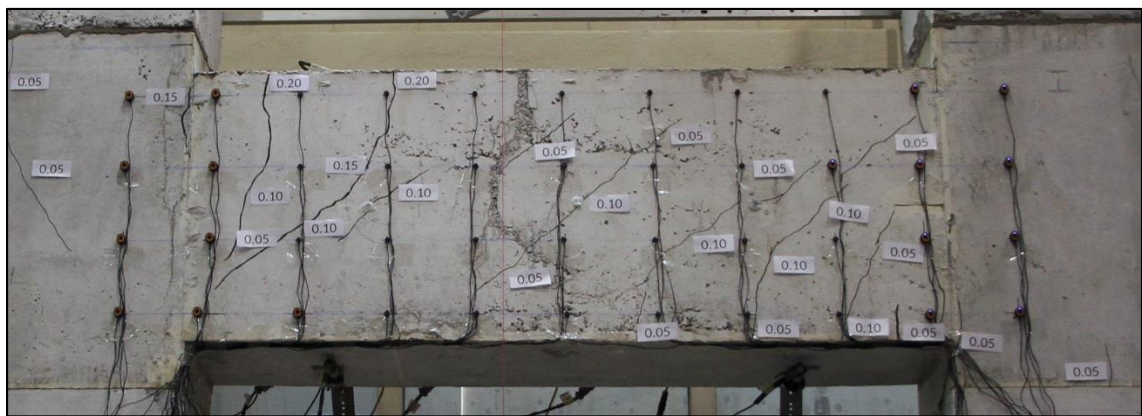


Figure D-50: South Face of CBF3 at Load Stage 3

$V = 1000 \text{ kN}$   $w_{M,max} = 0.20 \text{ mm}$   $w_{V,max} = 0.10 \text{ mm}$



Figure D-51: North Face of CBF3 at Load Stage 3

$V = 1000 \text{ kN}$   $w_{M,max} = 0.25 \text{ mm}$   $w_{V,max} = 0.10 \text{ mm}$

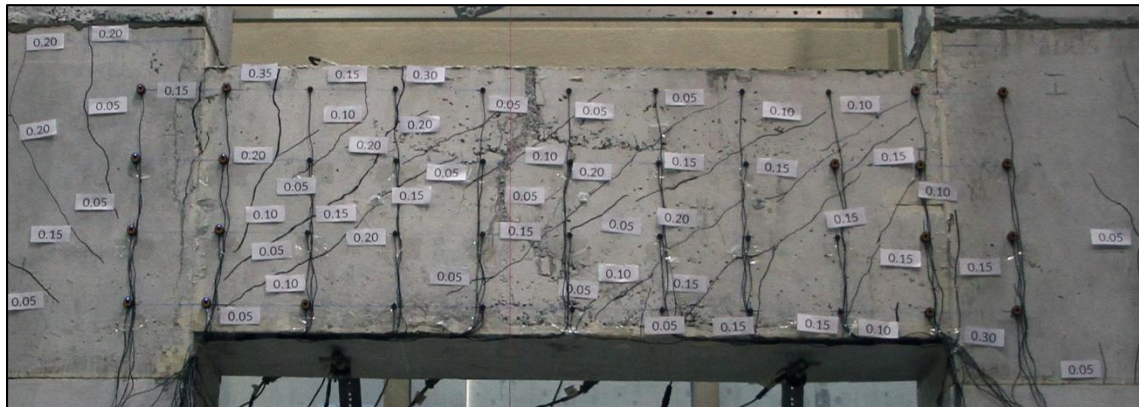


*Figure D-52: South Face of CBF3 at Load Stage 4*  
 $V = 1500 \text{ kN}$   $w_{M,\max} = 0.35 \text{ mm}$   $w_{V,\max} = 0.20 \text{ mm}$



*Figure D-53: North Face of CBF3 at Load Stage 4*  
 $V = 1500 \text{ kN}$   $w_{M,\max} = 0.65 \text{ mm}$   $w_{V,\max} = 0.30 \text{ mm}$

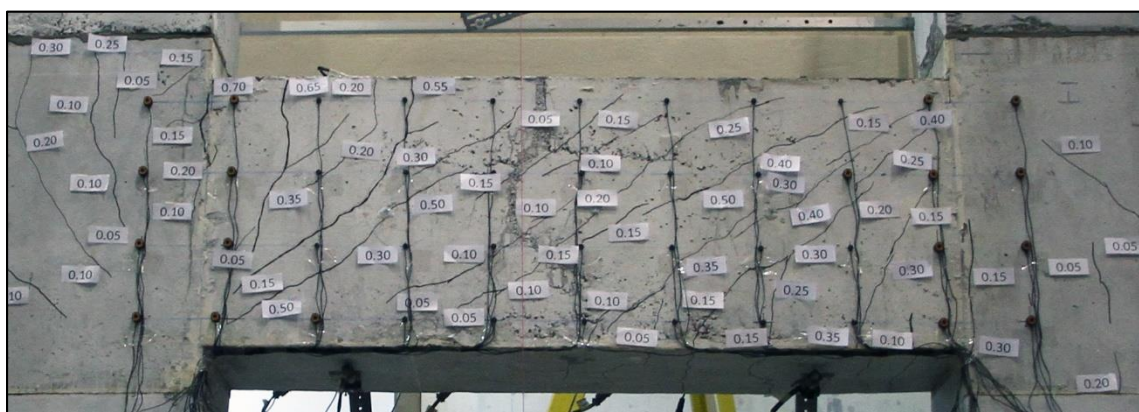


*Figure D-54: South Face of CBF3 at Load Stage 5*  
 $V = 1752 \text{ kN}$   $w_{M,\max} = 0.70 \text{ mm}$   $w_{V,\max} = 0.50 \text{ mm}$

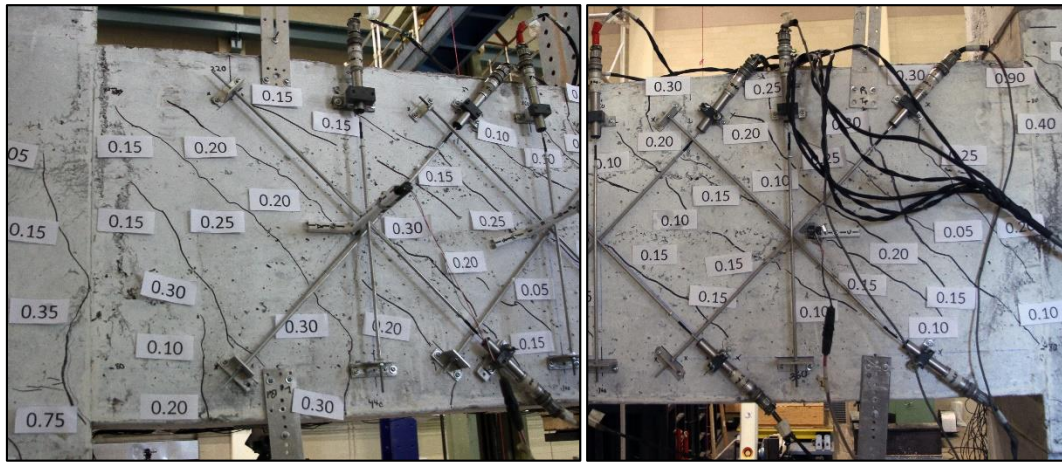


*Figure D-55: North Face of CBF3 at Load Stage 5*  
 $V = 1752 \text{ kN}$   $w_{M,max} = 0.90 \text{ mm}$   $w_{V,max} = 0.30 \text{ mm}$

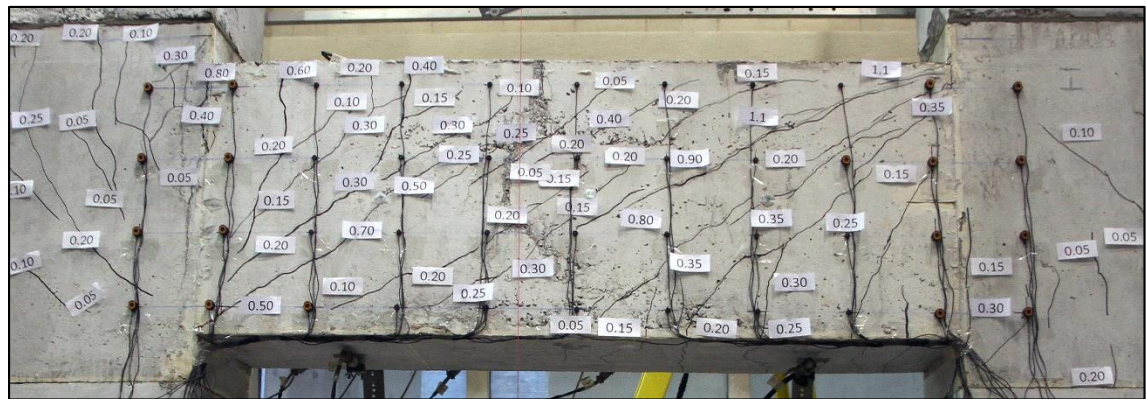


*Figure D-56: South Face of CBF3 at Load Stage 6*  
 $V = 1827 \text{ kN}$   $w_{M,max} = 0.80 \text{ mm}$   $w_{V,max} = 1.1 \text{ mm}$



*Figure D-57: North Face of CBF3 at Load Stage 6*  
 $V = 1827 \text{ kN}$   $w_{M,max} = 1.0 \text{ mm}$   $w_{V,max} = 0.30 \text{ mm}$



Figure D-58: Bottom Face of CBF3 at Load Stage 6  
 $V = 1827 \text{ kN}$



Figure D-59: South Face of CBF3 at Peak Load (Cycle 2 of Load Stage 6)  
 $V = 1830 \text{ kN}$

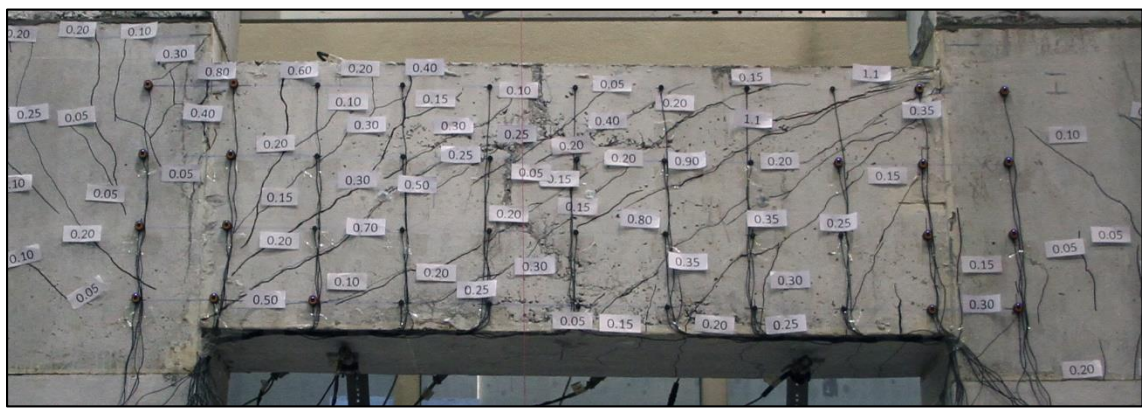


Figure D-60: South Face of CBF3 at Failure Load (Cycle 3 of Load Stage 6)  
 $V = 1785 \text{ kN}$



Figure D-61: South Face of CBF3 during Post-Peak at 90% Load  
 $V = 1647 \text{ kN}$

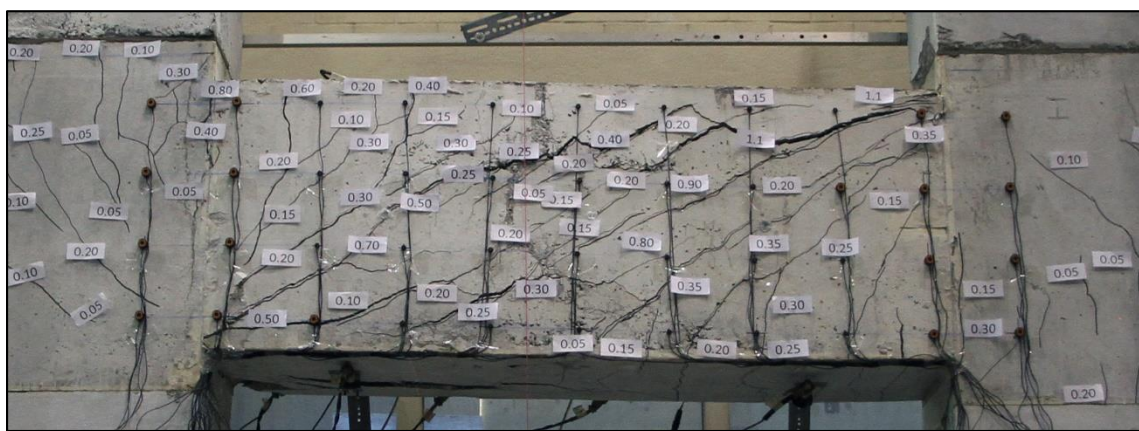


Figure D-62: South Face of CBF3 during Post-Peak at 80% Load  
 $V = 1464 \text{ kN}$

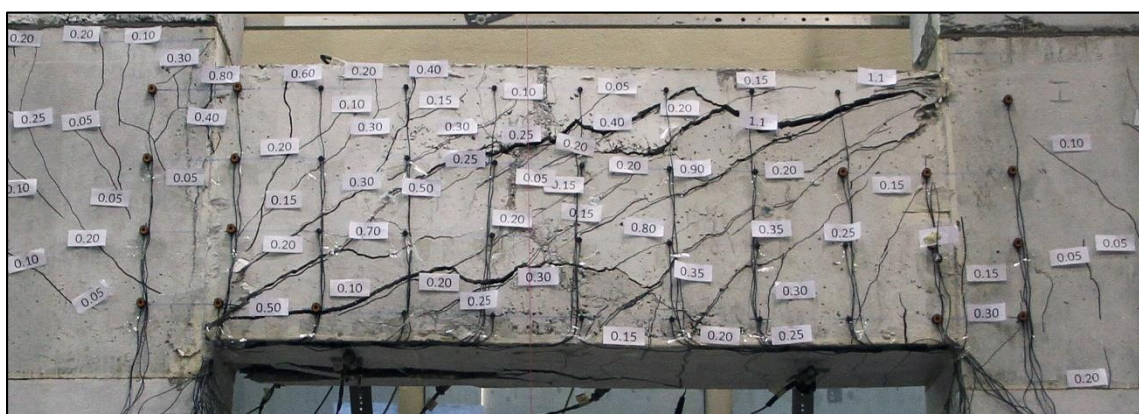


Figure D-63: South Face of CBF3 at End of Post-Peak  
 $V = 1138 \text{ kN}$

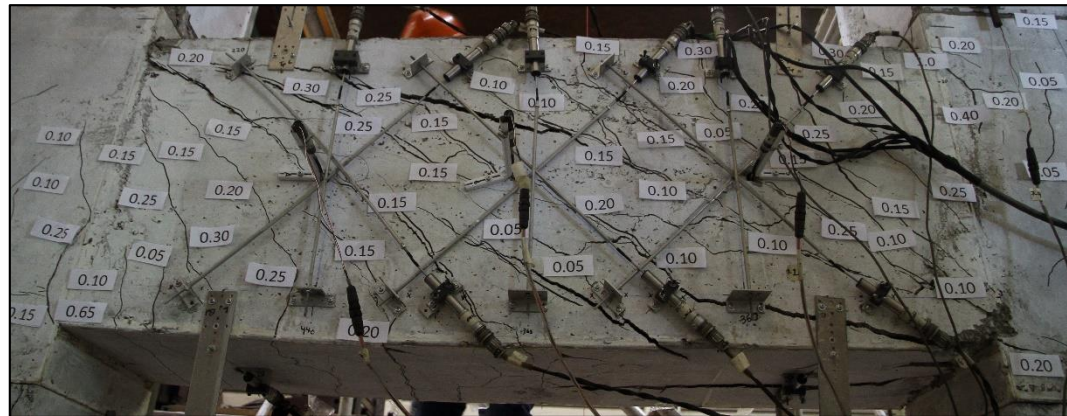


Figure D-64: North Face of CBF3 at End of Post-Peak  
 $V = 1138 \text{ kN}$

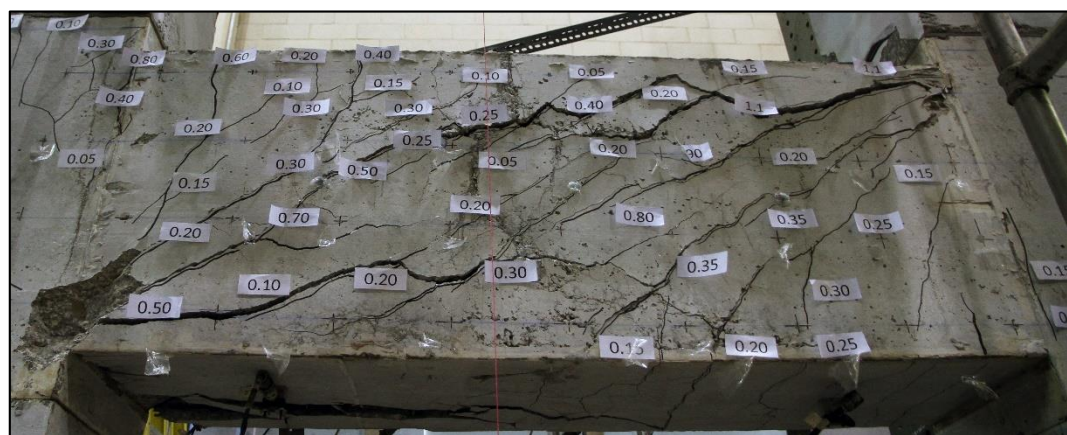


Figure D-65: South Face of CBF3 at End of Post-Peak  
 $V = 1138 \text{ kN}$



Figure D-66: Bottom Face of CBF3 at End of Post-Peak  
 $V = 1138 \text{ kN}$

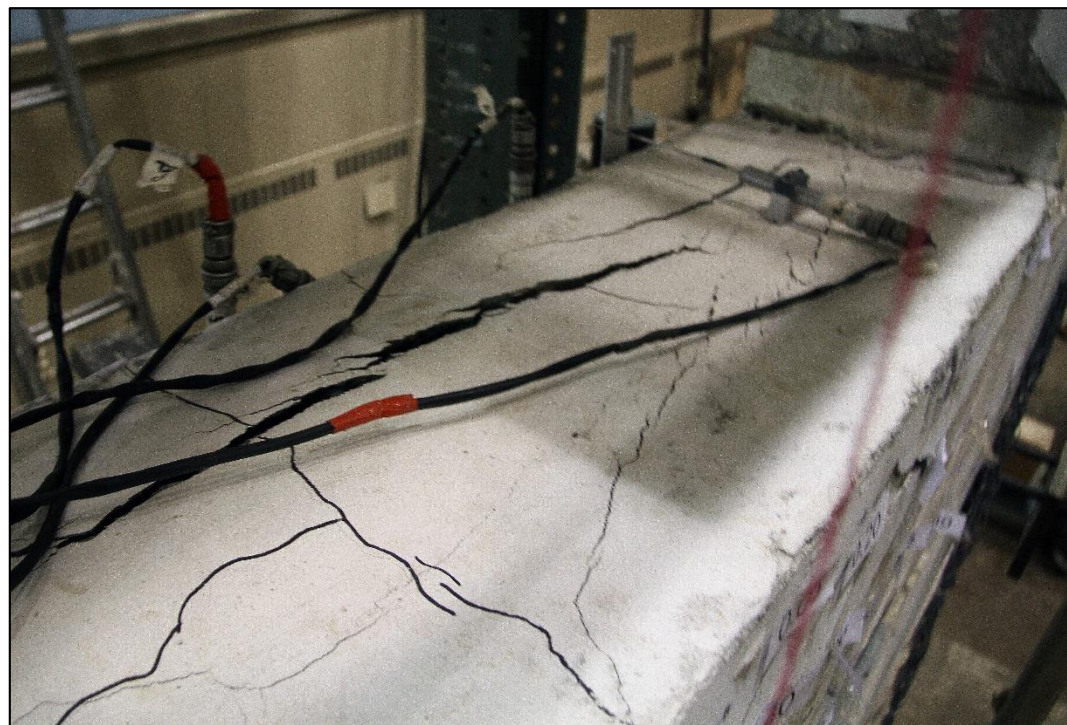
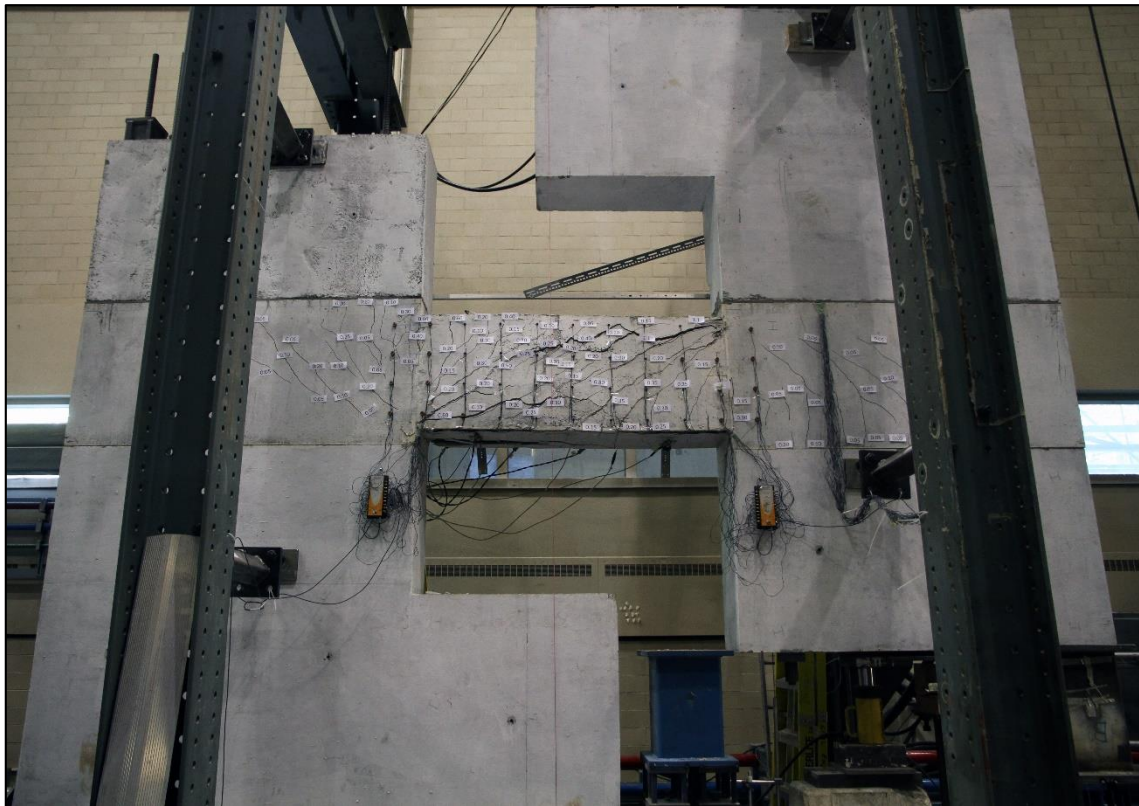


Figure D-67: Top Face of CBF3 at End of Post-Peak  
 $V = 1138 \text{ kN}$



Figure D-68: South-Top Corner of CBF3 at End of Post-Peak  
 $V = 1138 \text{ kN}$



*Figure D-69: South Face of CBF3 at End of Post-Peak*  
 $V = 1138 \text{ kN}$



*Figure D-70: South Face of CBF3 with Loose Cover Removed*



*Figure D-71: North Face of CBF3 with Loose Cover Removed*



*Figure D-72: North Face of CBF3 with Loose Cover Removed*

## D.4 Photographs of Specimen CBF4



Figure D-73: South Face of CBF4 at Load Stage 1  
 $V = 251 \text{ kN}$



Figure D-74: South Face of CBF4 at Load Stage 2  
 $V = 502 \text{ kN}$   $w_{M,max} = 0.10 \text{ mm}$

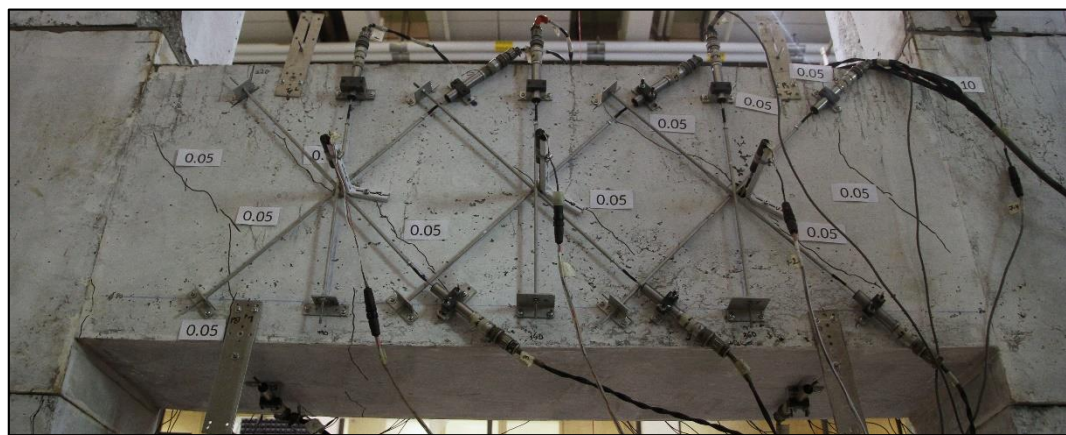


Figure D-75: North Face of CBF4 at Load Stage 2  
 $V = 502 \text{ kN}$   $w_{M,max} = 0.10 \text{ mm}$   $w_{V,max} = 0.05 \text{ mm}$

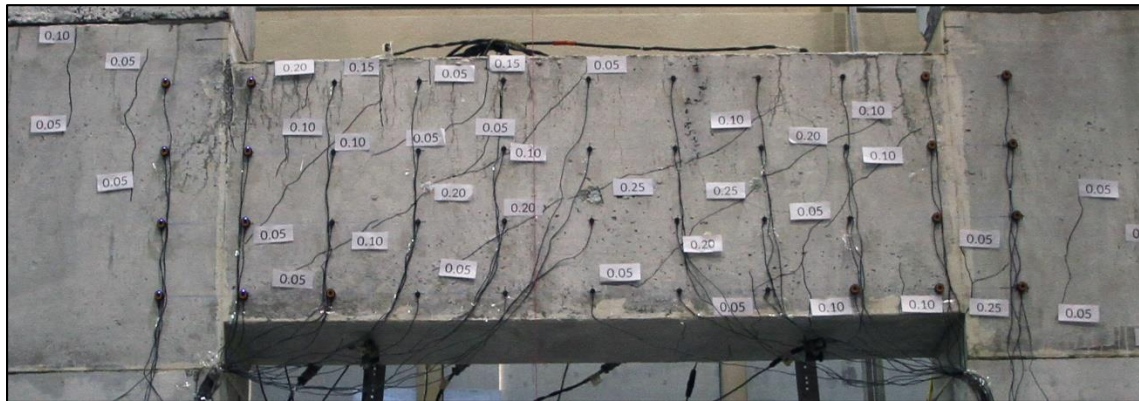


Figure D-76: South Face of CBF4 at Load Stage 3  
 $V = 1003 \text{ kN}$   $w_{M,max} = 0.25 \text{ mm}$   $w_{V,max} = 0.25 \text{ mm}$



Figure D-77: South Face of CBF4 at Load Stage 4  
 $V = 1130 \text{ kN}$   $w_{M,max} = 0.40 \text{ mm}$   $w_{V,max} = 0.30 \text{ mm}$

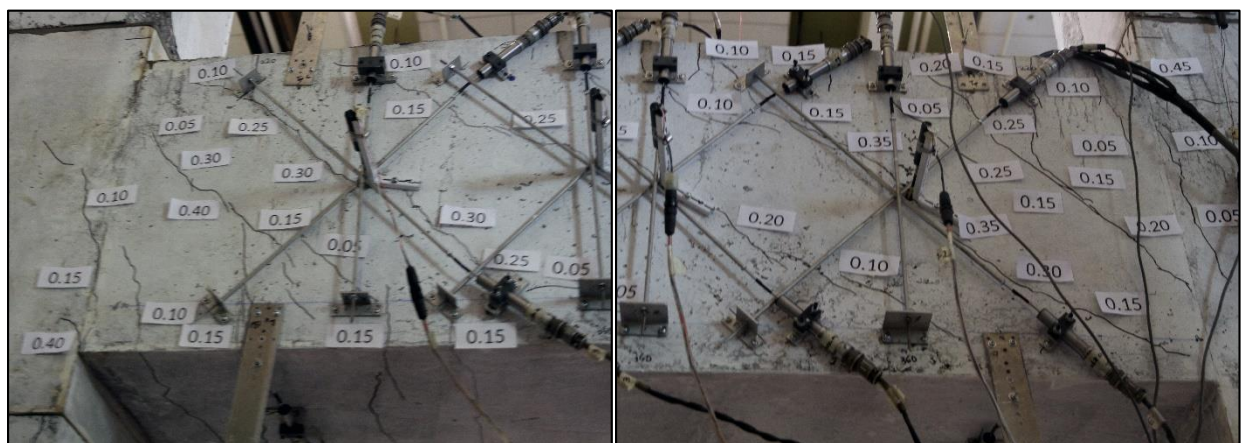
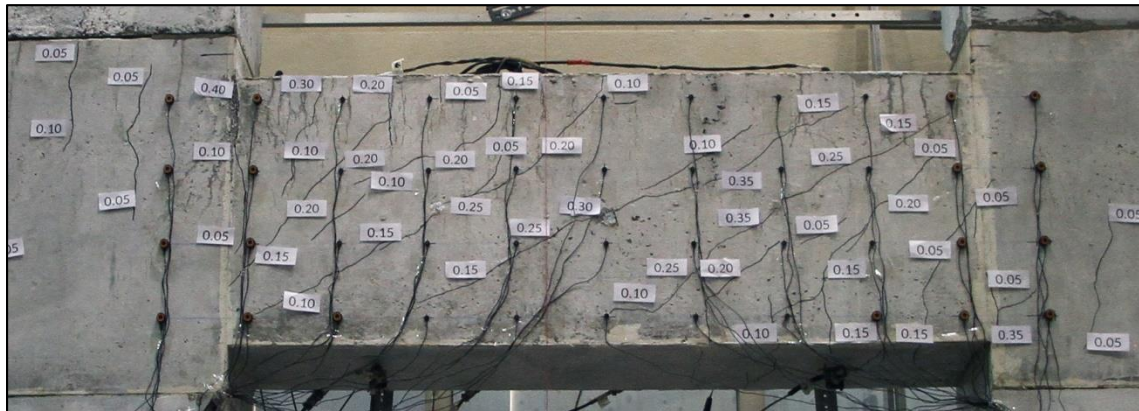
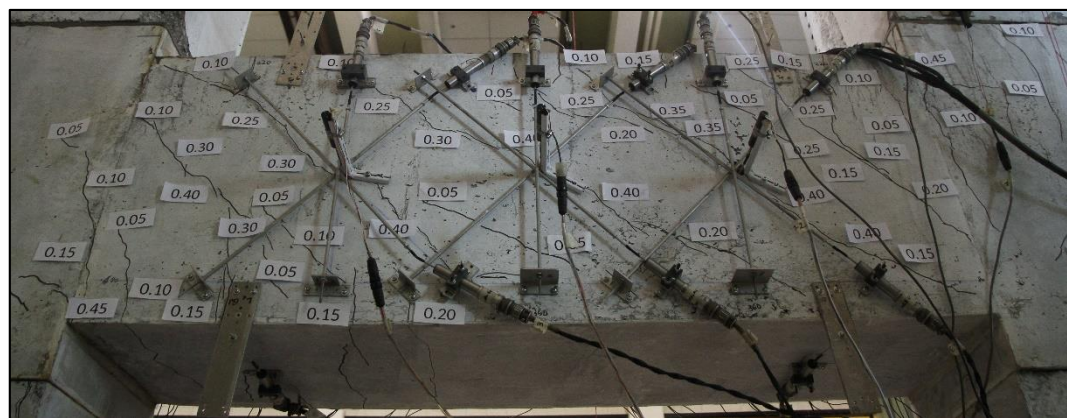


Figure D-78: North Face of CBF4 at Load Stage 4  
 $V = 1130 \text{ kN}$   $w_{M,max} = 0.45 \text{ mm}$   $w_{V,max} = 0.35 \text{ mm}$



*Figure D-79: South Face of CBF4 at Load Stage 5*  
 $V = 1251 \text{ kN}$   $w_{M,max} = 0.40 \text{ mm}$   $w_{V,max} = 0.35 \text{ mm}$



*Figure D-80: North Face of CBF4 at Load Stage 5*  
 $V = 1251 \text{ kN}$   $w_{M,max} = 0.45 \text{ mm}$   $w_{V,max} = 0.40 \text{ mm}$

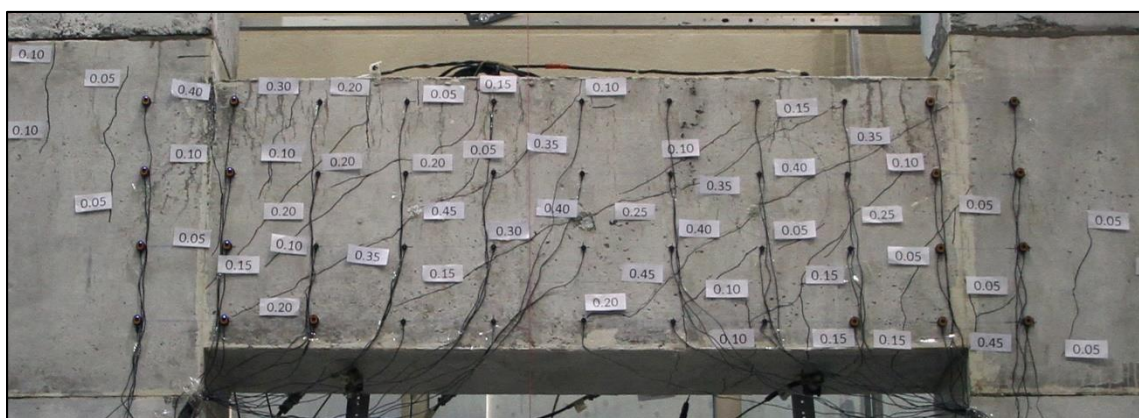


*Figure D-81: South Face of CBF4 at Load Stage 6*  
 $V = 1381 \text{ kN}$   $w_{M,max} = 0.45 \text{ mm}$   $w_{V,max} = 0.45 \text{ mm}$

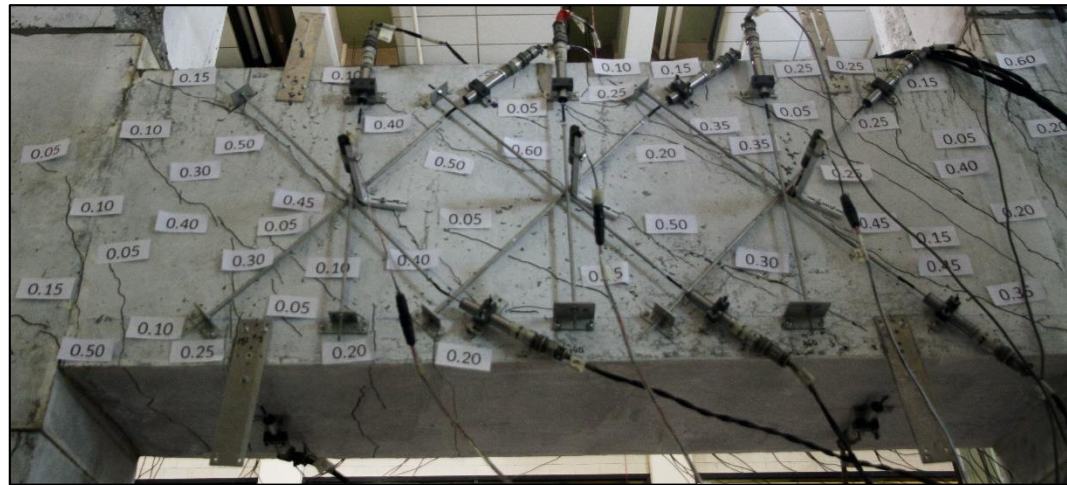


Figure D-82: North Face of CBF4 at Load Stage 6  
 $V = 1381 \text{ kN}$   $w_{M,max} = 0.60 \text{ mm}$   $w_{V,max} = 0.60 \text{ mm}$

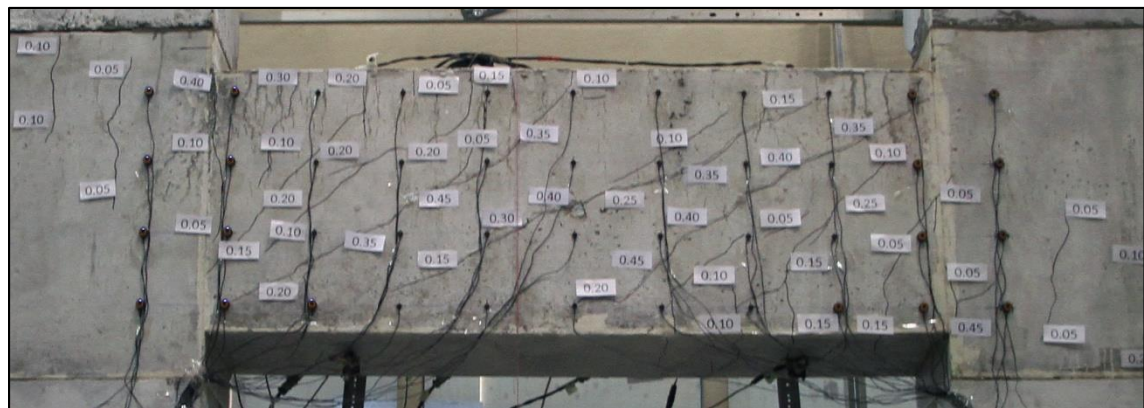


Figure D-83: South Face of CBF4 at Peak Load  
 $V = 1481 \text{ kN}$

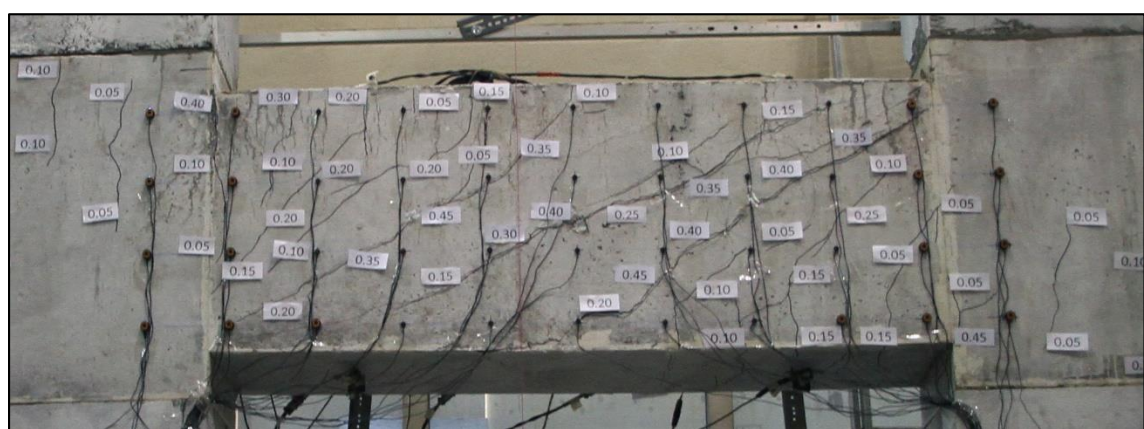


Figure D-84: South Face of CBF4 during Post-Peak at 90% Load  
 $V = 1333 \text{ kN}$



Figure D-85: South Face of CBF4 during Post-Peak at 80% Load  
 $V = 1185 \text{ kN}$

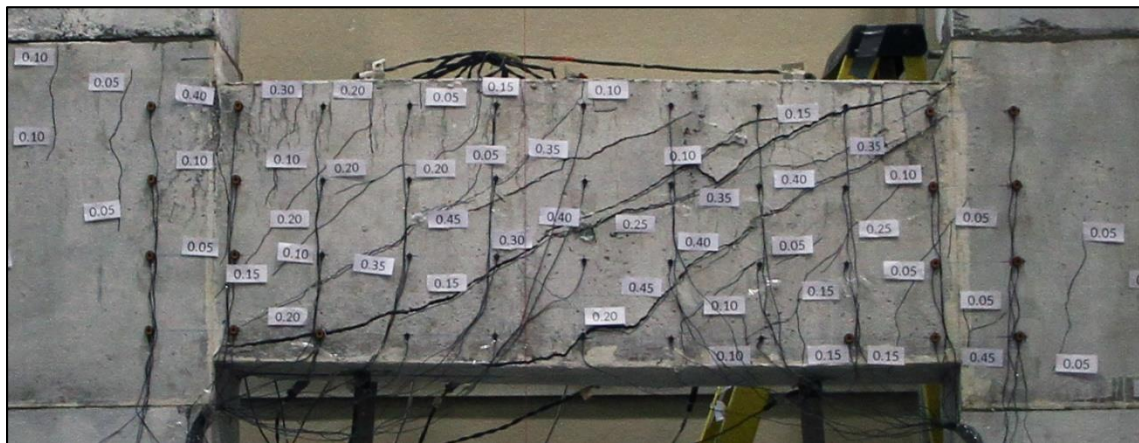


Figure D-86: South Face of CBF4 at End of Post-Peak  
 $V = 1076 \text{ kN}$



Figure D-87: North Face of CBF4 at End of Post-Peak  
 $V = 1076 \text{ kN}$



*Figure D-88: Bottom Face of CBF4 at End of Post-Peak*  
 $V = 1076 \text{ kN}$



*Figure D-89: South Face of CBF4 with Loose Cover Removed*



*Figure D-90: South Face of CBF4 with Loose Cover Removed*



Figure D-91: North Face of CBF4 with Loose Cover Removed



Figure D-92: Top Face of CBF4 with Loose Cover Removed



Figure D-93: Bottom Face of CBF4 with Loose Cover Removed



*Figure D-94: South Face of CBF4 with Loose Cover Removed*

## Appendix E: Strain Gauge Data

The strain measurements for all strain gauges have been plotted with the sectional shear stress of the coupling beam. Figure E-1, Figure E-2, and Figure E-3 show the stirrup strains, longitudinal bar strains, and tensile penetration strains respectively.

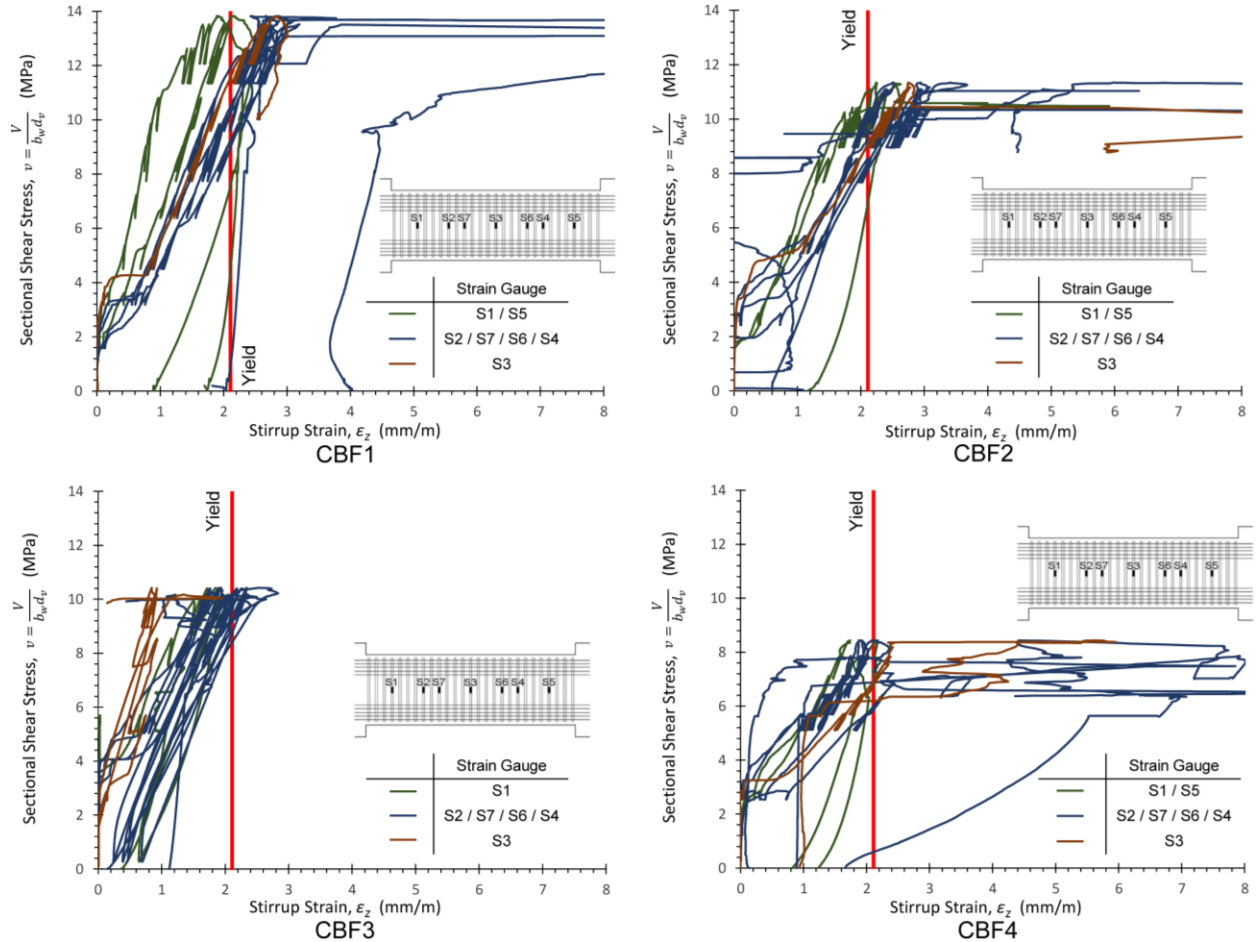


Figure E-1: Stirrup Stain Gauge Measurements for CBF1 to CBF4

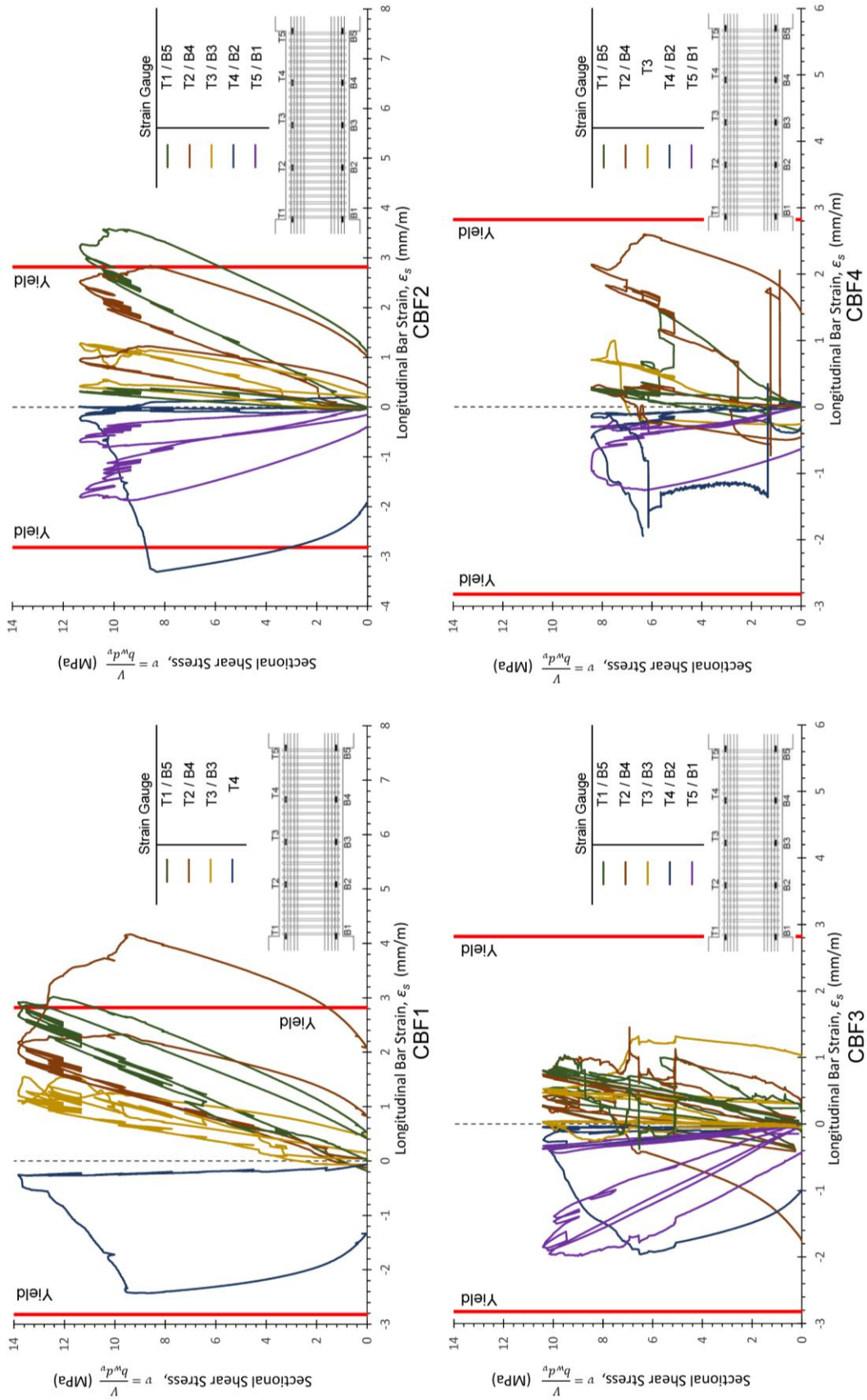


Figure E-2: Longitudinal Stain Gauge Measurements for CBF1 to CBF4

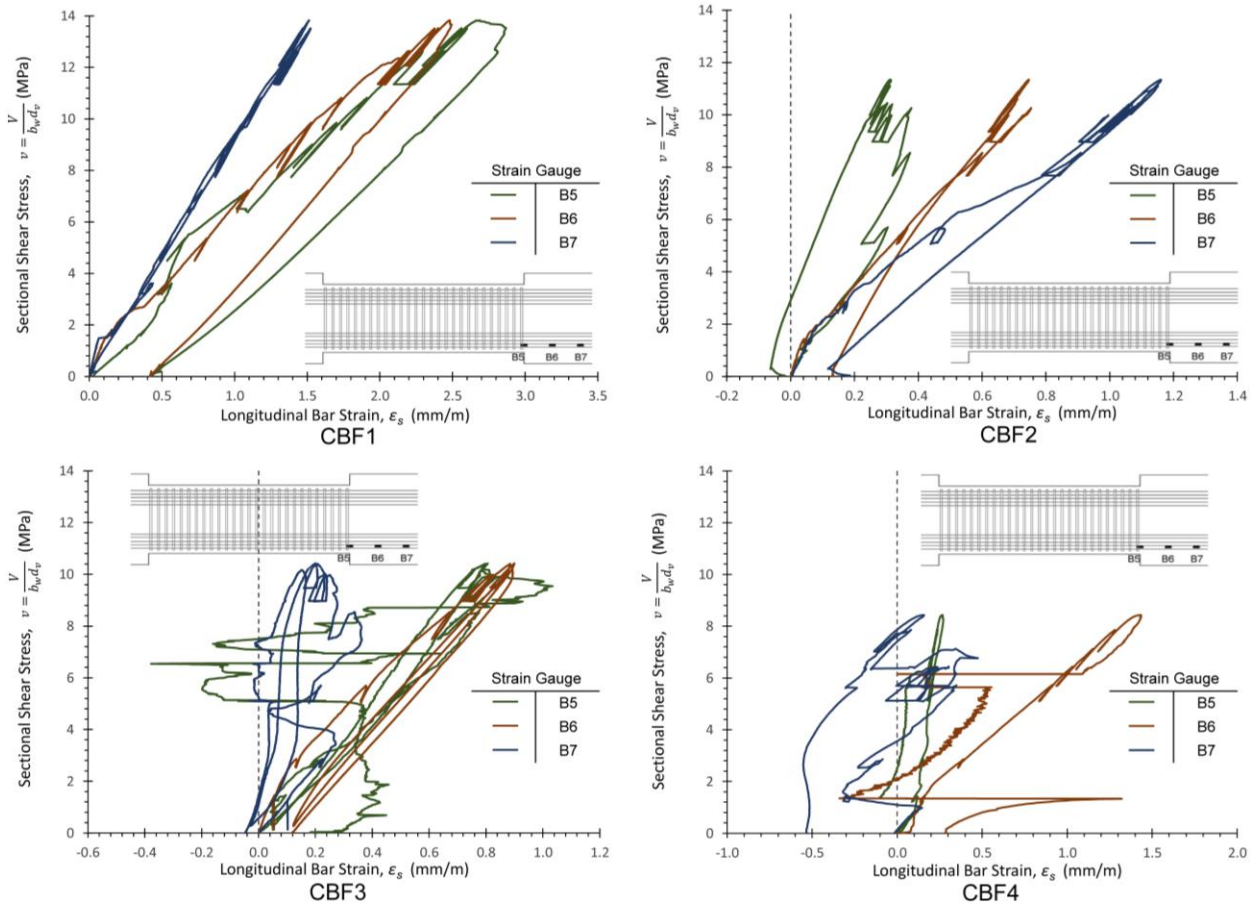


Figure E-3: Shear Wall Stain Gauge Measurements for CBF1-4

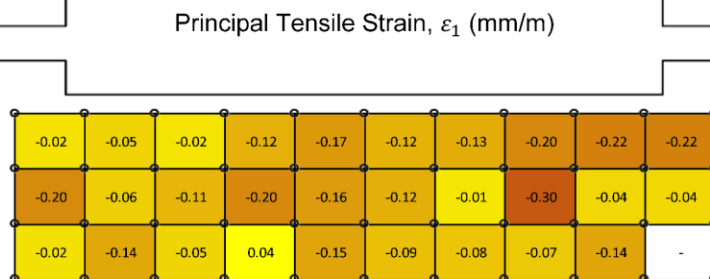
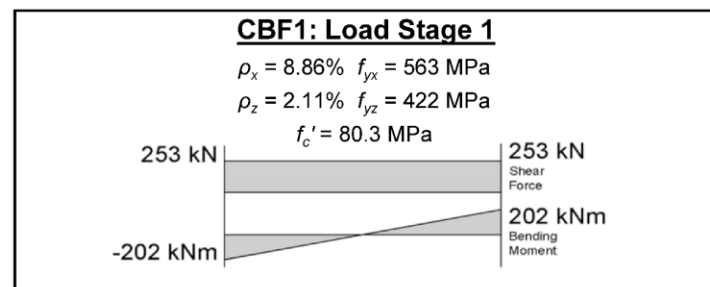
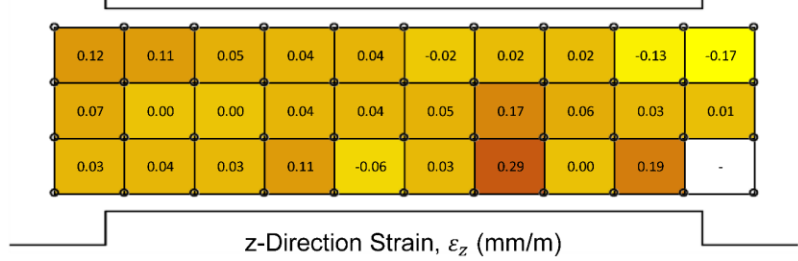
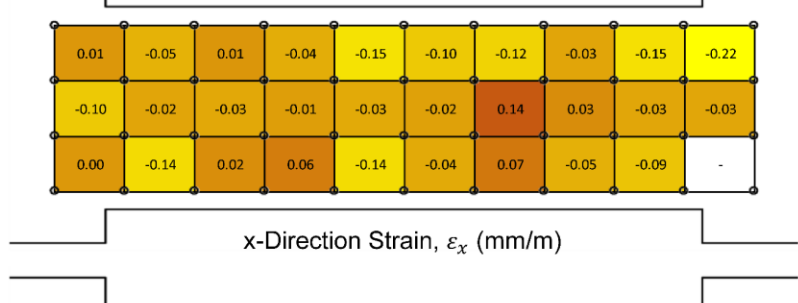
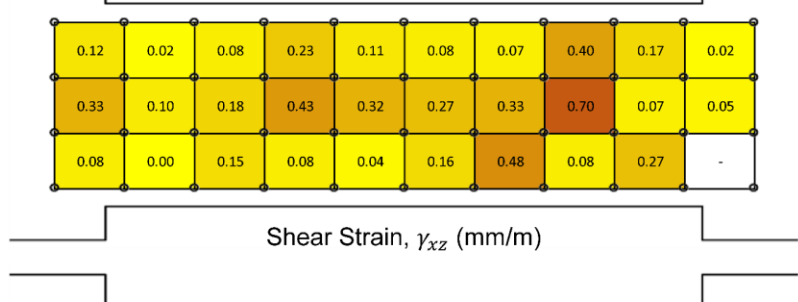
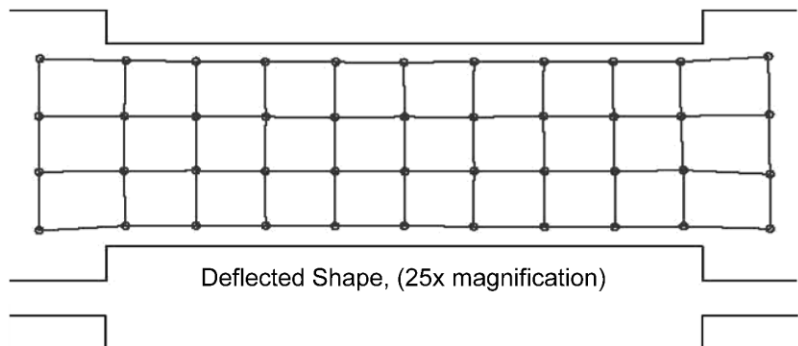
## Appendix F: LED Element Data

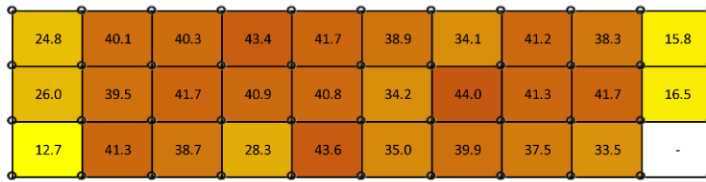
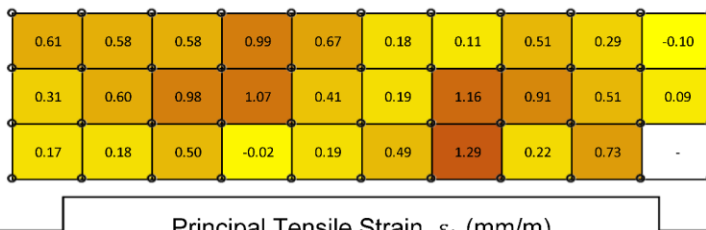
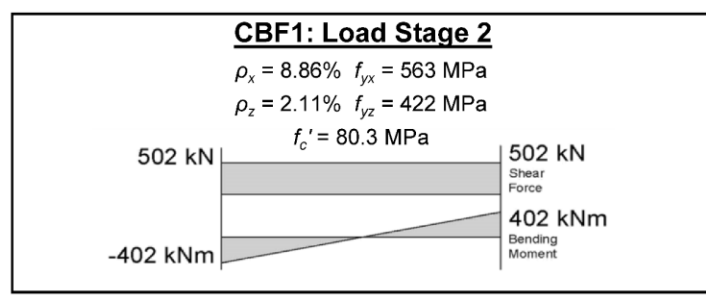
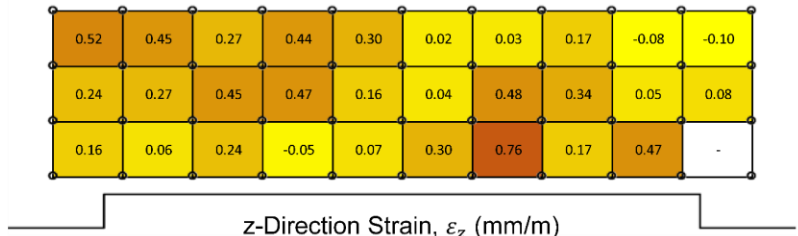
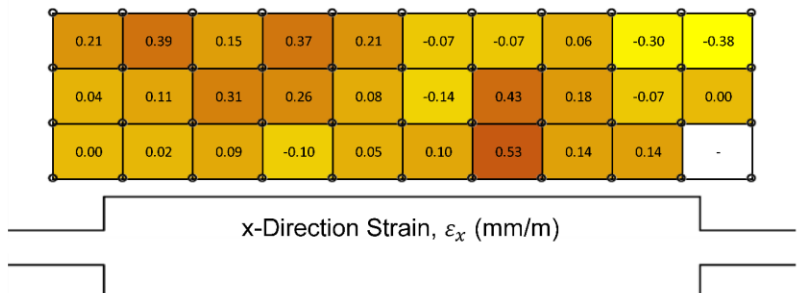
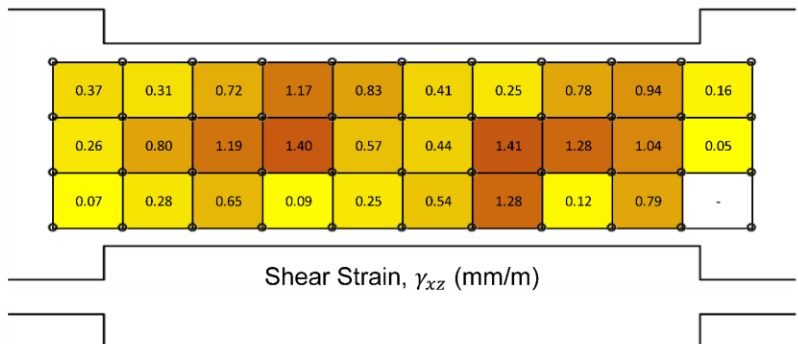
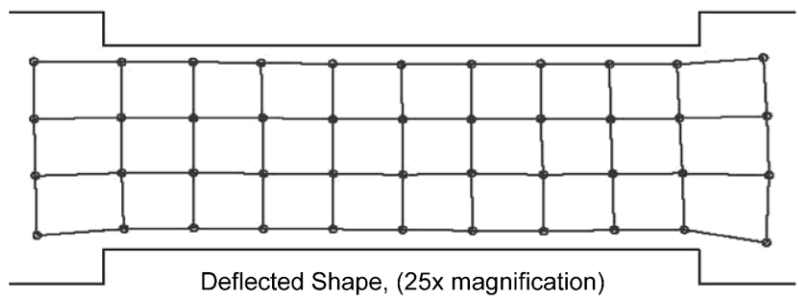
LED targets installed in an 11x4 grid were used to calculate local surface strains on the south face of the coupling beam specimens. The program Timeline written by Ruggiero [31] was used to determine the Mohr's circle of best fit for each LED element bound by four LED targets. The deflected shape, shear strains, x-direction and z-direction strains, principle tensile and compressive strains, and angle of principle compression are presented in Sections F.1 to F.4 for all load stages of specimens CBF1 to CBF4. The colour scale associated with each element strain is determined based on the highest and lowest values in the element grid, and isn't associated with any particular strain value. The colour scheme also varies for each load stage as the range of highest and lowest values changes.

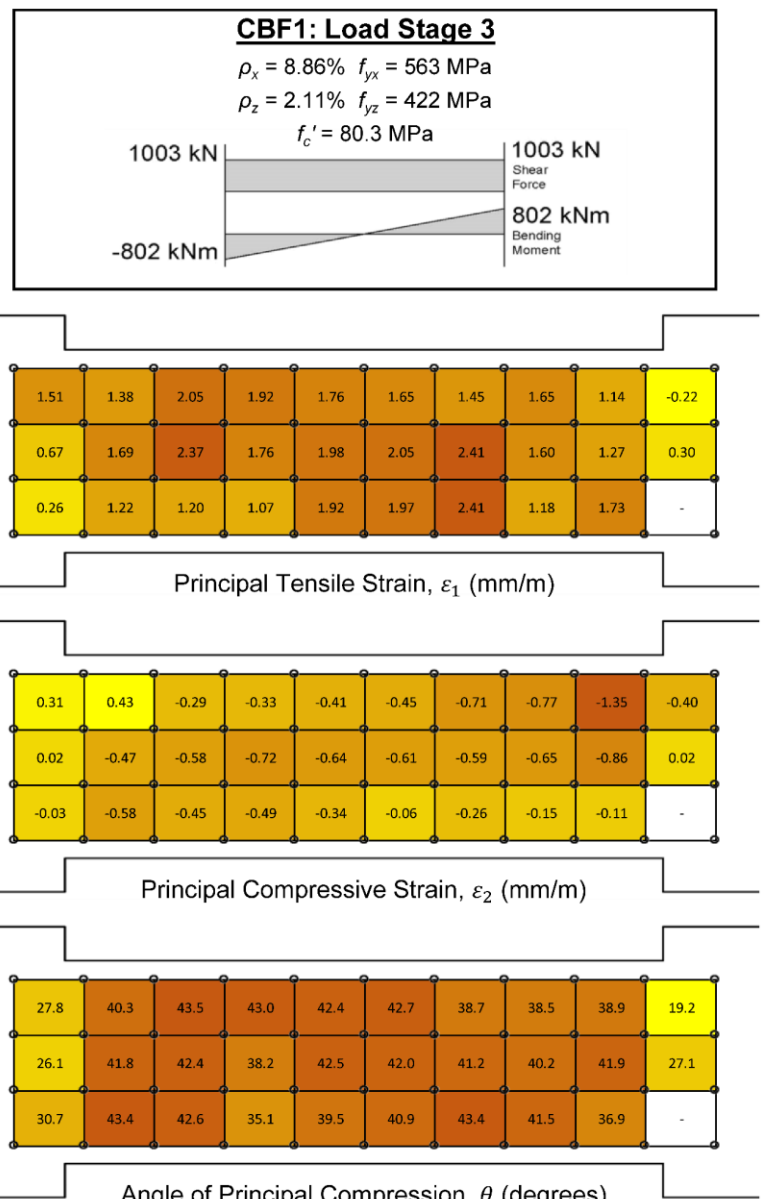
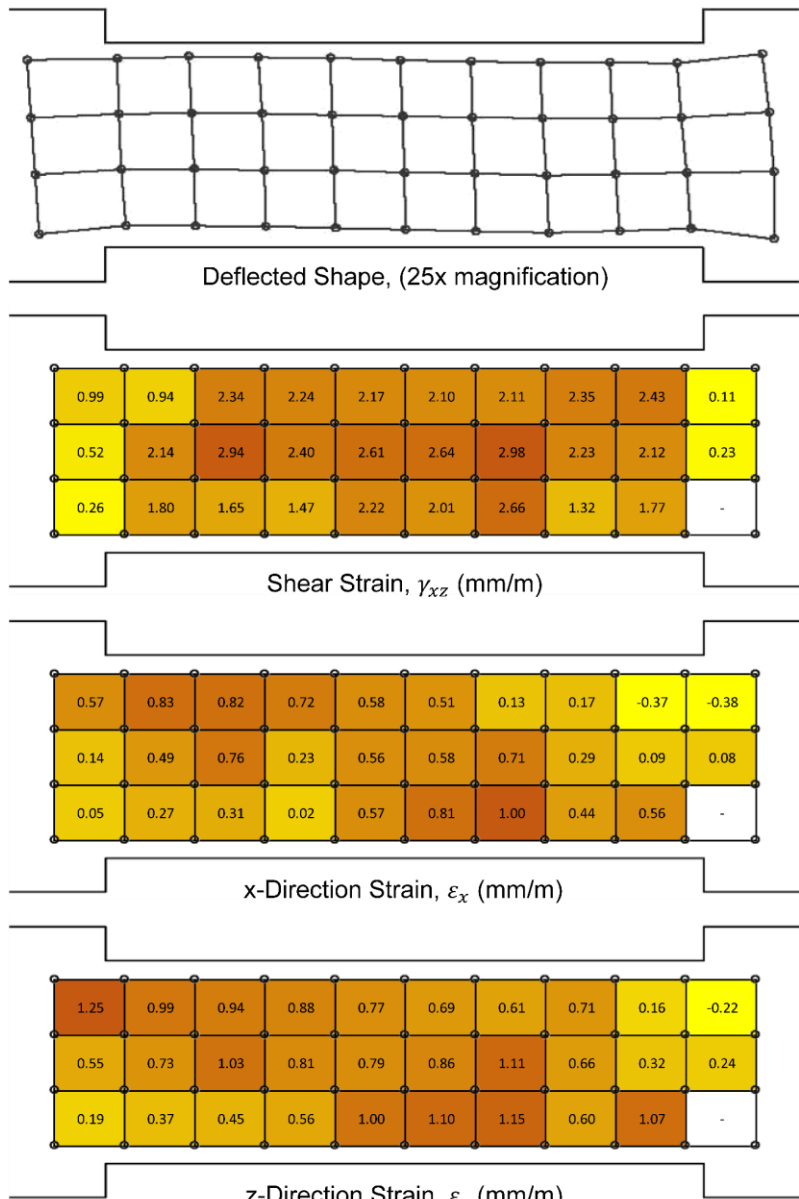
### F.1 LED Element Data for Specimen CBF1

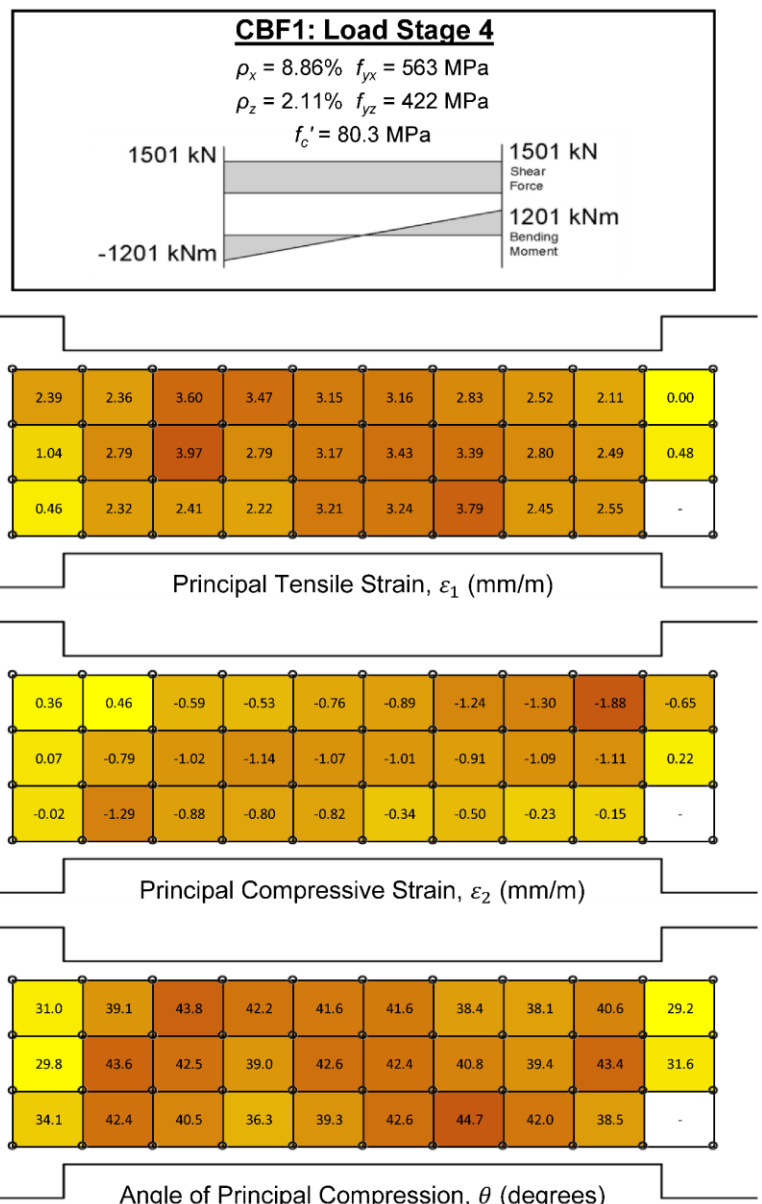
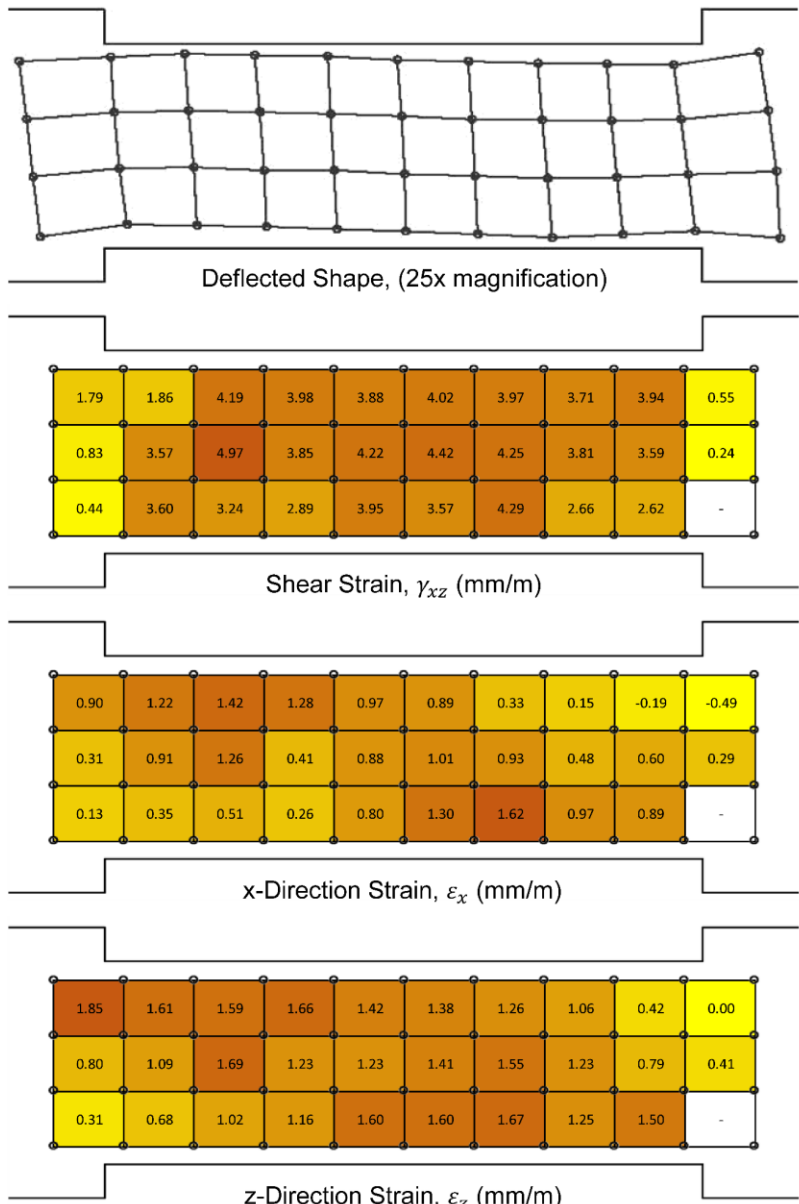
The LED targets placed on the shear wall end blocks were not on the same horizontal plane as the targets on the coupling beam due to the variation in concrete side cover. As a result, LED elements 1 to 3, and 28 to 30 do not accurately represent the strain state at the shear wall faces. The deflected shape of the beam is also influenced by these LED targets with the elements showing enlargement in the x and z-directions at the shear wall faces.

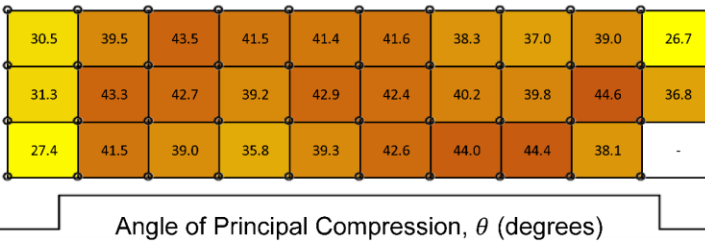
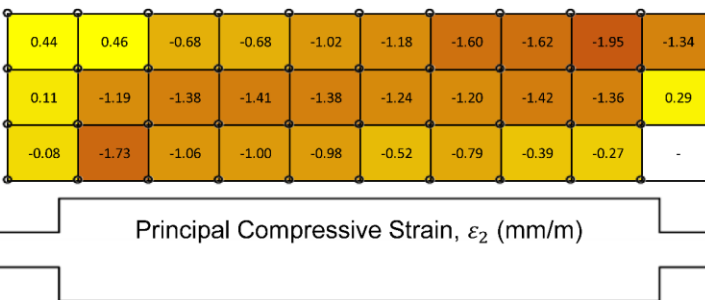
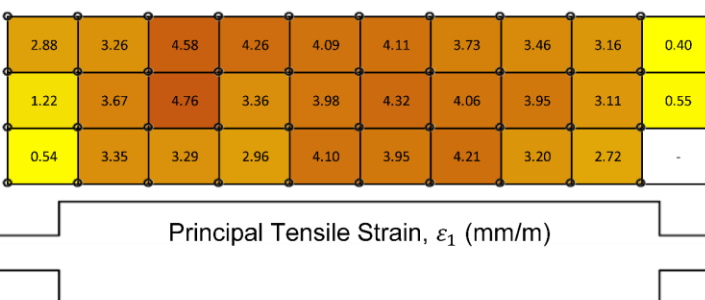
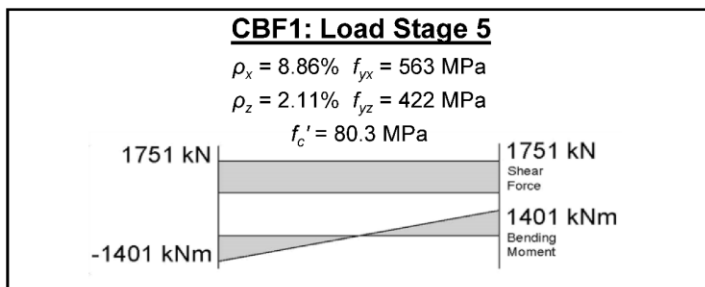
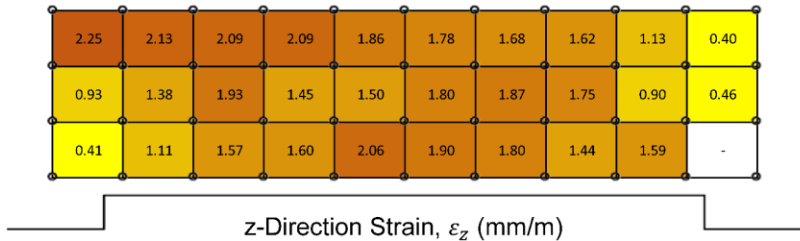
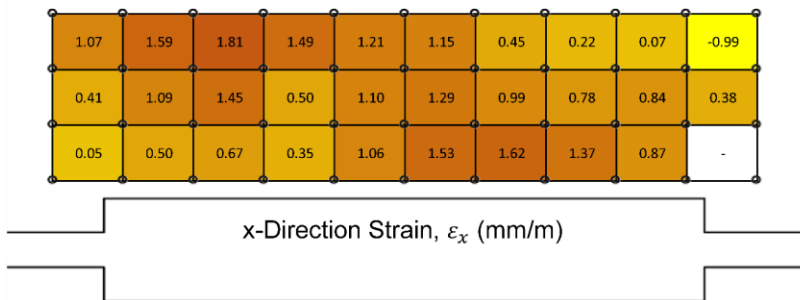
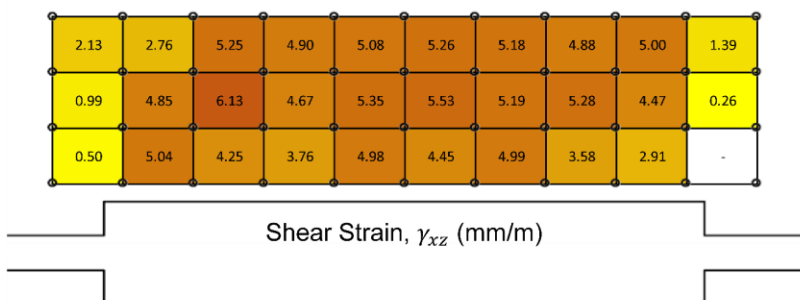
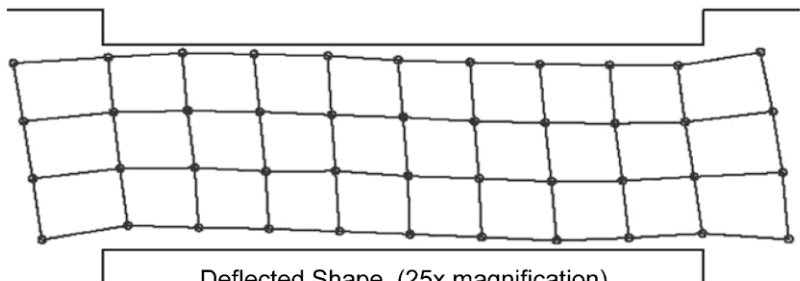
LED target 44, the bottom east target, kept flickering on and off during the test resulting in inaccurate strains for the bottom east element. The strains for element 30 were removed from the diagrams in order to prevent a skew of the colour distributions. LED target 44 was replaced halfway through the test, however the flickering persisted, indicating it was an issue with the LED connector box and not the target itself.

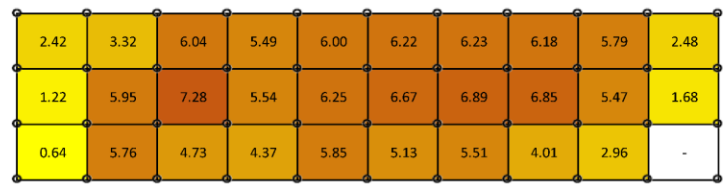
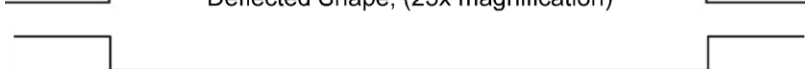
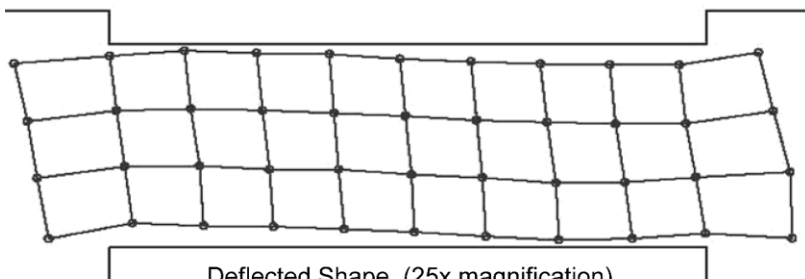












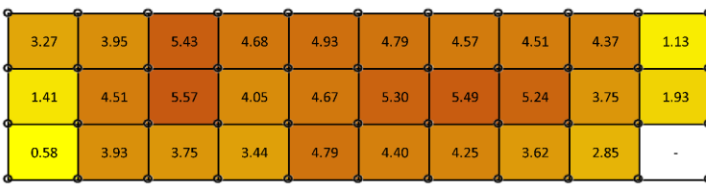
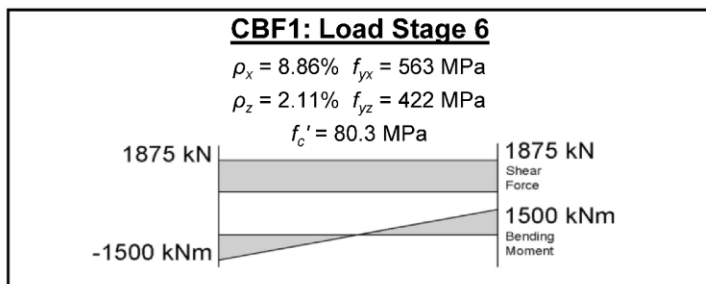
Shear Strain,  $\gamma_{xz}$  (mm/m)



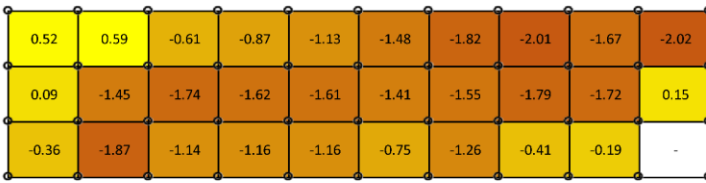
x-Direction Strain,  $\varepsilon_x$  (mm/m)



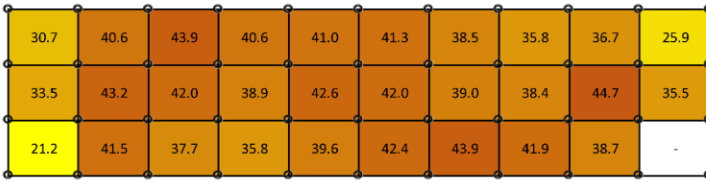
z-Direction Strain,  $\varepsilon_z$  (mm/m)



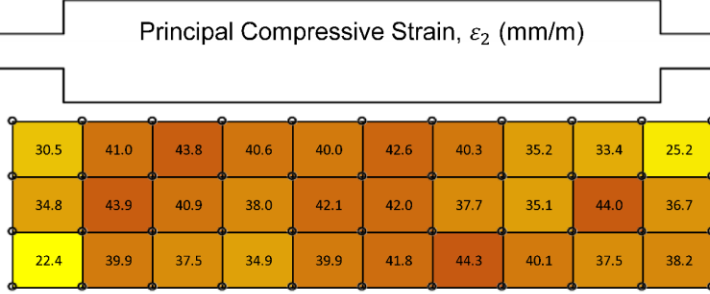
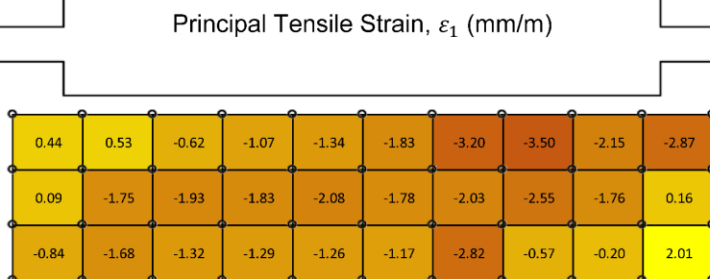
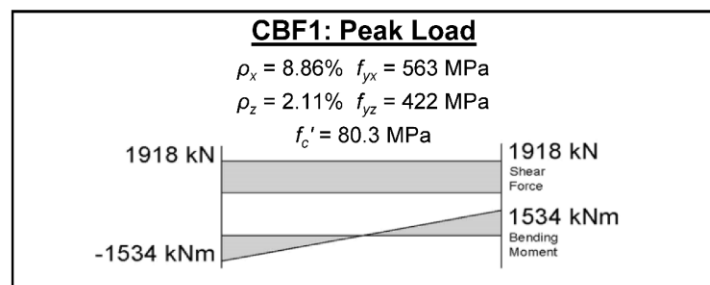
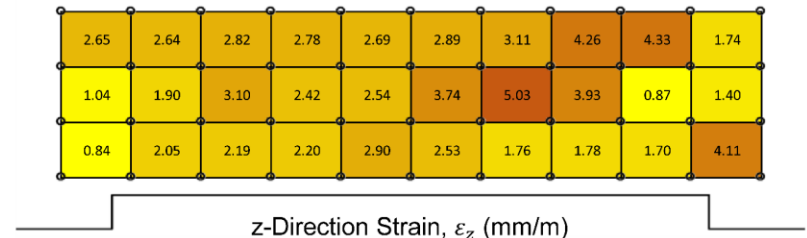
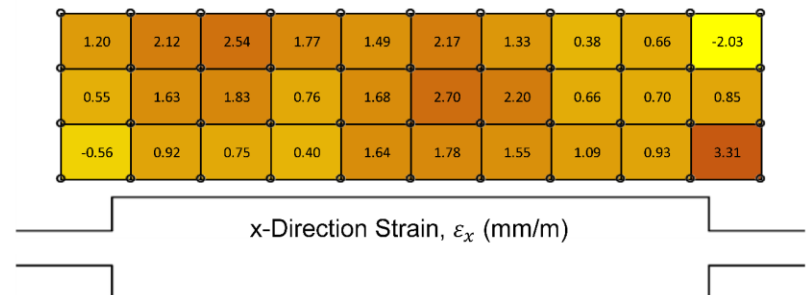
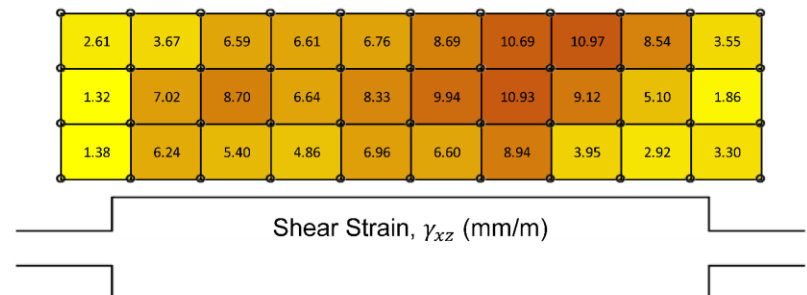
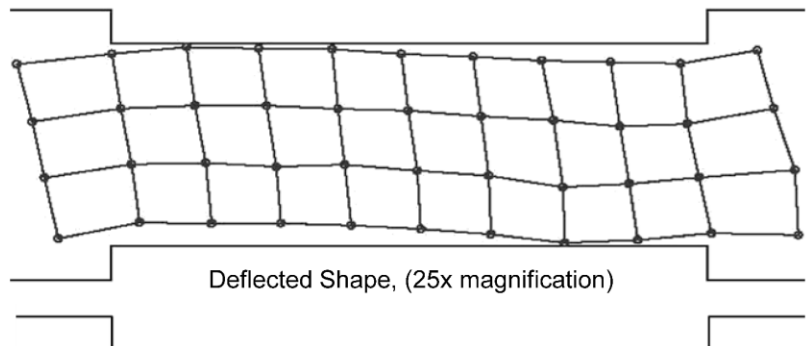
Principal Tensile Strain,  $\varepsilon_1$  (mm/m)

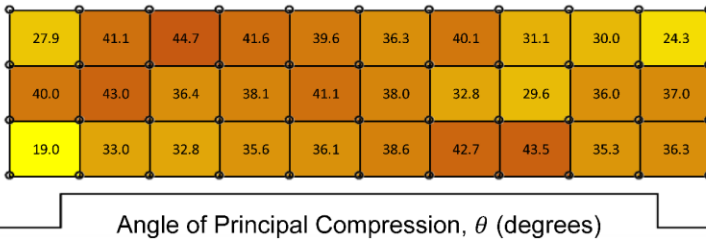
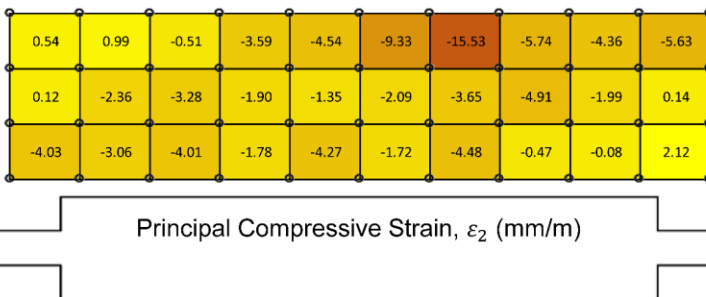
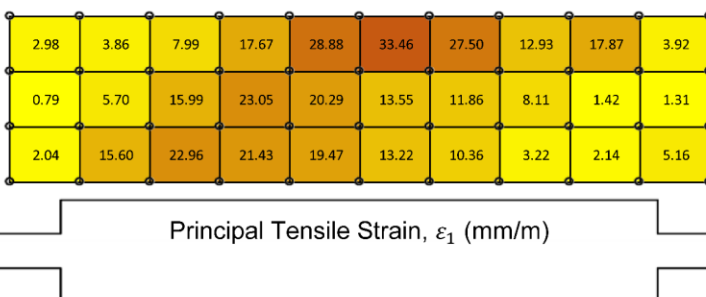
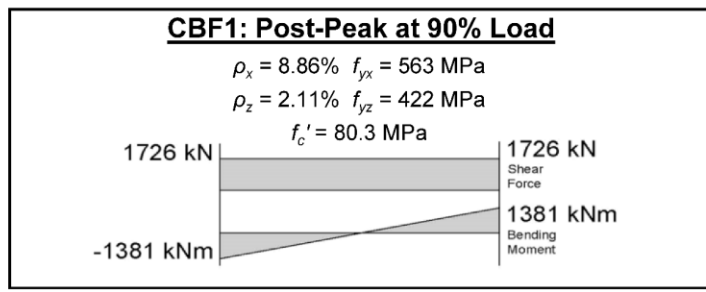
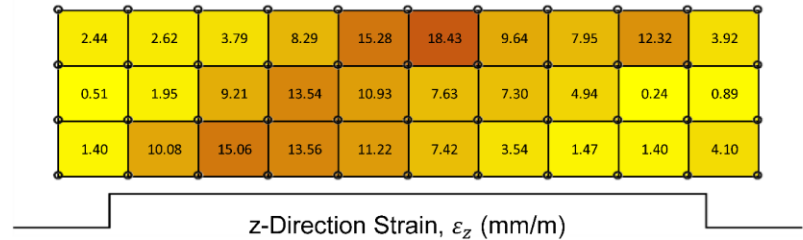
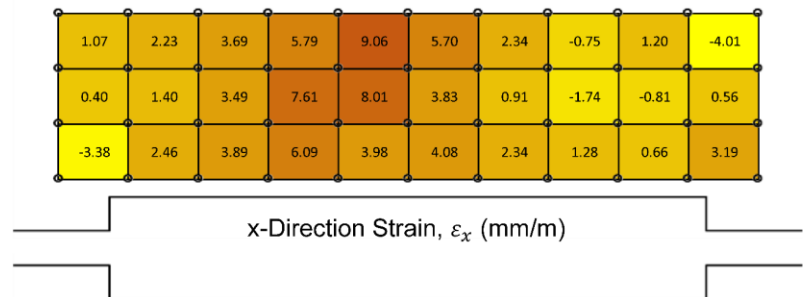
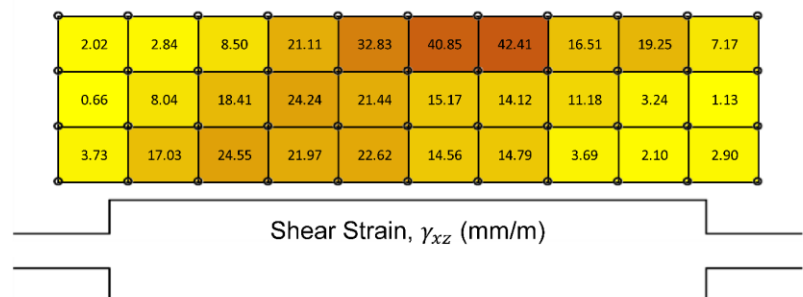
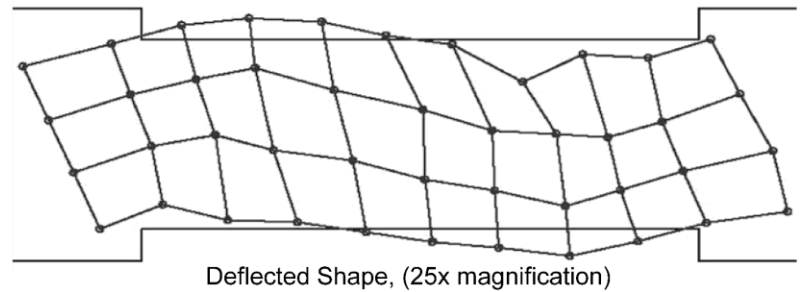


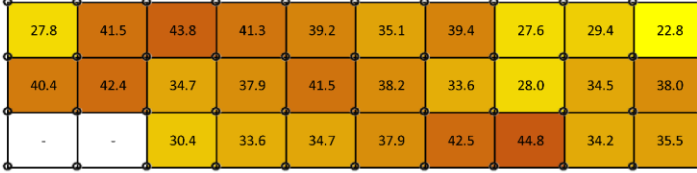
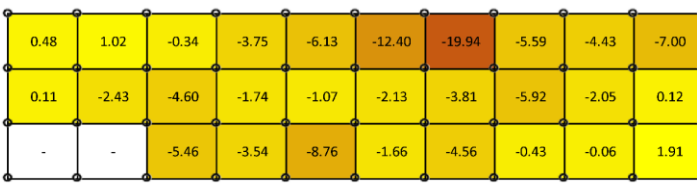
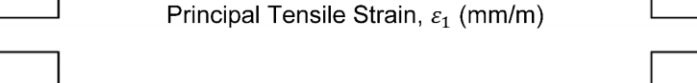
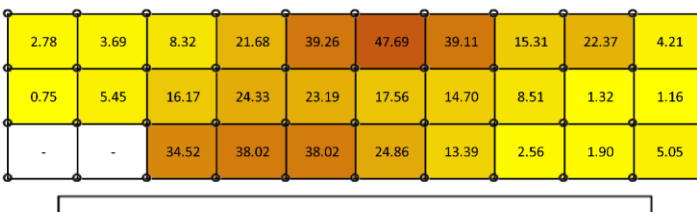
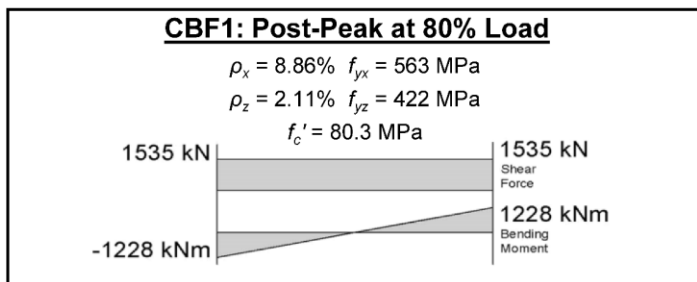
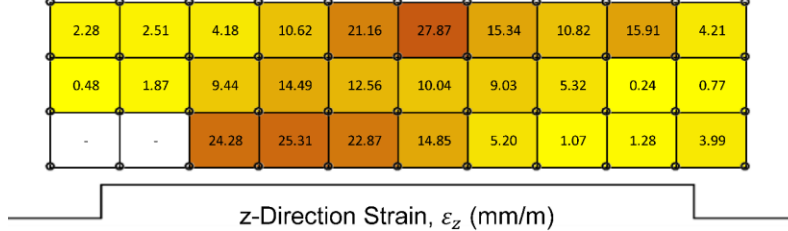
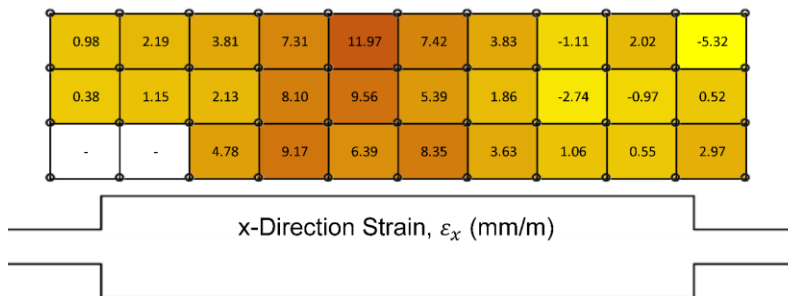
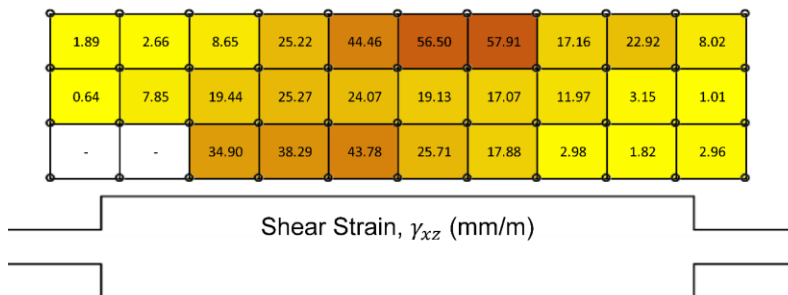
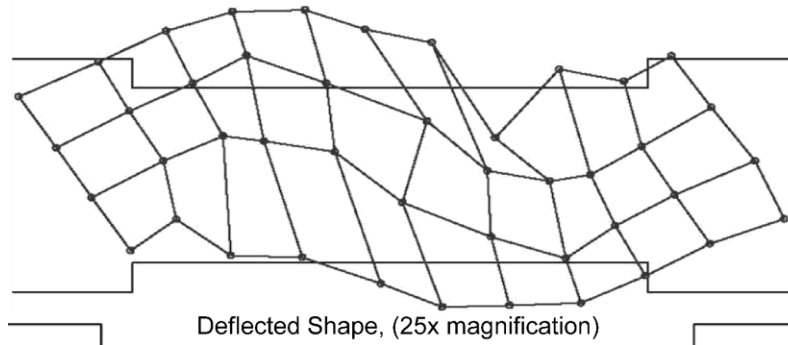
Principal Compressive Strain,  $\varepsilon_2$  (mm/m)

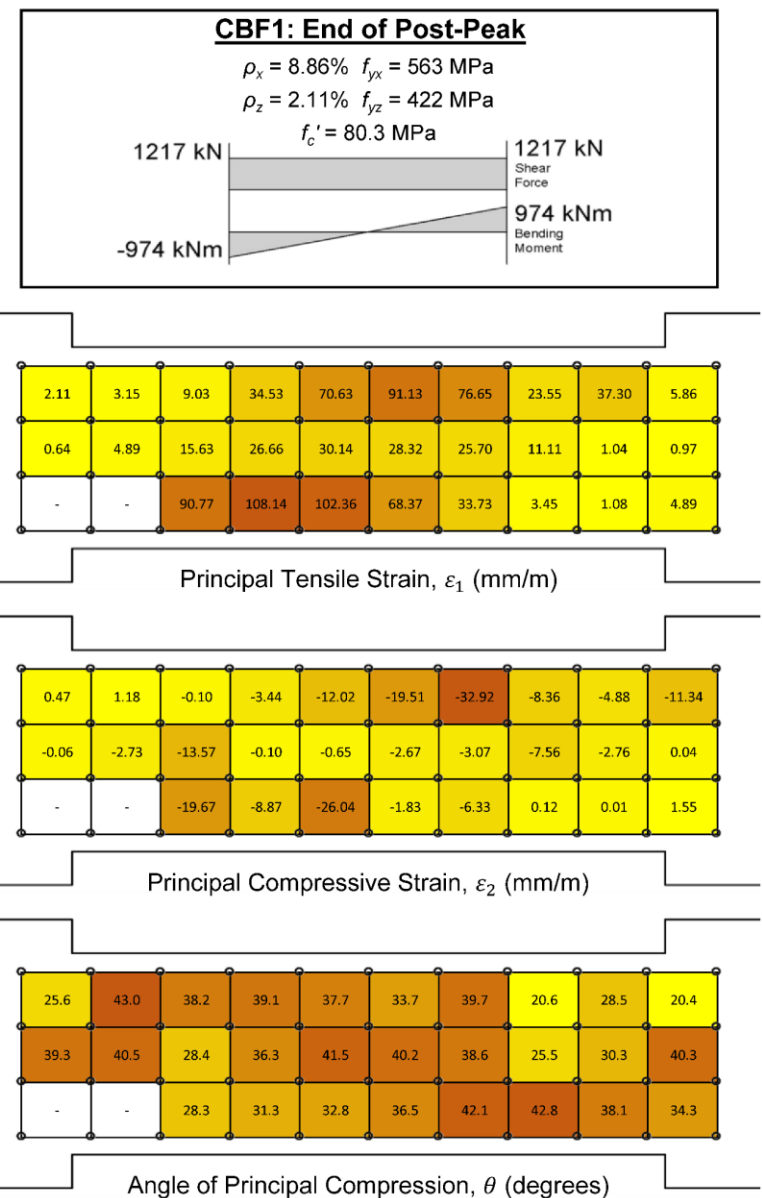
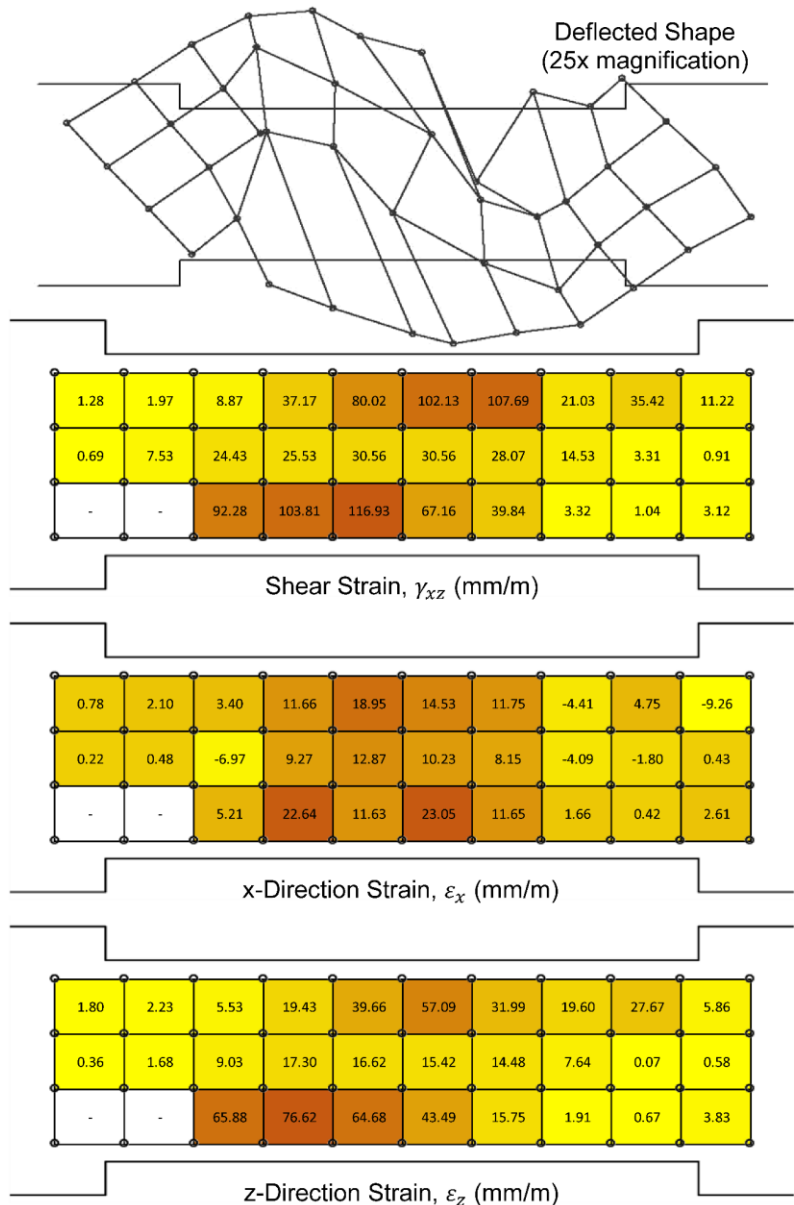


Angle of Principal Compression,  $\theta$  (degrees)



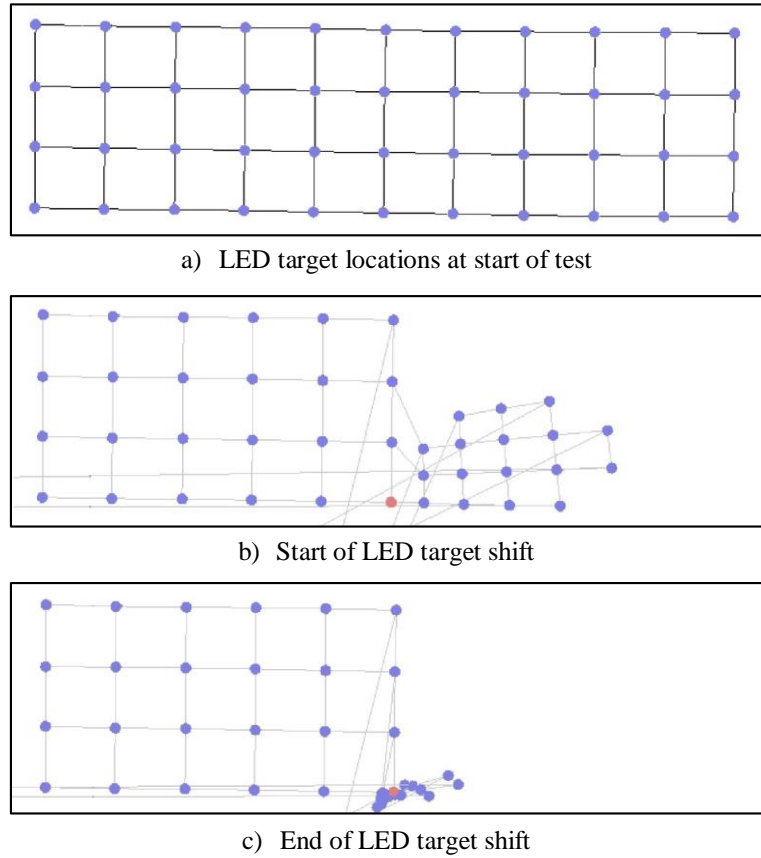






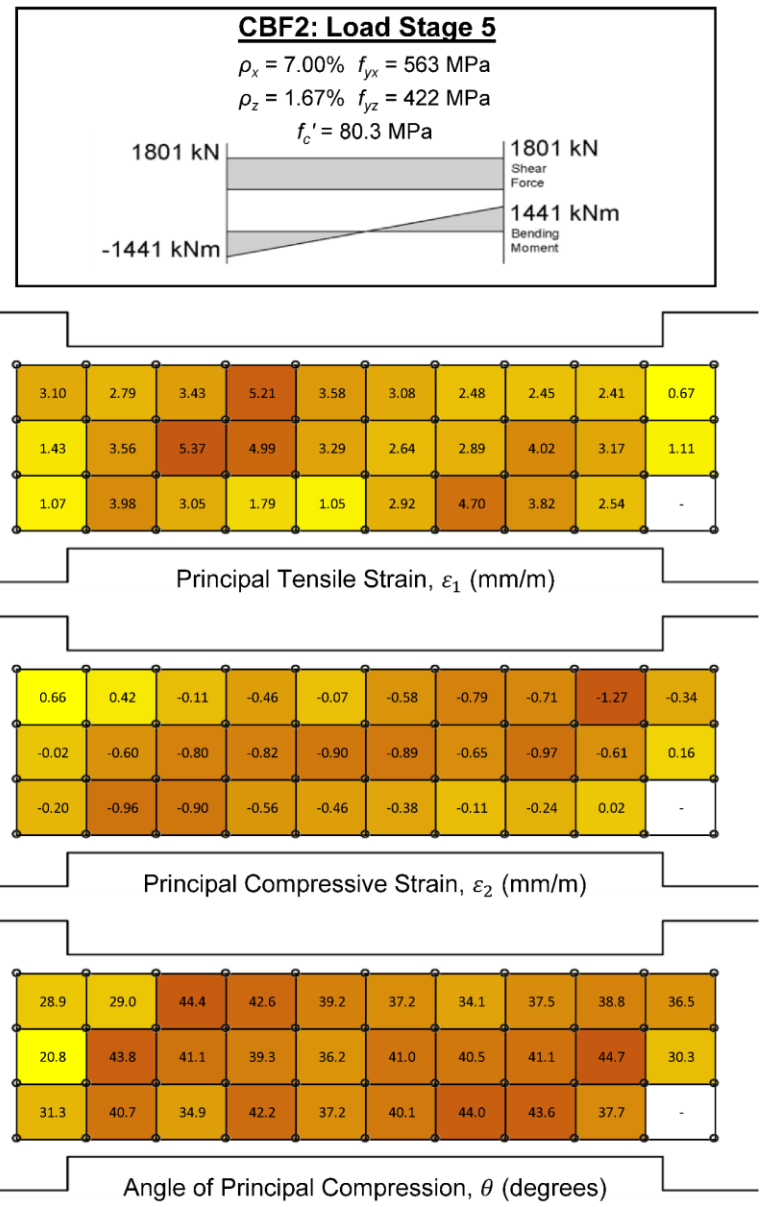
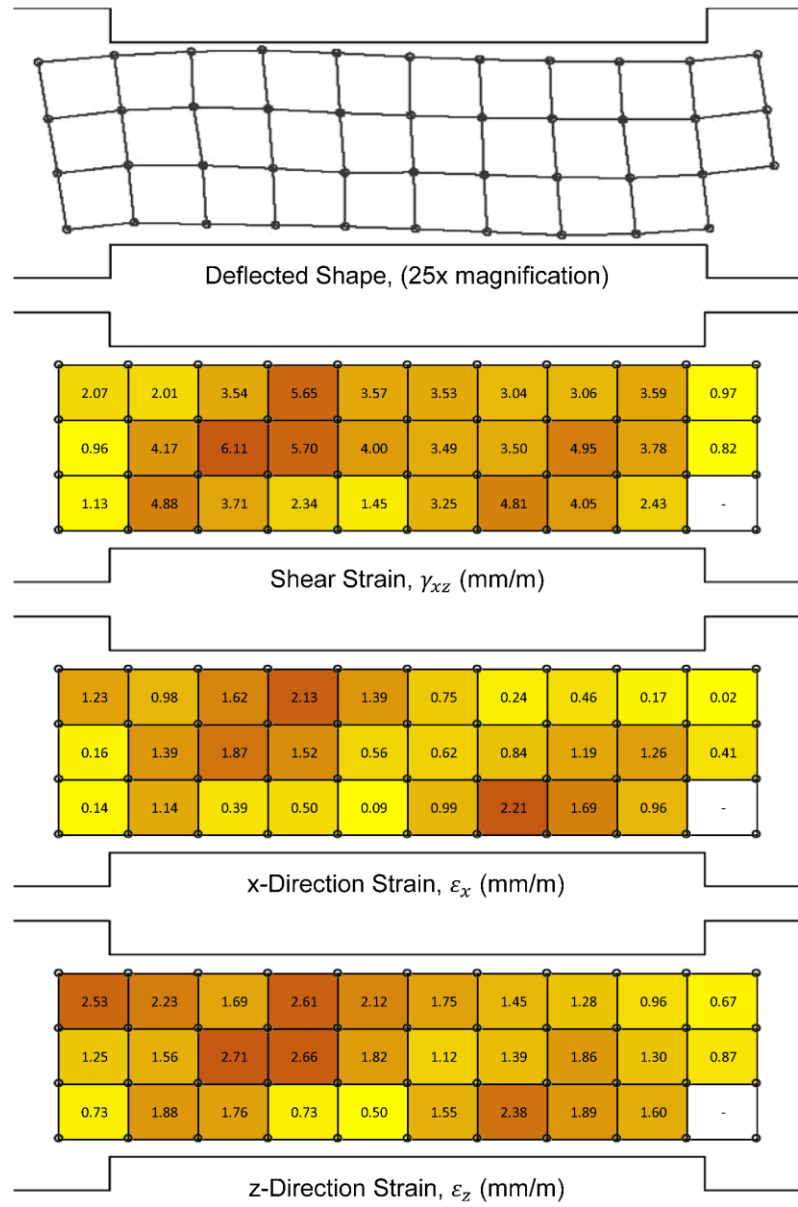
## F.2 LED Element Data for Specimen CBF2

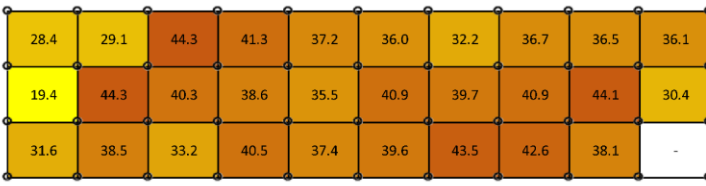
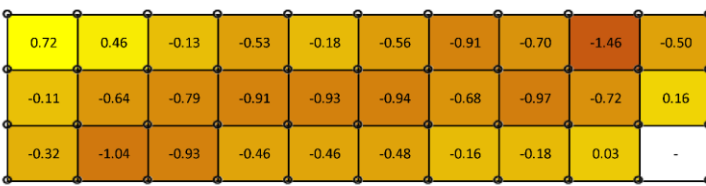
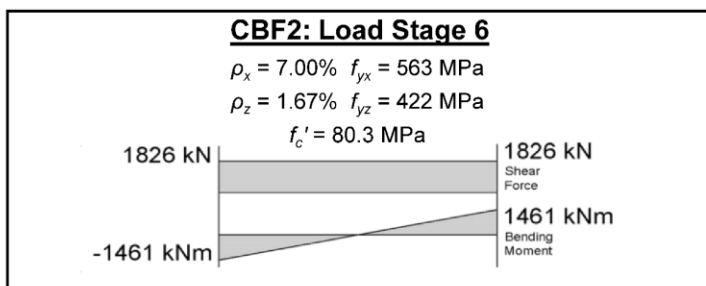
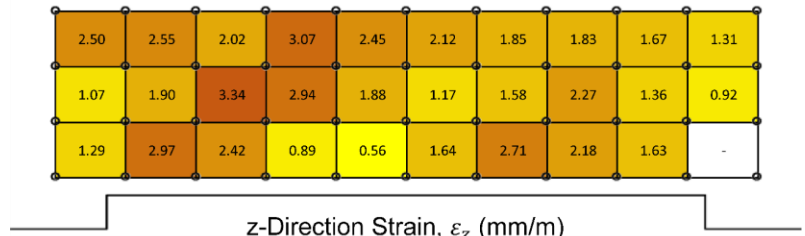
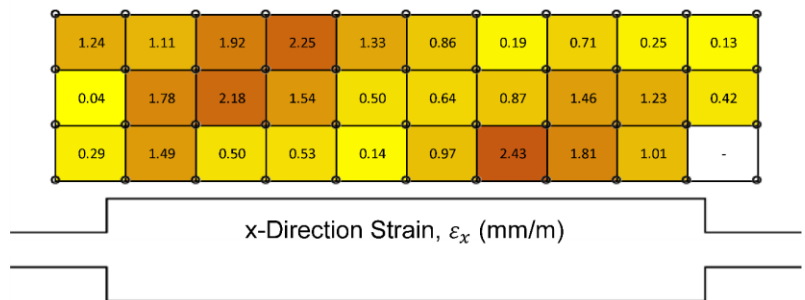
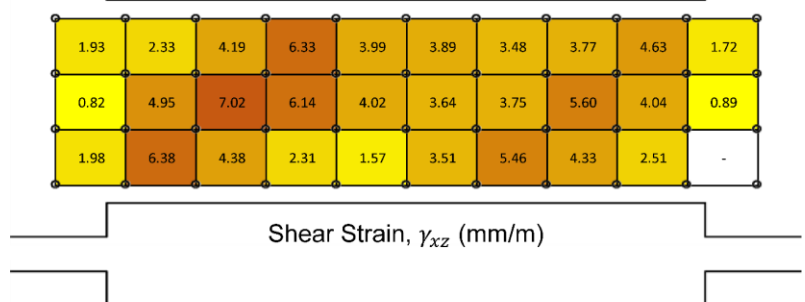
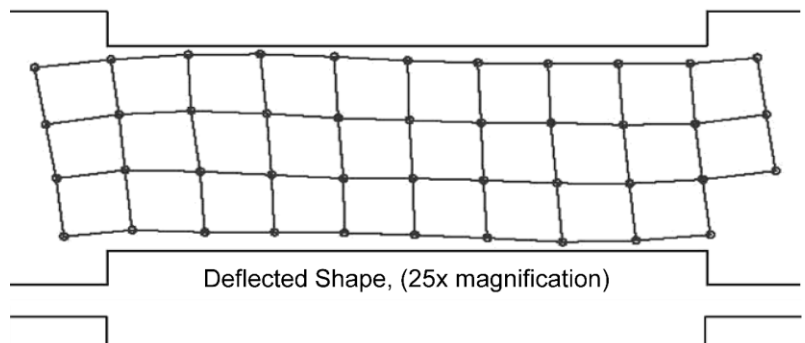
All LED data recorded up to and including load stage four was erroneous in nature due to an unknown bug in the LED software. Two cable boxes were used to connect the LED targets to the computer system, with each controlling half of the LED targets. The problem occurred with the east cable box. All of the LED target locations converged to the target in the first slot of the cable box. This shift occurred in less than a second and happened during the first load stage. The error was not noticed during testing since the camera software still recorded data and showed the targets as visible in their proper locations. Figure F-1 shows the LED location shift.

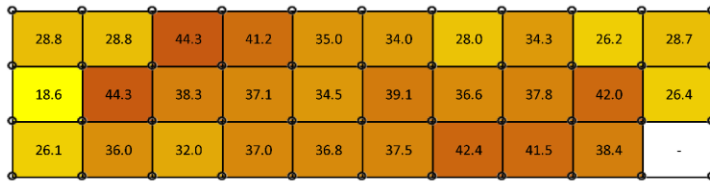
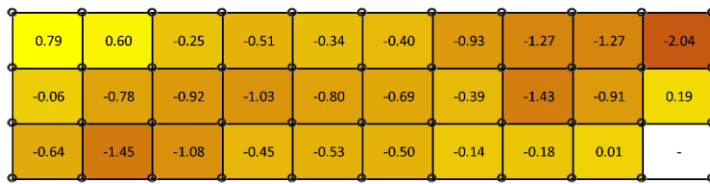
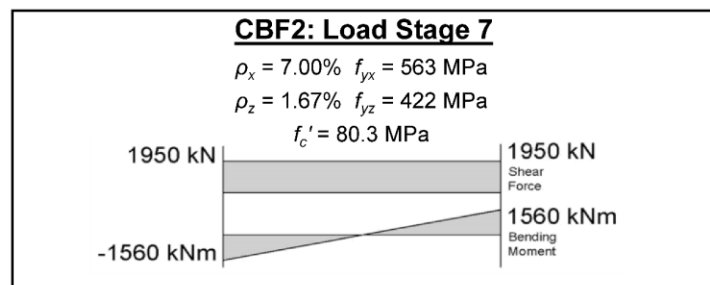
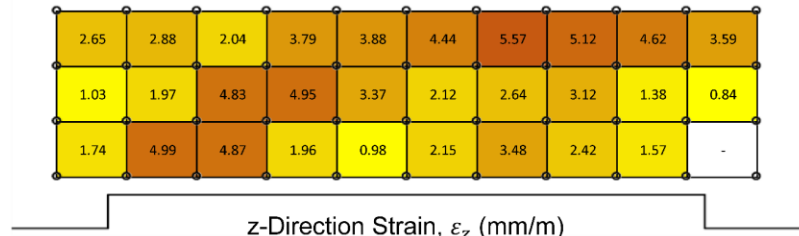
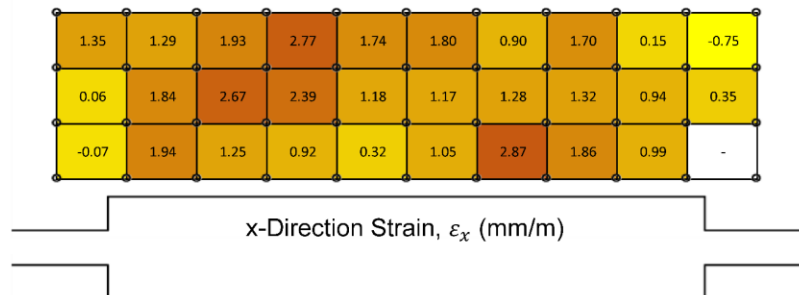
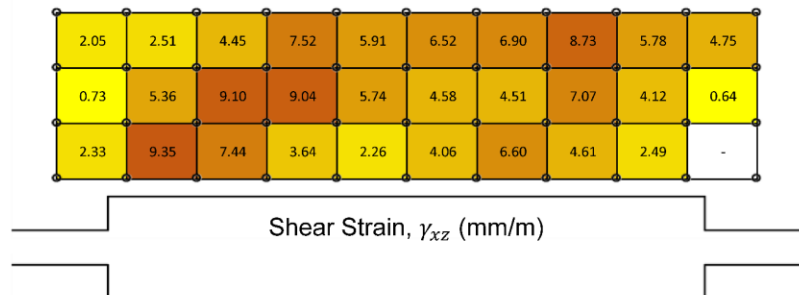
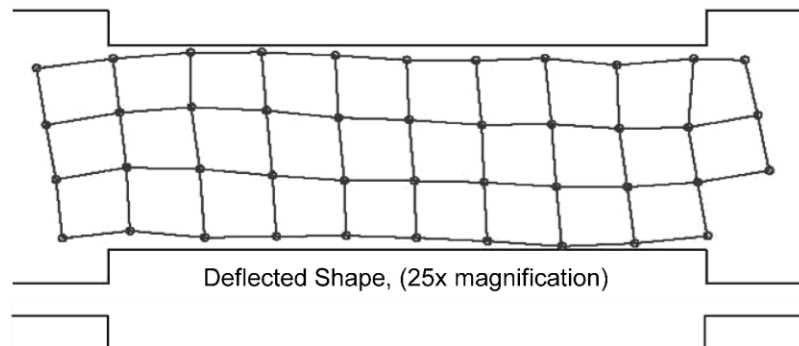


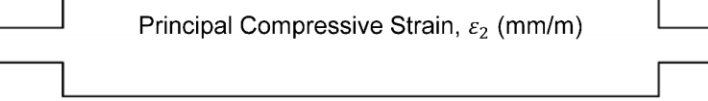
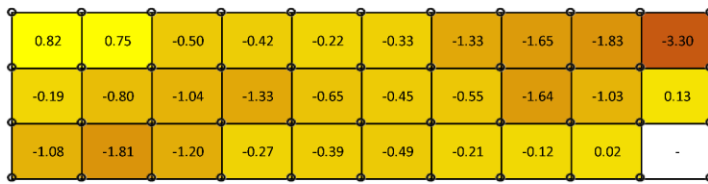
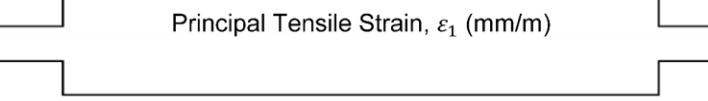
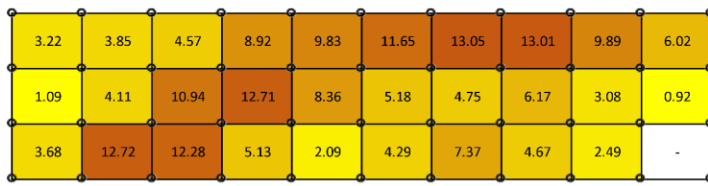
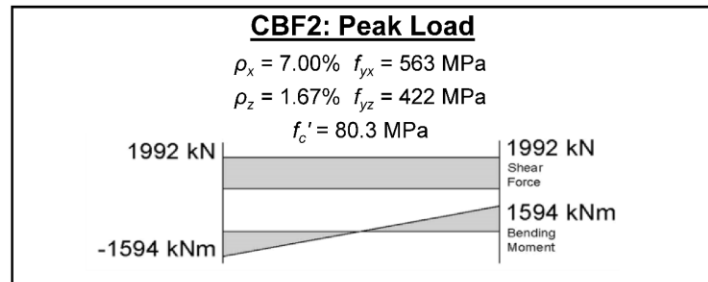
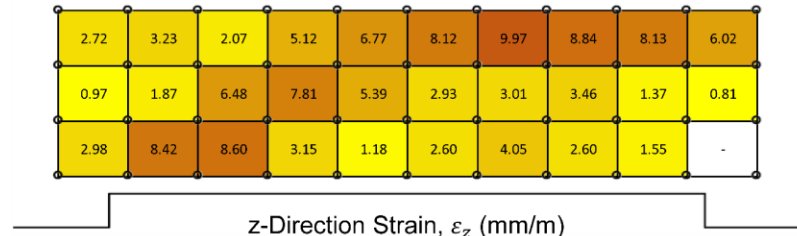
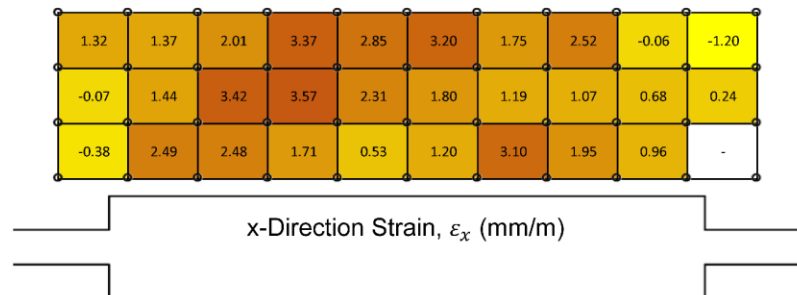
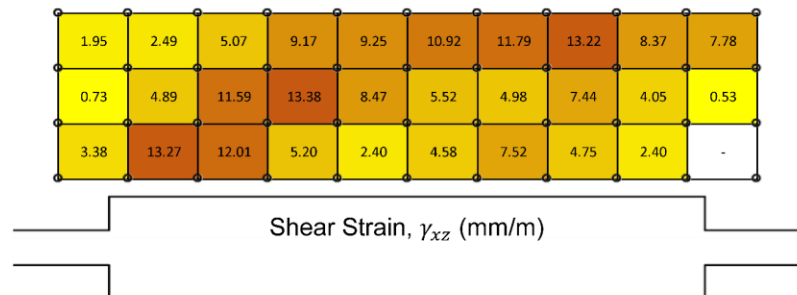
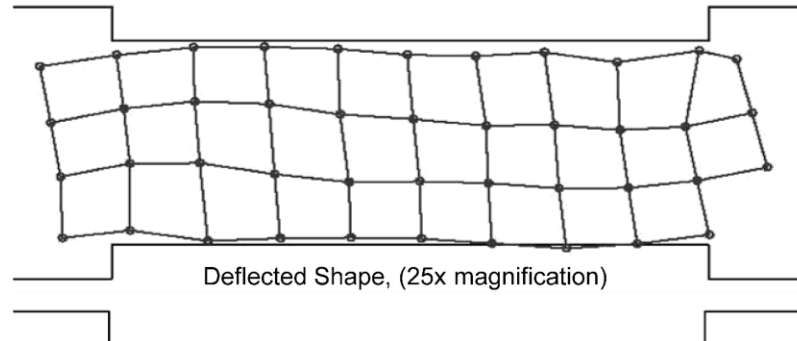
*Figure F-1: LED Target Shift for CBF2*

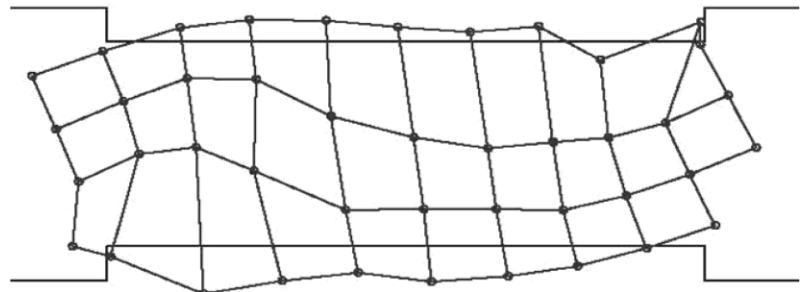
LED target 44, the bottom east target, kept flickering on and off during the measurements taken after load stage four, resulting in inaccurate strains for the bottom east element. The strains for element 30 were removed from the diagrams in order to prevent a skew of the colour distributions.



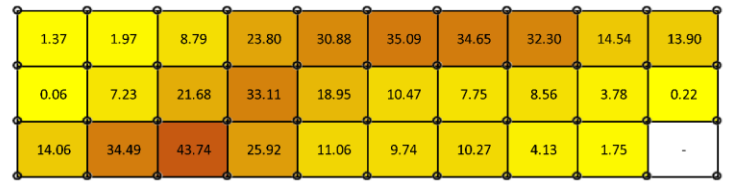




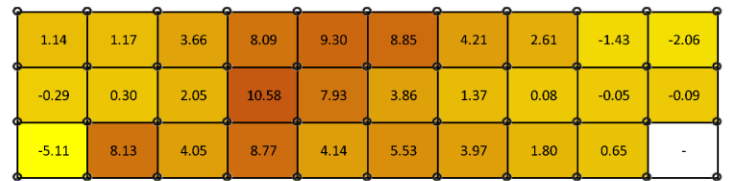




Deflected Shape, (25x magnification)



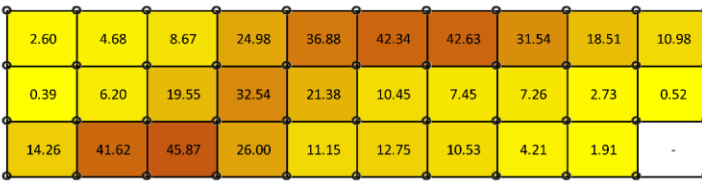
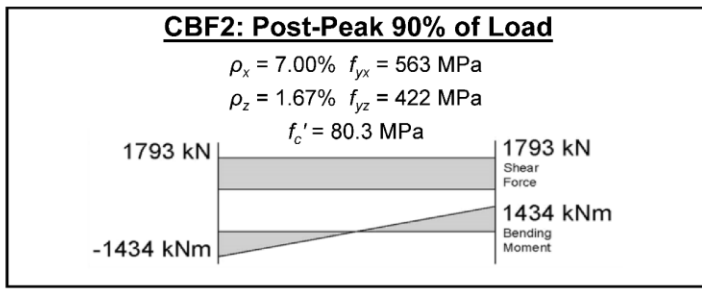
Shear Strain,  $\gamma_{xz}$  (mm/m)



x-Direction Strain,  $\varepsilon_x$  (mm/m)



z-Direction Strain,  $\varepsilon_z$  (mm/m)



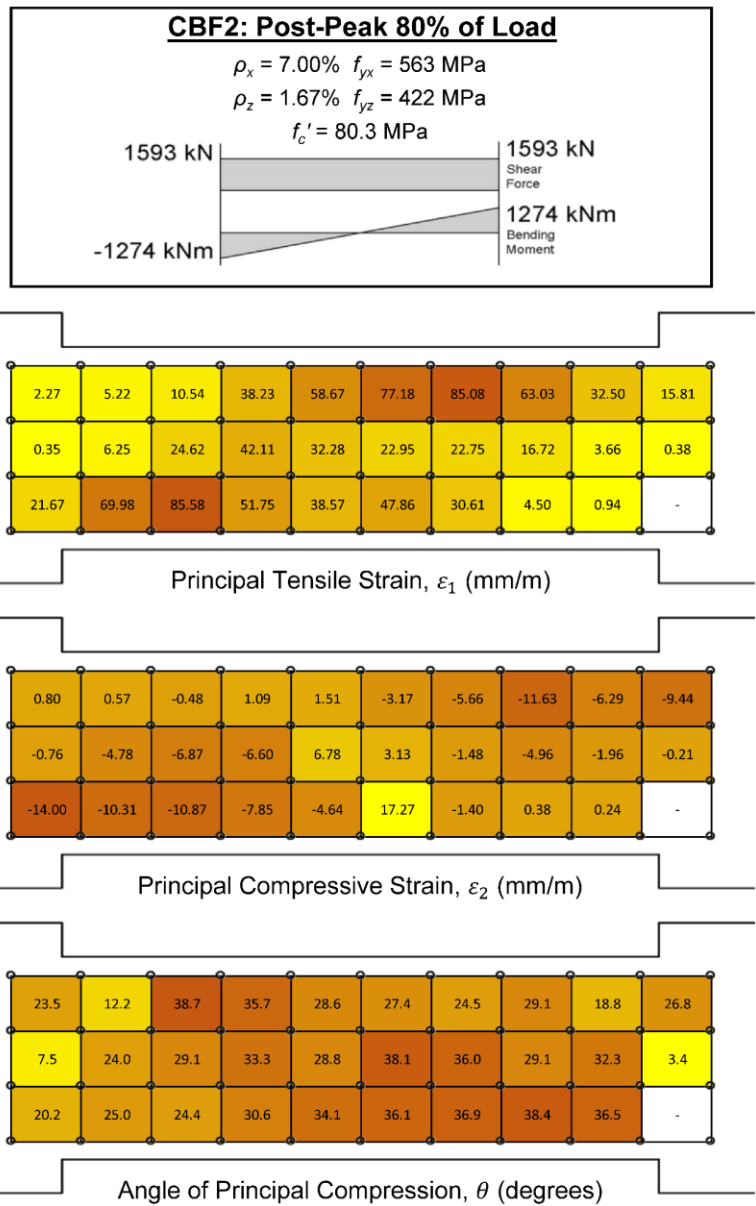
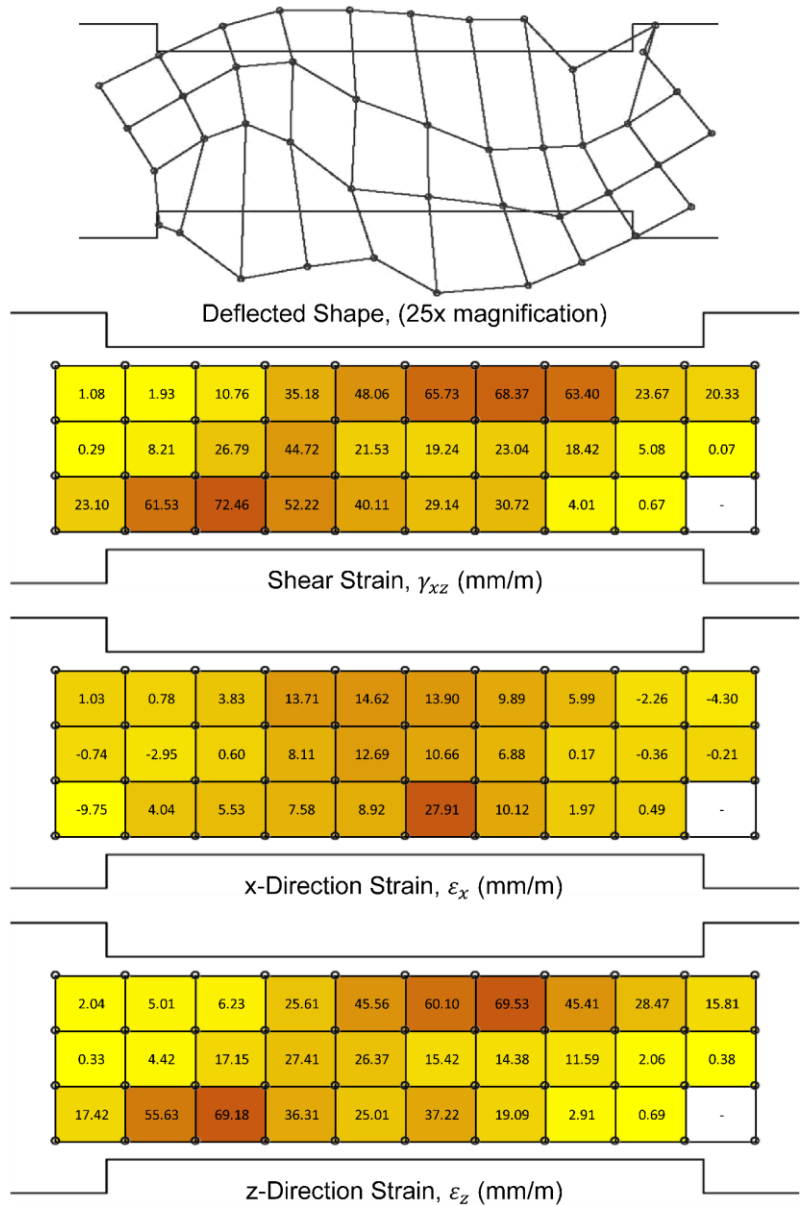
Principal Tensile Strain,  $\varepsilon_1$  (mm/m)



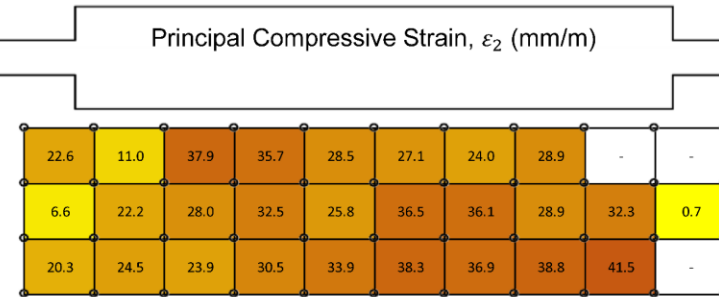
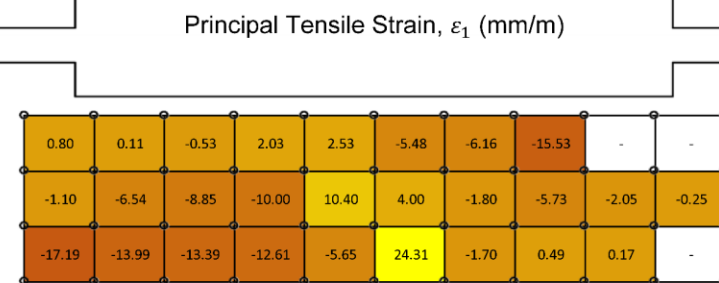
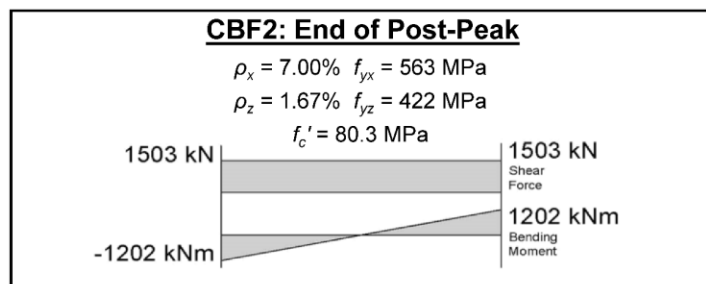
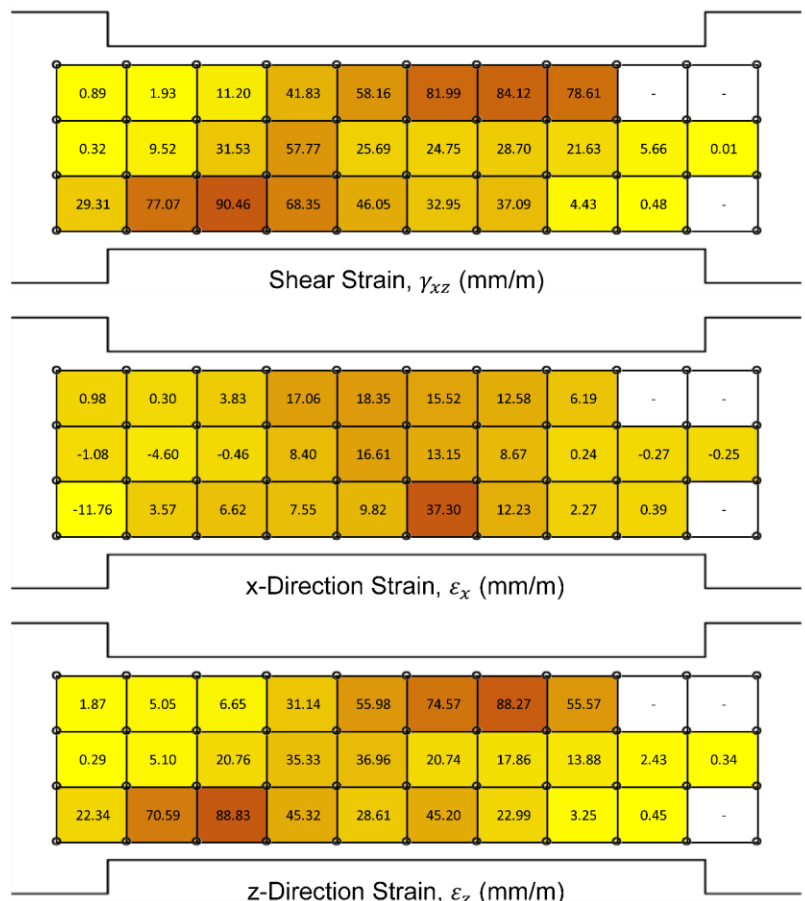
Principal Compressive Strain,  $\varepsilon_2$  (mm/m)



Angle of Principal Compression,  $\theta$  (degrees)



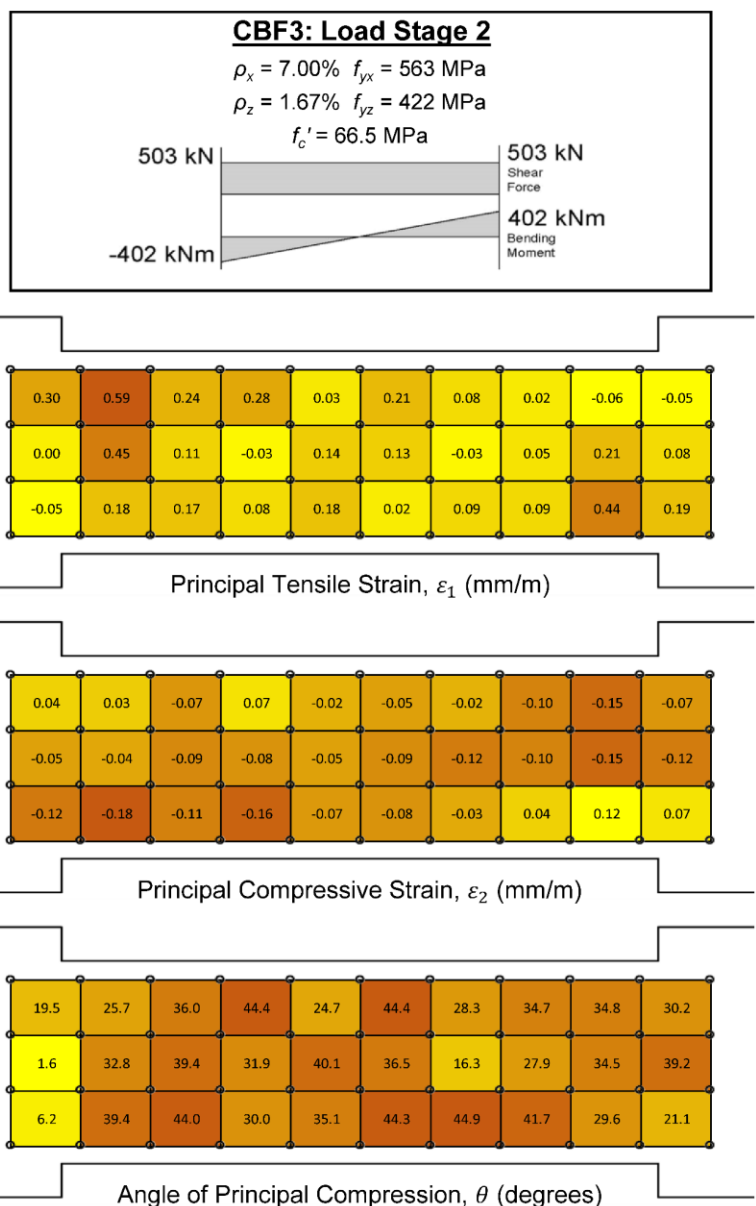
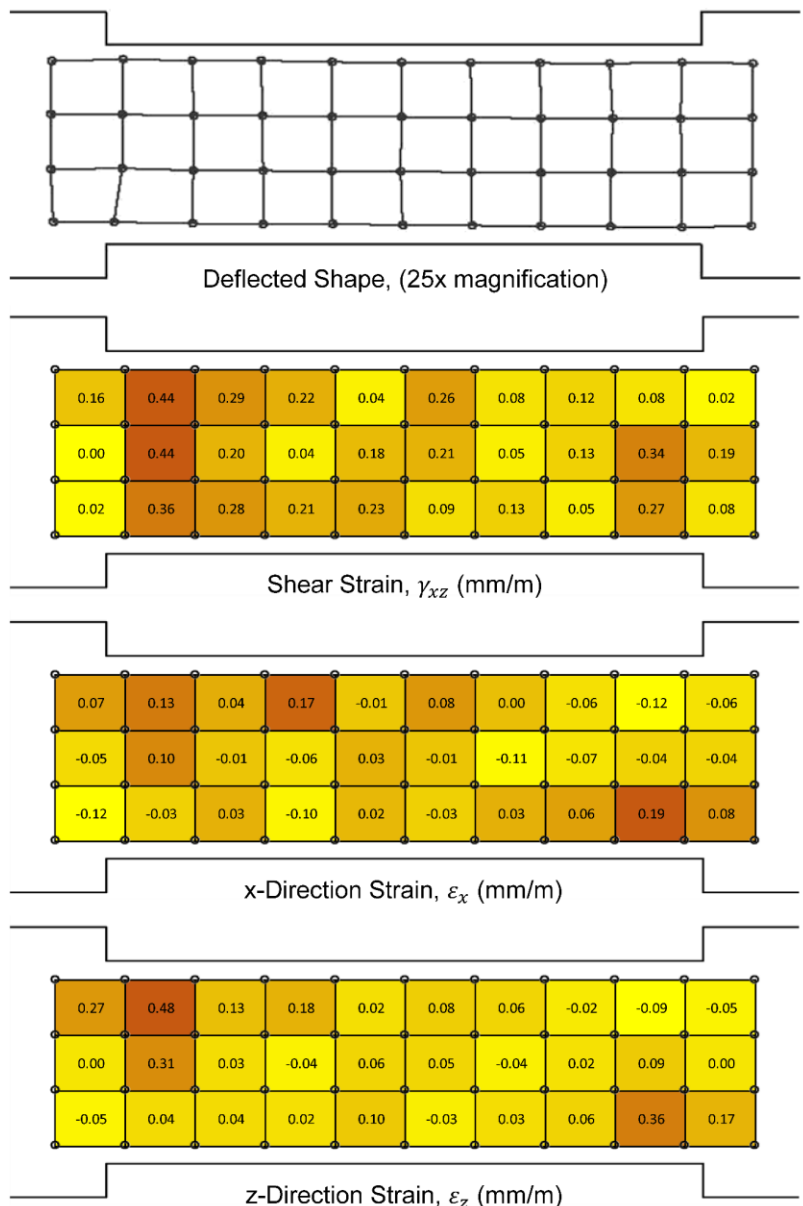
NO IMAGE AVAILABLE

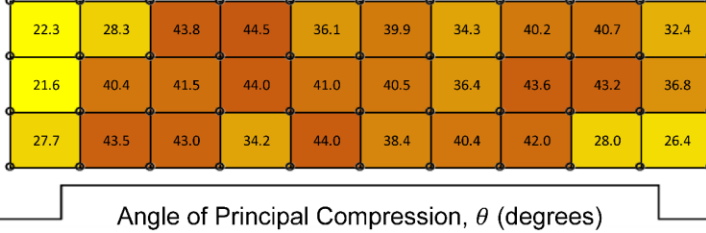
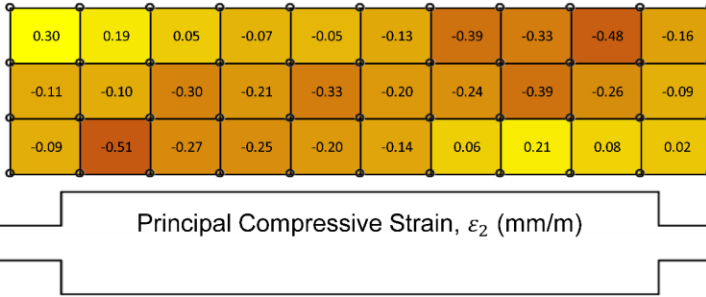
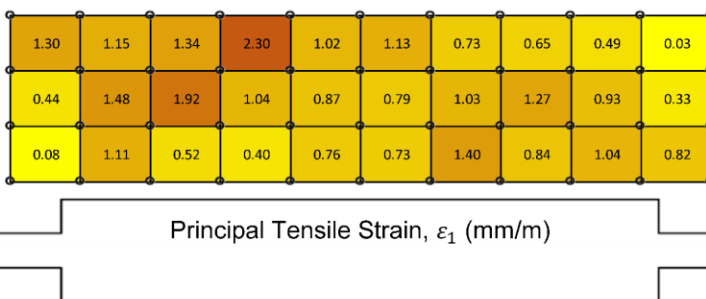
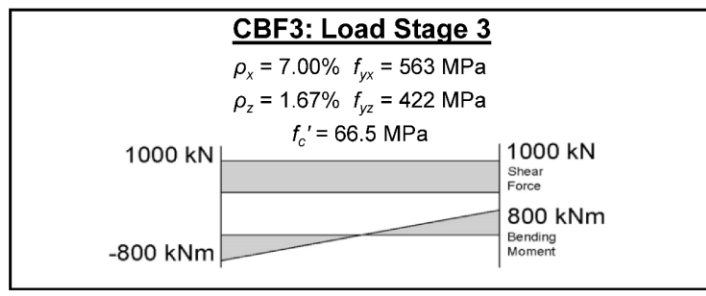
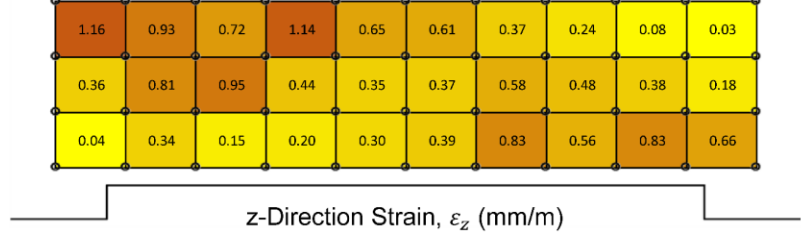
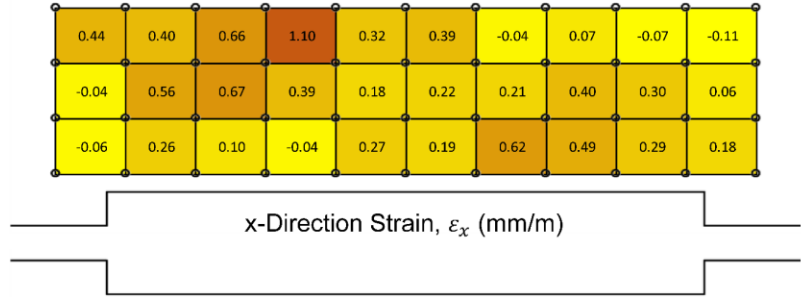
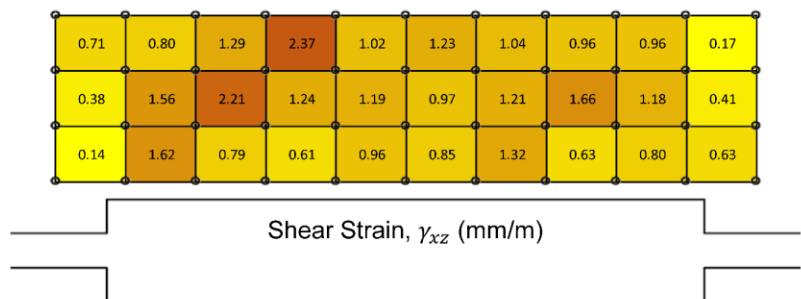
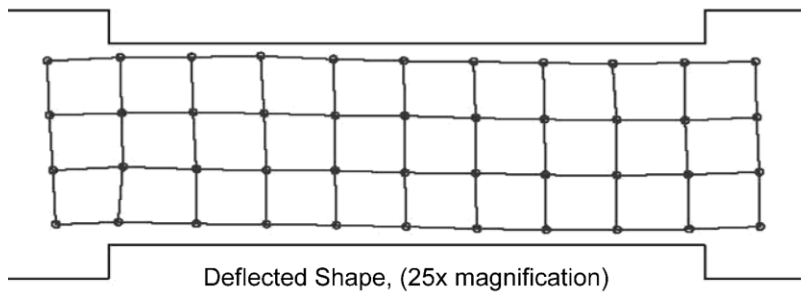


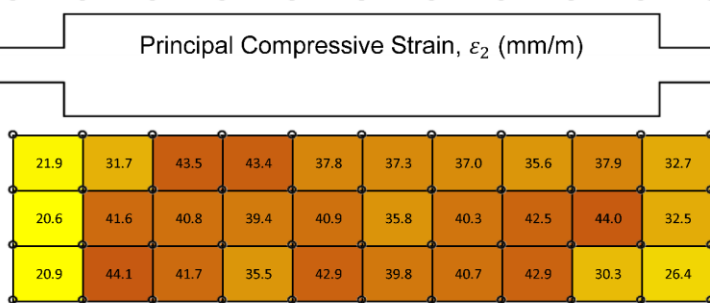
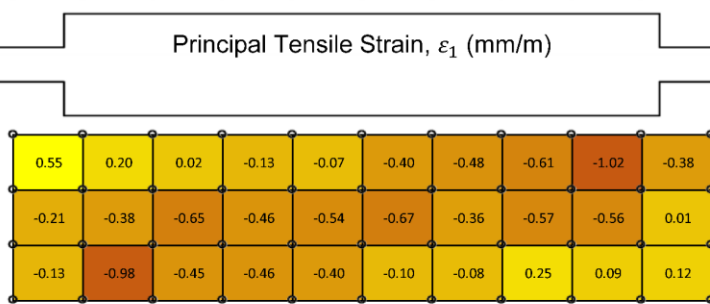
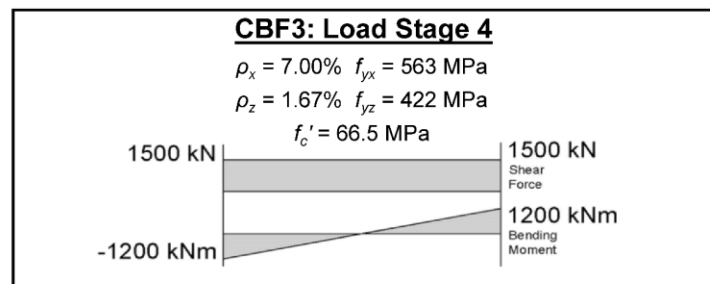
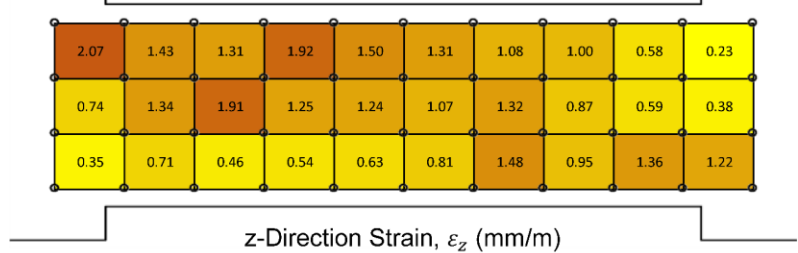
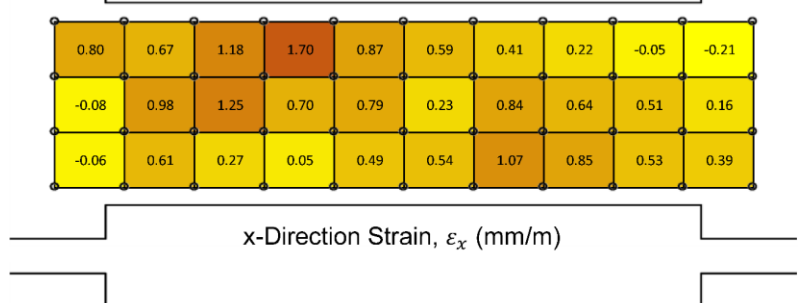
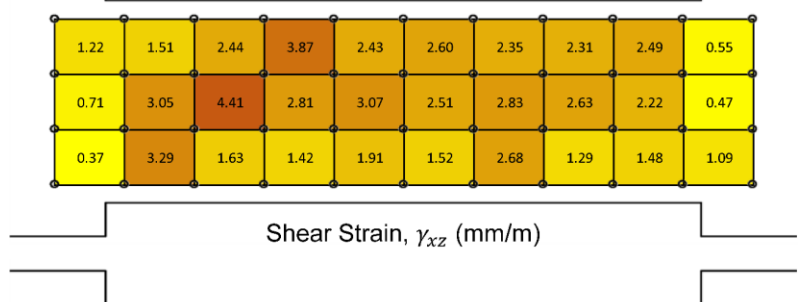
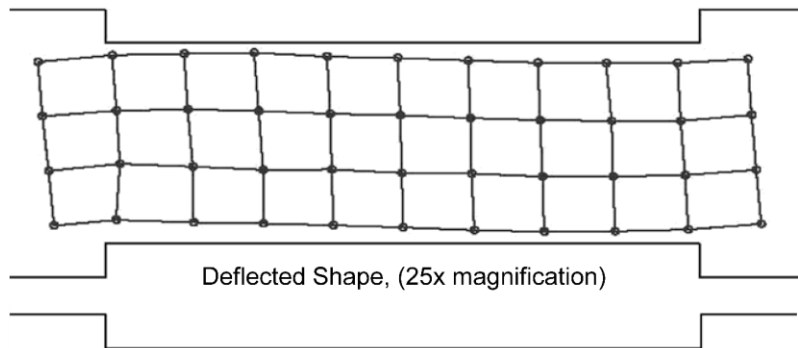
### F.3 LED Element Data for Specimen CBF3

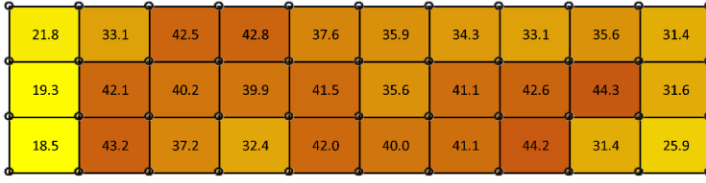
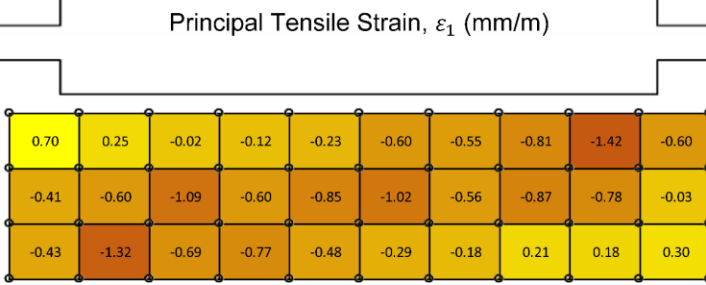
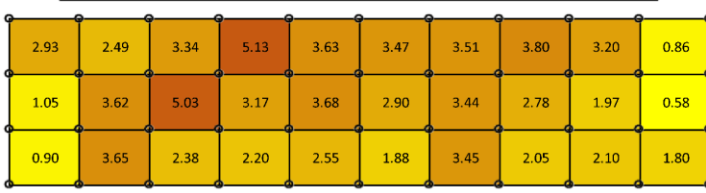
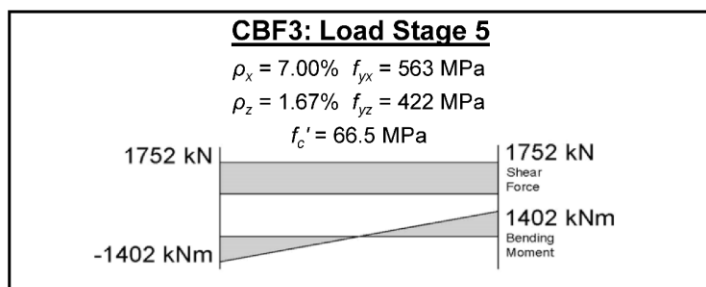
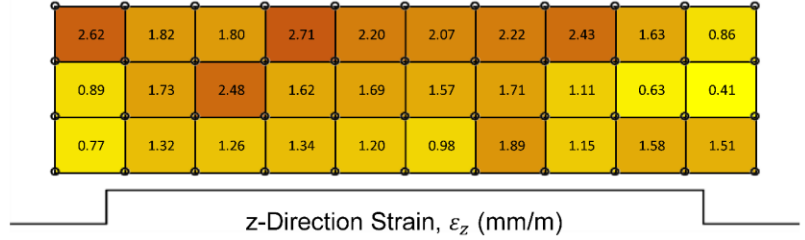
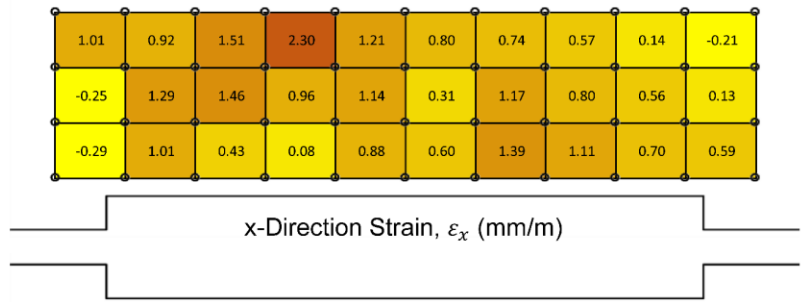
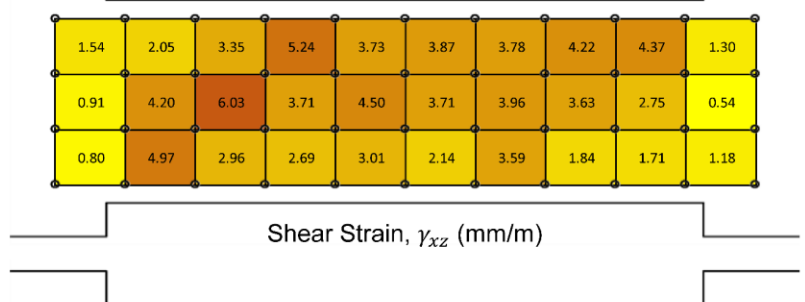
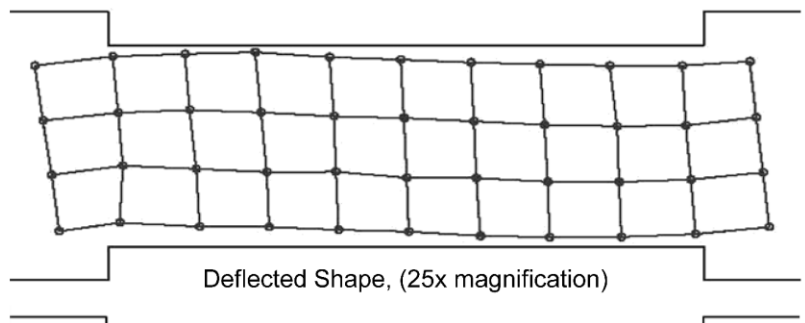
From the deformed shape of the coupling beam in the diagrams, it can be seen that LED target 8 (the bottom LED in column two) was not attached to the concrete surface in the correct location. This was not noticed until after the test was completed. As a result, LED elements 3 and 6 do not accurately represent the strain state at these locations.

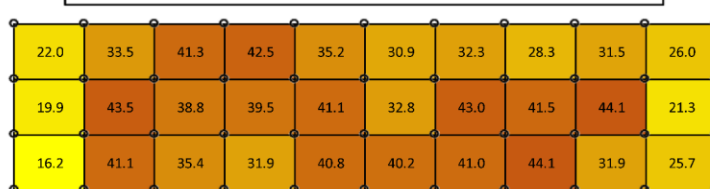
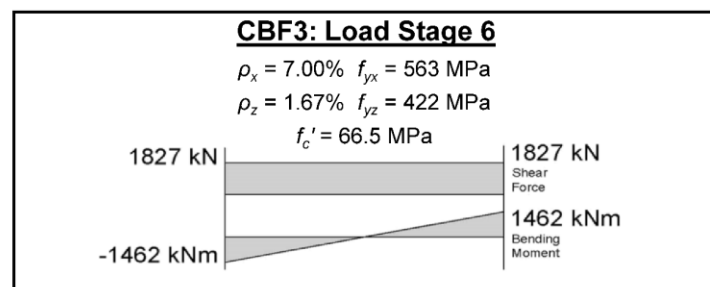
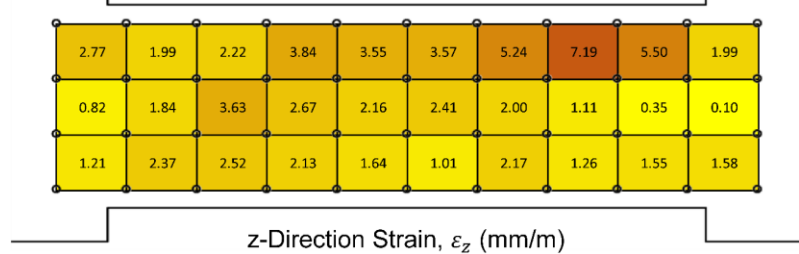
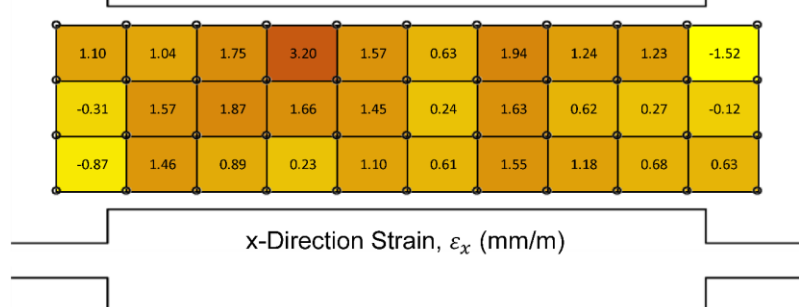
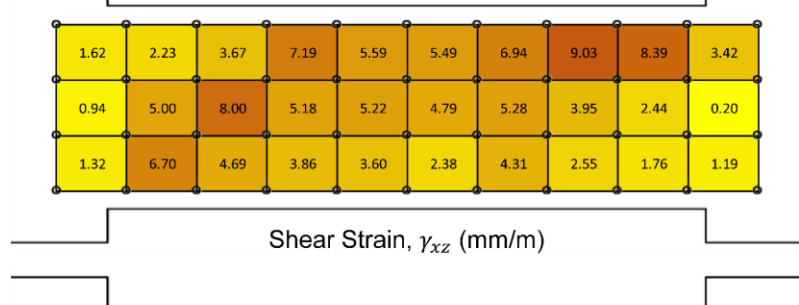
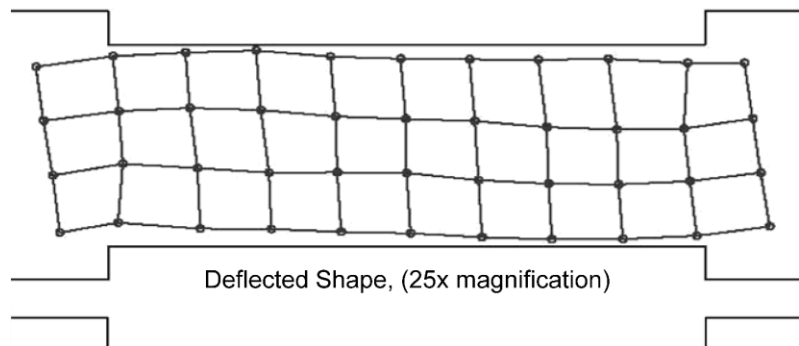
After the first load stage was completed, the LED camera system crashed resulting in a loss of LED data. The system was restarted without issue and was able to record measurements for the remainder of the test.

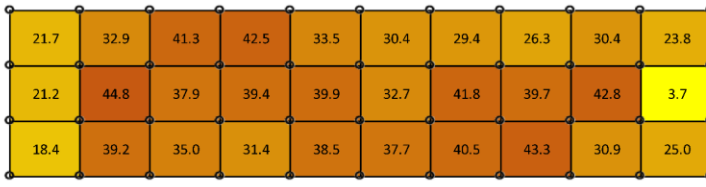
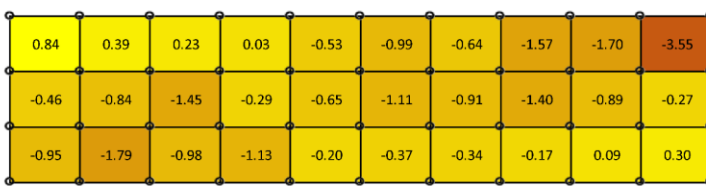
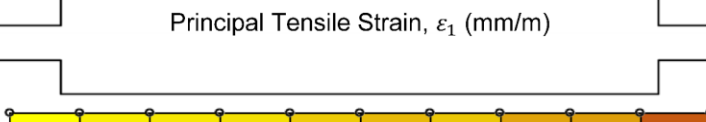
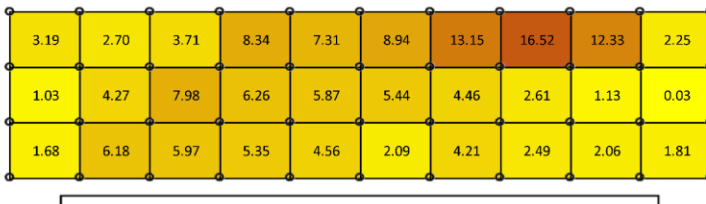
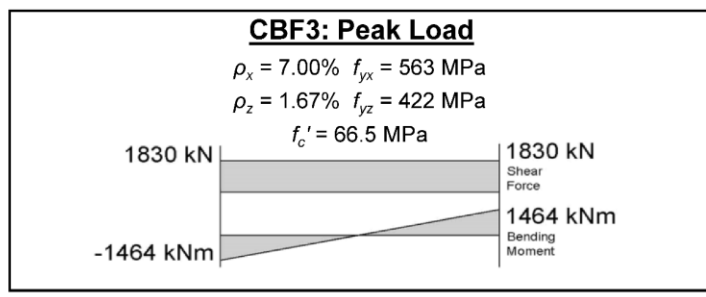
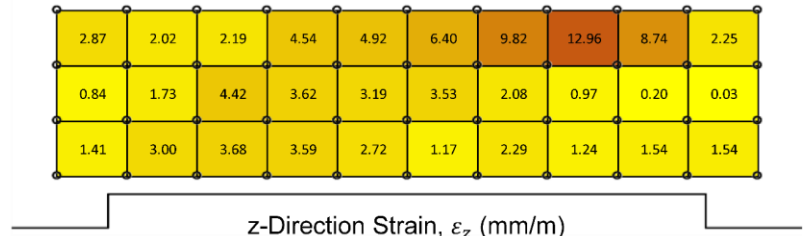
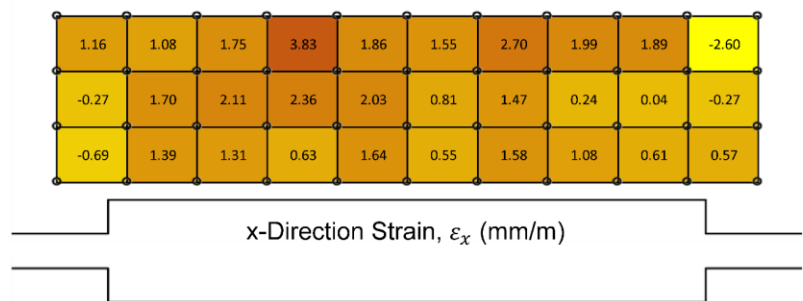
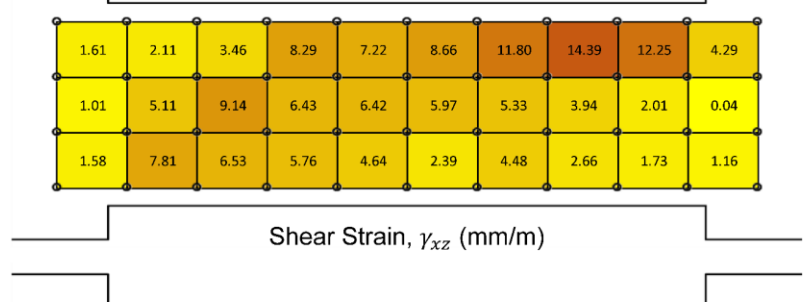
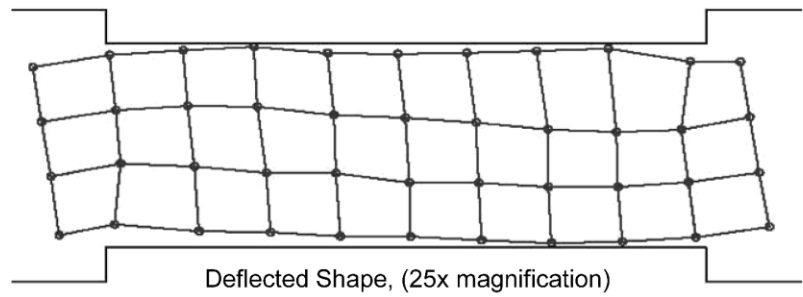


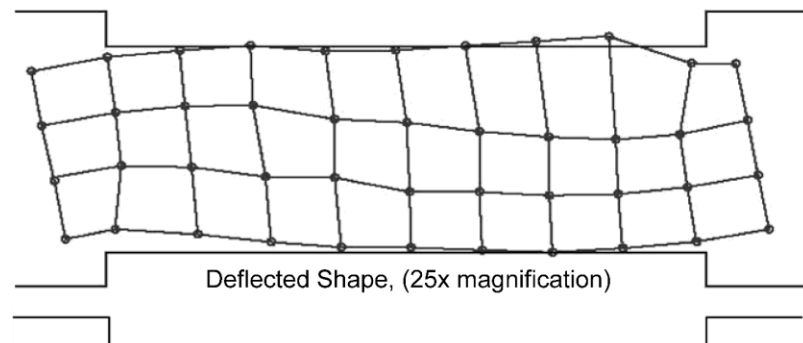








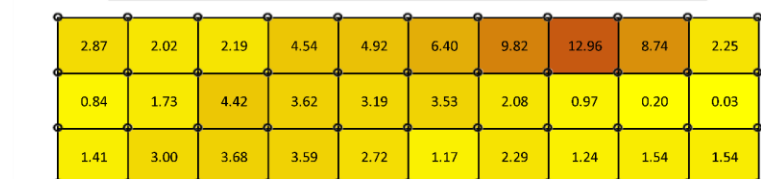




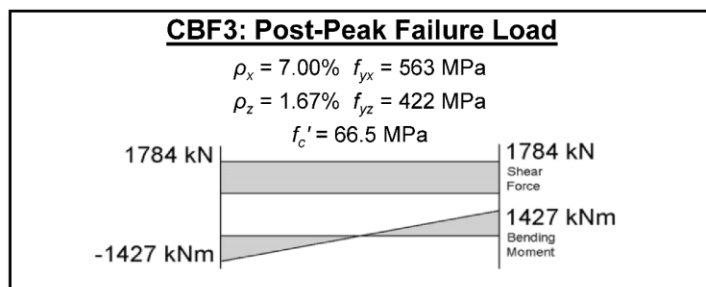
Shear Strain,  $\gamma_{xz}$  (mm/m)



x-Direction Strain,  $\varepsilon_x$  (mm/m)



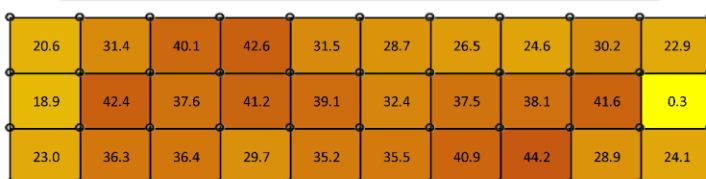
z-Direction Strain,  $\varepsilon_z$  (mm/m)



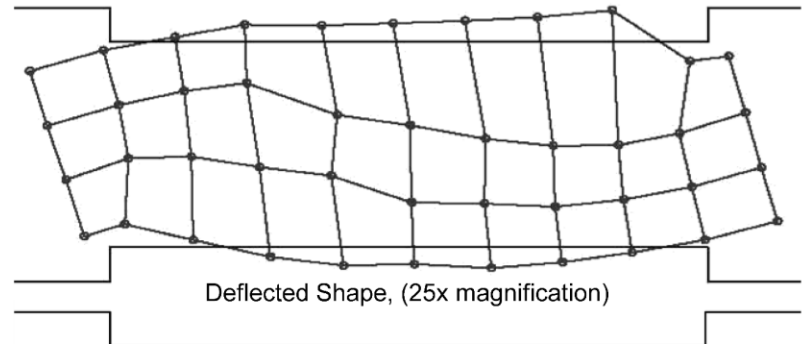
Principal Tensile Strain,  $\varepsilon_1$  (mm/m)



Principal Compressive Strain,  $\varepsilon_2$  (mm/m)



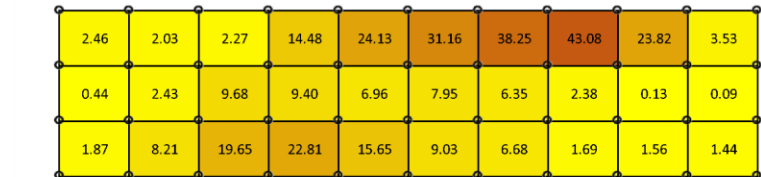
Angle of Principal Compression,  $\theta$  (degrees)



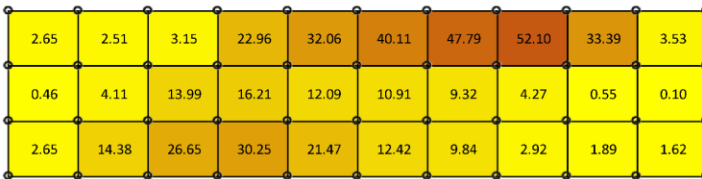
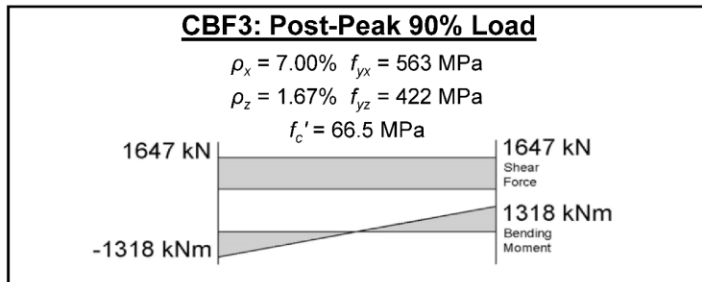
Shear Strain,  $\gamma_{xz}$  (mm/m)



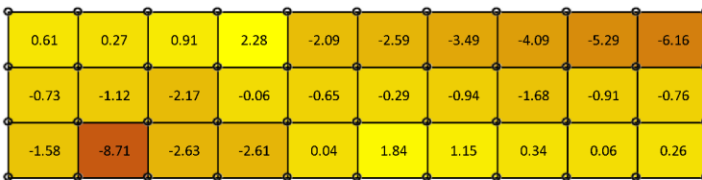
x-Direction Strain,  $\varepsilon_x$  (mm/m)



z-Direction Strain,  $\varepsilon_z$  (mm/m)



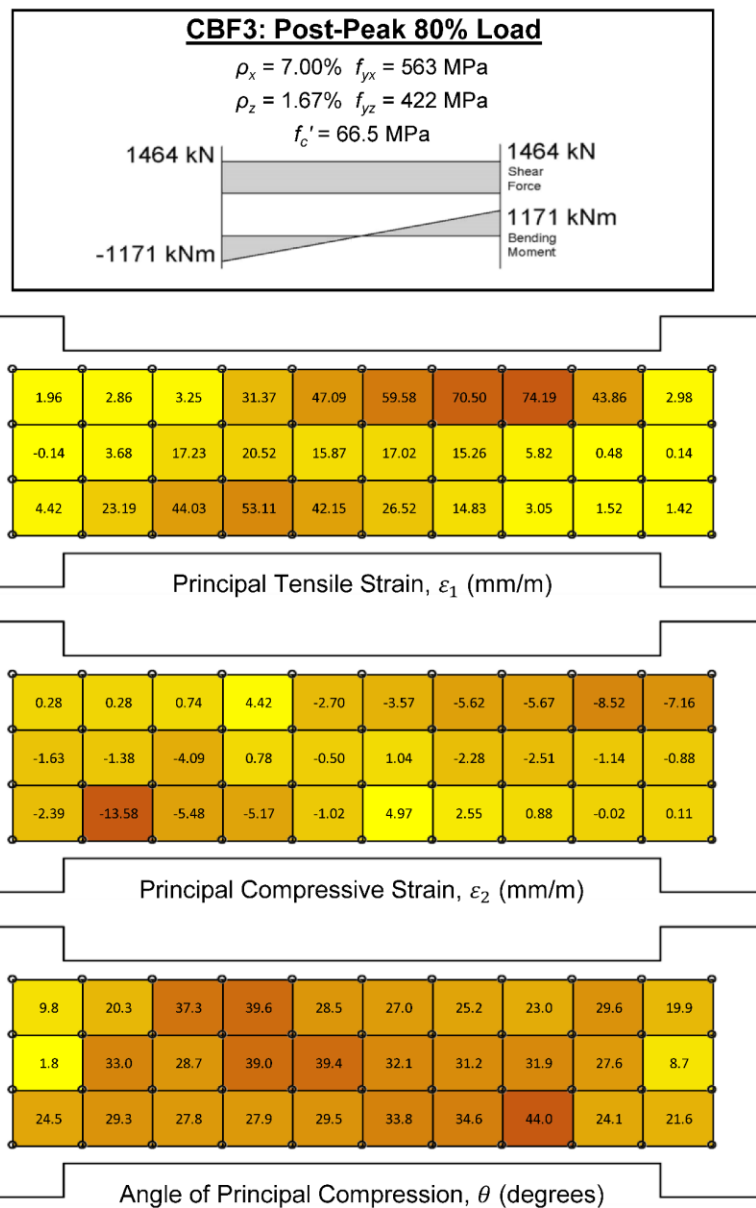
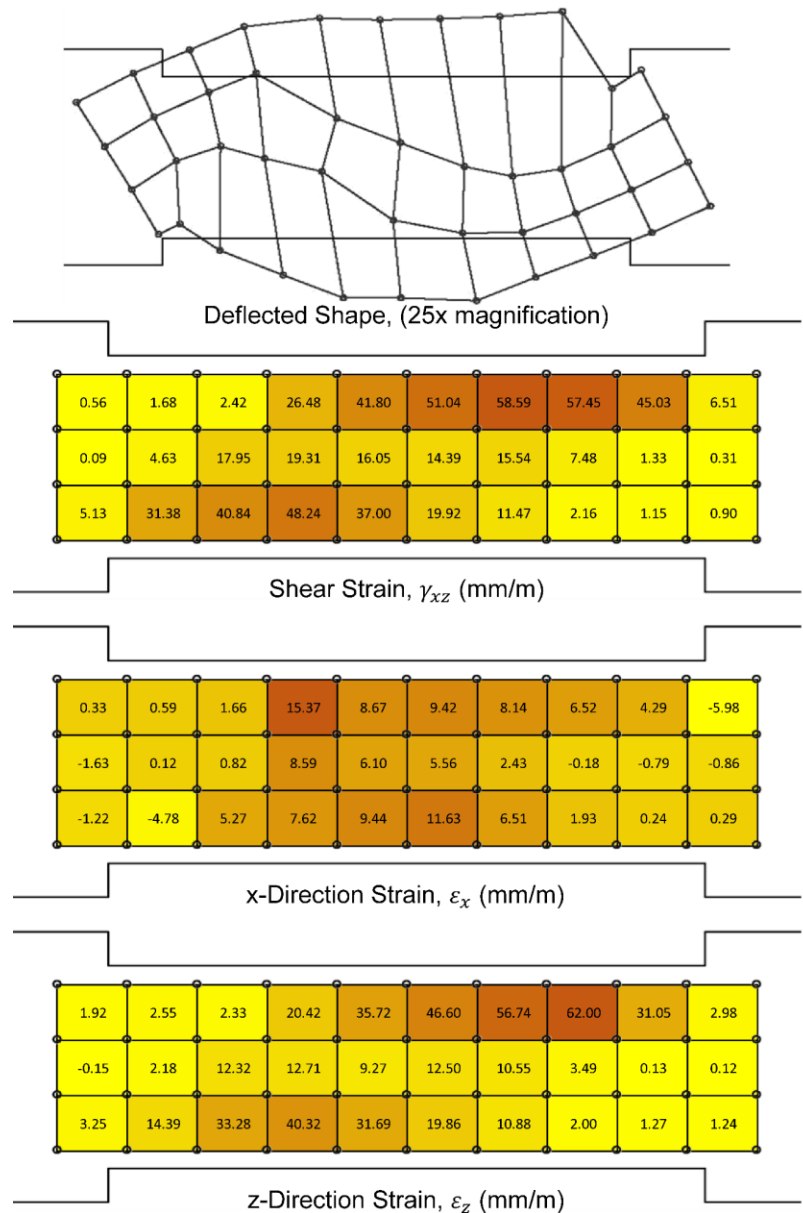
Principal Tensile Strain,  $\varepsilon_1$  (mm/m)

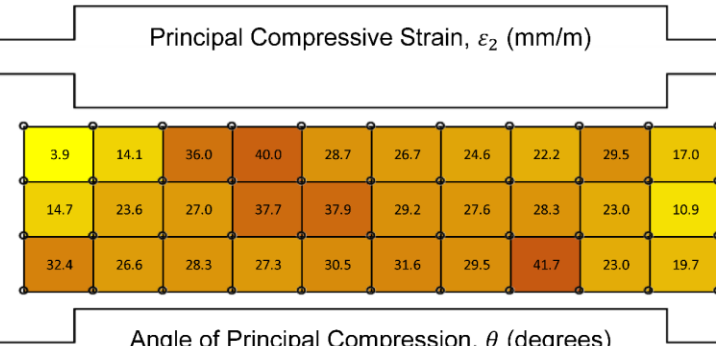
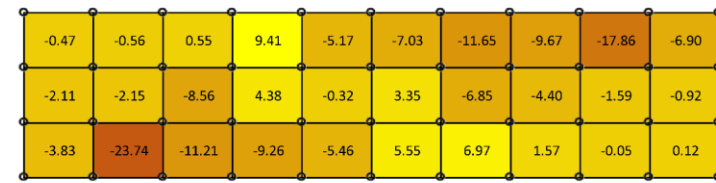
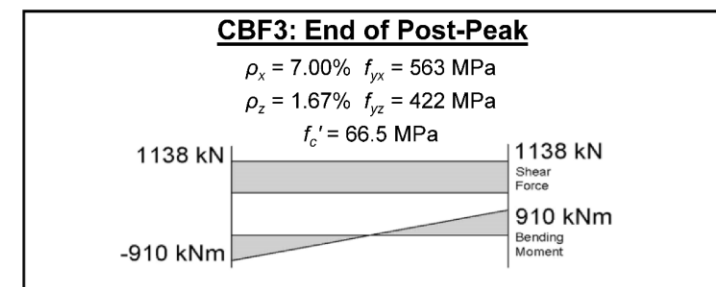
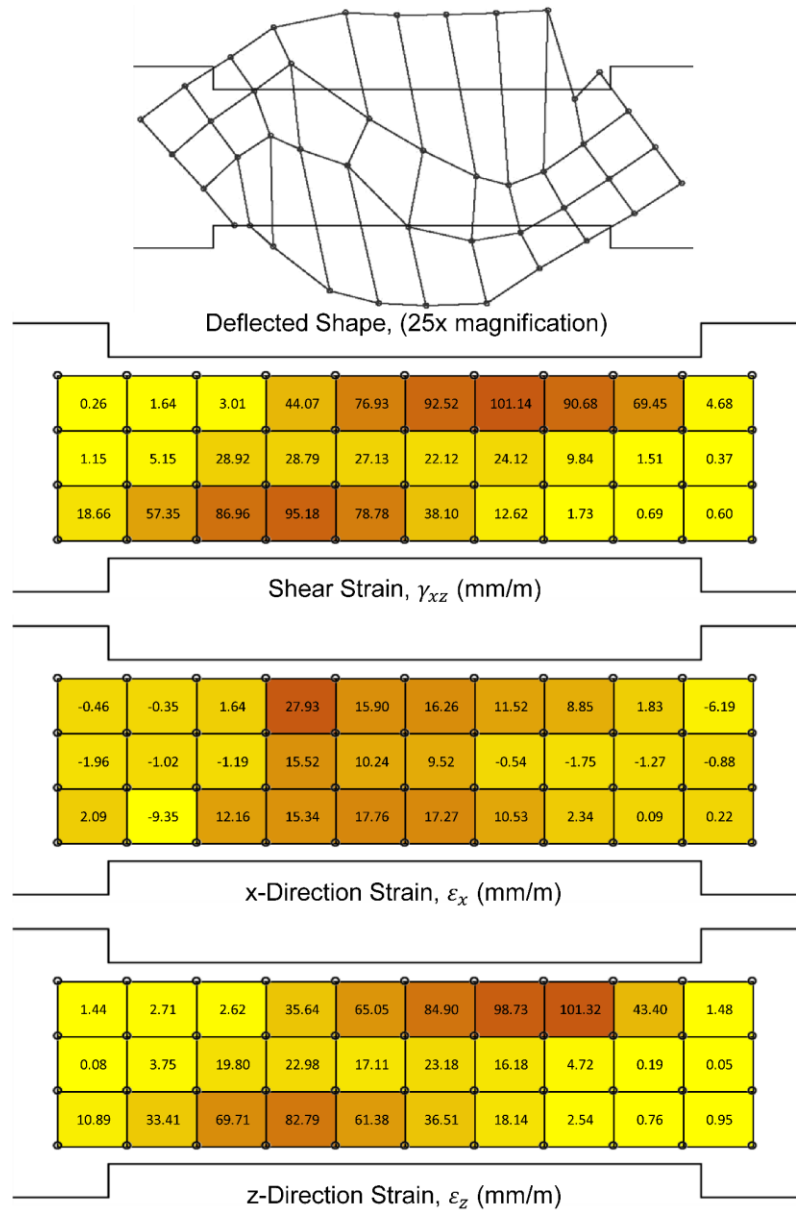


Principal Compressive Strain,  $\varepsilon_2$  (mm/m)

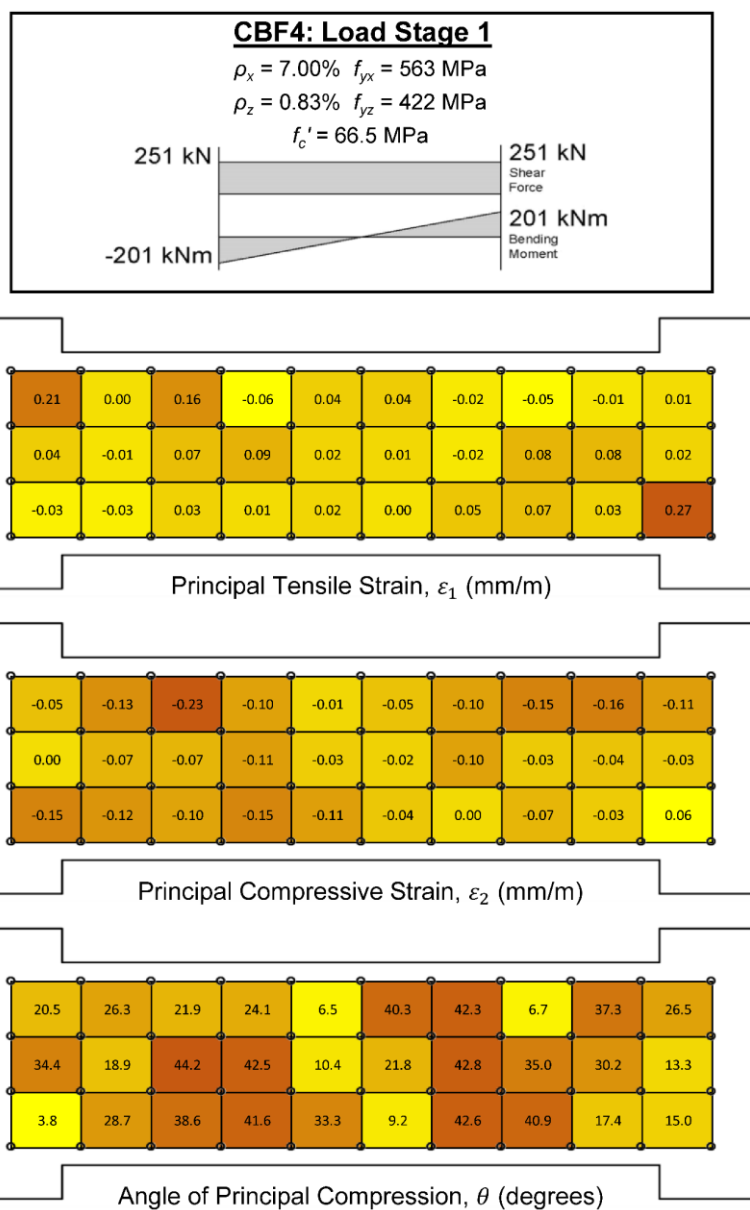
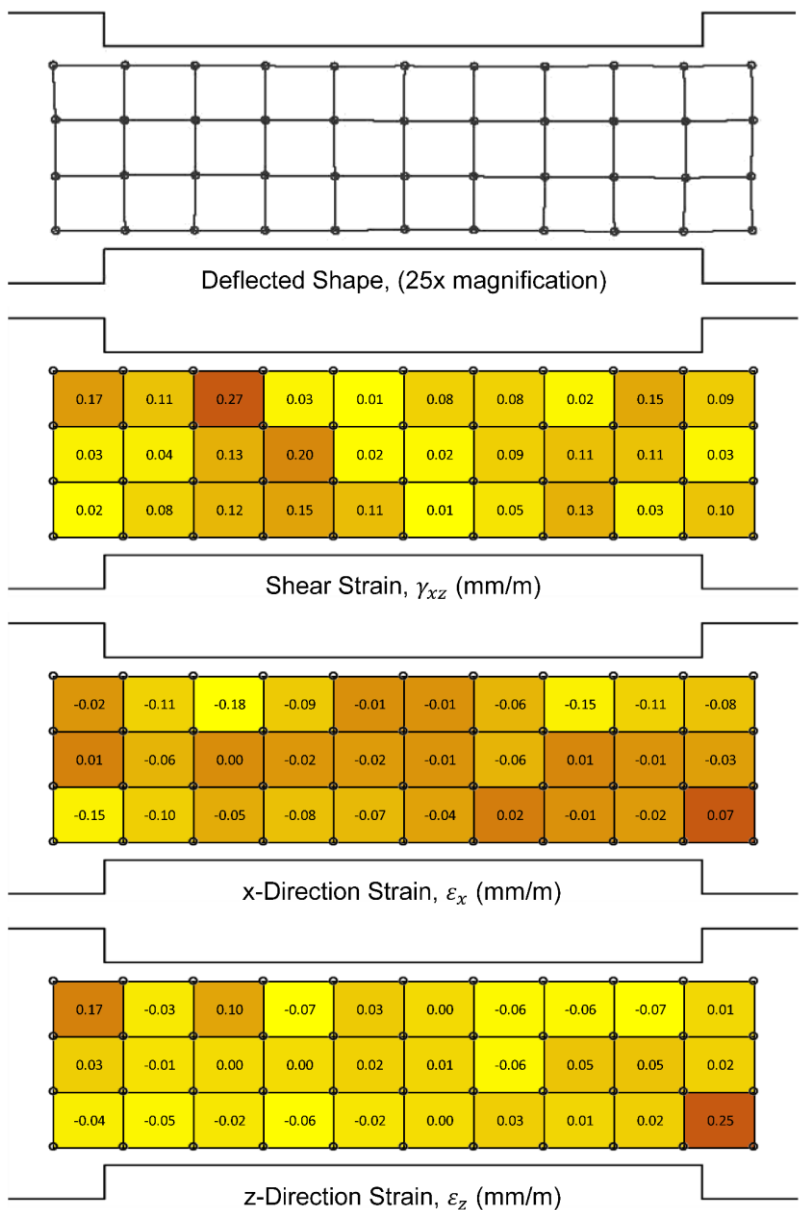


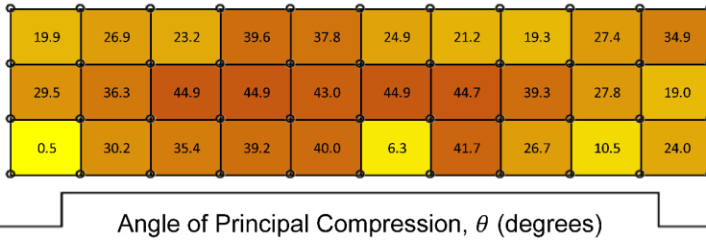
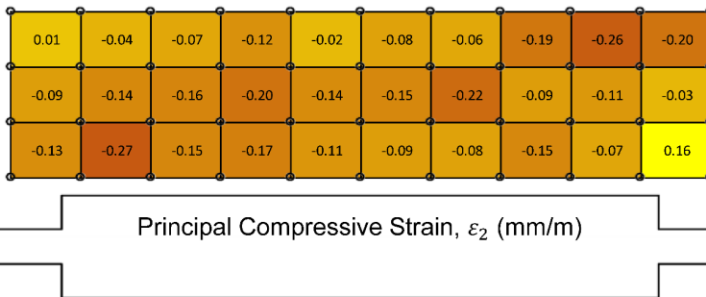
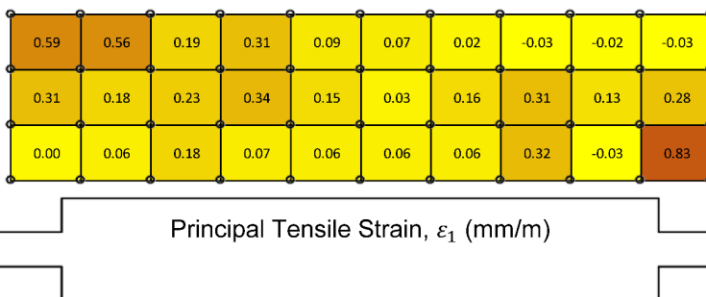
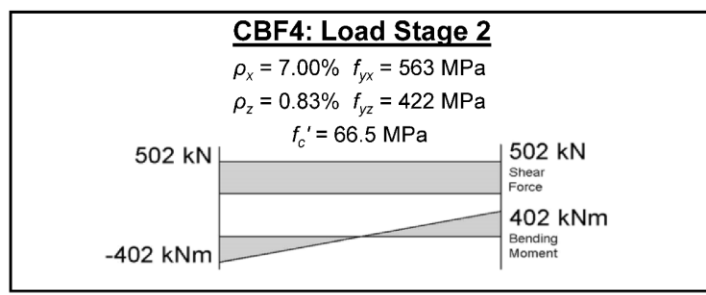
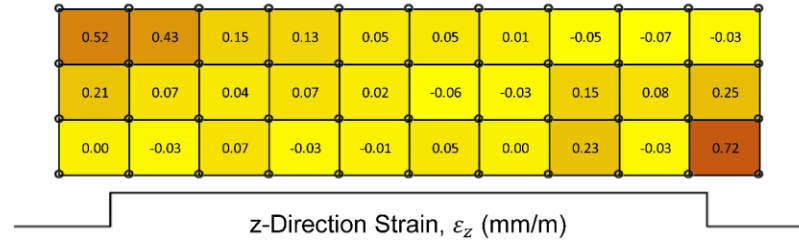
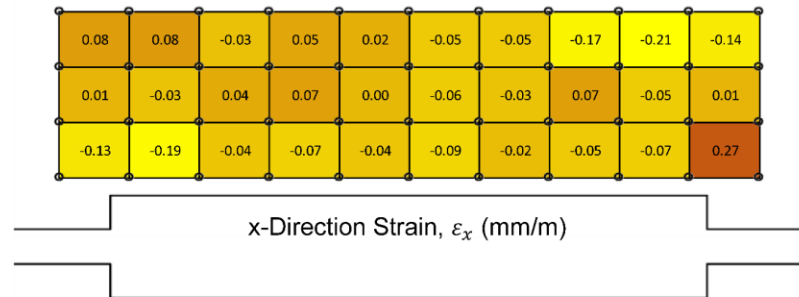
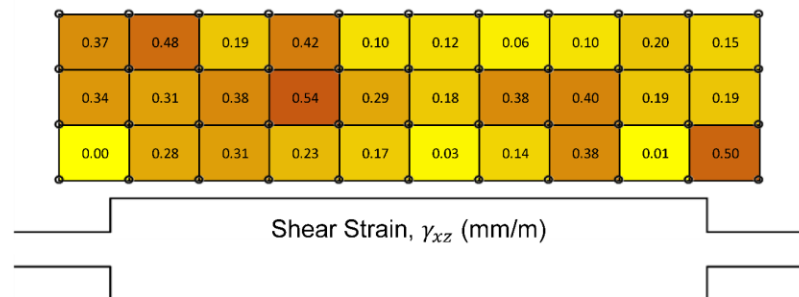
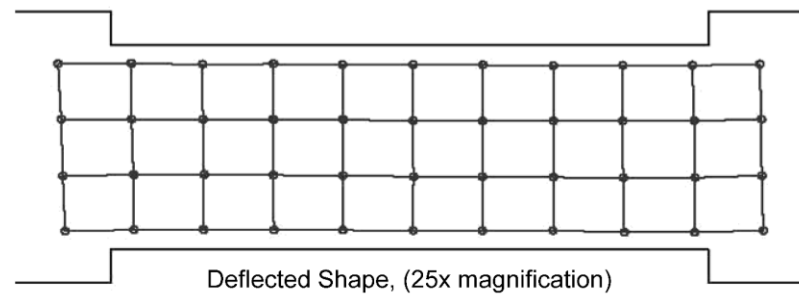
Angle of Principal Compression,  $\theta$  (degrees)

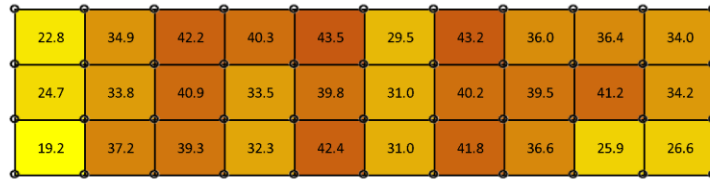
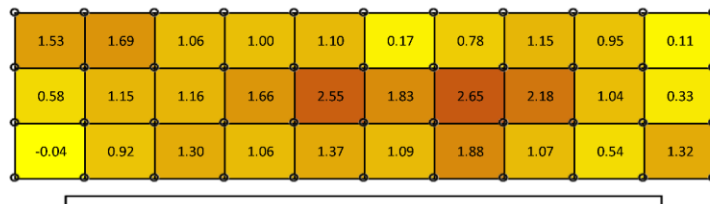
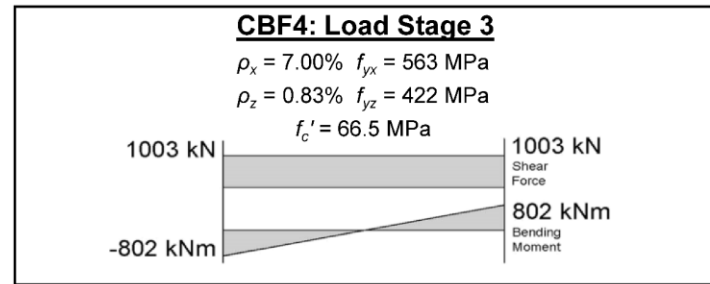
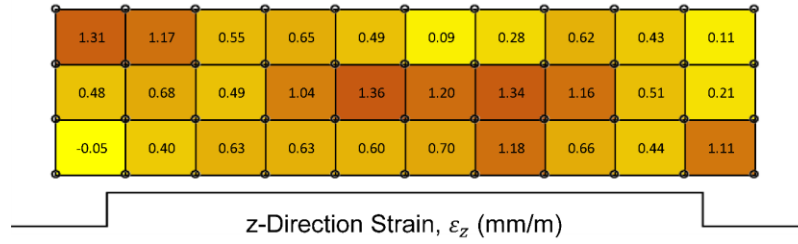
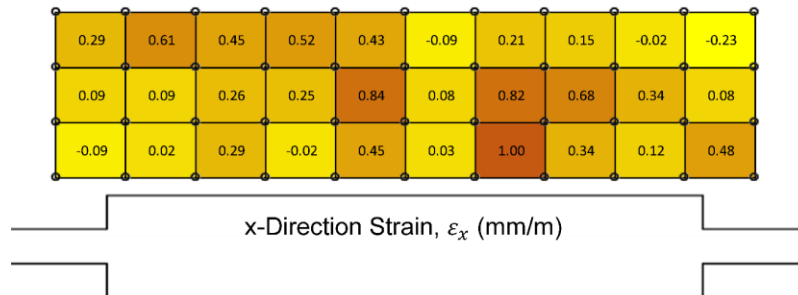
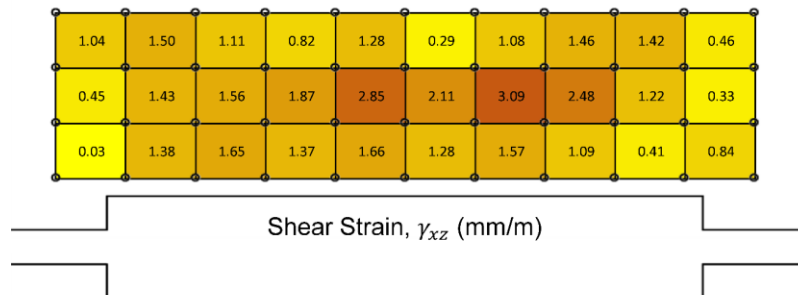
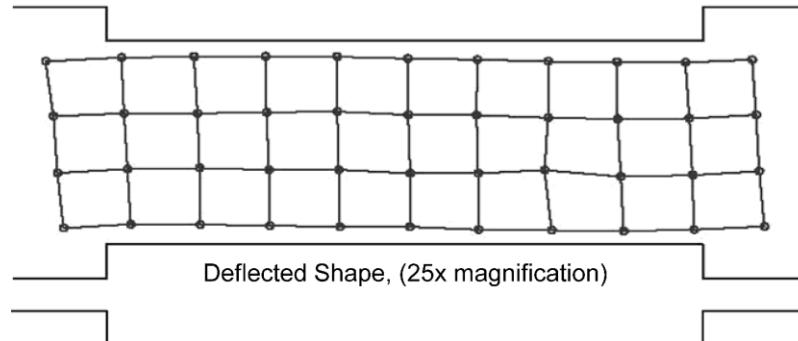


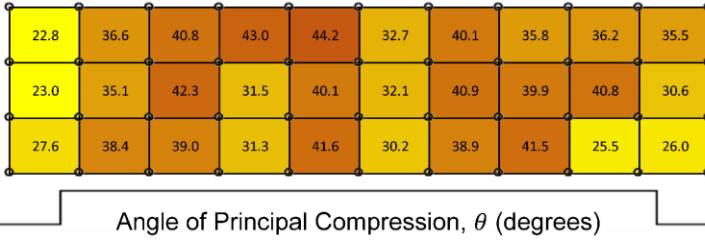
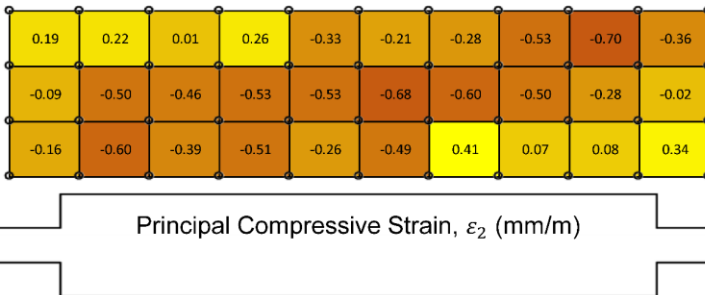
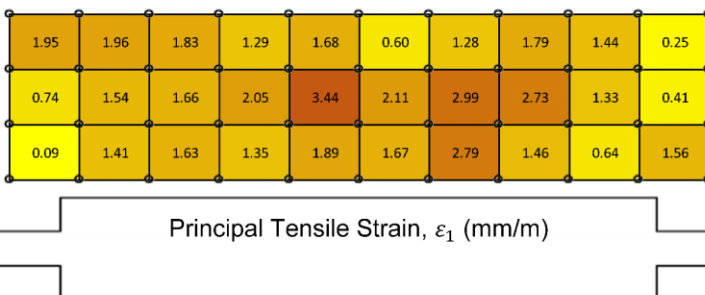
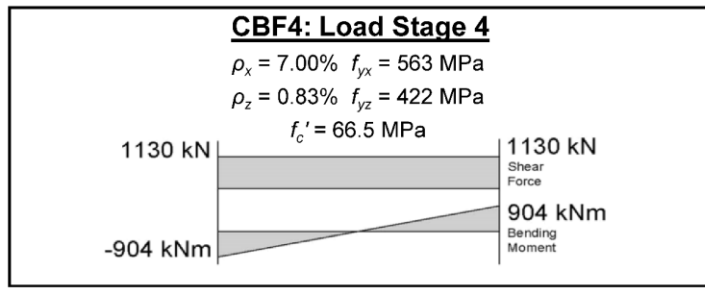
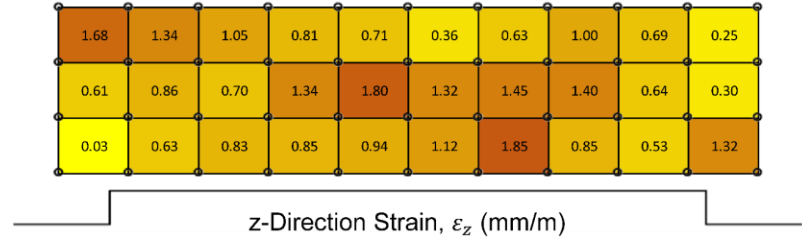
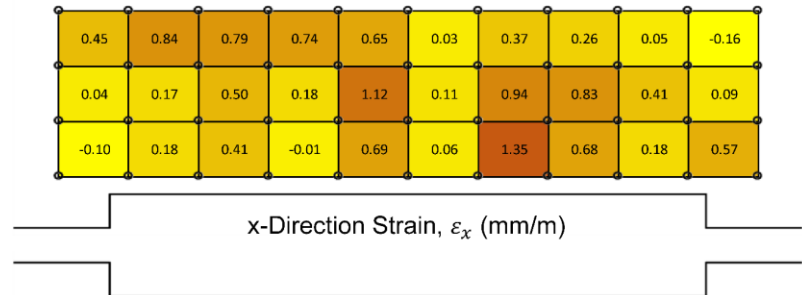
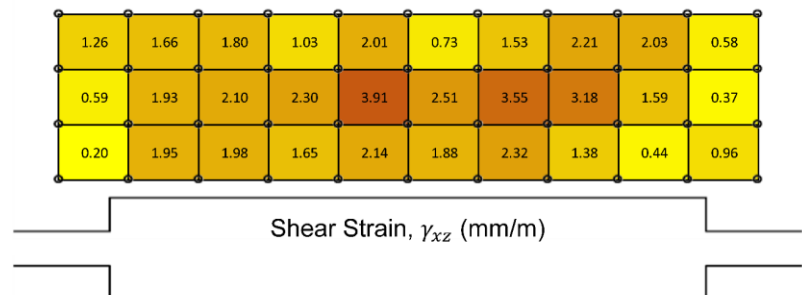
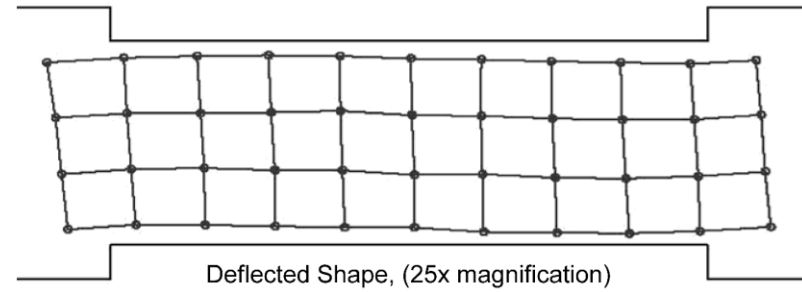


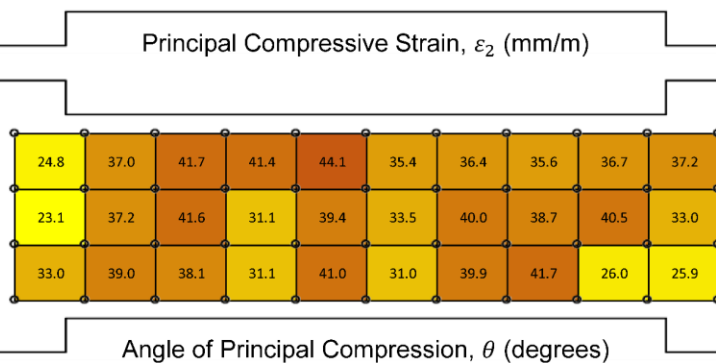
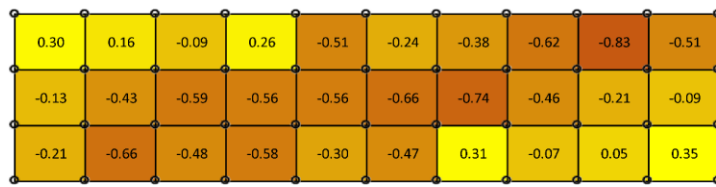
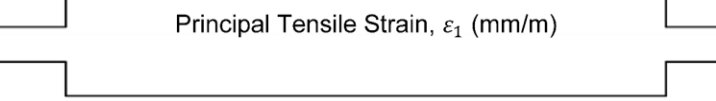
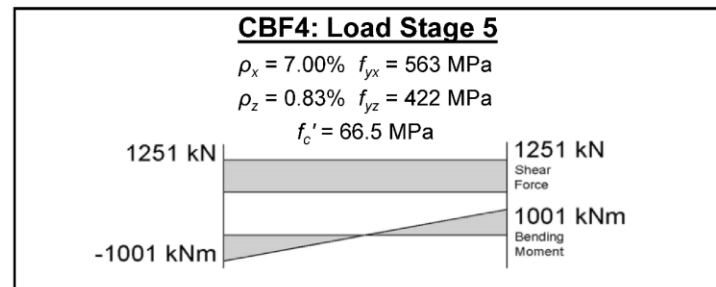
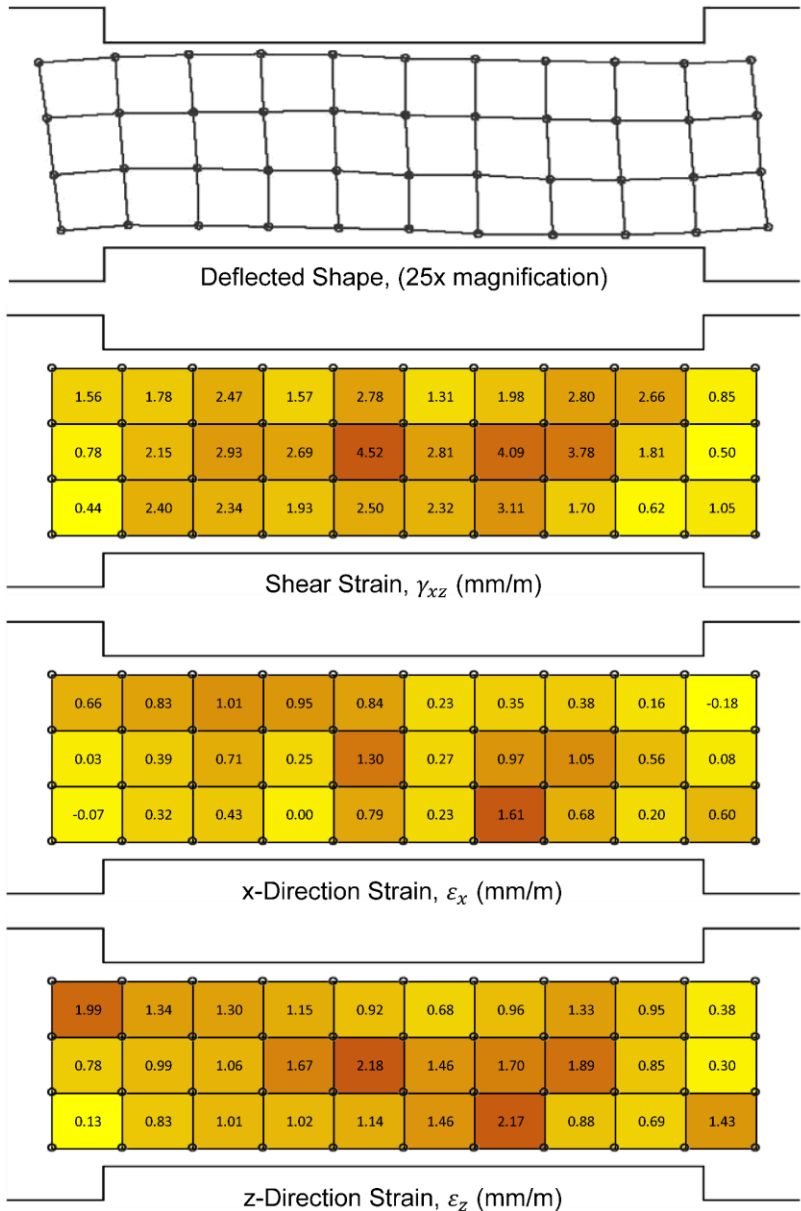
## F.4 LED Element Data for Specimen CBF4

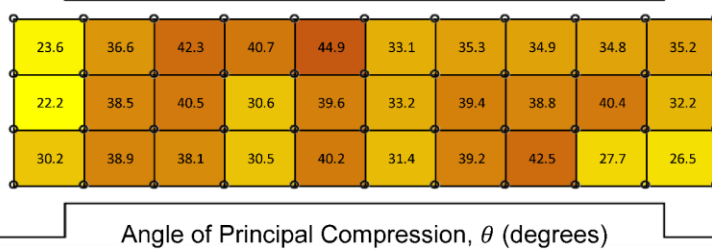
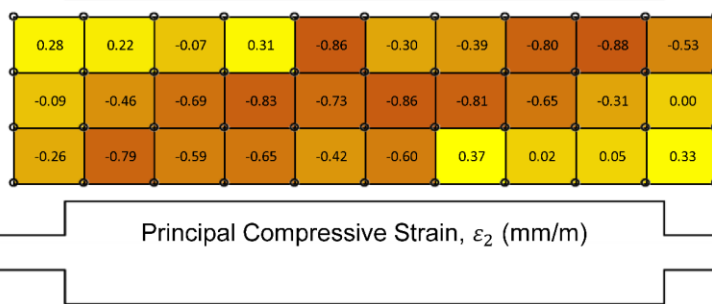
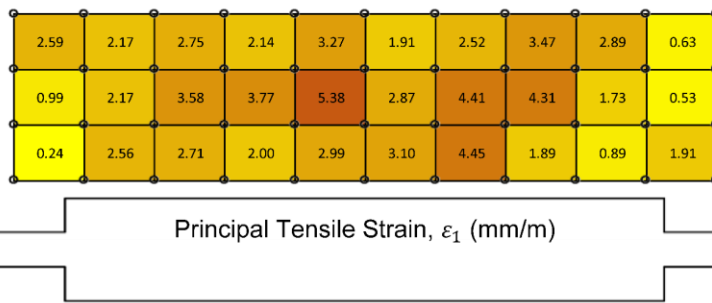
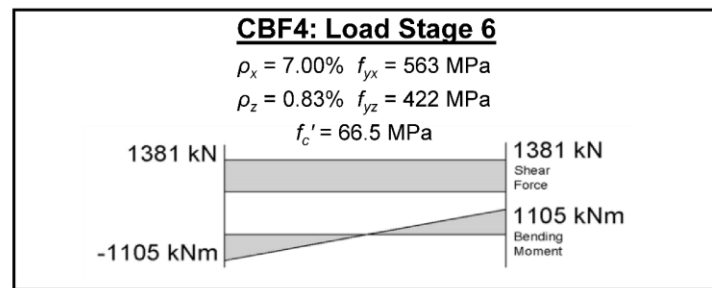
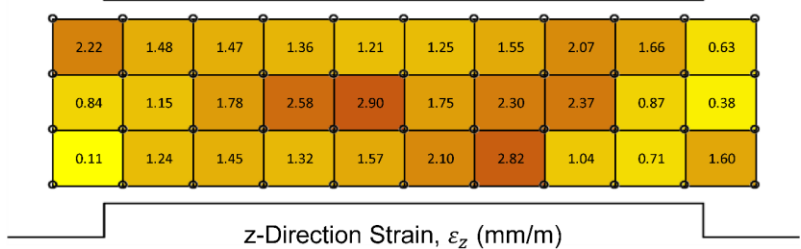
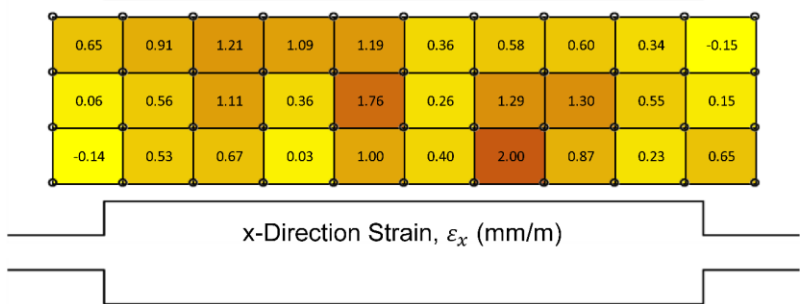
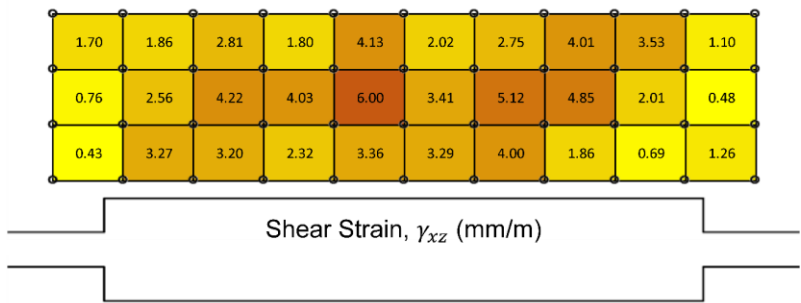
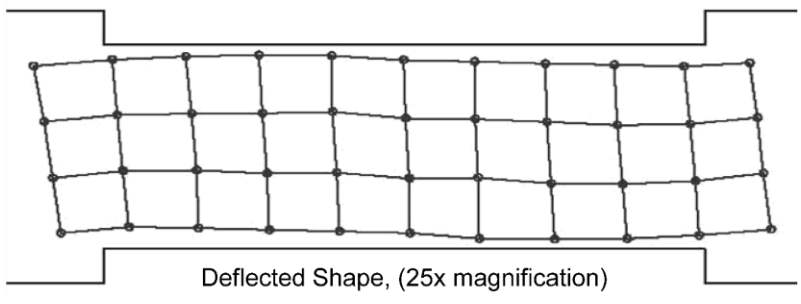


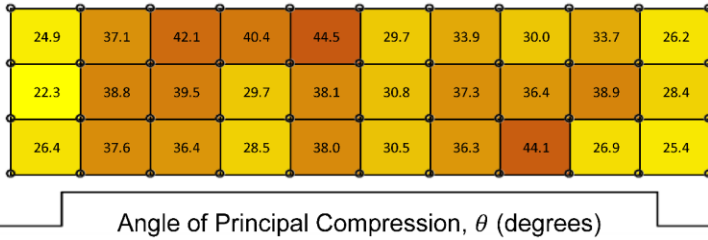
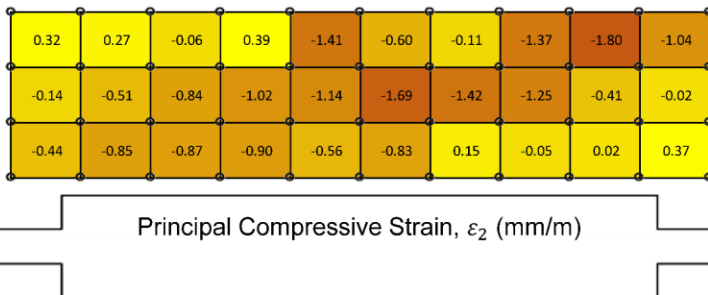
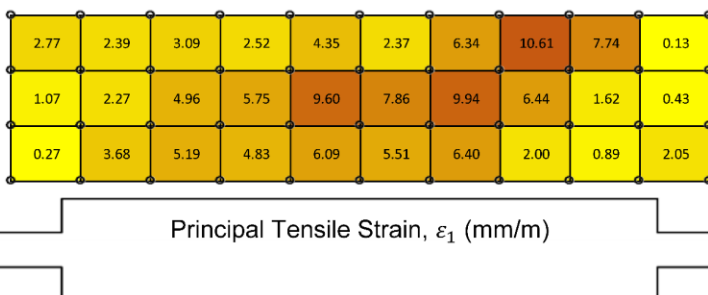
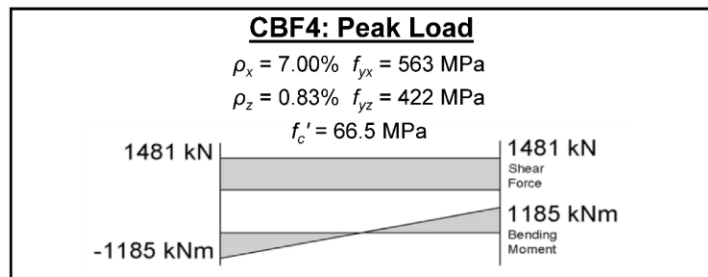
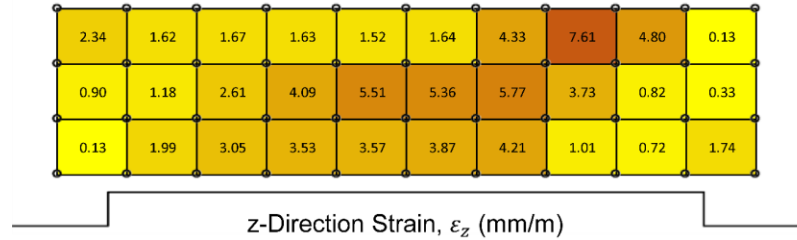
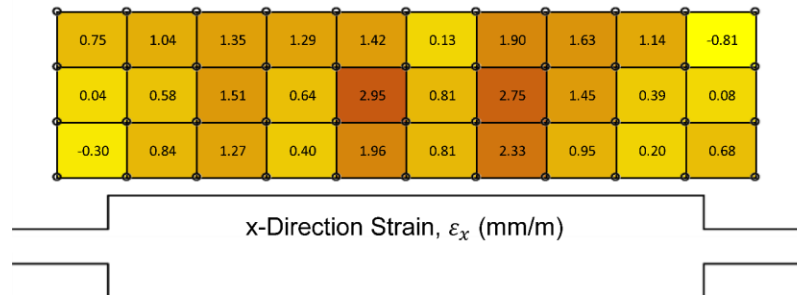
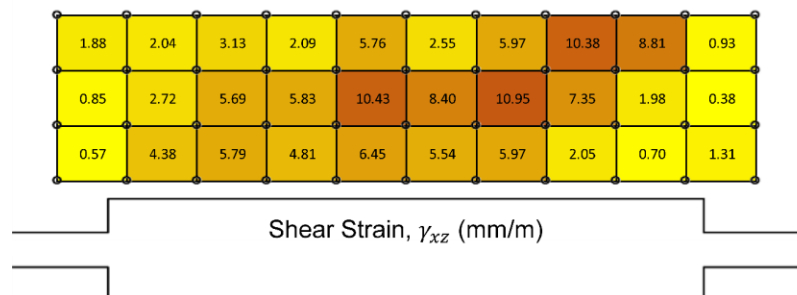
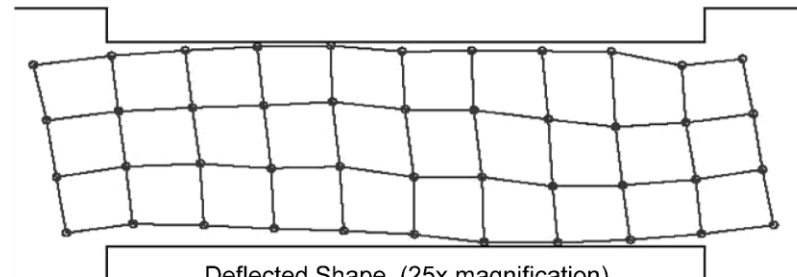


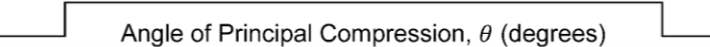
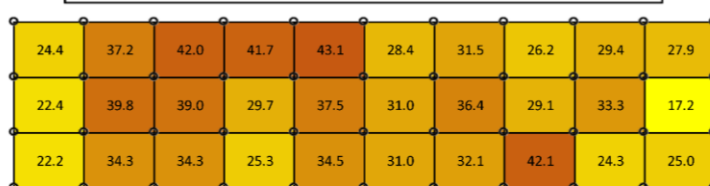
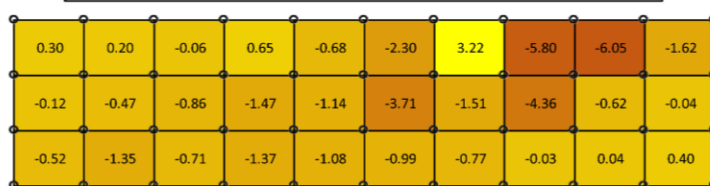
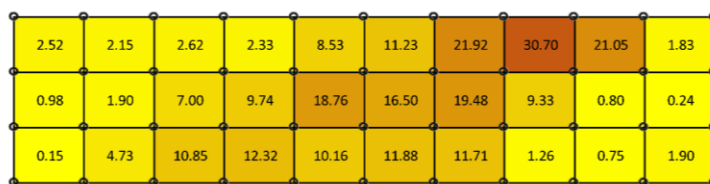
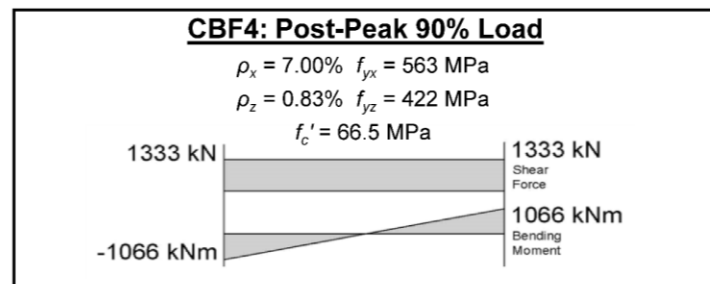
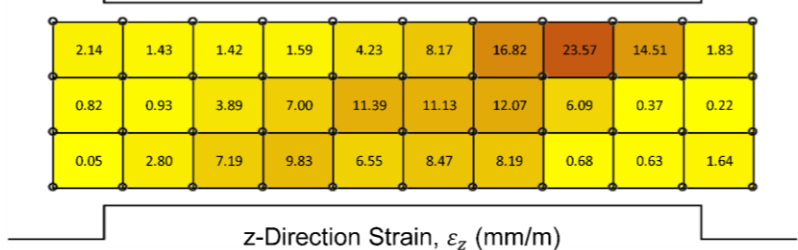
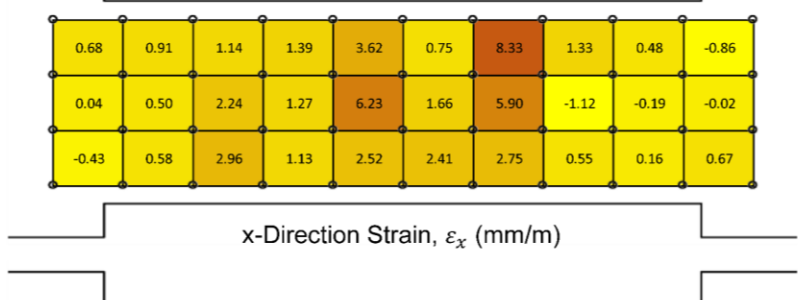
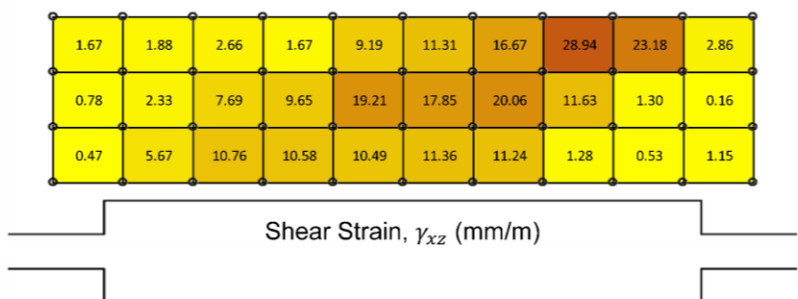
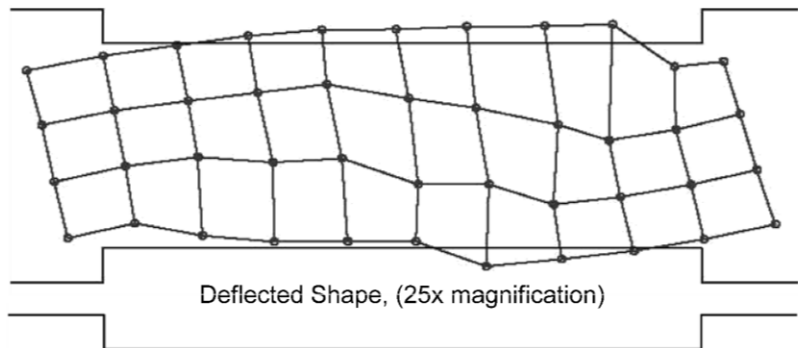


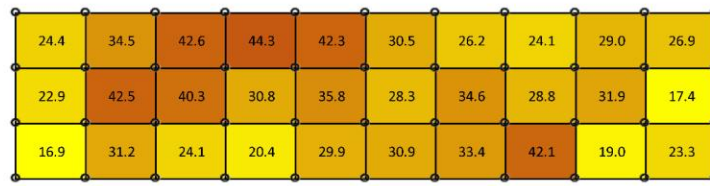
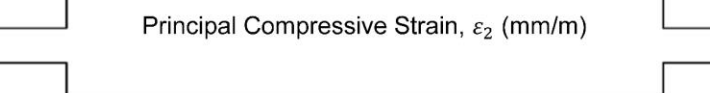
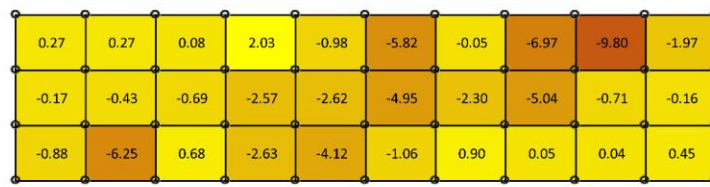
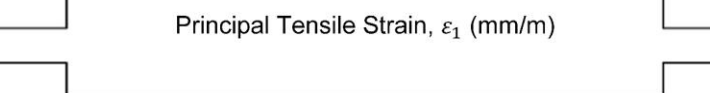
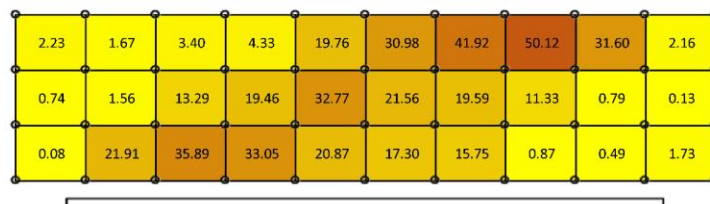
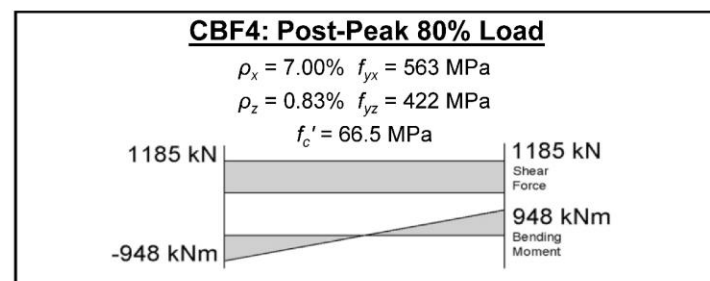
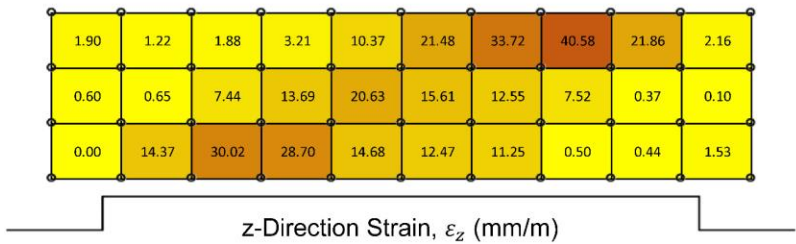
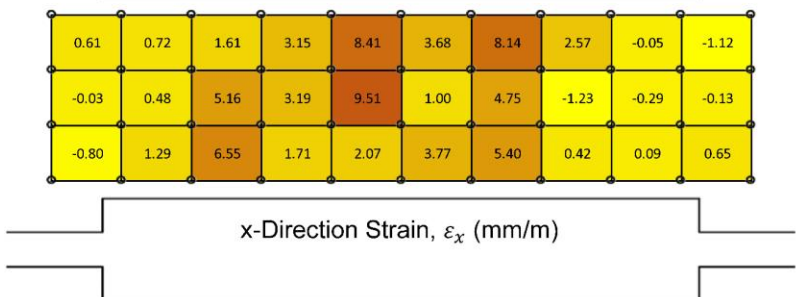
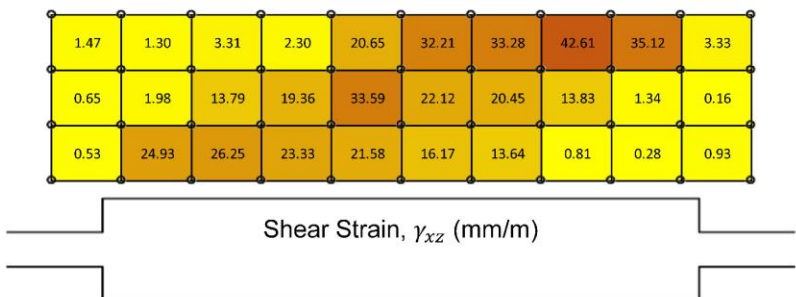
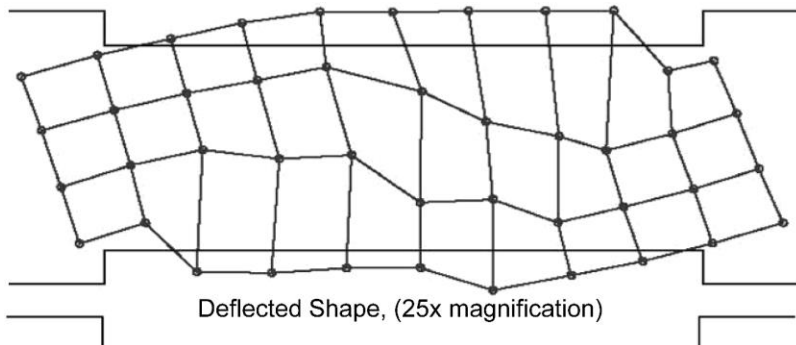


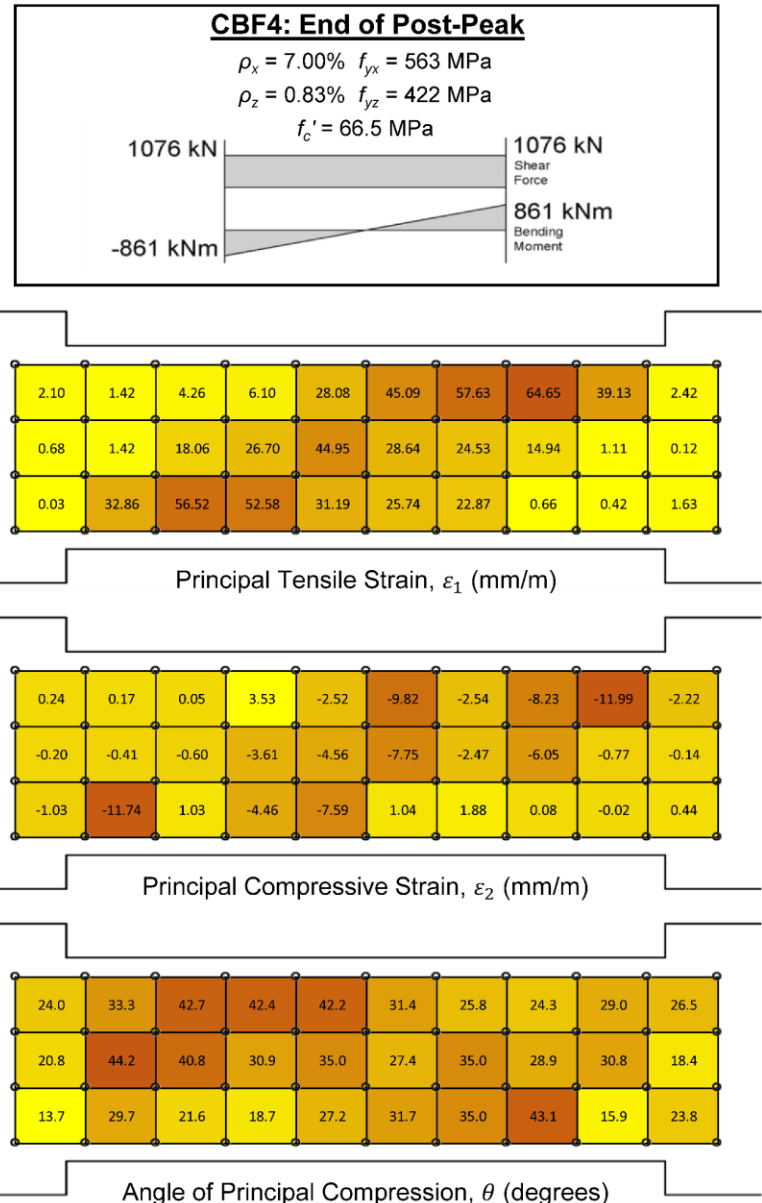
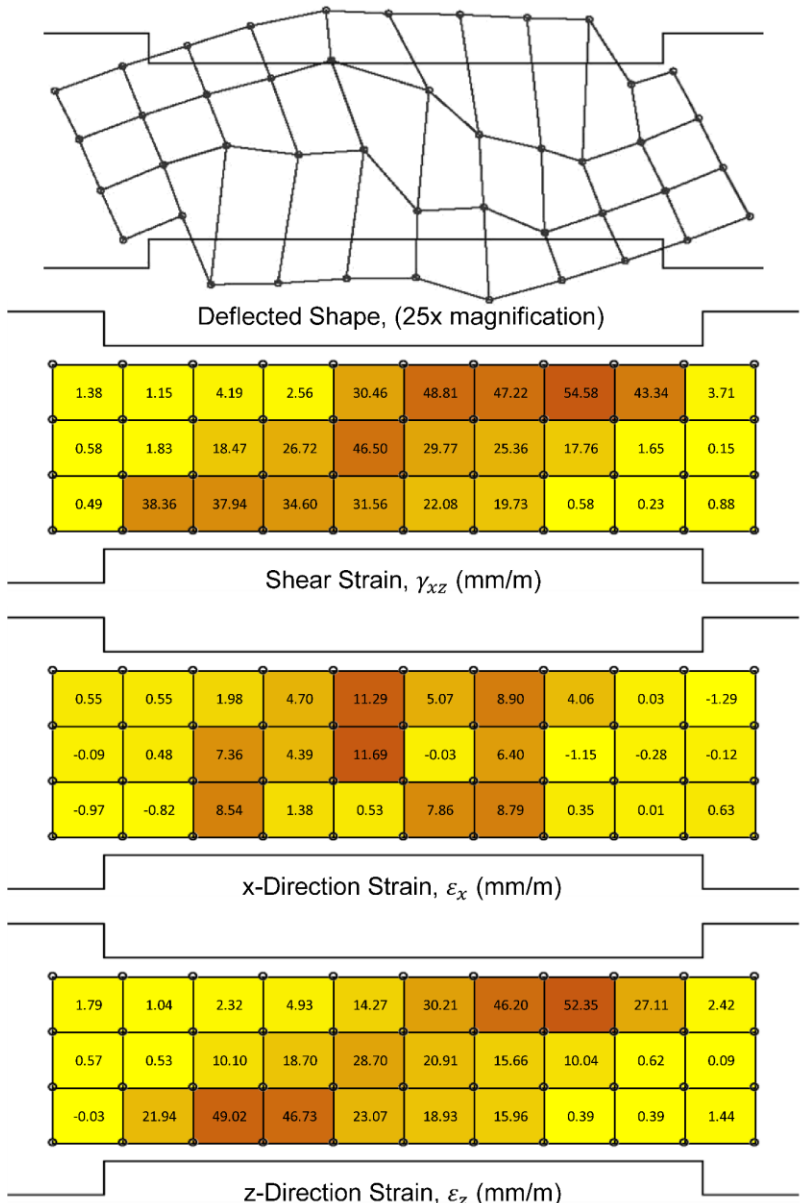












## Appendix G: Mander Model for Confined Concrete

In order to model the beneficial effects of the confined coupling beam core, the theoretical stress-strain model for confined concrete developed by Mander, Priestley, and Park (1988) [34] was implemented with the MCFT in the program Membrane. This model is defined by the following equations:

$$f_c = \frac{f'_{cc} \left( \frac{e_c}{e_{cc}} \right) r}{r - 1 + \left( \frac{e_c}{e_{cc}} \right)^r}$$

$$e_{cc} = e_{co} \left[ 1 + 5 \left( \frac{f'_{cc}}{f_{co}} - 1 \right) \right]$$

$$r = \frac{E_c}{E_c - E_{sec}} \quad E_{sec} = \frac{f'_{cc}}{e_{cc}} \quad E_c = 5000\sqrt{f'_c} \text{ (MPa)}$$

Where  $e_c$  is the longitudinal compressive strain;  $f'_{cc}$  and  $e_{cc}$  are the confined concrete strength and associated strain; and  $f_{co}$  and  $e_{co}$  are the unconfined concrete strength and associated strain. A visual representation of the listed variables is presented in Figure G-1 [34].

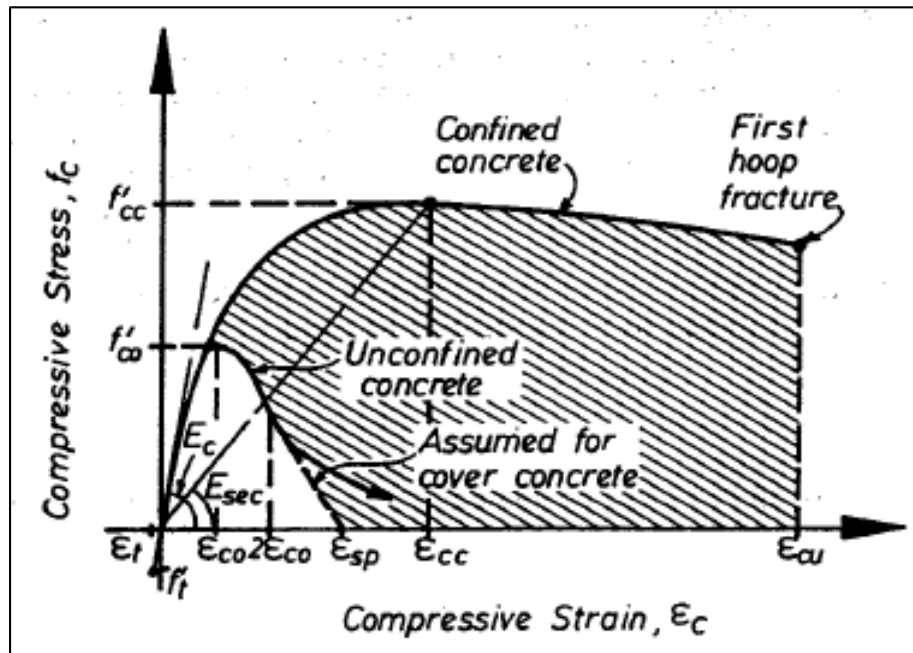


Figure G-1: Stress-Strain Model for Confined Concrete

The confined compressive strength of the concrete,  $f'_{cc}$ , is calculated using a robust formula that is based on the effective confinement area of the coupling beam core. The confined compressive strength for rectangular sections can be defined quickly with the help of Figure G-2 [34].

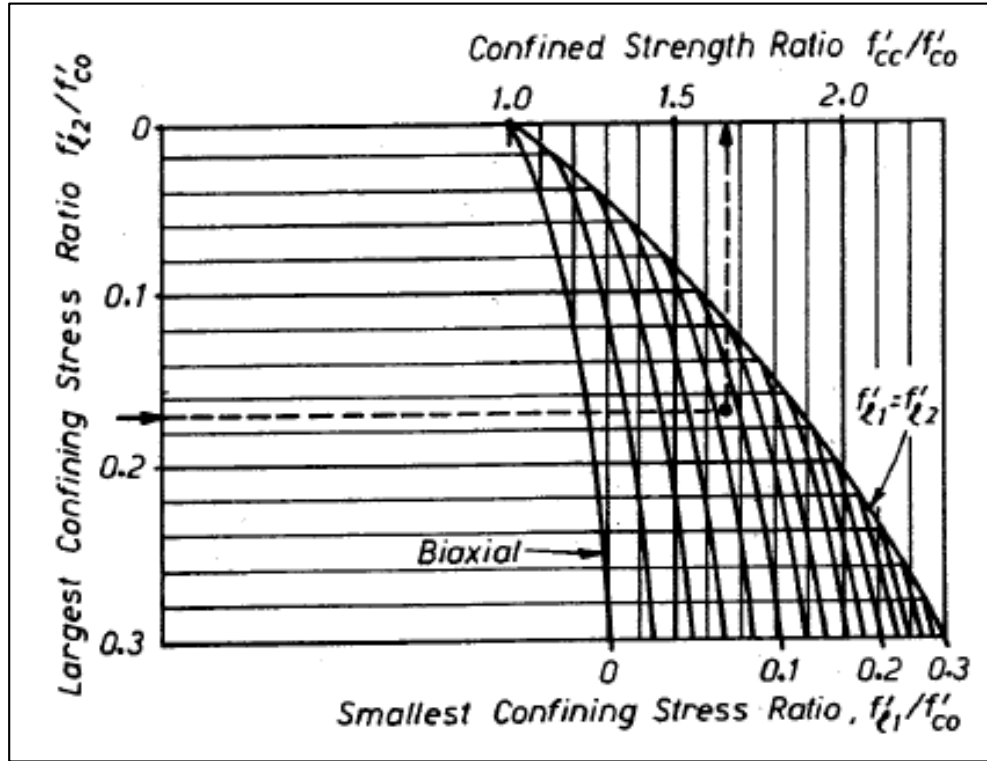


Figure G-2: Confined Strength Model for Rectangular Sections

In order to use the above chart, the lateral confining stresses for each side of the rectangular member are required. The confinement stresses are defined using the following formulas:

$$f'_{l1} = k_e \frac{A_{sx}}{sd_c} f_{yh} \quad f'_{l2} = k_e \frac{A_{sy}}{sb_c} f_{yh}$$

$$k_e = \frac{\left(1 - \sum_{i=1}^n \frac{(w'_i)^2}{6b_c d_c}\right) \left(\frac{s'}{2b_c}\right) \left(\frac{s'}{2d_c}\right)}{(1 - \rho_{cc})}$$

Where  $k_e$  is the unitless confinement effectiveness factor. The variables used in this formula are geometrically based on the rectangular section. Each geometric variable is illustrated in Figure G-3 [34].

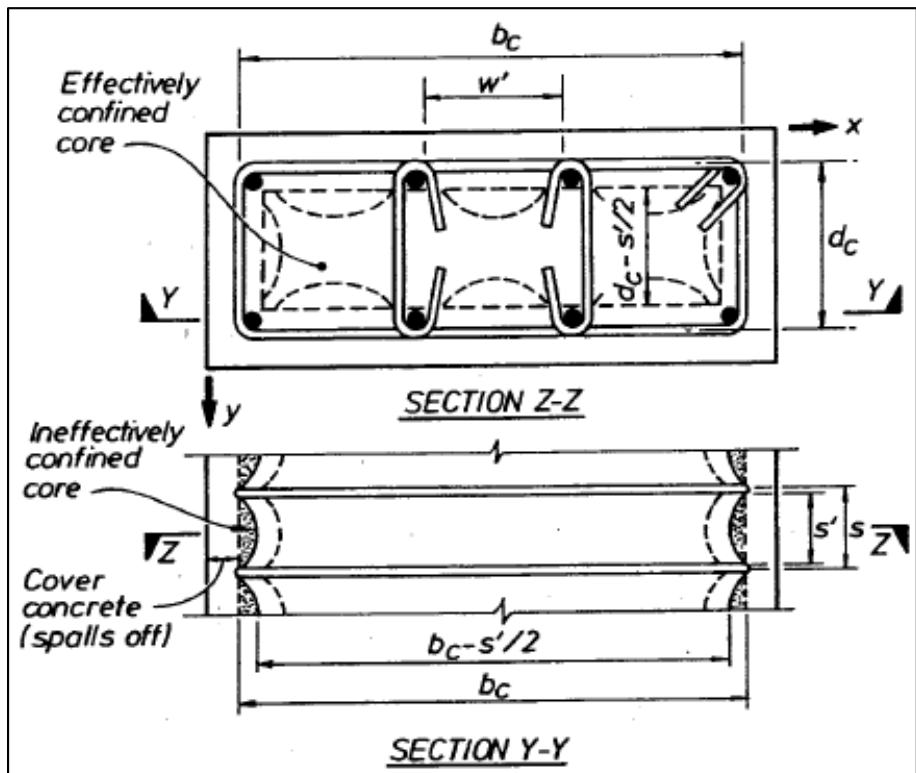


Figure G-3: Geometric Variables for Confinement Effectiveness Formula